Magneto-Rayleigh-Taylor Instability Seeding and Mitigation by Low-Density Plasma in Thin-Foil Liner Implosions

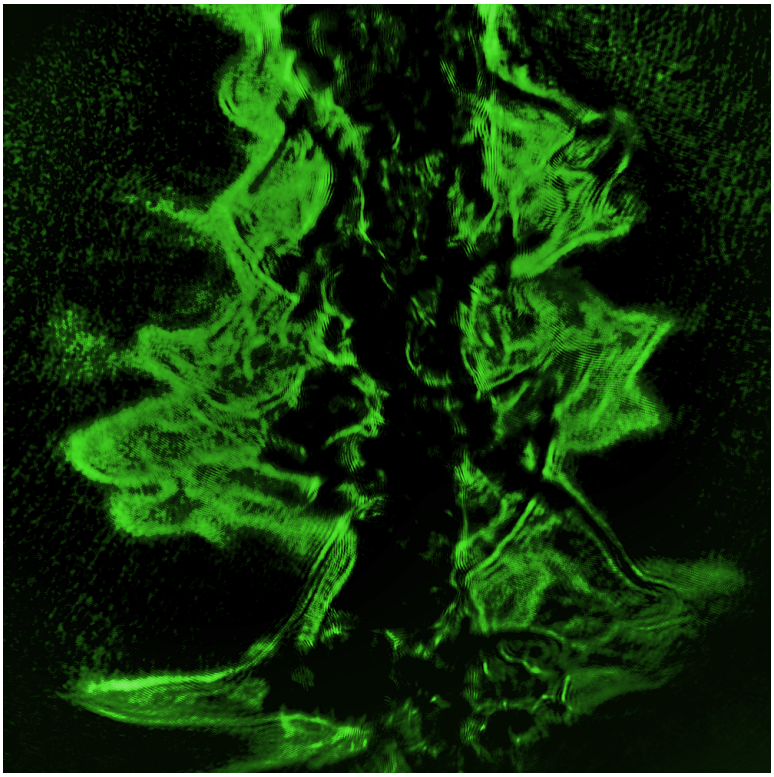
by

Joe M. Chen

A dissertation submitted in partial fulfillment
of the requirements for the degree of
Doctor of Philosophy
(Nuclear Engineering and Radiological Sciences)
in The University of Michigan
2025

Doctoral Committee:

Professor Ryan McBride, Chair
Associate Research Professor Nicholas Jordan
Associate Professor Benjamin Jorns
Professor Karl Krushelnick
David Yager-Elorriaga, Sandia National Laboratories



Joe M. Chen
joech@umich.edu
ORCID iD: 0000-0002-3432-8069

© Joe M. Chen 2025

ACKNOWLEDGEMENTS

I would like to start off by thanking Professor Sal Portillo at the University of New Mexico for his guidance, mentorship, and support throughout my years as an undergraduate student. He graciously took me into his lab and opened my eyes to the world of physics and science. Were it not for him, I would not have chosen a career path in pulsed power sciences, for which I am grateful. I will forever reminisce about the days, nights, and Saturdays (whether we liked them or not) when we all shared laughs.

To my advisor, Professor Ryan McBride, I would like to thank him for giving me the opportunity to be a part of his lab at UM, even when he barely had room for another graduate student. I am indebted to his support and mentorship over the four years I spent as a graduate student. His invaluable insights and teachings will stay with me throughout my many years as a scientist and researcher.

I would like to thank my committee members, Professor Nick Jordan, Professor Benjamin Jorns, Professor Karl Krushelnick, and Dr. David Yager-Elorriaga, for serving on and reading my dissertation. A special thanks to David, who helped and guided me throughout my experiments here at UM. I am very lucky to have him as a mentor, and I am thrilled to be working with him at Sandia. I would also like to thank Nick for his guidance through many technical issues in the lab.

I want to thank all the other students and colleagues I have met and shared joyful experiences with during my time as a student. There are too many to thank and too little time. I eagerly looked forward to coming into the lab every day, participating in conferences and workshops, and attending classes because of them. A special thanks to Shaho Hamadamin, Robert Beattie-Rossberg, Thomas Schmidt, Ryan Revolinsky, Landon Tafoya, Chris Swenson, Zach Rabine, Corey Gui, Chip Peterson, Adam Bedel, Brendan Sporer, George Dowhan, Akash Shah, Emma Guerin, and Adam Brusstar. I will remember all the fun times spent together in the lab!

I want to thank my parents for their support throughout my education and for instilling in me the pursuit of knowledge.

Finally, to my beloved wife, Madison Paulk, I am extremely lucky to have met you and to be loved by you; your unwavering support and partnership mean the world to me. I

want to thank you for your endless patience through long, stressful nights and for being my consistent source of encouragement throughout the writing of this thesis. Thank you for moving up from New Mexico to Michigan (and now back to New Mexico) with me. The times we have spent together exploring and discovering Michigan are unforgettable. I love you. To our dogs, Mia and Yogi, for keeping our lives exciting and hectic.

This work was supported by Sandia LDRD Project 226066 and NNSA SSAP under DOE Cooperative Agreement DE-NA0004148. Sandia is a multi-mission laboratory managed and operated by NTESS, LLC., a wholly owned subsidiary of Honeywell International, Inc., for the U.S. DoE's NNSA under contract DE-NA-0003525.

TABLE OF CONTENTS

ACKNOWLEDGEMENTS ii

LIST OF FIGURES vi

LIST OF APPENDICES xxi

ABSTRACT xxii

CHAPTER

1 Introduction 1

1.1 Z-Pinches 1
1.2 Pulsed Power 3
1.3 Plasma Confinement for Fusion and MagLIF 8
1.4 Observations of Enhanced Helical Modes 11
1.5 Dissertation Objective and Outline 18

2 Physics Background 20

2.1 Pulsed Power Circuit Theory 20
2.2 Pulsed Power Driven Implosion Physics 22
2.3 MHD Instabilities 29
2.4 Magneto Rayleigh Taylor Instability 30
2.5 Pitch Locking 35

3 MAIZE Pulsed Power Facility and Diagnostics 39

3.1 MAIZE LTD 39
3.2 Diagnostics 41
3.2.1 Current Diagnostics 42
3.2.2 Plasma Imaging Camera 44
3.2.3 Laser Probing Diagnostic 47

4 Magnetized Gas on Rod Experiment 57

4.1 Experiment and Diagnostic Setups 58
4.2 Implosion Trajectory 66
4.3 Instability Evolution and Stabilization 67
4.4 Helical Striation 72
4.5 Electron Density Measurements 78

4.6 Axial Magnetic Flux Compression . . . 87
4.7 Chapter 4 Summary . . . 90

5 Gas on Liner Experiment . . . 92

5.1 Introduction . . . 92
5.2 Experiment Setup . . . 93
5.2.1 Thin-Foil Targets . . . 93
5.3 Implosion Trajectory . . . 95
5.4 Instability Coupling . . . 106
5.5 MRTI Amplitudes . . . 118
5.6 Current Coupling . . . 128
5.7 Chapter 5 Summary . . . 132

6 Magnetized Gas on Liner Experiment . . . 134

6.1 Experiment Setup . . . 134
6.2 Helical Mode Coupling . . . 136
6.3 Implosion Dynamics . . . 143
6.4 Laser Probing Results . . . 150
6.5 Chapter 6 Summary . . . 154

7 Concluding Remarks . . . 156

APPENDICES . . . 159

BIBLIOGRAPHY . . . 168

LIST OF FIGURES

FIGURE

1.1 An illustration of common MHD instabilities in a Z-pinch. The current-driven (a) $m = 0$ "sausage" and (b) $m = 1$ "kink" instability. Note the increasing and decreasing magnetic field pressure causing the deformation of the current-carrying plasma column. The acceleration-driven MRT instability at (c) the initial frame and (d) during implosion. Note the effective acceleration (g) experienced by the boundary is outwards (+R direction), creating an unstable configuration where a lower-density "fluid" (i.e., the magnetic field) pushes on a higher-density fluid (i.e., the plasma). 2

1.2 Cross-section of the Z Pulsed Power Facility at Sandia National Laboratories, displaying its three main sections: the Marx generator, the intermediate pulse forming line, and the center MITLs. (Lower left) A plot demonstrating pulse compression, where the slower output pulse from the Marx (red) is compressed by the pulse forming line (blue). (Lower right) A photograph of Sandia personnel inside the central load region. Source: 4

1.3 (A) An illustration of a conical MITL structure (inside dashed red box) delivering current into the load region (inside dashed blue box). (B,C) Zoomed-in illustration of a liner implosion driven by P_{mag} (magnetic pressure) compressing and heating the internal fuel. Note that the magnetic pressure scales $\propto I^2/R^2$. 5

1.4 An illustration of a bi-polar LTD, where the green and red arrows indicate the path for the current delivered to the load and the path for parasitic current loss around the lid, respectively. (Source: 6

1.5 Illustration of the three main stages of an integrated MagLIF experiment. (1) magnetization: An axial magnetic field is applied to the cold fusion fuel (light blue) inside a beryllium liner (dark blue). (2) Laser pre-heating: A laser (green) heats the fuel.(3) Compression: A large electrical current generates an azimuthal magnetic field that implodes the liner, compressing the fuel to a hot, dense stagnated state (red) 10

1.6 Penetrating radiographs of an empty liner implosion with and without axial magnetic field. Note the differences between the instability structures. (A) Without axial magnetic field, azimuthally correlated structures appear which is characteristic of the $m = 0$ sausage mode. (B) With axial magnetic field, helical structures develop 12

1.7 Self emission images of the electrothermal instability forming on a metal surface as current is flowing in the vertical direction. (Top Row) Time montage of the ETI development in striation form, where $\partial\eta/\partial T > 0$ in solid metal. (Bottom Row) Time montage of the ETI development in filament form, where $\partial\eta/\partial T < 0$ due to plasma formation 14
1.8 PERSEUS simulations of low-density coronal plasma developing around a liner. The inclusion of Hall physics in the code leads to the formation of helical perturbations in this low-density plasma layer. Reprinted from 15
1.9 (a) A PERSEUS simulation at $t = 40$ ns showing low-density plasma from the power feed being compressed onto the liner. The simulation was initialized with a uniform 10 T axial magnetic field which is compressed to several hundreds of Tesla on the liner surface. (b) Illustration of the flux compression process, where the green line represents a shunted current sheath flowing along the edge of low-density power feed plasma at three different times. This current sheath flow along the edge of low-density power feed plasma. The process goes as follows: (1) Initial current shunting along the edge of low-density plasma, (2) the $J \times B$ force drives the shunted sheath towards the target, (3) the sheath sweeps up and compresses axial field in the return can onto the surface of the liner. Reprinted from 16
1.10 PIC simulations of desorbed plasma filling the load region MITL. (a) Plasma electron density map at $t = 60$ ns into the current pulse. Prior to the main implosion, the load region is already filled with a low-density plasma, with $n_e \approx 10^{15}$–10^{17} cm^{-3}. (b) Simulation of the MITL directly connected to load at $t = 25$ ns, showing plasma "roll-ups" as the electrons flow from the MITL into the load volume. (Source: 16
1.11 Experimental configuration and resultant helical structure of a flux compression experiment. (a) A cross-section of the return can configuration used to control the amount of available magnetic flux within the load region. (b) The resultant pitch angle of the instability formed. At the same CR, the reduced flux volume configuration produced a significantly smaller pitch angle. (Source: 17

2.1 (A) A simple schematic of a RLC discharge circuit, showing an equivalent capacitance (C_{eq}), a time-dependent resistor ($R(t)$), a time-dependent inductor ($L(t)$), and a closing switch. (B) A plot of the resulting half-cycles of the voltage ($V(t)$) and current ($I(t)$) waveforms for an ideal, lossless circuit ($R(t) = 0$) with an initial charge voltage of $V_0 = 140$ kV and static inductance of $L = 15$ nH. . . . 21
2.2 An example of an analytical model, simulating a 1D MagLIF implosion. 26
2.3 Illustration of the classic Rayleigh-Taylor instability. A small perturbation on the interface between the heavy fluid (red) and a light fluid (blue) grows when the interface is accelerated downwards (-z). 31

2.4 Illustration of a mode merging event for a helical perturbation with the form $\exp[(i(m\theta - k_z z)]$, for a constant radius. Prior to the mode merger event, as shown on the left, a helical mode characterized by $m = 4$ and $k_z = 4$ is presented. The red and blue lines represent two of the four intertwined helices, where $m = 4$ corresponds to a total of four intertwined helices. The solid lines trace the helical striations along the front surface of the helically twisted column, while the dashed lines trace the helical striations along the back surface. Subsequent to the mode merger event, both the azimuthal mode number and the axial wavenumber decrease to $m = 2$ and $k_z = 2$, respectively; the result is that the pitch p remains unchanged. The color-coded arrows illustrate the merger of the instability lobes from the red and blue helices into a single yellow helix post-merger. 36

2.5 Illustration of the pitch locking phenomenon for an $m = 2$ instability. The two intertwined helices are shown in red and blue, with solid lines representing the front-surface striations and dashed lines representing the back-surface striations. For a fixed azimuthal mode number m and axial wavevector k_z, the angle of the striation is determined by $\phi_{\text{plasma}}(t) \approx m/kR(t)$, with R representing the radius. Given that the pitch must remain constant, a reduction in $R(t)$ leads to an increase in the angle (implosion), whereas an increase in $R(t)$ results in a decrease in the angle (explosion). 38

3.1 The MAIZE pulsed power machine. (a) A CAD cross section showing the key components, including 40 spark-gap switches, eighty 40 nH capacitors, two ferromagnetic cores, the radial transmission line, the conical power feed, the vacuum and oil sections, and finally the load region. (b) An open shutter photograph of MAIZE firing with the lid removed, highlighting the internal components of MAIZE. The bright yellow arcs are the switches discharging electrical current into the transmission lines. (c) A CAD drawing of a single "Brick", which is comprised of two 40 nH capacitors isolated with a pressurized dry-air gas switch. There are 40 bricks contained within MAIZE's oil section. 40

3.2 XUV images of an argon gas-puff Z-pinch imploding onto a dense central rod. The images show the formation of azimuthally correlated instability structures, characteristic of an $m = 0$ sausage instability. 46

3.3 An illustration of a shadowgraphy diagnostic. A collimated probe beam of light passes through an underdense plasma, which causes the rays to refract in regions of varying electron density. This results in an image with bright and dark features (i.e., a "shadow") that corresponds to the second spatial derivative of the plasma's electron density. 51

3.4 Illustration of schlieren imaging principles. A collimated probe beam passes through an underdense plasma and is focused with a single lens of focal length f. This focuses the beam to the focal length where a spatial filter separates the refracted light from the unperturbed light. The spatial filter can consist of either: (a) a beam stop (bright image on dark field); or (b) an iris (dark image on bright field). This results in an image that corresponds the first spatial derivative of the plasma's electron density. 53

3.5 An illustration of a Mach-Zehnder interferometer and (b,c) synthetic interference pattern.(a) A collimated laser beam is split into a probe beam that passes through an underdense plasma and a reference beam. When recombined, they create an interference patter. This distortion of this pattern (fringe shift), is directly proportional to the line-integrated electron density of the plasma. A synthetic reference interferogram is shown (b), and a synthetic shot interferogram showing the fringe shift caused by a plasma object is shown in (c). 54

4.1 Illustration of the experimental setup and the gas-puff hardware assembly. . . . 59
4.2 Detailed cross-section of the experimental load. The main current (green) flows upward along the anode surface (blue) and return-current posts (blue), downward through the gas plasma (purple), and back to its source along the cathode surface (red). The resulting azimuthal magnetic pressure implodes the plasma, compressing the pre-embedded axial magnetic field (cyan) generated by the axial field coil (orange). The imploding low-density plasma then collides onto the central target (beige) 60
4.3 Cross-sections and corresponding photographs of the two targets used in the experiments. (a) Cross-section of the solid copper rod experiment. (b) Photograph of the solid copper rod target. (c) Cross-section of the experiment with a dielectric tube housing a B-dot probe. (d) Photograph of the dielectric tube with a B-dot probe inserted, where the dielectric tube has been installed in the MAIZE load region. Both target types have a radius of approximately 3 mm and a total height of 50 mm. Approximately 20 mm of this height is positioned within the load region, where it becomes surrounded by an argon gas shell upon gas injection 61
4.4 (a) Photographs of various B-dot probes constructed for this work. (b) A schematic of the final B-dot probe design. (c) The calibration pulser used. (d) The calibration coil used for ex-situ calibration of the B-dot probes. (e) A plot of the calibration waveforms from the pulser with the calibration target, showing the pulser current (blue), the B-dot probe's raw voltage (red), and the final calibrated magnetic field trace (green). 62
4.5 (a) A photograph of the ex-situ measurement of the axial field. In this image, a gauss probe is used to measure the peak axial field of the pulsed coils at $r = 0$. (b) A plot of the axial magnetic field strength as a function of height. Here, $z = 0$ mm is the cathode height, while $z = 20$ mm is the height of the anode mesh. The values plotted for each height are the values found on axis, at $r = 0$. (c) A current waveform from the axial field coil, measured with a current viewing resistor (CVR). The blue current trace shows a proper shot with the coil. Note that the sharp spike at the peak of the current trace is due to electromagnetic interference (EMI) from MAIZE discharging on a 100-ns time scale. This confirms that MAIZE fires at the peak magnetic field generated by the coils. The red current trace shows a fault discharge where the coil breaks down and shorts to the chamber of MAIZE, resulting in an RC decay after the discharge of MAIZE. 64

4.6 Schematic of the optical laser probing diagnostic setup. The laser beam (green) is expanded and filtered before an 80/20 beam splitter splits the beam into a reference beam and a probe beam. The probe beam is transported into the vacuum chamber, probes the plasma, and is collected by a 4f imaging telescope, while the reference beam travels concurrently through in free space. For interferometry, a portion of the probe beam is recombined with the reference beam to form an interferometric image that is captured by a DSLR camera. The rest of the probe beam is used for backlighting, where it is split to simultaneously form a dark field and bright field schlieren image. 65

4.7 (a) Representative visible-light self-emission images from an experiment with $B_{z0} = -0.75$ T at $z = 10$ mm. The field of view in each image is 21 mm $\times$ 21 mm. (b) The average drive current and its standard deviation over 17 shots, which includes shots with and without an applied B_{z0}. Also plotted are the implosion trajectories for three different axial heights: $z = 2.75$ mm (green), $z = 9.5$ mm (blue), and $z = 16.5$ mm (purple). The center rod is represented by the shaded gray area. From bottom to top, the imploding sheath impacts the rod over the time period of 194–260 ns. 68

4.8 Visible-light self-emission images of the $B_{z0} = 0$ experiment as the conical plasma sheath compresses onto the central rod. The plasma boundary was tracked for each image and is indicated by the blue lines, while the red line represents the initial radius of the copper rod. These images show a notable change in the instability amplitude past 230 ns, when the process transitions from implosion onto the rod to explosion away from the rod. These images also show the instability structures evolving from shorter wavelengths to longer wavelengths over time (i.e., the so-called "inverse cascade") due to mode merger events, and an upward axial drift in the plasma structure (in the $+z$ direction). 70

4.9 Schlieren images taken after peak compression onto the rod for four cases: (a) $B_{z0} = 0$; (b) $B_{z0} = +0.25$ T; (c) $B_{z0} = +0.5$ T; and (d) $B_{z0} = +0.75$ T. These B_{z0} values are for the fringe field at $z = 10$ mm. The plasma boundary was tracked for each image and is indicated by the green lines. The initial radius of the copper rod is indicated by the dashed red lines. (e) A plot of the power spectra of the schlieren boundaries. The colors of blue, green, red, and purple correspond to B_{z0} values of $0, +0.25, +0.5$, and $+0.75$ T, respectively. Stabilization of shorter wavelength modes is observed as $|B_{z0}|$ is increased. (f) A plot of the dominant wavelength of the schlieren images. Larger wavelengths tend to become more dominant as $|B_{z0}|$ is increased. 71

4.10 Analysis of the obstructed viewing effects that occur when attempting to observe helical instability troughs side-on with non-penetrating imaging diagnostics. (a,b) 2D views of 3D models of single-mode cycloidal perturbations. The pitch angle in (a) is $\phi = 0°$ (i.e., an azimuthally symmetric, $m = 0$ case), while in (b) it is $\phi = 30°$ (i.e., a steep helical case). In both cases, the true bubble-to-spike amplitude is 2 mm and the axial wavelength is 3 mm; however, in the helical case, the observed amplitude trough is not nearly as deep as in the $m = 0$ case, which shows the true depth of the perturbation. (c) The ratio of the observed instability amplitude (A_{obs}) to the true instability amplitude (A_{true}) for various ϕ, A_{true}, and λ_z. 73
4.11 Visible-light self-emission images taken as the imploding plasma sheath approaches the central rod for three different cases: (a) $B_{z0} = 0$; (b) $B_{z0} = +0.75$ T (at $z = 10$ mm); and (c) $B_{z0} = -0.75$ T (at $z = 10$ mm). With $B_{z0} > 0$, the helical instability structure is left handed relative to the z axis. With $B_{z0} < 0$, the helical instability structure is right handed relative to the z axis. (d,e) A sample of the striation tracing. Striations traced along the front surface are marked in blue. Striations traced along the back surface are marked in green. The left and right edges of the rod are marked in red. 74
4.12 Measured helical pitch angles along the height of the plasma at various times during the implosion for the three different applied axial magnetic field strengths tested: (a) $B_{z0} = -0.75$ T, (b) $B_{z0} = -0.5$ T, and (c) $B_{z0} = -0.25$ T. Solid and dashed lines with the same color are from the same shot, but at two different times. The earlier times (dashed lines) are from when the plasma near the bottom of the imploding plasma sheath is at a smaller radius than the plasma near the top of the sheath (i.e., while the zippering process along the rod is still in progress). The later times (solid lines) are from after the zippering process has completed. The green line in (a) represents the case where a dielectric rod was used instead of a copper rod. The black solid lines represent the scaling trends expected for the late-time (final) pitch angles when accounting for the axial variation in B_{z0}. Note that $B_{z0} = B_{z0}(z)$ because the fringe field (i.e., the field below the applied magnetic field coil) was used in these experiments. 76

4.13 Visible-light self-emission images taken as the imploding plasma sheath approaches the central copper rod for an axial magnetization of $B_{z0} = -0.75$ T (at $z = 10$ mm) and at time (a) $t = 173$ ns and (b) $t = 307$ ns. Striations traced along the front surface are marked in blue. The left and right edges of the rod are marked in red. (c) A plot of the traced instability pitch angles as a function of height. The dashed blue line shows the pitch angles earlier in the implosion ($t = 173$ ns), while the solid blue line shows the late time pitch angles ($t = 307$ ns). The dashed black line separates regions of fully imploded plasma from in-flight imploding plasma. Note that the pitch angles within the red circle are constant from the early to late times, since the plasma had already fully imploded by the earlier time of $t = 173$ ns. By contrast, for heights >4 mm, the pitch angles increased from the early to late times, since the plasma was still imploding (zippering). Also note that the final (fully imploded) pitch angles were larger for higher axial positions. This occurred because the initial axial field (B_{z0}) was stronger at higher axial positions. The field was stronger at higher axial positions because the axial field coil resided above the target, and thus it was the coil's fringe fields that were applied to the target. 77
4.14 Visible-light self-emission images of an argon gas-puff Z-pinch imploding without a central rod. The axial magnetic field value applied was $B_{z0} = +0.5$ T. Note the simultaneous presence of both vertical filaments and helical striations. The vertical filaments are present only in shots with B_{z0} applied. 79
4.15 Interference images taken of the plasma sheath stagnating onto a central copper rod. **Top Row** (shot 3135, $B_{z0} = -1$ T): (a) Reference interferogram before the shot. (b) Shot interferogram taken at $t = 334.0$ ns. (c) The resulting reconstructed map of the line-integrated electron density. **Bottom Row** (shot 3143, $B_{z0} = 0$ T): (d) Reference interferogram before the shot. (e) Shot interferogram taken at $t = 333.2$ ns. (f) The resulting reconstructed map of the line-integrated electron density. The boundary of the copper rod is indicated with a red line while the field of view (FOV) is marked in blue. 80
4.16 (a) Line-integrated electron density map of shot 3135 with $B_{z0} = -1$ T. The red lines denote the regions of the lineouts. (b) The resultant lineouts at various axial locations to illustrate the density of the peripheral plasma. 82
4.17 Interference images taken of the non-axially magnetized gas-puff plasma at stagnation without a central rod on axis. **Top Row** (shot 3181, $B_{z0} = 0$ T): (a) Reference interferogram before the shot. (b) Shot interferogram taken at $t = 139.9$ ns. (c) The resulting reconstructed map of the line-integrated electron density. **Bottom Row** (shot 3180, $B_{z0} = 0$ T): (d) Reference interferogram before the shot. (e) Shot interferogram taken at $t = 222.7$ ns. (f) The resulting reconstructed map of the line-integrated electron density. The field of view (FOV) is marked in blue. 83

4.18 (a) Line-integrated electron density map of shot 3181 at stagnation. The red lines denote the lineout regions. The axial field was not applied on this shot ($B_{z0} = 0$ T). (b) The resultant lineouts at various axial locations to illustrate the density of the peripheral plasma. (c) Line-integrated electron density map of shot 3180 during implosion. The red lines denote the lineout regions. The axial field was not applied on this shot ($B_{z0} = 0$ T). (d) The resultant lineouts at various axial locations to illustrate the internal density. 84
4.19 Interference images taken of the axially magnetized gas-puff plasma at stagnation without a central rod on axis. **Top Row** (shot 3178, $B_{z0} = -0.5$ T): (a) Reference interferogram before the shot. (b) Shot interferogram taken at $t =$ 139.9 ns. (c) The resulting reconstructed map of the line-integrated electron density. **Bottom Row** (shot 3179, $B_{z0} = -0.5$ T): (d) Reference interferogram before the shot. (e) Shot interferogram taken at $t = 229.1$ ns. (f) The resulting reconstructed map of the line-integrated electron density. The field of view (FOV) is marked in blue. 85
4.20 (a) Line-integrated electron density map of shot 3178 with $B_{z0} = -0.5$ T at stagnation. The red lines denote the lineout regions. (b) The resultant lineouts at various axial locations to illustrate the density of the peripheral plasma. (c) Line-integrated electron density map of shot 3179 during implosion. The red lines denote the lineout regions. The initial applied axial field was $B_{z0} = -0.5$ T for this shot. (d) The resultant lineouts at various axial locations to illustrate the internal density. 86
4.21 Schlieren images of an imploding gas-puff plasma for two cases: (a) without an applied axial magnetic field ($B_{z0} = 0$); and (b) with an applied axial magnetic field ($B_{z0} = -0.5$ T). Note the structural differences inside the plasma medium. For the case with $B_{z0} = 0$, the plasma structure is dominated by horizontal bands, which is consistent with a strong $m = 0$ presence. Conversely, the axially magnetized case shows a more complex structure, with significant density fluctuations in both the axial and radial directions. 87
4.22 (a) Magnetic flux compression measurements on shot 3151. Plotted is the MAIZE drive current (blue); the scaled dB_z/dt waveform measured by the B-dot probe (orange); the measured axial magnetic field, $B_z(t)$ (green); an ideal flux compression waveform (dashed black), calculated using $|B_{z0}| = 0.75$ T and the measured plasma radius, $r(t)$, at $z = 10$ mm; and the probe failure region (purple shading). (b) Plasma trajectories for the same shot at various axial locations. The grey shaded area represents the central rod. In both (a) and (b), the vertical black lines indicate times of peak dB/dt. 89

5.1 (a) Illustration of the experimental load. (b) Technical design of the thin-foil liner targets. (c) Cross-section of the GoL target. (d) Photograph of the constructed liner target with an 800-nm-thick foil. 94
5.2 Visible-light self-emission images showing the ablation, implosion, stagnation, and explosion phases for three liner thicknesses: (a) 400 nm; (b) 800 nm; and (c) 1500 nm. 97

5.3 Visible-light self-emission images showing the ablation, implosion, stagnation, and explosion phases for GoL configuration using a 400-nm-thick liner at various gas pressures. The panels show: (a) no gas; (b) −12 psig; (c) −5 psig; and (d) 0 psig. 99
5.4 Plots of the tracked liner boundaries as a function of height for (a) liner-only targets and (b) GoL targets. The black-blue color gradient indicates increasing time during the implosion up to the time of stagnation. The red arrows highlight regions of the instability structures. Note the significant axial shift in instability structure when gas is applied compared to the liner-only targets. Visible-light self-emission image of the (c) liner-only and (d) GoL targets. The red and blue lines indicate the initial position of the liner and gas plasma, respectively. . . . 100
5.5 (a) Visible-light self-emission image of shot 3305 with a liner thickness of 400 nm and gas pressure of −5 psig at $t = 206.8$ ns. (b) A magnified and contrast enhanced view showing vertical filaments on the liner surface attributed to pressure buckling from the gas. (c) A plot of an intensity line-out from the self-emission images showing the perturbation structure of the buckling. 101
5.6 Visible-light self-emission images showing various GoL configurations. The panels show: (a) 400 nm without gas; (b) 400 nm with gas; (c) 800 nm without gas; (d) 800 nm with gas; (e) 1500 nm without gas; and (f) 1500 nm with gas. Note the impact to the instability structure and implosion dynamics with and without gas. 103
5.7 (a) A plot of the implosion trajectories for liner thicknesses of 400 nm (blue), 800 nm (red), 1500 nm (green), and a 400 nm GoL configuration (purple). The support rod radius is indicated by the solid black line. (b) A plot of the stagnation radius as a function of gas pressures. (c) A plot of the stagnation time as a function of gas pressures. Liner thicknesses of 400 nm, 800 nm, and 1500 nm are represented by the blue circle, red square, and green triangle markers, respectively. The grey dashed line separates the liner-only targets (left) from the GoL targets (right). 104
5.8 Visible-light self-emission implosion boundaries for (a) liner-only and (b) gas-on-liner targets. The tracked plasma boundaries are separated in time by 25 ns intervals as a function of height. The red and green arrows trace the evolution of the instability's finger and bubble structure through the implosion. Note that in the liner-only case, a finger merger event is observed while the bubbles stay in the same axial position, consistent with expectations. Conversely, the GoL targets display an unusual event where a new finger emerges from an existing bubble. This is suggests that the liner's instability structure may develop decoupled from the overlying gas plasma. 107
5.9 (a) A plot of the self-emission plasma boundary for shot 3317 at $t = 231$ ns, overlaid with the waveform reconstructed from the five largest peaks of the power spectra. (b) The power spectra of the same boundary. 108
5.10 (a) A plot of self-emission implosion boundaries. Each tracked plasma boundary is separated in time by 25 ns intervals, ending at stagnation. (b) Power spectra of the left and right boundaries near stagnation. The blue and red lines indicate the left and right boundaries, respectively 109

5.11 Time evolution of the imploding self-emission boundaries for liners with foil thicknesses of (a) 400 nm, (b) 800 nm, and (c) 1500 nm. The black-blue color gradient indicates increasing time during the implosion of the left boundaries up to the time of stagnation. (d–f) The power spectra of the left boundaries for liners with foil thicknesses of 400 nm, 800 nm, and 1500 nm, respectively. (g–i) The power spectra of the right boundaries for liners with foil thicknesses of 400 nm, 800 nm, and 1500 nm, respectively. 110
5.12 Comparison of the implosion dynamics for three liner thicknesses: 400 nm (left column), 800 nm (middle column), and 1500 nm (right column). **Top Row** (a–c): time evolution of the imploding self-emission boundaries. Each tracked plasma boundary is separated in time by 25 ns intervals, ending at stagnation. The blue and red lines indicate the left and right boundaries, respectively. **Top-Middle Row** (d–f): the time-wavelength evolution of the normalized power spectra for the left boundaries. **Bottom-Middle Row** (g–i): the time-wavelength evolution of the normalized power spectra for the right boundaries. The dashed black line indicates time of stagnation. **Bottom Row** (j–l): the corresponding self-emission images at stagnation. The overlaid blue and red lines indicate the tracked left and right boundaries, respectively. 112
5.13 The time-wavelength evolution of the normalized power spectra for (a) liner-only and (b) gas-on-liner targets, corresponding to shots 3317 and 3318, respectively. The dashed black line indicates time of stagnation. Note the distinct features in liner-only spectra: the spectra is initially multi-moded at $t \approx 150$ ns, transitions to a single dominant mode by $t \approx 250$ ns, and then shows a mode merger event at $t \approx 300$ ns. By contrast, the GoL targets exhibit two dominant wavelengths at stagnation, $\lambda \approx 2$ mm and $\lambda \approx 3$–4 mm, which can be attributed to the dominant mode of the liner and gas plasma, respectively. 113
5.14 Comparison of the implosion dynamics for three GoL targets with increasing gas pressure: 800 nm (left column), 800 nm and -12 psig (middle column), and 1500 nm and -10 psig (right column). **Top Row** (a–c): time evolution of the imploding self-emission boundaries. Each tracked plasma boundary is separated in time by 25 ns intervals, ending at stagnation. The blue and red lines indicate the left and right boundaries, respectively. **Middle Row** (d–f): the time-wavelength evolution of the normalized power spectra for left boundaries. **Bottom Row** (g–i): the time-wavelength evolution of the normalized power spectra for right boundaries. The dashed black line indicates time of stagnation. Note the lack of small wavelength modes and increase in large wavelength modes as gas pressure increases. 114

5.15 Comparison of the implosion dynamics for two similar GoL targets, both with 800 nm and −12 psig. **Top Row** (a,b): time evolution of the imploding self-emission boundaries. Each tracked plasma boundary is separated in time by 25 ns intervals, ending at stagnation. The blue and red lines indicate the left and right boundaries, respectively. **Middle Row** (c,d): the time-wavelength evolution of the normalized power spectra for left boundaries. **Bottom Row** (e,f): the time-wavelength evolution of the normalized power spectra for right boundaries. The dashed black line indicates time of stagnation. Note the absence of large wavelengths ($\lambda > 3$ mm) in the power spectra for shot 3319. This may suggest that shot 3319 is more liner-dominated than gas-dominated. 115
5.16 Comparison of the implosion dynamics for two similar gas-on-rod (GoR) targets, both with copper rods and −12 psig. **Top Row** (a,b): time evolution of the imploding self-emission boundaries. Each tracked plasma boundary is separated in time by 33 ns intervals, starting at post-stagnation. The blue and red lines indicate the left and right boundaries, respectively. **Middle Row** (c,d): the corresponding post-stagnation time-wavelength evolution of the normalized power spectra. The gray region is during the implosion phase. **Bottom Row** (e,f): the visible-light self-emission images of the GoR targets. Note the absence of strong small wavelengths ($\lambda < 2$ mm) in both power spectra. This suggest that the gas loads produce large wavelengths ($\lambda > 3$ mm) post-stagnation. 116
5.17 Time evolution of the dominant instability wavelength for liners with foil thicknesses of (a) 400 nm, (b) 800 nm, and (c) 1500 nm. The blue and red lines indicate the left and right boundaries, respectively. 117
5.18 Time evolution of the dominant instability wavelength for two GoL targets: (a) 800 nm liner with −12 psig of gas; and (b) 400 nm liner with −12 psig of gas. The blue and red lines indicate the left and right boundaries, respectively. . . . 118
5.19 A comparison of liner-only targets with varying liner thicknesses: 400 nm (shot 3308), 800 nm (shot 3317 and 3318), and 1500 nm (shot 3324). The plots show: (a) implosion trajectories; (b) drive current waveforms; (c) instability amplitudes as a function of normalized distance moved; (d) magnetic pressures; (e) velocities; and (f) accelerations. 120
5.20 A comparison of GoL targets with constant gas pressure of −10 psig and varying liner thicknesses: 400 nm (shot 3301), 800 nm (shot 3310), and 1500 nm (shot 3295). The plots show: (a) implosion trajectories; (b) drive current waveforms; (c) instability amplitudes as a function of normalized distance moved; (d) magnetic pressures; (e) velocities; and (f) accelerations. 121
5.21 (a) Evolution of the peak-to-peak instability amplitude as a function of normalized distance moved. The blue and red curves correspond to liner-only and gas-on-liner targets, respectively. The arrows indicate the trajectory. The corresponding visible-light self-emission image for (b) liner-only and (c) GoL targets at $\delta R = 0.28$ and $\delta R = 0.36$, respectively. 122

5.22 A plot of the maximum peak-to-valley instability amplitude as a function of injected gas mass density. The grey dashed line separates the liner-only targets (left) from the GoL configured targets (right). The blue circle and red square markers denote the 400 nm and 800 nm liner thickness, respectively. Note that all GoL targets exhibit smaller instability amplitude compared to liner-only targets. 122
5.23 (a) A plot of the calculated growth rate as a function of injected gas mass density. The grey dashed line separates the liner-only targets (left) from the GoL targets (right). The blue circles and red squares denote liners with thicknesses of 400 nm and 800 nm, respectively. (b) Time evolution of the peak-to-peak instability amplitude for liner-only targets. (c) Time evolution of the peak-to-peak instability amplitude for GoL targets. The red curve is an exponential fit to the data. Note that the quality of fit suggests that the instability growth is in the linear growth regime. 124
5.24 (a) A plot of self-emission boundary curves. The blue, red, and green curves denote $t = 206.6$ ns, 256.6 ns, and 306.6 ns, respectively. (b) The corresponding normalized power spectra of shot 3318. Analysis plots of the power spectra evolution for two wavelength ranges: (c) $\lambda = 0.8$–1.2 mm; and (d) $\lambda = 1.2$–1.6 mm. The log of the spectral powers are indicated by the blue markers, the differences in the logs of the integrated powers are indicated by the red markers, and the A/λ ranges are indicated by the green shaded regions. The solid red line denotes a constant value of e, and the grey line denotes the stagnation times. The solid black line estimates the slope of the linear and non-linear regions. . . 125
5.25 (a) A plot of selected self-emission boundary curves. The blue, red, and green curves denote $t = 206.6$ ns, 256.6 ns, and 306.6 ns, respectively. (b) The corresponding normalized power spectra of shot 3317. Analysis plots of the power spectra evolution for three wavelength ranges: (c) $\lambda = 0.5$–1.0 mm, (d) $\lambda = 1.0$–1.5 mm, and (e) $\lambda = 1.5$–3.0 mm. The log of the spectral powers are indicated by the blue marker, markers, the differences in the logs of the integrated powers are indicated by the red markers, and the A/λ ranges are indicated by the green shaded regions. The solid red line denotes a constant value of e, and the grey line denotes the stagnation times. The solid black line estimates the slope of the linear and non-linear regions. 126
5.26 A comparison of GoL targets with constant 400 nm liner thickness and varying gas pressures: no gas (shot 3308), −12 psig (shot 3321), and −10 psig (shot 3301). The plots show: (a) implosion trajectories; (b) drive current waveforms; (c) instability amplitudes as a function of normalized distance moved; (d) magnetic pressures; (e) velocities; and (f) accelerations. 129
5.27 A comparison of GoL targets with constant 800 nm liner thickness and varying gas pressures: no gas (shot 3318), −12 psig (shot 3316), and −10 psig (shot 3310). The plots show: (a) implosion trajectories; (b) drive current waveforms; (c) instability amplitudes as a function of normalized distance moved; (d) magnetic pressures; (e) velocities; and (f) accelerations. 130

6.1 (a) Cross-section of the MGoL target. (b) Photograph of a target installed in MAIZE's central load region. (c) An overview of the MAIZE vacuum chamber with the primary diagnostics labeled. 135
6.2 (a) A processed image of frame 9 (t =322 ns) of shot 3392 for an MGoL target. (b) The result of the automated tracing algorithm, identifying the dark (blue) and bright (red) helical striations. (c) Intermediate steps in the image processing, including contrast enhancement, Gaussian blurring, and an unsharp mask filter. 136
6.3 (a) A synthetic image of the instability, reconstructed from the results of the Bayesian analysis. (b) The corresponding trimmed and processed self-emission image used as the input for the analysis. (c) A plot of the resultant helical pitch angle as a function of normalize distanced moved, comparing the results from the direct tracing method with the more robust Bayesian approach. 137
6.4 Visible-light self-emission images showing the implosion, stagnation, and explosion phases for various liner targets. The panels show: (a) $B_{z0} = 0$ liner-only; (b) $B_{z0} = 0.75$ T liner-only; (c) $B_{z0} = 0.25$ T and -12 psig MGoL; and (d) $B_{z0} = 0.75$ T and -12 psig MGoL. Note the pronounced helical structures as the liner explodes radially outwards. 139
6.5 Measured instability pitch angles for various target configurations as a function of normalized distance moved. The targets include $B_{z0} = 0$ liner-only (purple), $B_{z0} = 0.75$ T liner-only (cyan), $B_{z0} = 0$ GoL (green), $B_{z0} = 0.25$ T MGoL (blue), and $B_{z0} = 0.5$ T MGoL (red). The larger positive x-axis values correspond to a smaller implosion radius, and the dashed black line indicates the initial 3 mm radius. The star markers represent data from the MGoR experiments, with applied axial magnetic field of $B_{z0} = 0.25$ T (blue) and $B_{z0} = 0.5$ T (red), showing the final instability pitch angle of the gas as it stagnated onto the solid rod. Notably, the stagnated pitch angle of the gas in the MGoR experiments is very similar to the initial pitch angle measured on the liner in the MGoL experiments when B_{z0} is the same for both cases. 140
6.6 (a) Shadowgraph of an imploding gas plasma beginning to impact the thin-foil liner. (b) A self-emission image of the liner from the same shot, taken approximately 75 ns later from a 30° viewing angle off of the laser line of sight (LOS). The initial perturbation wavelength in the gas plasma (≈ 1.5 mm) is larger than the resulting perturbation wavelength observed on the liner. 141
6.7 (a) A self-emission image of a MGoL target late in the explosion phase (t = 375 ns). The front-facing helical striations (solid lines) are clearly visible, which allows us to infer the approximate location of the back-facing helical striations (dashed lines) using simple connectivity arguments. (b) The same shot at a much earlier time ($t = 200$ ns). Although the striations are not visible on either surface in (b), the instabilities at the left and right edges of the image left and right edges of the image must connect. The overlaid lines in (b) show the inferred path of these striations, with the pitch angle determined by assuming pitch locking from the later-time measurements shown in (a). 142

6.8 A collage of plots showing: (a) stagnation radii; (b) stagnation times; (c) peak-to-peak instability amplitudes; (d) instability growth rates; (e) peak target velocities; and (g) peak cumulative accelerations as a function of applied axial magnetic field. Across this dataset, the foil thickness (400 nm) and gas pressure (−12 psig) were held constant. Note that the cyan markers denote axially magnetized liner-only targets while the rest are MGoL targets. 144
6.9 Collage of plots showing: (a) implosion trajectories; (b) drive current waveforms; (c) instability amplitudes as a function of normalized distance moved; (d) magnetic pressures; (e) velocities; and (f) accelerations. The plots compare MGoL targets with increasing axial magnetic field strength: $B_{z0} = 0$ (shot 3403, blue); $B_{z0} = 0.25$ T (shot 3399, red); $B_{z0} = 0.5$ T (shot 3394, green); and $B_{z0} = 0.75$ T (shot 3393, purple). Across this dataset, the foil thickness (400 nm) and gas pressure (−12 psig) were held constant. 146
6.10 Collage of plots showing: (a) implosion trajectories; (b) drive current waveforms; (c) instability amplitudes as a function of normalized distance moved; (d) magnetic pressures; (e) velocities; and (f) accelerations. The plots compares: $B_{z0} = 0$ GoL target (shot 3403, blue); a $B_{z0} = 0.25$ T MGoL target (shot 3399, red); and a $B_{z0} = 0.75$ T liner-only target (shot 3407, green). 147
6.11 The reconstruction process for the reference interferogram. (a) The original interferogram with the central region obscured by the target. (b) The obscured region is masked in gray. (c) The final image after the masked area has been filled with a synthetically generated fringe pattern. 150
6.12 Comparison of interferometry results for a liner-only target and MGoL targets. Each row shows a single shot with the **top row** (a–c) representing a liner-only target (3404). The **middle row** (d–f) represents an MGoL target with $B_{z0} = 0.25$ T. The **bottom row** (g–i) represents an MGoL target with $B_{z0} = 0.75$ T. Each column represents the (left) reference interferogram, (center) shot interferogram, and (right) reconstructed areal density map. (j) A plot comparing radial lineouts of the line-integrated density for each case. 151
6.13 XUV images of a MGoL target at different stages. (a) The initial impact of the gas plasma onto the liner. (b) A later-time image showing a potentially stable liner column persisting underneath the surrounding gas plasma. (c) Helical features are visible during the liner's explosion phase. 152

A.1 (Left) A bulls-eye pattern of the angular Fourier filter. (Right) The fabricated AFR. 160
A.2 Deflection angle as a function of radius on the Fourier plane. The grey bars indicated the opaque bands while the black vertical line indicate the upper deflection limit. 161
A.3 (Left) Calibration with a concave lens showing angular bands. (Middle) Calibration with a cylindrical lens showing horizontal bands. (Right) 1951 USAF resolution target at load center. 162
A.4 Electron density profile with radial and axial lineouts. (Top left) The electron density map. (Bottom left) The axial lineout. (Top right) The radial lineout. . 162

A.5 (a) The rays exiting the plasma. (b) The angle distribution of the refracted rays. (c) The image at the Fourier plane where the AFR resides. (d) The resultant schlieren image at the detector plane. 163

LIST OF APPENDICES

A Angular Filter Refractometer 159

B MATLAB Code for Helical Angle Tracing 165

ABSTRACT

Magnetized Liner Inertial Fusion (MagLIF) offers a promising path to generate thermonuclear plasma, demonstrating fusion relevant temperatures ($\sim$ 3 keV) and significant fusion yields ($\sim 10^{13}$ DD neutrons). However, its performance is potentially limited by implosion asymmetries and mixing of high Z material into the fuel during implosion. This is due to the growth of detrimental instabilities on the liner surface, such as the Magneto-Rayleigh-Taylor instability (MRTI). The axial magnetic field (10–30 T) used in MagLIF targets modifies MRTI, generating steep helical plasma striations on the liner surface. It is hypothesized that the amplification of the axial magnetic field, resulting from flux compression occurring in a low-density plasma (LDP) surrounding the liner, could explain the large pitch angle. To investigate the effects of the LDP layer, an experimental platform has been developed at the University of Michigan's MAIZE pulsed power facility (1 MA with a rise time of 100–200 ns).

The first set of experiments involved imploding an axially magnetized gas plasma layer onto an electrically thick target. Visible-light self-emission imaging revealed steep helical striations forming in the LDP layer, with pitch angles of up to approximately 44° for a small value of $B_{z,0}/B_{\theta,\text{peak}} \approx 3.7\%$. Furthermore, it was determined that the gas plasma is able to compress the embedded axial magnetic field, with the measured axial flux compression being approximately 50% efficient relative to ideal flux compression.

The second set of experiments studied the coupling between low-density gas plasma and an *imploding* thin-foil aluminum liner. The motivation for this set of experiments was to distinguish between two potential instability seeding mechanisms: density imprinting and magnetic imprinting. The power spectra collected during these experiments show two dominant modes simultaneously: a small wavelength for the liner ($\approx$ 2 mm) and a larger wavelength for the gas ($\gtrapprox$ 3 mm). The persistence of both spectra throughout the implosion suggests that they may either evolve independently from each other (decoupled evolution of the two interfaces), or there may be mode competition occurring between them.

The final set of experiments investigated the role of magnetic imprinting of helical instabilities in a fully integrated magnetized gas-on-liner (MGoL) target (with an axial magnetic field). It was revealed that a liner-only target with a strong axial magnetic field ($B_{z0} = 0.75$ T) produced pitch angles of only $8 \pm 1°$. By contrast, an MGoL target with a

much weaker axial magnetic field ($B_{z0} = 0.25$ T) produced significantly steeper pitch angles of $16 \pm 2^\circ$ at a similar radius. *The presence of an axially magnetized LDP imploding onto a thin-foil liner target resulted in a more pronounced and steeper helical instability on the liner compared to the configuration without LDP.*

Additionally, a significant finding from these experimental campaigns is that a magnetized gas layer provides a powerful stabilizing effect on an imploding liner. The MGoL targets provide a significant stabilizing effect against MRTI compared to their liner-only counterparts. Specifically, the instability amplitude for the MGoL target decreases from approximately 1 mm down to 0.2 mm as B_{z0} is increased from 0 T to 0.75 T. This can be contrasted with the axially magnetized liner-only target, which had an instability amplitude of 0.8–1 mm with $B_{z0} = 0.75$ T.

This work demonstrates that an axially magnetized, low-density plasma can be an important factor in seeding liner instabilities. Additionally, a modest axial magnetic field in tandem with a low-density gas outer layer significantly mitigates the MRTI growth for a thin-foil liner implosion.

CHAPTER 1

Introduction

1.1 Z-Pinches

Fast Z-pinches can be created by driving a fast rising, large amplitude current pulse through a cylindrical conductor. In accordance with Ampère's law, this axial current (I_z) induces an azimuthal magnetic field (B_θ) which encircles the conductor. The resulting Lorentz force ($J_z \times B_\theta$) is directed radially inward, exerting a substantial radial force on the conductor that drives the conductive material towards the central axis. As this material rapidly implodes and stagnates on the axis, its kinetic energy is efficiently converted into thermal energy, giving rise to an extremely hot and dense plasma [1]. This mechanism produces intense bursts of radiation, such as x-rays or neutrons, depending on the target material. In fact, Z-pinches are one of the most powerful laboratory sources of soft x-ray bursts [2–5].

Z-pinch configurations come in various forms, most of which are cylindrically symmetric. Common examples of such configurations include single wires [6], cylindrical wire arrays [7–10], X-pinches [11, 12], hollow metallic liners [13–18], dense plasma focuses (DPF) [19–21], and gas puff Z-pinches [22–26]. While several premier high energy density (HED) facilities exist, such as the OMEGA and OMEGA-EP laser facilities at the Laboratory of Laser Energetics (LLE) at the University of Rochester [27, 28], and the National Ignition Facility (NIF) at Lawrence Livermore National Laboratory (LLNL) [29, 30], the Z pulsed power facility at Sandia National Laboratories (SNL) is the premier facility dedicated to fast Z-pinch research [5].

The extreme conditions generated by Z-pinches are leveraged across a broad range of scientific fields. Principal applications include driving inertial confinement fusion targets [31–33], radiation sciences [34], studying materials under extreme conditions [35], and providing data for stockpile stewardship [5]. Furthermore, Z-pinches are used to create astrophysical conditions in a laboratory setting to investigate phenomena such as magnetic reconnection [36–38] and accretion disks [39]. Their applications further extend to advanced imaging

techniques [40] and planetary science [41].

A significant challenge in the utilization of Z-pinches lies in their inherent susceptibility to fast-growing magnetohydrodynamic (MHD) instabilities, as shown in Fig. 1.1. As the driving current ionizes the conductor into a plasma state, the system becomes vulnerable to several current-driven modes, most notably the $m = 0$ sausage instability and the $m = 1$ kink instability, where m is the azimuthal mode number [1]. As the plasma surface of the Z-pinch begins to accelerate inward due to magnetic pressure, it is further subjected to the powerful acceleration-driven magneto-Rayleigh-Taylor (MRT) instability (MRTI) [16, 42–50]. Left unmitigated, these instabilities are detrimental to confinement schemes, as they induce asymmetries, redistribute mass, and cause material mixing of the target, consequently resulting in a substantial reduction of radiation yields and disruption of the target.

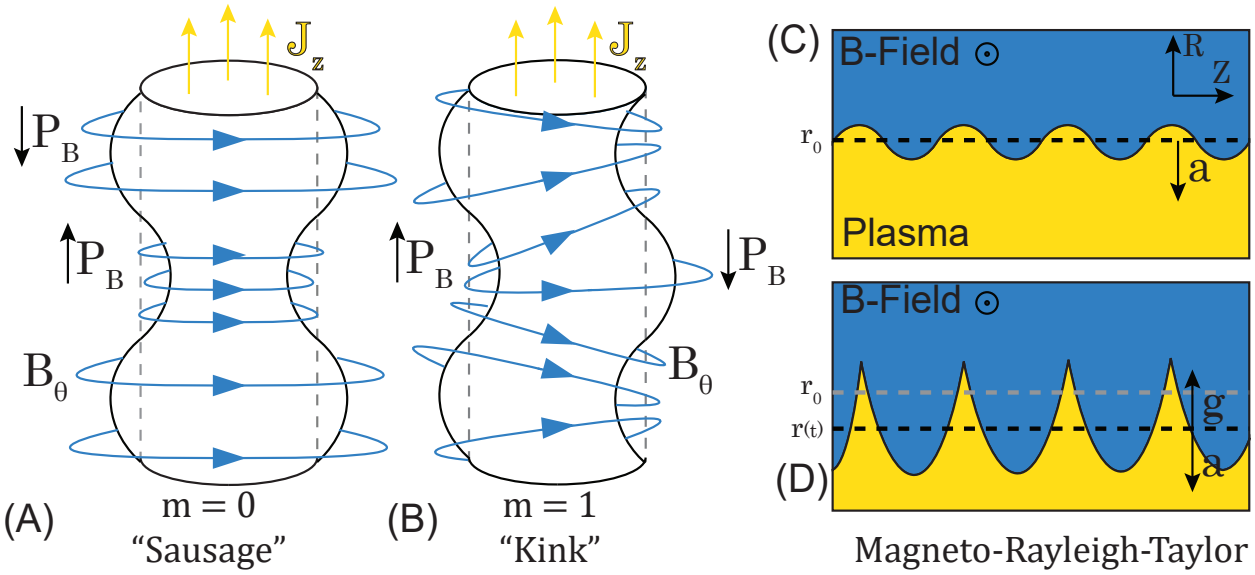


Figure 1.1: An illustration of common MHD instabilities in a Z-pinch. The current-driven (a) $m = 0$ "sausage" and (b) $m = 1$ "kink" instability. Note the increasing and decreasing magnetic field pressure causing the deformation of the current-carrying plasma column. The acceleration-driven MRT instability at (c) the initial frame and (d) during implosion. Note the effective acceleration (g) experienced by the boundary is outwards (+R direction), creating an unstable configuration where a lower-density "fluid" (i.e., the magnetic field) pushes on a higher-density fluid (i.e., the plasma).

Generally speaking, the fastest growing modes in Z-pinches are the sausage and kink instabilities. The development of these modes can be suppressed by the application of an external magnetic field along the axis of the Z-pinch [17]. However, doing this typically results in helical instabilities with $m > 1$. Understanding the formation and evolution of

these various instabilities remains a critical area of modern Z-pinch research. Even though Z-pinches are riddled with instabilities, they remain an extremely efficient source of X-rays and fusion neutrons. The understanding and ultimate control of these instabilities is essential to further enhance the performance of Z-pinch-based systems.

1.2 Pulsed Power

Pulsed power is the conventional method to obtain a fast rising, large amplitude current pulse (>0.1 MA in ∼100 ns), which is essential for initiating and compressing Z-pinches. The fundamental principle of pulsed power is the temporal compression of energy. During this process, a bank of capacitors is DC charged over a relatively long time period (minutes). Subsequently, the stored energy is then rapidly discharged via a fast plasma switch into a load over a considerably shorter period of time (ns–µs). This process effectively compresses the discharge pulse temporally, thereby substantially enhancing the peak power of the pulse delivered to the load.

At a fundamental level, a pulsed power system can be modeled as a series RLC circuit [51], where the current delivery is limited by the total inductance and resistance of the system, including the load. Power density may be further amplified through spatial compression, where energy from a large generator is concentrated onto a substantially smaller target. Distinct architectures of pulsed power exist, such as Marx banks and linear transformer drivers (LTD), which represent unique methods of configuring the capacitors and switches to attain the extreme currents and voltages required to drive HED loads.

One of the most common architectures for pulsed power systems is the Marx generator [5, 52]. This generator consists of capacitors that are initially charged in parallel and isolated from the load using pressurized gas switches. Once the capacitors are fully charged, the switches rapidly reconfigures the circuit to connect the capacitors in series. This reconfiguration permits the voltages across each capacitor to be summed, thereby producing a singular high-voltage, high-power electromagnetic pulse that is delivered to the load.

Pressurized switches are essential components in pulsed power technology as they provide the necessary isolation during the charging phase and control the timing of the discharge. One of the most common switch types is the three-electrode field-triggered switch [53, 54]. In this design, the two terminal electrodes are biased to some high potential difference, while a third, floating electrode is positioned between them. The switch is activated when the central electrode is pulsed to an additional high potential. This generates an intense electric field between the central and terminal electrodes, leading to the rapid breakdown of the insulating gas and the formation of a conductive plasma channel; a process known

as triggering the switch. The resultant plasma arc completes the circuit, serving as the conductor that connects the main capacitors in series.

While Marx generators are effective, achieving the fast rise times needed for modern Z-pinches presents challenges. High energy systems require large capacitance, resulting in capacitors that are physically large and energetic. This would naturally produce longer rise time (often ∼1 µs) electromagnetic pulses. Furthermore, the plasma switches are not ideal conductors. The plasma arc has an inherent resistance and inductance, which are multiplied by the number of stages since they are connected in series. This further slows the pulse and can reduce the peak current delivered to the load.

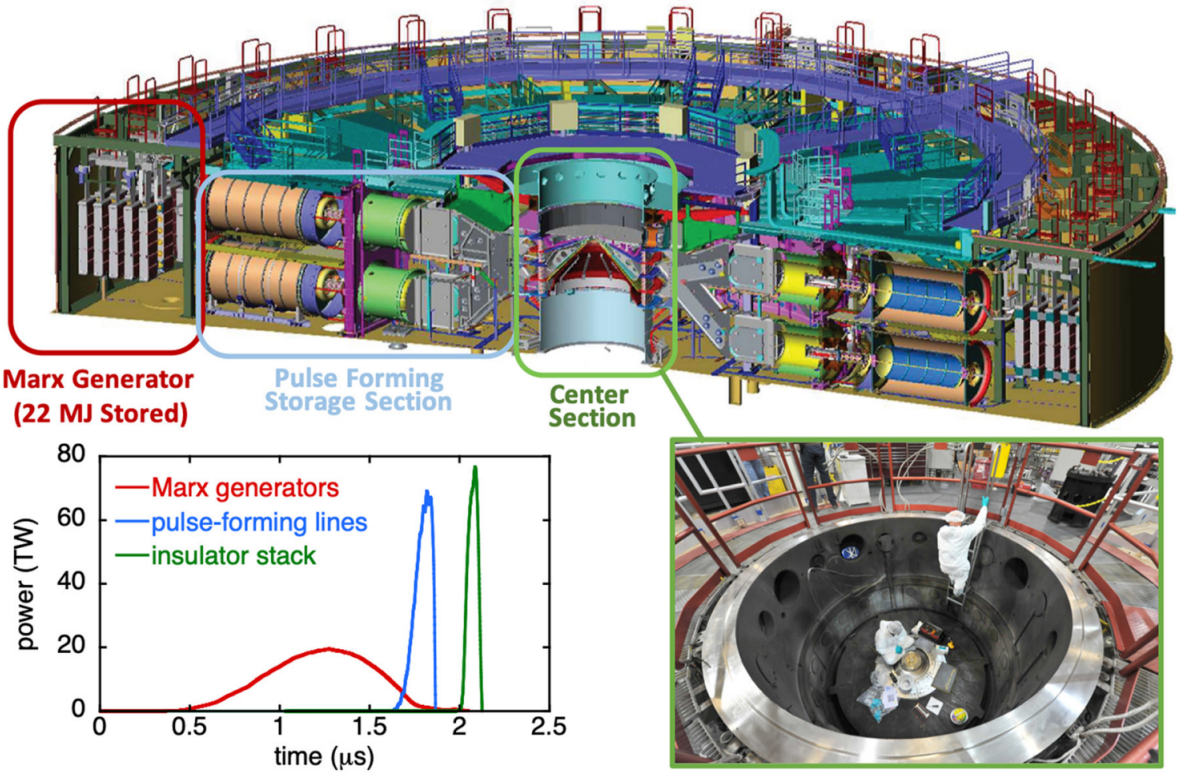


Figure 1.2: Cross-section of the Z Pulsed Power Facility at Sandia National Laboratories, displaying its three main sections: the Marx generator, the intermediate pulse forming line, and the center MITLs. (Lower left) A plot demonstrating pulse compression, where the slower output pulse from the Marx (red) is compressed by the pulse forming line (blue). (Lower right) A photograph of Sandia personnel inside the central load region. Source: [5]; licensed under a Creative Commons Attribution (CC BY) license.

To shorten the rise time to ∼100 ns, the implementation of a secondary stage of pulse compression becomes necessary. A pulse-forming section, consisting of intermediate storage capacitors (ISCs) and pulse forming lines (PFLs), effectively serves this function by facili-

tating further pulse compression, as shown for the Z facility in Fig 1.2 [5, 55]. Typically, the ISCs and PFLs are designed as capacitors fabricated from materials with high dielectric constants, such as deionized water. Water (when pulsed) possesses one of the highest relative dielectric constants ($\epsilon_r \approx 81$), in contrast to materials like air, which has a constant of 1, and plastics, which can achieve ≤ 10 [56]. In typical configurations, the ISCs and PFLs are positioned between the Marx generator and the transmission lines. The ISC's output is isolated by a plasma switch, which allows for charge retention throughout the Marx bank's output duration. Upon reaching full charge, the ISCs are rapidly discharged into the PFLs via plasma switches. Given that the ISCs and PFLs have a much lower capacitance and inductance compared to the main Marx bank, their discharge times are significantly shorter, thereby effectively "sharpening" the leading edge of the power pulse.

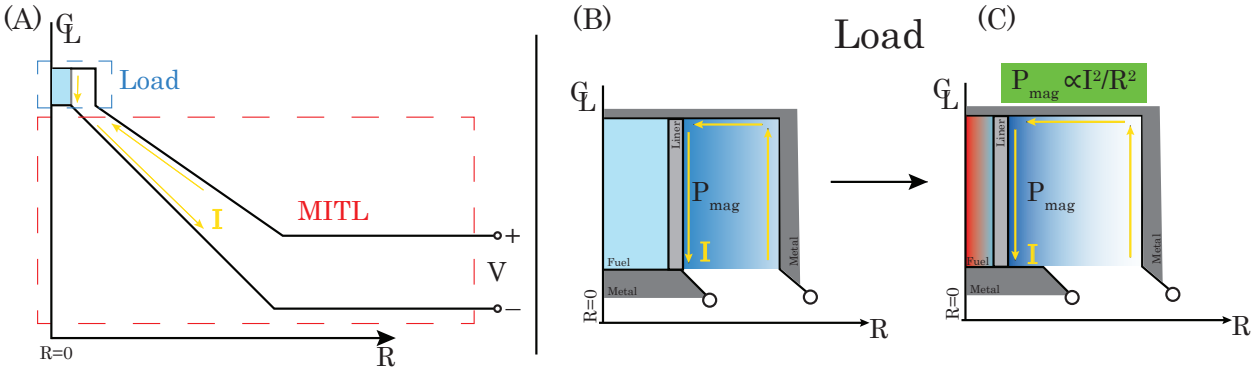


Figure 1.3: (A) An illustration of a conical MITL structure (inside dashed red box) delivering current into the load region (inside dashed blue box). (B,C) Zoomed-in illustration of a liner implosion driven by P_{mag} (magnetic pressure) compressing and heating the internal fuel. Note that the magnetic pressure scales $\propto I^2/R^2$.

The output pulse from the pulse forming section is subsequently transmitted to magnetically insulated transmission lines (MITLs) in the vacuum section of the machine. The MITLs are responsible for delivering the pulse to the load, as seen in Fig. 1.3. As the current travels toward the small, cylindrical load at the center of the machine, the overall system radius decreases, resulting in a significant increase in local magnetic field and current densities at the conducting surface. The applied voltage (electric field) that drives the power pulse into the MITLs can strip electrons from the cathode surface, posing a risk of significant current loss if these electrons cross the anode-cathode (AK) gap. This consideration is important to bear in mind throughout the examination of this dissertation. Fortunately, the potential current loss is prevented via magnetic insulation in the MITLs [57–59]. By virtue of Ampère's law, the immense currents conducted along the MITL electrode surfaces result in powerful magnetic fields (B), where $B = \frac{\mu_0 I}{2\pi r}$, that fill the anode-cathode gaps within the

MITL structures. These magnetic fields prevent electrons and plasmas from crossing the AK gaps within the MITL structures via the Lorentz force. Here, the Lorentz force can be thought of as a magnetic "pressure", which is

$$P_{\text{mag}} = \frac{B^2}{2\mu_0} = \frac{\mu_0 I^2}{8\pi^2 r^2}, \tag{1.1}$$

where μ_0 is the permeability of free space, r is the radius of interest within the MITL structure, and I is the driving current. This means that the magnetic pressure increases as the radius decreases, which helps keep the AK gaps open and clear of plasma even close to the target or load, where the current density, ohmic heating, and electrode plasma formation can become very large. Although magnetic insulation is highly effective, understanding the behavior and determining the effects of electrode plasmas and any minor current losses is an important aspect of power flow in these systems.

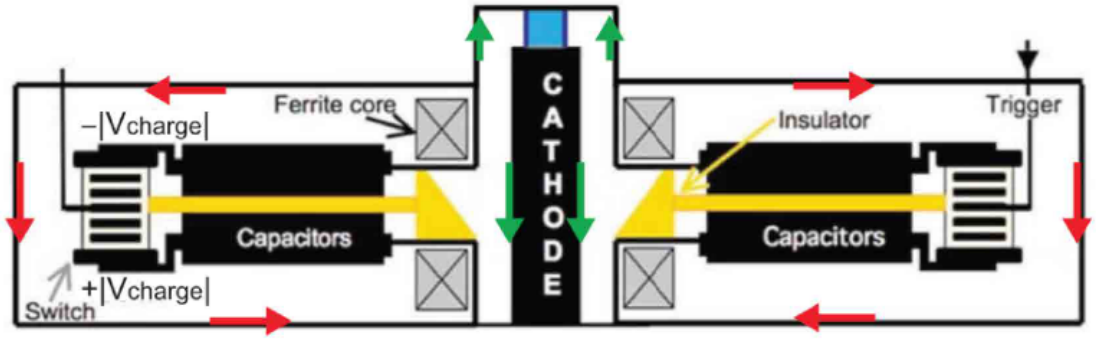


Figure 1.4: An illustration of a bi-polar LTD, where the green and red arrows indicate the path for the current delivered to the load and the path for parasitic current loss around the lid, respectively. (Source: [60])

A modern, novel pulsed power architecture, the linear transformer driver (LTD), was developed to minimize the spatial requirements of high-energy pulsed systems [60–64]. An LTD consists of small-capacitance capacitor-switch-capacitor units, referred to as "bricks," which are configured to charge and discharge in parallel, as shown in Fig. 1.4. In contrast to the Marx generator, the bricks are discharged in parallel. This fundamental distinction enables the LTD to achieve a faster rise time and greater amplitude current. The parallel discharge configuration is the key advantage of the LTD, as the inductances and resistances of the parallel switches sum reciprocally, resulting in an exceptionally low total system impedance. Consequently, an LTD is capable of generating a rapidly rising, high-amplitude current pulse without the need for a subsequent pulse compression stage. The output pulse

is delivered directly to the magnetically insulated transmission lines (MITLs).

The primary trade-off for an LTD is the lower output voltage, constrained by the charge voltage of an individual brick, and its lower overall system impedance. This limitation is not particularly problematic for Z-pinches, as the loads are typically low impedance and the inductance is generally small ($\sim$10 nH) [60]. Nonetheless, these constraints can be addressed by configuring multiple LTD cavities in series, thereby summing their voltages and enhancing both the total energy and impedance of the machine. A common method to increase the output voltage involves the utilization of a bipolar brick. This design modifies a standard brick to accommodate two capacitors instead of one. The capacitors are charged to opposite polarities (for example, +V and -V), effectively doubling the voltage delivered by a single switch. The principal practical limitation of the LTD architecture is the substantial number of individual bricks necessary to construct a system that is energetically viable for scientific research.

An essential component in the design of a LTD is the ferrite core combined with the metal enclosure. These enclosures function as a Faraday cage, greatly reducing the electromagnetic interference (EMI) that originates from the discharge of the bricks. In the field of pulsed power, controlling EMI is critically important due to its potential to damage adjacent electronics and introduce undesirable noise within experimental measurements. Nonetheless, the presence of the metal lid presents a conduit for parasitic current loss, establishing an unwanted parallel current path and thereby redirecting some of the current away from the load. To alleviate this issue, a ferromagnetic core is positioned within the enclosures to mitigate the loss attributable to the lid. For a fast rising current pulse, the path encircling the ferrite material acts as a high impedance pathway to the parasitic current, with this impedance being substantially greater than that of the load, which effectively directs the current to the intended load. Over many shots, the magnetic hysteresis will invert, leading to the magnetic saturation of the core, which in turn reopens the pathway for parasitic current losses. The core's magnetic characteristics can be restored by driving a current pulse in the reverse direction, making the core a highly reusable component of an LTD.

These two pulsed power architectures are utilized by leading research laboratories worldwide. Notable facilities utilizing the Marx architecture include the Z Facility at Sandia National Laboratories [5], COBRA at Cornell University [65], MAGPIE at Imperial College London [66], ZEBRA at the University of Nevada Reno [67], and MELBA at the University of Michigan [68]. Conversely, significant LTD facilities include MAIZE at the University of Michigan [60, 63, 69], CESZAR at the University of California San Diego [70], LOBO at the University of New Mexico [71], MACH at Imperial College London, and HADES at the University of Rochester [72].

In recent years, there has been a significant resurgence of interest in pulsed power technology and Z-pinch research. A substantial influx of private investment has prompted the emergence of numerous startup companies exploring a variety of fusion reactor concepts. This renewed interest is partially attributed to the recent nuclear fusion ignition and propagating burn results achieved by the NIF [73]. Many of these new private companies are leveraging modern pulsed power technology as a potentially cost-effective and efficient driver for their projects. Notably, companies such as Pacific Fusion and Fuse Energy are focusing on the development of next-generation pulsed power technology to directly drive Z-pinch-like targets for inertial confinement fusion [33, 74]. Other enterprises, including Zap Energy, are utilizing Z-pinches directly to generate thermonuclear fusion [32]. Although this commercial interest is a recent development, the approach is grounded in decades of foundational research. Sandia National Laboratories, which hosts the world's most powerful pulsed-power driver (the Z machine), has long been at the forefront of studying Z-pinches and their application to magneto-inertial fusion schemes.

1.3 Plasma Confinement for Fusion and MagLIF

A fusion reaction occurs when two or more atomic nuclei overcome their mutual Coulombic repulsion, allowing the attractive nuclear force to bind them into a heavier metastable nucleus that then blows itself apart, releasing the stored binding energy, which is carried away by the fusion reaction products. This phenomenon is the driving mechanism behind energy production in stellar bodies (such as our Sun), facilitates the operation of nuclear weaponry, and represents the objective of controlled fusion energy systems. A fundamental parameter to evaluate the efficiency of a fusion energy system is the Lawson criterion [75], which assesses the ratio of energy generated by fusion reactions to the energy losses incurred. In the context of a pulsed system, the Lawson criterion is determined by the plasma temperature T in conjunction with the product of plasma density n and confinement time τ, commonly referred to as the triple product $nT\tau$. The popular fusion reaction chain is composed of the deuterium-tritium (D-T) and deuterium-deuterium (D-D) reactions:

$$\mathrm{D} + \mathrm{T} \longrightarrow \alpha(3.5\,\mathrm{MeV}) + n\,(14.1\,\mathrm{MeV}) \tag{1.2}$$

$$\mathrm{D} + \mathrm{D} \longrightarrow \mathrm{T}\,(1.01\,\mathrm{MeV}) + p\,(3.02\,\mathrm{MeV}), \quad (50\%) \tag{1.3}$$

$$\mathrm{D} + \mathrm{D} \longrightarrow {}^{3}_{1}\mathrm{He}\,(3.6\,\mathrm{MeV}) + n\,(2.45\,\mathrm{MeV}), \quad (50\%) \tag{1.4}$$

Where D is a deuteron, T is triton, α is a Helium-4 ion/alpha particle ($^4He^{2+}$), p is a proton, and n is a neutron.

Three primary approaches to thermonuclear fusion are being actively explored: magnetic confinement fusion (MCF), inertial confinement fusion (ICF), and magneto-inertial fusion (MIF). In the MCF approach, magnetic fields are employed to control and confine plasma across an extensive volume for prolonged durations. The plasma density is comparatively low (10^{14}/cm^3), whereas the confinement time is relatively long ($>10^{-1}$s). Notable MCF devices include tokamaks [76], stellarators [77], magnetic mirrors [78], and field reversed configurations [79], among others. By contrast, ICF represents the other extreme, with objectives of attaining elevated plasma density (10^{26}/cm^3) and pressure within a constrained timeframe ($<10^{-10}$s) and a minimal volume. This state is achieved via the application of lasers to initiate implosions of capsules loaded with fusion fuel. The ensuing imploded fuel is confined by its own inertia during the burn phase. Distinguished ICF facilities include NIF, OMEGA, and Laser MegaJoule. Notably, inertial laser fusion has been the first experiment to achieve a target gain (Q) exceeding unity, indicating that the energy output from implosions exceeds the laser energy input [73]. The aforementioned techniques have received substantial investment and scholarly attention over several decades. The third approach, MIF, occupies an intermediary position between the prior strategies. MIF leverages both magnetic fields and inertial confinement to realize thermonuclear fusion under conditions of moderate plasma density, volume, and time scales. As mentioned previously, there has been a significant recent investment into the MIF approach. Among the various MIF concepts, magnetized liner inertial fusion (MagLIF) experiments have demonstrated thermonuclear production [80, 81] and are regarded as a promising pathway toward achieving ignition.

The MagLIF concept is a flagship MIF experiment conducted at the Z pulsed power facility at Sandia National Laboratories [5, 31, 80, 82, 83]. A MagLIF target is composed of a hollow cylindrical shell (liner) filled with deuterium fusion fuel, as shown in Fig. 1.5. The liner is typically constructed from a metal with a low atomic number, such as beryllium. The concept relies on a sequence of three distinct stages:

1. Magnetization. External Helmholtz coils are used to apply an axial magnetic field (10–30 T) to the entirety of the load region, pre-embedding the target with axial magnetic field.

2. Laser Preheating. A multi-kJ laser preheats the fuel to hundreds of eV through a laser entrance hole located at the top of the target. This preheating makes it easier to reach fusion temperatures at stagnation.

3. Compression. The Z facility delivers a 20-MA, 100-ns current pulse axially through the

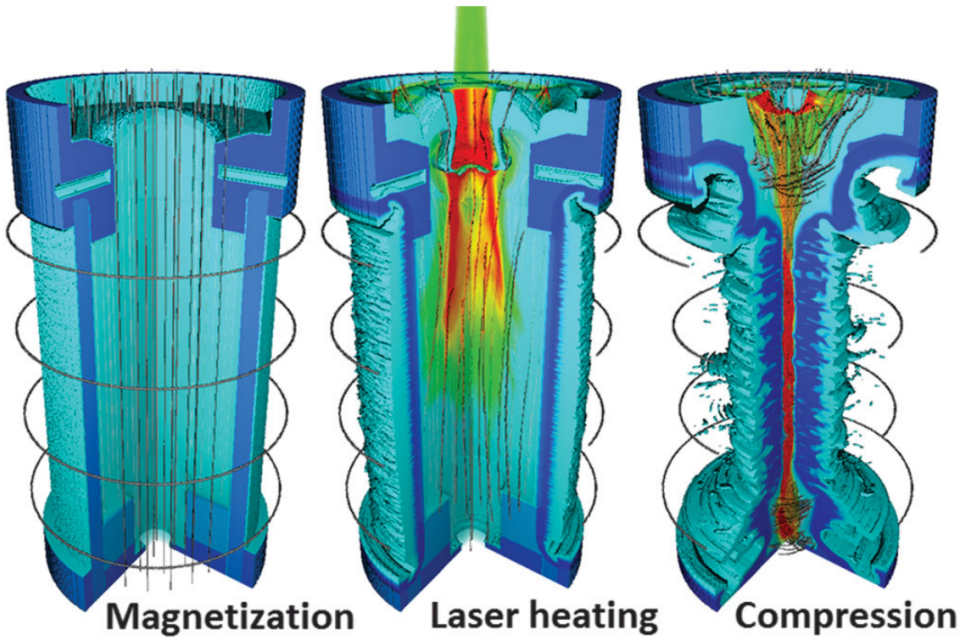


Figure 1.5: Illustration of the three main stages of an integrated MagLIF experiment. (1) magnetization: An axial magnetic field is applied to the cold fusion fuel (light blue) inside a beryllium liner (dark blue). (2) Laser pre-heating: A laser (green) heats the fuel.(3) Compression: A large electrical current generates an azimuthal magnetic field that implodes the liner, compressing the fuel to a hot, dense stagnated state (red) [80]. Reprinted (figure) with permission. Copyright 2025 by the American Physical Society.

liner. The liner is then compressed radially by the $\mathbf{J} \times \mathbf{B}$ force density. This magnetic drive implodes the liner at a high velocity ($\sim$ 100 km/s), performing adiabatic "PdV" work on the fuel and compressing it to thermonuclear conditions.

The effectiveness of the scheme is contingent upon the structural integrity of the imploding liner. As the liner accelerates to the axis, its outer surface is susceptible to MRTI as well as sausage, kink, and helical instabilities. The progression of these instabilities can permeate through the liner wall, ultimately compromising the uniformity and confinement of the resultant assembled fuel.

An integral element of the MagLIF concept is the applied axial magnetic field (initially $\sim$10–30 T). This field is pre-embedded within the entire load volume prior to the implosion. It is generated from a large external Helmholtz-like coil pair that encircles the load region and is pulsed over an extended time scale ($\sim$3 ms) [84]. The prolonged time scale allows the axial field to diffuse into the liner, fuel, and surrounding metallic electrodes prior to the liner implosion. During the fast ($\sim$100 ns) liner implosion, the axial magnetic field cannot diffuse out of the preheated fuel or through the liner wall, thereby confining the magnetic flux within the fuel, ensuring its preservation throughout the implosion process. The resulting flux compression process amplifies the magnetic field strength within the fuel to >1000 T by the time of stagnation. This intense amplification to the magnetic field yields two essential advantages: it suppresses the thermal conduction losses from the hot fuel to the cold liner wall, and it traps charged fusion products within the fuel, promoting self-heating during the fusion burn at stagnation.

Despite the necessity of the axial field, its implementation introduces a significant mystery. Experiments on the Z machine revealed that with axial magnetization, instabilities along the surface of the imploding liner evolve into an unanticipated and pronounced helical structure [14, 15]. The formation of these prominent helical modes is not well understood and constitute an important gap in the foundational knowledge required for the advancement of MagLIF.

1.4 Observations of Enhanced Helical Modes

Penetrating radiography conducted at the Z facility has demonstrated that the application of an axial field modifies the instability structure of imploding MagLIF liners, as shown in Fig. 1.6. In the absence of an axial field, the observed instability structure exhibits azimuthal symmetry ($m = 0$) [13, 85]. Conversely, upon the application of a 10 T axial field, the instability structure assumes a helical configuration, characterized by pitch angles

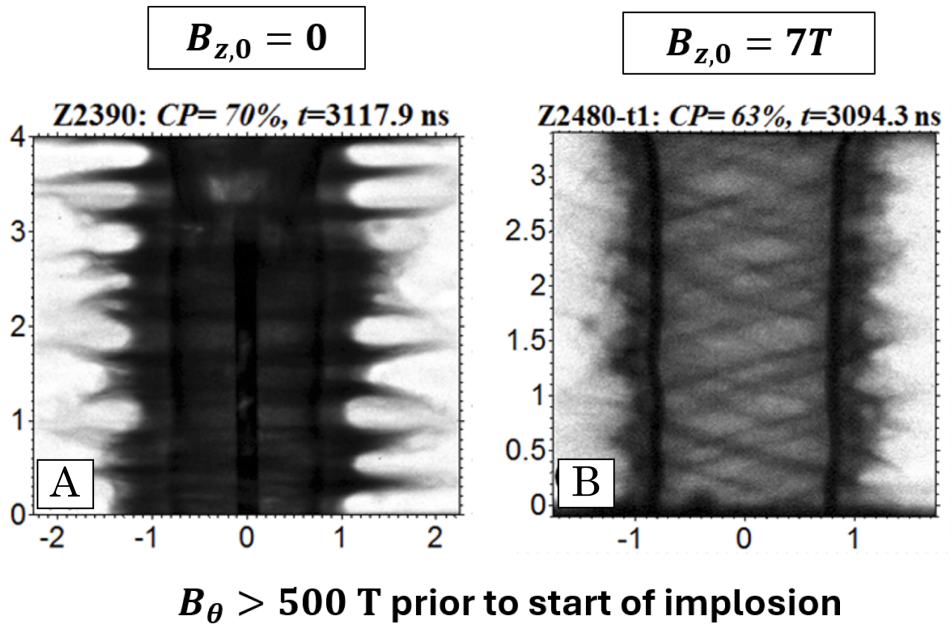


Figure 1.6: Penetrating radiographs of an empty liner implosion with and without axial magnetic field. Note the differences between the instability structures. (A) Without axial magnetic field, azimuthally correlated structures appear which is characteristic of the $m = 0$ sausage mode. (B) With axial magnetic field, helical structures develop [15]. Reprinted (figure) with permission. Copyright 2025 by the American Physical Society.

of approximately 30° and $m \approx 6$ at a fuel convergence ratio of ≈7 [14, 15]. The convergence ratio is defined as the ratio of the initial radius to the final radius of the liner's inner (fuel confining) surface.

The steepness of these helical angles indicates a significant gap in knowledge. The observed magnetic pitch angles are inconsistent with expectations based solely on the ratio of magnetic field strength, where the pitch angle was expected to be proportional to the magnetic field components ($\phi \propto \arctan(B_z/B_\theta)$). In the initial phase of the current pulse, prior to the start of the implosion, the azimuthal magnetic field generated can be >500 T, while the applied magnetic field is approximately 10 T. This ratio would imply a pitch angle < 2°, which appears to not agree with the experimental radiographs. A more accurate depiction of the pitch angle is given by $\phi \propto \arctan(p/[2\pi r_l(t)]) \approx m/[k_z r_l(t)]$, where p denotes the pitch angle, $r_l(t)$ represents the radius of the liner, m is the mode number, and k_z is the axial wavenumber [14, 16, 17]. The specifics of this equation will be explored in this dissertation. These helical structures likely feed through to the fuel by the time of stagnation [80], potentially degrading the confinement and yield of the hot fuel. Additionally, such helical instabilities are also observed in other Z-pinch configurations, including gas-puff Z-pinches [23, 86] and non-imploding metal liners [16, 17, 87, 88].

Several hypotheses have been proposed to explain the substantial helical pitch angles observed in MagLIF liner implosions. One leading hypothesis is centered on the electrothermal instability (ETI) [89], which arises due to nonuniform resistive heating along the liner's surface. The surface of the liner is imperfect and is likely to contain voids, protrusions, and material inclusions, thereby seeding an initial perturbation preceding the liner implosion. The manifestation of ETI is contingent upon the variation in the material's resistivity (η) as a function of temperature (T), and it can present itself in two primary forms, as shown in Fig. 1.7.

The first is the striation form of ETI, which arises when the material's resistivity increases with temperature $\partial\eta/\partial T > 0$. In this situation, a hot spot within the liner would locally divert current away from the hot spot towards the cooler regions with lower resistivity within the liner. As a consequence, the lateral edges of the hot spot undergo increased Joule heating, leading to horizontal expansion. In the context of a cylindrical system, such horizontal growth would be in the azimuthal direction, resulting in a horizontal striation around the liner. Conversely, the filamentary form occurs when the material's resistivity decreases with increasing temperature ($\partial\eta/\partial T < 0$). For instance, a hot spot on the surface would be less resistive compared to the remainder of the liner. Consequently, the hot spot would provide a preferential pathway for current, functioning as a localized current sink. This would lead to current bunching above and below the hot spot, thereby further reducing resistivity and

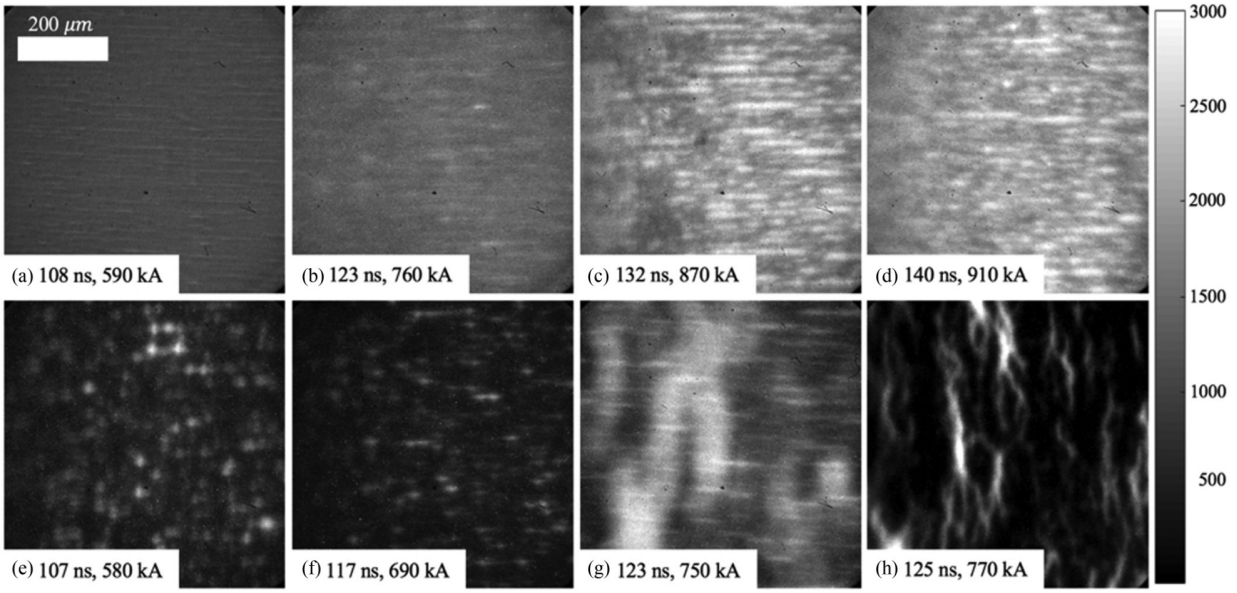


Figure 1.7: Self emission images of the electrothermal instability forming on a metal surface as current is flowing in the vertical direction. (Top Row) Time montage of the ETI development in striation form, where $\partial\eta/\partial T > 0$ in solid metal. (Bottom Row) Time montage of the ETI development in filament form, where $\partial\eta/\partial T < 0$ due to plasma formation [90]. Reprinted (figure) with permission. Copyright 2025 by the American Physical Society.

causing the hot spot to expand in the axial direction (in the direction of current flow). This feedback loop persists, culminating in the formation of a vertical filament parallel to the direction of the current flow.

An alternate hypothesis considers the Hall Interchange Instability (HII), which develops in the low-density coronal plasma that surrounds the liner at the onset of the current pulse [91, 92]. The HII facilitates the flow of magnetic-field-aligned (force-free) currents, which can induce helical striations imprinted upon the outer surface of the dense liner material, as shown in Fig. 1.8. The theoretical basis for this phenomenon is enabled by the generalized Ohm's law,

$$\mathbf{E} + \mathbf{v} \times \mathbf{B} = \eta \mathbf{J} + \frac{1}{en_e}\mathbf{J} \times \mathbf{B} - \frac{1}{en_e}\nabla \mathbf{p_e} \tag{1.5}$$

where $\mathbf{E}$ is the electric field, $\mathbf{B}$ is the magnetic field, $\mathbf{v}$ is the plasma velocity, $\mathbf{J}$ is the current density, η is the resistivity, n_e is the electron density, and p_e is the electron pressure. The three terms on the right-hand side of this equation are, respectively, the resistivity term, the Hall term, and the electron pressure gradient term. The Hall term becomes important at lower densities as a result of its $1/n_e$ dependence. In turn, it can generate an additional azimuthal current, potentially increasing the applied axial field.

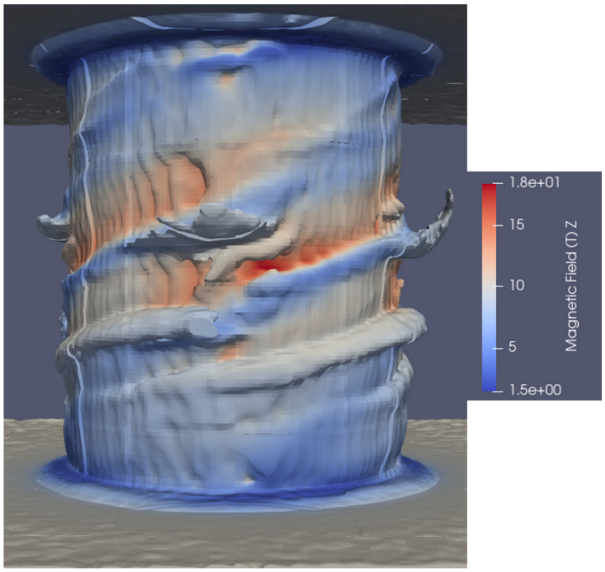


Figure 1.8: PERSEUS simulations of low-density coronal plasma developing around a liner. The inclusion of Hall physics in the code leads to the formation of helical perturbations in this low-density plasma layer. Reprinted from [91], with the permission of AIP Publishing.

A third hypothesis [93, 94] involves magnetic flux compression within the low-density plasma encasing the liner, sourced from the MITLs of the Z facility, as shown in Fig. 1.9. These MITLs deliver immense power (electrical current and magnetic pressure) to the imploding MagLIF liner. As the power pulse travels towards the liner, the MITLs are subjected to high current densities (> 1 MA/cm^2) and intense electric fields. Such conditions induce joule heating on the surfaces of the MITLs, resulting in the desorption of neutral particles initially entrapped within the metal's porous structure. These desorbed neutrals, typically consisting of hydrocarbons and water, undergo ionization and transition into a low-density ($n_e \approx 10^{15}$–10^{18}/cm^3) plasma [95, 96]. This low-density plasma can shunt current across the AK gap, whereas the melted MITL surface transforms into a denser plasma ($n_e \approx 10^{18}$–10^{21}/cm^3) located closer to the initial electrode surface. Monte Carlo particle-in-cell (PIC) simulations are used to study the generation and evolution of these electrode plasmas in the MITL during the early stages of the power pulse [95], as shown in Fig. 1.10. Such phenomena may exert unpredictable effects potentially detrimental to the experiment. For instance, the low-density plasma may conduct current across the AK gap, thereby diminishing the current and the magnetic drive pressure delivered to the liner target. By 60 ns into the current pulse, these simulations indicate that the MITL leading up to the liner target is filled with low-density plasma, possessing an electron number density of $n_e \lesssim 10^{17}$ cm^{-3} [95].

The proposed mechanism suggests that the presence of this low-density plasma provides

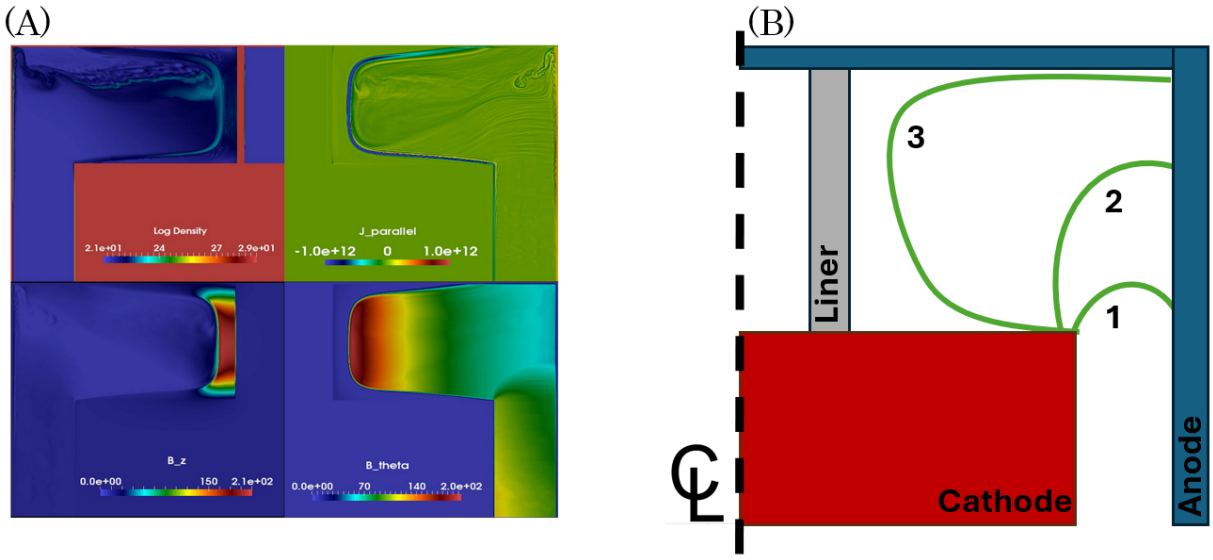


Figure 1.9: (a) A PERSEUS simulation at $t = 40$ ns showing low-density plasma from the power feed being compressed onto the liner. The simulation was initialized with a uniform 10 T axial magnetic field which is compressed to several hundreds of Tesla on the liner surface. (b) Illustration of the flux compression process, where the green line represents a shunted current sheath flowing along the edge of low-density power feed plasma at three different times. This current sheath flow along the edge of low-density power feed plasma. The process goes as follows: (1) Initial current shunting along the edge of low-density plasma, (2) the $J \times B$ force drives the shunted sheath towards the target, (3) the sheath sweeps up and compresses axial field in the return can onto the surface of the liner. Reprinted from [93, 94], with the permission of AIP Publishing.

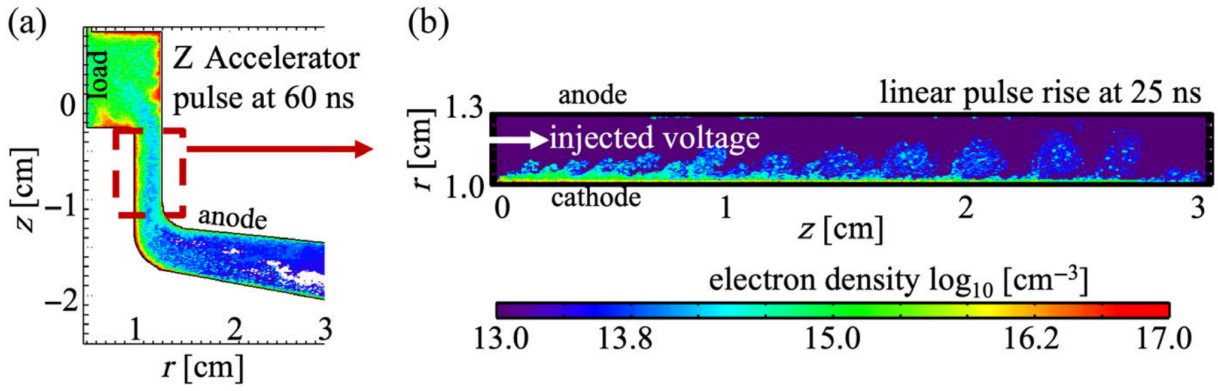


Figure 1.10: PIC simulations of desorbed plasma filling the load region MITL. (a) Plasma electron density map at $t = 60$ ns into the current pulse. Prior to the main implosion, the load region is already filled with a low-density plasma, with $n_e \approx 10^{15}$–10^{17} cm^{-3}. (b) Simulation of the MITL directly connected to load at $t = 25$ ns, showing plasma "roll-ups" as the electrons flow from the MITL into the load volume. (Source: [95])

a path for a portion of the main drive current to be shunted across the AK gap. Should this phenomenon transpire, the Lorentz force arising from the shunted current will drive this plasma towards the main load. Since the entire load region was pre-embedded with an axial magnetic field ($B_{z,0}$), the imploding low-density plasma traps and compresses the axial magnetic flux onto the liner's outer surface. Instability structures within the magnetized low-density plasma may subsequently imprint themselves, potentially via perturbations in current density, onto the liner's dense outer surface.

Studies have identified that low-density ($n_e < 10^{17}$) plasma contributes to current loss in Z [97, 98]. However, this observation does not address the impact of this low-density plasma on the load. Extended MHD (X-MHD) simulations have been used to investigate the influence of this plasma on an imploding MagLIF liner [91, 94]. Evidence suggests that if such low-density plasma is present in the power feed close to the load, it can be swept up, collect magnetic field, and compress the field onto the surface of the liner. This phenomenon can result in the amplification of the axial field, which could explain the observed helical modes.

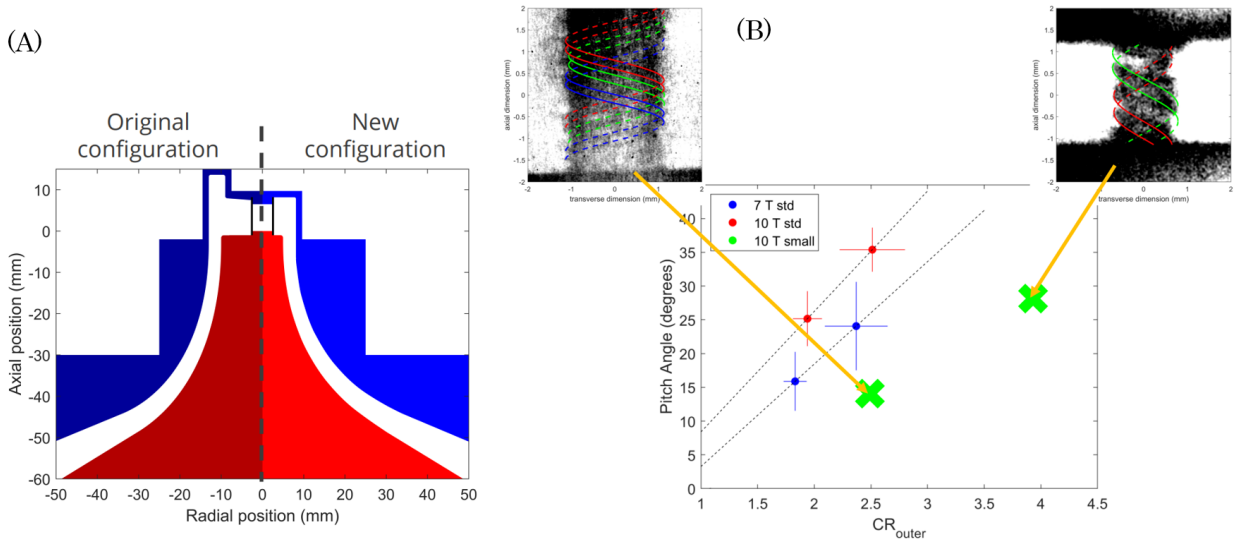


Figure 1.11: Experimental configuration and resultant helical structure of a flux compression experiment. (a) A cross-section of the return can configuration used to control the amount of available magnetic flux within the load region. (b) The resultant pitch angle of the instability formed. At the same CR, the reduced flux volume configuration produced a significantly smaller pitch angle. (Source: [99])

Furthermore, while direct measurements are challenging, suggestive evidence is derived from a dedicated experiment conducted on the Z machine. In this experiment [99], the load volume was deliberately reduced to decrease the amount of axial flux compression,

as shown in Fig. 1.11. This experimental setup maintained a constant target geometry and inductance to ensure a similar drive current, thus preserving the constancy of B_θ. An applied $B_{z,0} = 10$ T was utilized for both scenarios, with a reduction in the volume of the target region by approximately 4×. The outcomes, while not definitive, suggest that a decreased striation pitch angle can be expected when using a decreased load volume surrounding the target. Under the standard configuration, the pitch angle was measured to be $\sim 35^\circ$ at a $CR \approx 2.5$, whereas the reduced flux volume yielded a smaller angle of $\sim 13^\circ$ at a similar CR. This observation supports the hypothesis that the helical instabilities observed on the Z facility are due to magnetic flux compression occurring in the low-density plasma of the final power feed. Should this picture be correct, it warrants further study to understand the role of low-density plasmas in seeding instabilities in metal liner implosions.

Although the findings are suggestive, they remain inconclusive, primarily due to the observations being conducted within a complex, integrated environment where additional phenomena, such as ETI and Hall physics, may also influence the outcomes. The principal mechanism responsible for the observed helical instabilities in MagLIF liner implosions remains uncertain. Furthermore, it is feasible that a combination of the aforementioned processes may contribute to these observations. Therefore, it is imperative to undertake a dedicated, simplified experiment aimed at unraveling the physics of magnetic flux compression by a low-density plasma. This necessity forms the central motivation for the work presented in this dissertation.

1.5 Dissertation Objective and Outline

This dissertation experimentally investigates the instability imprinting of a low-density gas-plasma imploding onto a thin metal liner. These experiments were designed and carried out at the MAIZE pulsed power facility at the University of Michigan, with the purpose of emulating, at a reduced scale, the phenomena anticipated in MagLIF experiments.

Chapter 1 presents a general introduction to the concepts of Z-pinches, pulsed power systems, and MagLIF experiments, alongside the motivations of this research study. Chapter 2 discusses theory relevant to the experimental discussion. Chapter 3 discusses a summary of the MAIZE facility and the main diagnostics used throughout the investigation. Chapter 4 presents an experimental campaign to study axially magnetized, low-density gas implosions onto a thick central conductor. Chapter 5 presents an experimental campaign to study the instability coupling between the gas layer and the thin-foil liner implosion. Chapter 6 presents an integrated experimental campaign studying the helical instability of the axially magnetized gas on the liner target. Finally, Chapter 7 concludes this dissertation with final

remarks.

CHAPTER 2

Physics Background

This chapter provides a review of the theoretical concepts governing pulsed power driven Z-pinch implosions and the development of magnetohydrodynamic (MHD) instabilities. It begins with the foundational principle of pulsed power circuit theory and magnetic pressure, which constitute the primary driving mechanisms for these implosions. Following this, it then details the physics of a dynamic implosion, deriving the partitioning of magnetic energy, the skin effect in pulsed regimes, and the frozen-in-flux theorem. Finally, this chapter covers the theoretical foundations of prevalent MHD instabilities, including the current-driven sausage mode ($m = 0$) and kink mode ($m = 1$), the classical fluid Rayleigh-Taylor (RT) instability, and the phenomenon of pitch locking in liner implosions. This theoretical framework provides the necessary context for interpreting the experimental data, presented in the subsequent chapters.

2.1 Pulsed Power Circuit Theory

Majority of Z-pinches are driven by intense electrical currents generated by pulsed power systems [6]. In this context, we shall derive the ideal current drawn from a pulsed power source when applied to an inductive load, which serves as a representation of a Z-pinch target. A generic pulsed power system can be simply modeled as a series RLC discharge circuit, as shown in Fig. 2.1(a). This circuit comprises a static capacitance C which represents the total capacitance of the energy storage, a variable resistor $R(t)$, a variable $L(t)$ that represents the dynamic load, and a time-dependent switch that discharges the charge stored in the capacitors into the load. Applying Kirchhoff's voltage law yields the governing equation for the circuit current, $I(t)$ and a static L (L = constant):

$$V_R + V_L + V_C = I(t)R + L\frac{dI(t)}{dt} + \frac{1}{C}\int I(t) = 0, \tag{2.1}$$

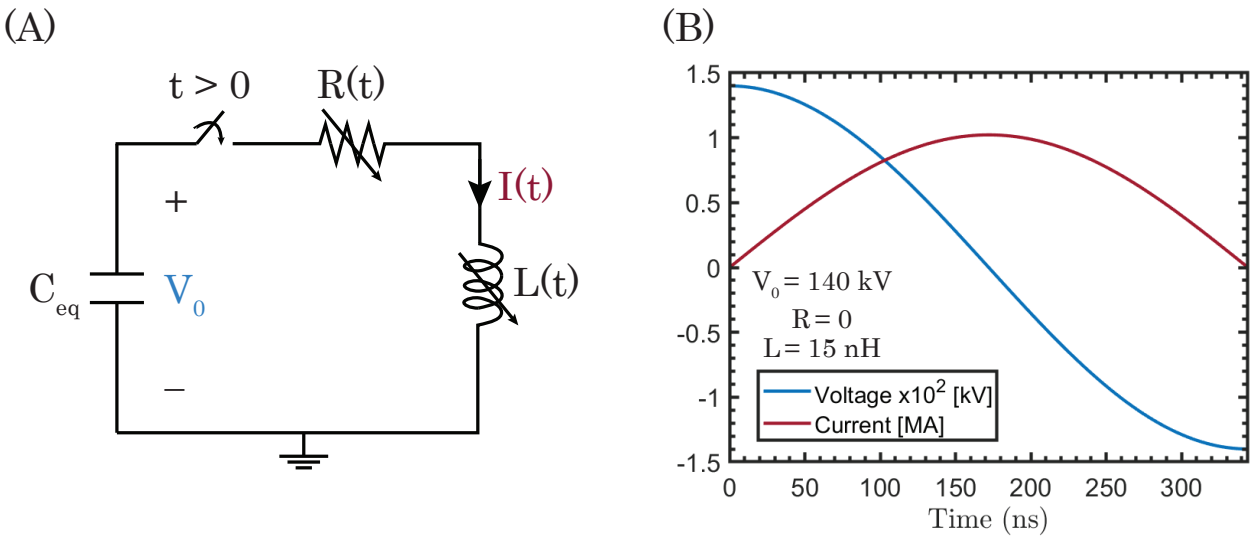


Figure 2.1: (A) A simple schematic of a RLC discharge circuit, showing an equivalent capacitance (C_{eq}), a time-dependent resistor ($R(t)$), a time-dependent inductor ($L(t)$), and a closing switch. (B) A plot of the resulting half-cycles of the voltage ($V(t)$) and current ($I(t)$) waveforms for an ideal, lossless circuit ($R(t) = 0$) with an initial charge voltage of $V_0 = 140$ kV and static inductance of $L = 15$ nH.

where V_R, V_L, and V_C are the voltages across the resistor, inductor, and capacitor, respectively.

We can further simplify the system by letting $R = 0$ for a lossless system. This reduces the system to an oscillating magnetic cavity, an LC circuit. In this case, energy oscillates between the capacitor's electric field and the inductor's magnetic field; no energy is lost. Differentiating Kirchhoff's voltage law equation gives the second-order ordinary differential equation for a simple harmonic oscillator:

$$L\frac{d^2I(t)}{dt^2} + \frac{1}{C}I(t) = 0. \tag{2.2}$$

The solution for the current is a sinusoidal waveform:

$$I(t) = I_{\text{peak}} \sin(\omega t), \tag{2.3}$$

where I_{peak} is the peak current of the discharge and ω is the resonant frequency of the oscillator. These quantities are given by:

$$I_{\text{peak}} = V_0\sqrt{C/L}, \quad \omega = \sqrt{1/LC}. \tag{2.4}$$

An example of a typical LC discharge current and voltage waveforms is shown in Fig. 2.1(b).

Generally, in a pulsed power machine, the capacitance is constant, and the charge voltage (V_0) and inductance (L) can vary. The charge voltage is generally set to the highest safe voltage; on MAIZE, it is ±70 kV. Therefore, to maximize the drive current, it is important to minimize the inductance of the load. Additionally, in a lossy system with resistance, the peak current further decreases in the form of Joule heating. Depending on the R, L, and C values, this makes the system critically damped, under-damped, or over-damped.

2.2 Pulsed Power Driven Implosion Physics

Maximizing the current delivered is important in generating large magnetic pressure in the load region to implode the target [60]. Consider a cylindrically symmetric current-carrying conductor, carrying a current in the z-direction. From Ampère's law, the conductor is enclosed by the generated magnetic field (B_θ) from the flowing current. This magnetic field generated in the vacuum region is given by:

$$B = B_\theta(r,t) = \frac{\mu_0 I(t)}{2\pi r}, \tag{2.5}$$

where μ_0 is the permeability of free space and r is the radius in the vacuum region where the field is evaluated. The magnetic field generates magnetic pressure $p_{\text{mag}} = B^2/2\mu_0$ that will apply a force on the current-carrying surfaces within the load. Note, the concept of magnetic pressure is a convenient way to describe the Lorentz force acting on a current-carrying surface. Very large magnetic pressures can be obtained by channeling large currents into a small radius. This is necessary to drive fast Z-pinches and compression of ICF targets such as MagLIF [31, 60, 100]. To understand where magnetic pressure comes from, consider a planar, perfect conductor with the current flowing uniformly on the surface of the conductor at an infinitesimal skin depth (δx). The surface current (J_s) is given by:

$$J_s = J\delta x. \tag{2.6}$$

The magnetic field $B(x)$ generated within the conductor increases linearly from $B(x=0) = 0$ to $B(\delta x) = B_0 = \mu_0 J_s$.

$$B(x) = B_0 \frac{x}{\delta x}, \quad 0 \le x \le \delta x. \tag{2.7}$$

The resultant magnetic force imparted on the surface of the conductor can be found by integrating the Lorentz force ($\mathbf{J} \times \mathbf{B}$), where the total surface area is $A_s = z_0 y_0$. This results

in

$$F = \iiint_V J \times B \, dV \tag{2.8}$$

$$= \int_0^{z_0} \int_0^{y_0} \int_0^{\delta x} JB(x) \, dx \, dy \, dz \tag{2.9}$$

$$= \frac{JB_0}{\delta x} z_0 y_0 \int_0^{\delta x} x dx \tag{2.10}$$

$$= \frac{JB_0 A_s \delta x}{2}. \tag{2.11}$$

Since pressure is force per unit area, we divide the force by the total surface area, which results in the magnetic pressure,

$$P_{\text{mag}} = F/A_s \tag{2.12}$$

$$= \frac{J\delta x B_0}{2} = \frac{B_0 J_s}{2} \tag{2.13}$$

$$= \frac{B_0^2}{2\mu_0}. \tag{2.14}$$

Additionally, for a cylindrically symmetric system with $B_\theta = \frac{\mu_0 I}{2\pi r}$ in the vacuum region, the derived magnetic pressure is expressed as

$$P_{\text{mag}} = \frac{\mu_0 I^2}{8\pi^2 r^2}. \tag{2.15}$$

Magnetic pressure is the fundamental driving force for a Z-pinch implosion. Because the magnetic pressure scales proportionally to I^2/r^2, achieving high pressure requires delivering the largest possible current (I) to the smallest possible radius (r). For a radially imploding target, $r \to 0$, as the radius decreases, the pressure is further amplified. On high-current drivers like the Z machine, this process can generate pressures exceeding 100's of Mbar [60]. This extreme drive pressure propels many scientific experiments, such as ICF targets and radiation sources. Additionally, for modest current drivers, such as MAIZE operating at 0.5 MA, the pressures attainable can reach up to 1 Mbar at a radius of 200 µm, thereby facilitating access to high energy density physics (HEDP) regimes.

Furthermore, the total magnetic energy (U_B) within the load region can be calculated by integrating the magnetic pressure (energy density) over the volume of the system. In a

typical Z-pinch system, the load is coaxial with the inner and outer radius shorted together. The current (I) runs axially along the cylindrical central load with a radius (r_{in}) and returns through the outer conductor with radius r_{out}. The integral is shown below:

$$U_B = \iiint_V P_{\text{mag}}\, dV \tag{2.16}$$

$$= \int_{r_{in}}^{r_{out}} \int_0^{2\pi} \int_0^h \frac{\mu_0 I^2}{8\pi^2 r^2} r\, d\theta\, dr\, dz \tag{2.17}$$

$$= \frac{\mu_0 h I^2}{4\pi} \ln\left(r_{\text{out}}/r_{\text{in}}\right) \equiv \frac{1}{2} L I^2. \tag{2.18}$$

From this expression, we find that the inductance of the system is

$$L = \frac{\mu_0 h}{2\pi} \ln\left(r_{\text{out}}/r_{\text{in}}\right). \tag{2.19}$$

This is simply the inductance of a coaxial cable, where h is the length of the coaxial cable. Note that in our system, the length of the coaxial conductor is often taken to be the length (or height) of the imploding liner target, hence the use of h. The peak current I_{peak} drawn by the target is affected by L, since $I_{\text{peak}} \propto \sqrt{L^{-1}}$. To further show the importance of L, let's consider a moving target that implodes to the central axis such that $r_{\text{in}}(t) \to 0$. Since the conductor is able to move radially, the inductance also changes with time ($L \to L(t)$). Differentiating $L(t)$ with respect to time, we find:

$$\frac{dL}{dt} = \dot{L} = -\frac{\mu_0 h}{2\pi} \left(\dot{r}_{\text{in}}/r_{\text{in}}\right). \tag{2.20}$$

It is noted that the radial implosion velocity $v(t) = \dot{r}(t)$ directly relates the change in inductance to the implosion velocity of the target. Allowing the parameter L to vary results in a modification of the magnetic energy within the target cavity. Taking the derivative of the magnetic energy leads to the magnetic power (P_B) generated in the cavity:

$$P_B = \frac{dU_B}{dt} \tag{2.21}$$

$$= \frac{d}{dt}\left(\frac{1}{2} L I^2\right) \tag{2.22}$$

$$= \frac{1}{2}\dot{L} I^2 + L\dot{I}, \tag{2.23}$$

where $\dot{I}$ is the rate of change of current. The total inductive power delivered to the cavity P_t is given by:

$$P_t = VI \tag{2.24}$$

$$= \dot{\Phi} I = \frac{d}{dt}\left(LI\right) I \tag{2.25}$$

$$= \dot{L} I^2 + L \dot{I} I, \tag{2.26}$$

where V is the inductive voltage from Faraday's law ($V = \dot{\Phi} = \frac{d}{dt}\left(LI\right)$). Subtracting Eq. 2.23 from Eq. 2.26, we get the following:

$$P_{\mathrm{KE}} = P_t - P_B = \frac{1}{2}\dot{L}(t) I(t)^2. \tag{2.27}$$

The magnetic energy delivered to a dynamic load is partitioned in two ways. A portion is converted into kinetic energy of the imploding conductor (Eq. 2.27). The remainder goes into increasing the magnetic energy stored in the growing vacuum volume behind the imploding target (Eq. 2.23), which is the rate of new magnetic field generation in the new vacuum region. To maximize the kinetic energy delivered to the target, one must maximize both the current (I) and the rate of change of inductance ($\dot{L}$).

An implosion cannot stagnate to $r_{\mathrm{in}} = 0$ because the internal pressure of the target eventually halts the compression. As the magnetic pressure performs PdV work on the target, the internal thermal pressure of the compressed material rises. Stagnation occurs when this internal pressure balances the driving magnetic pressure. Following this, the material explodes outward once the internal pressure exceeds the driving magnetic pressure. For fast Z-pinches, this internal pressure stimulates the release of radiation. For an ICF target, such as MagLIF, the pressure balance can be written as:

$$P_{\mathrm{gas}} + P_{B_z} = P_{B_\theta} + P_{\mathrm{ram}}. \tag{2.28}$$

Here, the total pressure is composed of the thermal pressure of the fusion fuel (P_{gas}), the pressure of the compressed axial magnetic field in the fuel (P_{B_z}), the driving pressure from the azimuthal magnetic field (P_{B_θ}), and finally, the hydrodynamic ram pressure of the shell (P_{ram}). This method of pressure balance can be used to simulate liner implosions by solving a system of coupled ODEs, as shown in Fig. 2.2. Additionally, it permits the straightforward incorporation of additional physics [100–103].

The magnetic pressure derived previously was under the assumption of a perfect conductor, where a surface current density J_s flows only through an infinitesimal depth δx. This is

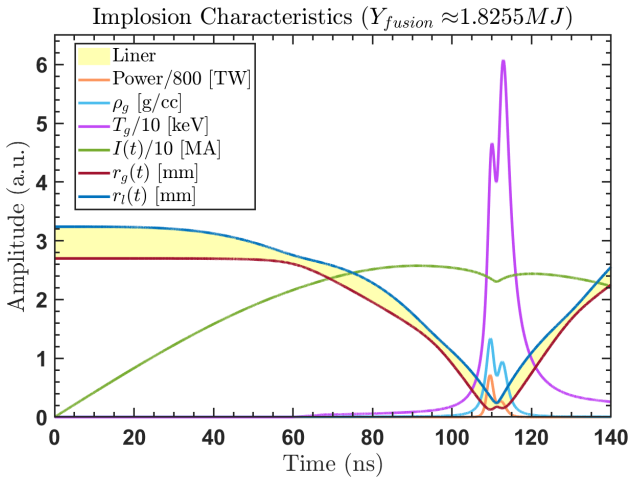


Figure 2.2: An example of an analytical model, simulating a 1D MagLIF implosion.

not the case for a thick conductor with finite resistivity, where a current pulse will penetrate a finite distance into the conductor and distribute the magnetic field. This is known as the skin effect. To show this effect, we start with the differential form of Faraday's law and Ampère's law with the substitutions: $\mathbf{E} = \mathbf{J}/\sigma$ (Ohm's law). We assume the electrical conductor has a high enough conductivity (σ) that the displacement current can be neglected. For a pulsed current with a characteristic frequency ω, the Fourier equations result in:

$$\nabla \times \mathbf{E} = -i\omega\mathbf{B} \quad \rightarrow \quad \nabla \times \mathbf{J} = -i\omega\sigma\mathbf{B} \tag{2.29}$$

$$\nabla \times \mathbf{B} = \mu_0\mathbf{J} \tag{2.30}$$

Now consider a current flowing in the z-direction (J_z) on the surface of a conductor, penetrating in the y-direction. This current generates a magnetic field (B_x) in the x-direction from the curl of J_z. The vector equations reduce to a coupled set of first-order differential equations:

$$\frac{\partial J_z}{\partial y} = -i\omega\sigma B_x \tag{2.31}$$

$$-\frac{\partial B_x}{\partial y} = \mu_0 J_z \tag{2.32}$$

By combining these two first-order equations, we can obtain a single second-order differential equation for the current density (J_z):

$$\frac{\partial^2 J_z}{\partial y^2} = i\omega\mu_0\sigma J_z. \tag{2.33}$$

This differential equation has a general solution $J_z(y) = J_1 e^{\kappa y} + J_2 e^{-\kappa y}$, where

$$\kappa = \sqrt{i\omega\mu\sigma} = (1+i)\sqrt{\omega\mu\sigma/2}. \tag{2.34}$$

The real part of κ describes the exponential decay of the current's amplitude as a function of depth into the conductor. We define the characteristic length for this decay as the electrical skin depth:

$$\delta_{\text{skin}} = \sqrt{\frac{2\eta}{\omega\mu}} \tag{2.35}$$

$$= \sqrt{\frac{4\eta\tau_r}{\pi\mu}}. \tag{2.36}$$

Note that here we have defined δ_{skin} in terms of the resistivity of the conductor ($\eta = 1/\sigma$) and (practical for pulsed systems) the rise time ($\tau_r = \frac{\pi}{2\omega}$) of the current pulse. By setting the initial conditions for $J_z(y \to 0) = J_z(0)$ and $J_z(y \to \infty) = 0$, the skin depth decays exponentially within the conductor:

$$|J_z(y)| = J_z(0)e^{-y/\delta_{\text{skin}}}. \tag{2.37}$$

The skin depth is quite important for the formal treatment of liner targets since it dictates the distribution of J_z and thus the amount of magnetic pressure exerted on the liner. For thin-foil liners, with a shell thickness $\delta_{\text{wall}} < \delta_{\text{skin}}$, the current and magnetic field quickly diffuse through the liner wall at early times in the current pulse. However, through heating and ionization into the plasma state, the thickness of the thin-foil liner shell is hypothesized to expand to the point where it becomes greater than the skin depth. During this early-time process, the plasma from the liner's inner surface can be advected along with B_θ to the central axis. The accumulation of this plasma and magnetic field within the liner interior can limit the final convergence ratio obtained by the imploding liner at later times. In the case of MagLIF, liners with thick walls are used to mitigate instability feedthrough from the liner's outer surface to the liner's inner (fuel confining) surface. It turns out that the MagLIF liner walls are thicker than the electrical skin depth, which prevents the drive current and magnetic field from diffusing through the liner wall and getting to the fuel.

In a highly conductive fluid, such as plasma, the magnetic field lines embedded within the fluid are convected with it. However, in cases involving low-density, desorbed plasma

with finite resistivity, it remains uncertain whether the magnetic field lines will be completely expelled and diffuse throughout the plasma volume, or if they will be entrapped and confined within the plasma. To show proof that the magnetic field lines are confined within the conductive plasma volume (i.e., the rate of change in magnetic flux ($\dot{\Phi}$) is zero), one considers the situation in which the magnetic Reynolds number ($R_m = \mu_0 L u_0/\eta$) is large ($R_m \gg 1$), thereby allowing the convective term to dominate, resulting in the following magnetic induction equation:

$$\frac{\partial \mathbf{B}}{\partial t} - \nabla \times (\mathbf{u} \times \mathbf{B}) = 0, \tag{2.38}$$

where $\mathbf{B}$ and $\mathbf{u}$ are the magnetic field and velocity vectors, respectively. Firstly, the magnetic flux (Φ_B) lines through a closed surface area ($d\mathbf{S}$) are defined as:

$$\Phi_B(t) = \int_S \mathbf{B}(t) \cdot d\mathbf{S}. \tag{2.39}$$

Consider an initial surface S at time t through which the magnetic field lines pass. Moving the surface by δS over a period of time δt results in:

$$\Phi_B(t + \delta t) = \int_{S+\delta S} \mathbf{B}(t + \delta t) \cdot d\mathbf{S}. \tag{2.40}$$

Now, calculating the rate of change of magnetic flux at the new surface (S_2) and time will yield:

$$\frac{d\Phi_B(t + \delta t)}{dt} = \lim_{\delta t \to 0} \left[\int_{S_2} \frac{\mathbf{B}(t + \delta t)}{\delta t} \cdot d\mathbf{S}_2 - \int_{S_1} \frac{\mathbf{B}(t)}{\delta t} \cdot d\mathbf{S}_1 \right]. \tag{2.41}$$

By applying the principle of magnetic flux conservation (Gauss's law for magnetism, $\oint_s \mathbf{B} \cdot d\mathbf{A} = 0$) to the closed surfaces S_1, S_2, and S_3, which serve to connect the boundaries of S_1 and S_2, the magnetic flux transitioning from surface S_1 to S_2 is

$$\int_{S_1} \mathbf{B}(t + \delta t) \cdot d\mathbf{S}_1 = \int_{S_2} \mathbf{B}(t + \delta t) \cdot d\mathbf{S}_2 + \int_{S_3} \mathbf{B}(t + \delta t) \cdot d\mathbf{S}_3. \tag{2.42}$$

The change in the surface area due to velocity $\mathbf{u}$ is given by $\delta t(\mathbf{u} \times d\mathbf{l})$. Subsequently, applying the vector identity ($\mathbf{A} \cdot \mathbf{B} \times \mathbf{C} = \mathbf{A} \times \mathbf{B} \cdot \mathbf{C}$) gives:

$$\int_{S_1} \mathbf{B}(t+\delta t)\cdot d\mathbf{S}_1 = \int_{S_2} \mathbf{B}(t+\delta t)\cdot d\mathbf{S}_2 + \oint_{\Delta S} \mathbf{B}(t+\delta t)\cdot \delta t(\mathbf{u}\times d\mathbf{l}) \tag{2.43}$$

$$= \int_{S_2} \mathbf{B}(t+\delta t)\cdot d\mathbf{S}_2 + \oint_{\Delta S} \delta t[\mathbf{u}\times \mathbf{B}(t+\delta t)]\cdot d\mathbf{l}. \tag{2.44}$$

Substituting this expression into (2.41) results in

$$\frac{d\Phi_B(t+\delta t)}{dt} = \lim_{\delta t\to 0}\left[\int_{S_1} \frac{\mathbf{B}(t+\delta t)-\mathbf{B}(t)}{\delta t}\cdot d\mathbf{S}_1 - \oint_{\Delta S}[\mathbf{u}\times\mathbf{B}(t+\delta t)]\cdot d\mathbf{l}\right]. \tag{2.45}$$

Applying Stokes' theorem ($\oint_C \mathbf{B}\cdot d\mathbf{l} = \int_S (\nabla\times\mathbf{B})\cdot d\mathbf{A}$) to the far right term on the right hand side of this expression results in Alfvén's frozen-in flux theorem:

$$\frac{\partial\Phi_B}{\partial t} = \int_{S_1}\frac{\partial\mathbf{B}}{\partial t}\cdot d\mathbf{S}_1 - \int_{S_1}\nabla\times(\mathbf{u}\times\mathbf{B})\cdot d\mathbf{S}_1 \tag{2.46}$$

$$= \int_{S_1}\left[\frac{\partial\mathbf{B}}{\partial t} - \nabla\times(\mathbf{u}\times\mathbf{B})\right]\cdot d\mathbf{S}_1 = 0. \tag{2.47}$$

The importance of the "frozen-in flux" theorem is that the embedded magnetic field lines move in conjunction with the bulk plasma. In the case of an axially magnetized target undergoing implosion, such as metal liners [104, 105] or gas puff Z-pinches [106, 107], the magnetic field within the imploding medium is restricted from diffusing outwards. Consequently, the axial field lines become confined and are forced to undergo compression during the implosion. This is an essential condition for high yield fusion designs, as the compressed axial magnetic field serves to confine the charged particles. Moreover, should low-density plasma be present at the peripheral, along the outer surface of the liner, and if this plasma exhibits sufficient electrical conductivity, it too can trap and compress the axial magnetic field [91, 94, 95]. This can potentially seed the helical instability observed in MagLIF radiographs [14, 15].

2.3 MHD Instabilities

Current driven plasmas are susceptible to numerous magnetohydrodynamic (MHD) instabilities. Specifically, in the context of a Z-pinch described using cylindrical coordinates, with the current oriented along the z-axis, the system is vulnerable to the $m = 0$ sausage and $m = 1$ kink instabilities. Here, m is the azimuthal mode number. Understanding the dynamics and stability of Z-pinch plasmas is an active area of research [31].

Small perturbations from equilibrium along the conducting surface will initiate these instability modes. The sausage instability is an axisymmetric mode where a section of the plasma column necks down. Due to the decrease in radius of the neck region, the magnetic pressure within this region will be stronger than the surrounding larger radius region. This will radially drive the neck region of the plasma column inwards. Since $P_{\text{mag}} \propto I^2/r^2$, the portion driven radially inwards will be subjected to an even stronger magnetic pressure, thereby establishing a positive feedback loop that persists until the conductor is disrupted. Consequently, in wire and gas puff Z-pinches, this instability may induce the formation of multiple discrete "hotspots" (point sources of radiation) within the pinch, as opposed to a uniform column of radiation [108].

The kink instability is a non-axisymmetric mode in which the plasma column undergoes a bending deformation. Perturbations on one side of the plasma boundary have higher magnetic pressure relative to the unperturbed, opposing side. Consequently, the unperturbed side is displaced radially outwards, thereby further reducing the magnetic pressure on this side, while the magnetic pressure on the perturbed side increases. This process constitutes a positive feedback loop, ultimately leading to the disruption of the plasma column.

2.4 Magneto Rayleigh Taylor Instability

The Magneto-Rayleigh-Taylor Instability (MRTI) is an acceleration-driven instability that occurs in fast Z-pinches and liner implosions. It arises when a light fluid (vacuum magnetic field) accelerates into a heavy fluid (solid liner). This instability is inherently detrimental to the uniformity of the implosion, as it can effectively disrupt the current-carrying column. In the context of imploding liners, this instability ultimately limits how thin the liner walls can be. If the liner walls are too thin, the MRTI is capable of penetrating through the liner walls.

A primary objective of imploding a liner filled with fusion fuel is to maximize kinetic energy, which subsequently serves to compress the fuel. Achieving high kinetic energy necessitates high velocities and, consequently, high acceleration, which increases the growth rate of the MRTI. To demonstrate that the growth rate is $\propto \sqrt{g}$, where g represents acceleration, we begin with the classical fluid Rayleigh-Taylor instability (RTI), in which the lighter fluid supports a denser fluid as the system is being acted on by gravity [109–111].

The classical RTI derivation begins with the conservation of mass and momentum, which are, respectively:

$$\frac{\partial \rho}{\partial t} + \nabla \cdot (\rho \mathbf{u}) = 0 \tag{2.48}$$

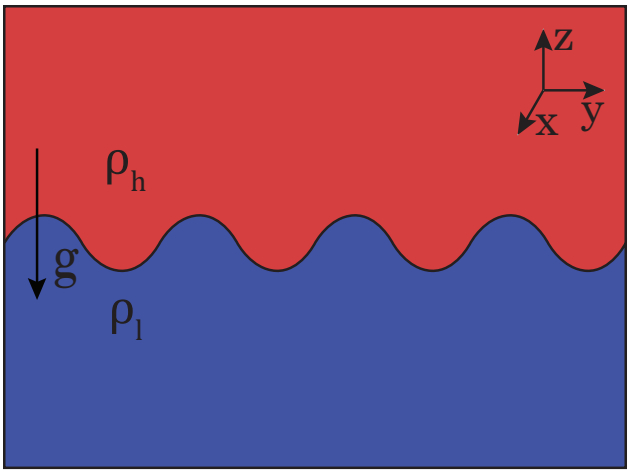


Figure 2.3: Illustration of the classic Rayleigh-Taylor instability. A small perturbation on the interface between the heavy fluid (red) and a light fluid (blue) grows when the interface is accelerated downwards (-z).

$$\rho\left(\frac{\partial \mathbf{u}}{\partial t} + \mathbf{u}\cdot\nabla\mathbf{u}\right) = \rho\mathbf{g} - \nabla p, \tag{2.49}$$

where ρ is the mass density, $\mathbf{u}$ is the fluid velocity, $\mathbf{g}$ is the acceleration, and p is the pressure. These equations are linearized to first-order perturbations, where the 0th-order quantities are in equilibrium and the 1st-order quantities are the small amplitude perturbations. We let $\rho = \rho_0 + \rho_1$, and the resultant first-order equation of the continuity and momentum equations becomes, respectively:

$$\frac{\partial \rho_1}{\partial t} + \nabla\cdot(\rho_0\mathbf{u}_1 + \rho_1\mathbf{u}_0) = 0 \tag{2.50}$$

$$(\rho_0+\rho_1)\left[\frac{\partial(\mathbf{u}_0+\mathbf{u}_1)}{\partial t} + (\mathbf{u}_0+\mathbf{u}_1)\cdot\nabla(\mathbf{u}_0+\mathbf{u}_1)\right] = (\rho_0+\rho_1)\mathbf{g} - \nabla(p_0+p_1). \tag{2.51}$$

We assume the equilibrium velocity $\mathbf{u}_0 = 0$, and in the equilibrium state $\nabla p_0 + \rho_0\mathbf{g} = 0$. The product of two 1st-order terms is considered relatively small and is neglected. This reduces Eq. 2.50 and Eq. 2.51 to:

$$\frac{\partial \rho_1}{\partial t} + \mathbf{u}_1\nabla\cdot\rho_0 = 0 \tag{2.52}$$

$$\rho_0\frac{\partial \mathbf{u}_1}{\partial t} = \rho_1\mathbf{g} - \nabla p_1. \tag{2.53}$$

The acceleration in the z-direction is constant in time and uniform in space. The perturbation is in the x–y plane and quantities of the perturbation vary as a function of z, as shown in Fig. 2.3. For this system, we perform Fourier analysis on the 1st-order continuity (Eq. 2.52) and momentum (Eq. 2.53) equations, where $\nabla \rightarrow ik$ and $\partial/\partial t \rightarrow -i\omega$. This results in the set of equations listed below:

$$-i\omega\rho_1 + u_{1z}\frac{\partial}{\partial z}\rho_0 = 0 \tag{2.54}$$

$$-i\omega\rho_0 u_{1z} = -\frac{\partial}{\partial z}p_1 + \rho_1 g \tag{2.55}$$

$$-i\omega\rho_0 u_{1y} = -ik_y p_1 \tag{2.56}$$

$$-i\omega\rho_0 u_{1x} = -ik_x p_1, \tag{2.57}$$

where k is the spatial frequency and ω is the temporal frequency. We assume the fluid is an incompressible fluid $\nabla \cdot \mathbf{u} = 0$ for this system, and linearize and Fourier analyze to get:

$$-\frac{\partial}{\partial z}u_{z1} + ik_y u_{y1} + ik_x u_{x1} = 0. \tag{2.58}$$

We combine the equations (2.56), (2.56), and (2.58) to get:

$$\frac{\partial u_{1z}}{\partial z} + ik_y\frac{k_y p_1}{\omega\rho_0} + ik_x\frac{k_x p_1}{\omega\rho_0} = 0 \tag{2.59}$$

$$-\frac{\partial}{\partial z}u_{z1} + i\frac{p_1 k^2}{\omega\rho} = 0. \tag{2.60}$$

We let the comprised perturbation modes be $k^2 = k_x^2 + k_y^2$. Rearranging the terms to obtain an equation for p_1 gives:

$$p_1 = \frac{\partial u_{1z}}{\partial z}\frac{i\omega\rho_0}{k^2}. \tag{2.61}$$

Substituting the z-component of the Fourier momentum equation (2.55) into the Fourier continuity equation (2.54) leads to:

$$\frac{\partial}{\partial z}p_1 = i\omega\rho_0 u_{1z} + \rho_1 g \tag{2.62}$$

$$= i\omega\rho_0 u_{1z} - i\left(\frac{\partial\rho_0}{\partial z}\frac{u_{1z}g}{\omega}\right). \tag{2.63}$$

Substituting (2.61) into (2.63) and rearranging the terms leads to:

$$\frac{\partial}{\partial z}\left(\frac{\partial u_{1z}}{\partial z}\frac{i\omega\rho_0}{k^2}\right) = i\omega\rho_0 u_{1z} - i\left(\frac{\partial \rho_0}{\partial z}\frac{u_{1z}g}{\omega}\right) \tag{2.64}$$

$$\frac{\partial}{\partial z}\left(\frac{\partial u_{1z}}{\partial z}\rho_0\right) = k^2\rho_0 u_{1z} - \frac{k^2}{\omega^2}u_{1z}g\frac{\partial \rho_0}{\partial z}. \tag{2.65}$$

In the bulk fluid (not interface) $\frac{\partial \rho_0}{\partial z} = 0$, thus (2.65) reduces down to:

$$\frac{\partial^2 u_{1z}}{\partial z^2} - k^2 u_{1z} = 0. \tag{2.66}$$

This has a solution in the form of:

$$u_{1z}(z) = Ae^{kz} + Be^{-kz}. \tag{2.67}$$

Using the boundary conditions that $u_{1z} \to 0$ as $z \to \pm\infty$, the piecewise solution is:

$$u_{1z}(z) = \begin{cases} u_{1z}(0)e^{kz}, & z \leq 0 \\ u_{1z}(0)e^{-kz}, & z \geq 0 \end{cases} \tag{2.68}$$

Revisiting (2.65), we integrate across the interface from $\pm\epsilon$:

$$\int_{-\epsilon}^{+\epsilon}\left[\frac{\partial}{\partial z}\left(\frac{\partial u_{1z}}{\partial z}\rho_0\right)\right]dz = \int_{-\epsilon}^{+\epsilon}\left[k^2\rho_0 u_{1z} - \frac{k^2}{\omega^2}u_{1z}g\frac{\partial \rho_0}{\partial z}\right]dz. \tag{2.69}$$

This results in:

$$\rho_0\frac{\partial u_{1z}}{\partial z}\bigg|_{+\epsilon} - \rho_0\frac{\partial u_{1z}}{\partial z}\bigg|_{-\epsilon} = k^2(\rho_l + \rho_h)\epsilon u_{1z} - \frac{k^2}{\omega^2}g\left(\rho_0\Big|_{+\epsilon} - \rho_0\Big|_{-\epsilon}\right)u_{1z}, \tag{2.70}$$

where ρ_l is the light density and ρ_h is the heavy density. Taking the limit where $\epsilon \to 0$ and applying the piecewise solution (2.68) for u_{1z}, the jump condition is written as:

$$(-\rho_l k - \rho_h k)(u_{1z}) = -\frac{k^2}{\omega^2}g(\rho_l - \rho_h)u_{1z}. \tag{2.71}$$

Rearranging gives the dispersion relation gives:

$$w = \sqrt{\frac{\rho_l - \rho_h}{\rho_l + \rho_h}kg}. \tag{2.72}$$

We let $\omega = \omega_R + i\gamma$ such that the unstable growth rate γ is expressed as:

$$\gamma = \sqrt{A_t k g}, \tag{2.73}$$

where $A_t = \frac{\rho_l - \rho_h}{\rho_l + \rho_h}$, which is also known as the Atwood number. The configuration is unstable when $\rho_l < \rho_h$ (i.e. $\nabla\rho \cdot \nabla p < 0$) and $\mathrm{Im}(\omega) = \gamma$. By integrating $\int u_z dt = \int u_{z0} e^{\gamma t} dt$, we show that the perturbation amplitude grows exponentially in the linear regime:

$$A(t) = A_0(t) e^{\gamma t}. \tag{2.74}$$

In magnetized plasmas, RTI growth is modified by the presence of the magnetic field. For example, in fast Z-pinch implosions, the implosion-driving magnetic field assumes the role of the light fluid density, and the imploding cylindrical shell represents the heavy fluid density [42, 112]. If left unmitigated, this instability proves detrimental to the integrity of the imploding column. An approach to mitigate the growth of MRTI is to apply a background magnetic field ($\mathbf{B}$), oriented parallel to the perturbation wavevector ($\mathbf{k}$). For a planar geometry, the modified growth rate is:

$$\gamma = \sqrt{A_t k g - \frac{(\mathbf{k} \cdot \mathbf{B})^2}{\mu_0 \rho}}. \tag{2.75}$$

For sufficiently large magnetic fields, MRTI growth can be reduced via tension in the magnetic field lines. Generally, the most unstable modes that can develop are those satisfying $\mathbf{k} \cdot \mathbf{B} = 0$. In the presence of both axial and azimuthal components of a magnetic field, the resultant angle of the total magnetic field is described by $\phi_B = \arctan(B_z / B_\theta)$. Thus, it would be expected that the most dominant modes would align with this orientation and satisfy $\mathbf{k} \cdot \mathbf{B} = 0$. Nevertheless, such behavior does not appear to be the case in experimental radiographs [14, 15], where the measured angle is greater than that which would be expected from the ratio of nominal magnetic fields. This suggests that there could be an anomalous increase in the axial magnetic field component on the liner surface, possibly due to flux compression occurring in the low-density plasma flowing into the liner from the power feeds.

One method to take advantage of $\mathbf{k} \cdot \mathbf{B}$ is to drive a dynamic magnetic field ($B_z(t)$) that changes on the time scale of the implosion [113–118]. This can be done using a dynamic screw pinch (DSP) where the original straight return structure (for a standard Z-pinch) is replaced with a helical structure. This helical structure will generate both an axial and azimuthal magnetic field proportional to the current drive. Since $B_z \propto I(t)$ and $B_\theta \propto I(t)/r(t)$, the helical pitch angle of the implosion-driving magnetic field (ϕ_B) will rotate as a function of liner radius, $r(t)$. This results in a spectrum of modes being driven throughout the implosion, where each mode has a different helical pitch angle and is driven as the dominant mode in

the system for only a short period of time. By contrast, in a standard Z-pinch implosion, azimuthally correlated modes ($m = 0$) are dominant for the entire implosion and they are driven for the entire implosion. This leads to larger cumulative instability growth for the case of the standard Z-pinch configuration, relative to the DSP configuration.

2.5 Pitch Locking

While linear instability theory is important for target design, its primary limitation is that a real implosion transitions from the linear to the non-linear regime very early in the process [119]. The transition to non-linearity is often estimated to occur when the ratio of the instability amplitude (A) to its wavelength (λ) exceeds a threshold of $A/\lambda \approx 0.1$ [120]. This criterion is from classical fluid dynamics, and it provides a useful rule of thumb for Z-pinch instabilities. Given the rapid exponential growth during the linear phase, this threshold is reached quickly, meaning that the majority of the implosion occurs in the more complex non-linear regime. However, the transition to non-linearity for this threshold can be delayed due to the process of mode merging, which alters the dominant wavelength towards larger values, consequently necessitating a greater perturbation amplitude to fulfill $A/\lambda \approx 0.1$.

The non-linear process of mode merging is also referred to as an inverse cascade, since smaller structures merge into larger structures. This process is shown in Fig. 2.4. Experiments show that linear implosions are typically seeded with short wavelength (large k) perturbations. As the implosion evolves, these small structures merge into progressively larger ones, causing the dominant wavevector to increase over time. For $m = 0$ cases, the azimuthal mode number remains unchanged throughout the implosion process; however, the perturbation wavelength in the axial direction shows an increase. For helical modes ($|m| \geq 1$), this process is governed by the conservation of pitch. The pitch (p) of a helix is defined as $p = \lambda_z m = 2\pi m/k_z$, where λ_z is the perturbation wavelength projection in the axial direction. When two helices merge, both the mode number (m) and the axial wavenumber (k_z) decrease by a factor of two, which conserves the overall pitch. This cascade continues until the instability approaches a final state of $m = 1$ and not $m = 0$.

We note that "pitch locking" (constant pitch throughout the implosion) occurs because axial outflows (or axial inflows) are not permitted due to anode and cathode end caps. A consequence of pitch locking is that the pitch *angle* must increase throughout the implosion to conserve the pitch. This can be understood by considering the following. For an imploding, helically twisted plasma column, the plasma's perturbation pitch angle is given by

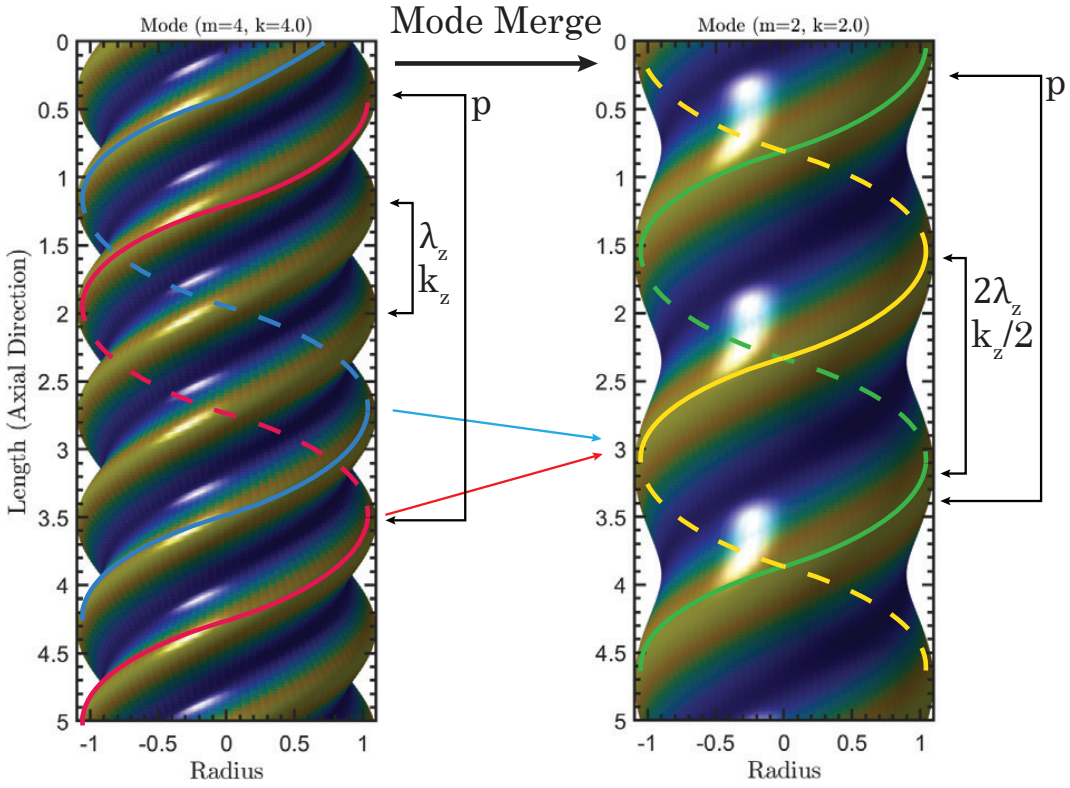


Figure 2.4: Illustration of a mode merging event for a helical perturbation with the form $\exp[(i(m\theta - k_z z)]$, for a constant radius. Prior to the mode merger event, as shown on the left, a helical mode characterized by $m = 4$ and $k_z = 4$ is presented. The red and blue lines represent two of the four intertwined helices, where $m = 4$ corresponds to a total of four intertwined helices. The solid lines trace the helical striations along the front surface of the helically twisted column, while the dashed lines trace the helical striations along the back surface. Subsequent to the mode merger event, both the azimuthal mode number and the axial wavenumber decrease to $m = 2$ and $k_z = 2$, respectively; the result is that the pitch p remains unchanged. The color-coded arrows illustrate the merger of the instability lobes from the red and blue helices into a single yellow helix post-merger.

$$\phi_{\text{plasma}}(t) \approx \arctan\{p/[2\pi r(t)]\} \approx m/[k_z r(t)]. \tag{2.76}$$

Thus, as the column radius decreases during the implosion, the pitch angle ϕ_{plasma} will increase due to the constant pitch p. We note that this is the case even in the presence of mode-merger events, since the ratio m/k_z remains constant during mode-merger events (*cf.* Fig. 2.4). Conversely, after stagnation, during the subsequent explosion phase of the fast Z-pinch process, the pitch angle must decrease to preserve constant pitch. This is illustrated in Fig. 2.5. The work presented in this dissertation relies heavily on the concept of pitch conservation.

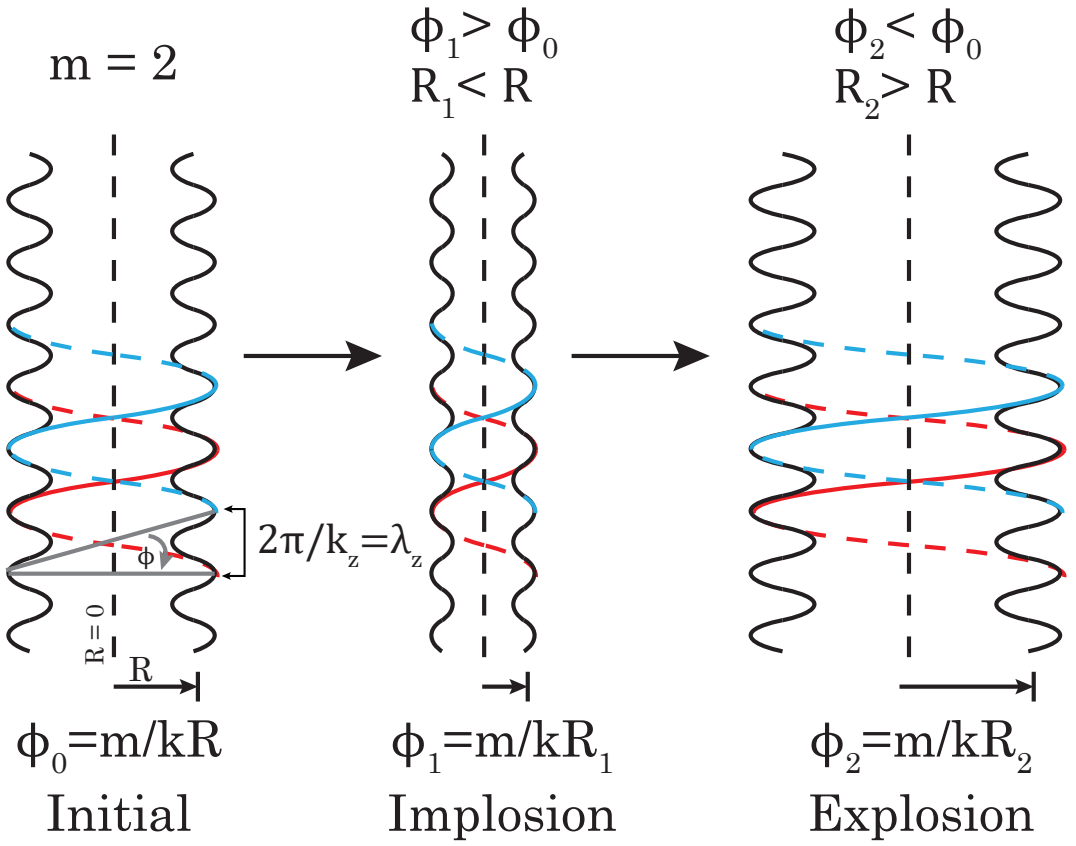


Figure 2.5: Illustration of the pitch locking phenomenon for an $m = 2$ instability. The two intertwined helices are shown in red and blue, with solid lines representing the front-surface striations and dashed lines representing the back-surface striations. For a fixed azimuthal mode number m and axial wavevector k_z, the angle of the striation is determined by $\phi_{\text{plasma}}(t) \approx m/kR(t)$, with R representing the radius. Given that the pitch must remain constant, a reduction in $R(t)$ leads to an increase in the angle (implosion), whereas an increase in $R(t)$ results in a decrease in the angle (explosion).

CHAPTER 3

MAIZE Pulsed Power Facility and Diagnostics

3.1 MAIZE LTD

The MAIZE facility, situated within the Plasma, Pulsed Power, and Microwave Laboratory at the University of Michigan in Ann Arbor, is a 3-meter diameter pulsed power device [69], as shown in Fig. 3.1. It operates as a single cavity, low impedance ($\sim$0.1 Ω) linear transformer driver (LTD), consisting of 80 capacitors, each with a capacitance of 40 nF, and 40 triggered spark-gap switches, collectively referred to as 40 "bricks". When bipolar charged to a maximum voltage of $\pm$100 kV, MAIZE stores 16 kJ of electrical energy. The generator's coaxial transmission line feeds into a radial transmission line with interchangeable inserts, thus establishing a versatile load region capable of supporting a variety of experimental setups, including metal liners [16, 17], gas-puff Z-pinches [121], and wire x-pinches [122, 123].

In our experiments, we used an inductive annular gas piston designed to inject an annular gas jet into the load region's anode-cathode gap. The original nozzle apparatus was engineered to accommodate three jets, comprising two concentric annular jets and one central jet. Currently, only the two concentric annular jets are operational. For the purposes of this dissertation, we utilized solely the inner annular jet; however, future experimental work may exploit the outer nozzles to achieve a higher rate of change of the inductive load (dL/dt).

The operation of the gas-puff nozzles are described as follows. The gas manifold is situated next to MAIZE's charging power supplies, where a gas feed pressurizes the plenum within the gas puff system. This plenum retains the pressurized gas in the MAIZE target region. A puck presses against an O-ring seal to prevent gas leakage into the vacuum. A pulser fires a 400–700 V, µs–long pulse into the inductive puck. The puck is driven backward into a spring mechanism, releasing the seal and permitting the gas jet to escape into the vacuum system. The gas then traverses a choke area and exits through the nozzle, which augments the shape of the gas. The nozzle exits into the target anode-cathode (AK) gap of MAIZE,

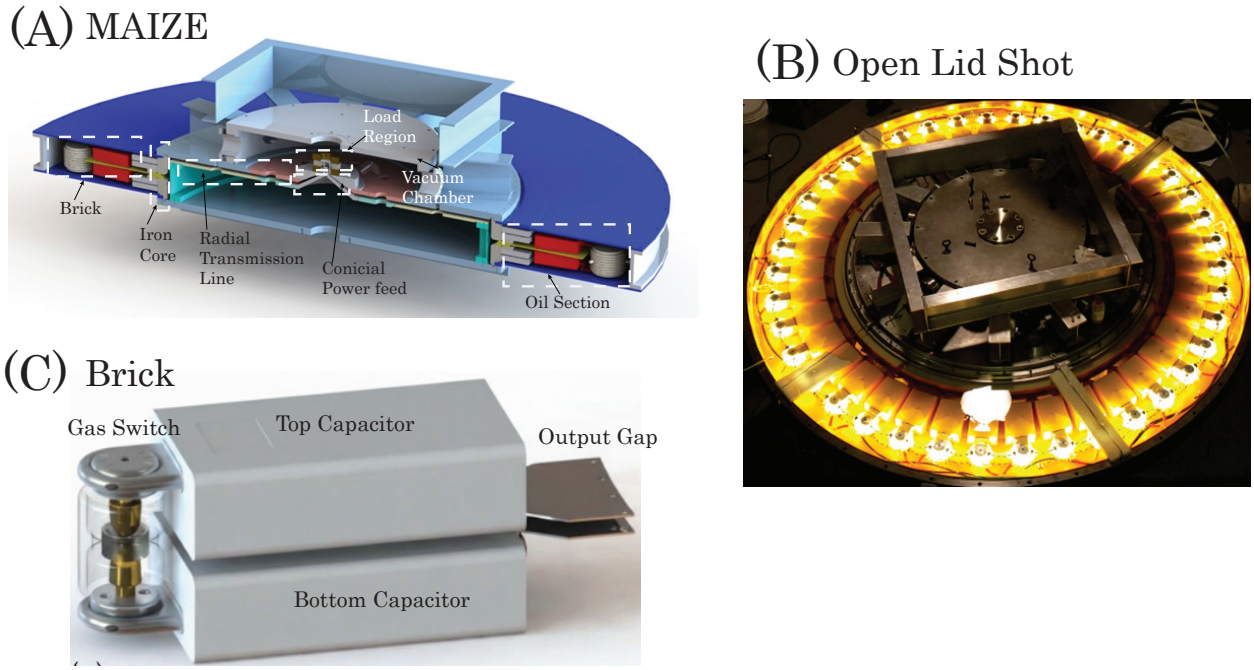


Figure 3.1: The MAIZE pulsed power machine. (a) A CAD cross section showing the key components, including 40 spark-gap switches, eighty 40 nH capacitors, two ferromagnetic cores, the radial transmission line, the conical power feed, the vacuum and oil sections, and finally the load region. (b) An open shutter photograph of MAIZE firing with the lid removed, highlighting the internal components of MAIZE. The bright yellow arcs are the switches discharging electrical current into the transmission lines. (c) A CAD drawing of a single "Brick", which is comprised of two 40 nH capacitors isolated with a pressurized dry-air gas switch. There are 40 bricks contained within MAIZE's oil section.

passing through the anode mesh to prevent gas accumulation in the target area. MAIZE subsequently fires into this region, ionizing the gas in the AK gap, thereby establishing a conductive channel and subsequently imploding the conductive channel.

The velocity of the gas is significantly slower than the MAIZE pulse. Based on previous tests, the inductive mechanism is initiated 500–800 ms before the onset of the MAIZE current to ensure that the gas traverses the target AK gap in time. A notable limitation of this system is the current inability to ascertain the presence of gas in the gap when MAIZE is fired. If the gas puff misfires, MAIZE will discharge into an open load, which can significantly damage MAIZE. This is because the open circuit results in a voltage pulse being reflected with twice the amplitude back into the capacitor, thereby risking capacitor failure. Efforts are ongoing to develop a detection system to address this issue.

Because of its low impedance, the current pulse supplied by MAIZE is highly sensitive to the load impedance. For these experiments, the initial load inductance was calculated to be 6.4 nH, while the final load inductance reached 11.7 nH (i.e., $\Delta L = 5.3$ nH). Additionally, the experiments were conducted at a charge voltage of ± 70 kV. Under these conditions, a nominal peak current of approximately 500 kA was observed, with a current rise time of about 150 ns.

3.2 Diagnostics

MAIZE is equipped with an extensive array of diagnostics, including current diagnostics, laser probing diagnostics, and radiation emission cameras. The vacuum chamber on MAIZE is approximately 1 meter in diameter. The chamber includes several vacuum ports for radial lines of sight, and two ports for axial lines of sight (one above and one below the load region). These ports are often equipped with large viewing windows to provide visible-light imaging diagnostics with radial and axial views of the targets. Some characteristics of the diagnostics suite on MAIZE include:

- Current diagnostics: Rogowski coils and B-dot probes
- Visible and XUV radiation imaging: Fast 12-frame self-emission camera, open-shutter camera, 4 frame MCP XUV imaging
- Laser-based probing: Schlieren, shadowgraphy, interferometry, faraday rotation imaging
- X-ray diagnostics: Time integrated pinhole camera, bolometer, silicon diodes, photoconducting diamond (PCD)

- Time-gated fiber coupled visible spectroscopy
- Neutron diagnostics: Bubble detectors, beryllium activation probe, and silicon activation probe.

For the experiments presented in this dissertation, three primary categories of diagnostics were employed: current diagnostics, laser-based imaging, and radiation emission imaging. Each of these systems is described in detail in the following subsections.

3.2.1 Current Diagnostics

3.2.1.1 Rogowski Probe

The total current delivered to the load was measured by a Rogowski coil positioned in a groove on the anode side of the conical feed. The main coil extends to a length of 69 cm and consists of 34 turns, constructed from a stripped coaxial cable [63]. This location is situated ∼10 cm upstream from the target. It is important to acknowledge that this diagnostic specifically measures the total current entering the final load assembly, but does not account for any potential losses that may transpire between the coil and the target itself.

A Rogowski coil does not measure the current directly; rather, it measures the rate at which the current changes over time ($V \propto dI/dt$) via Faraday's law of magnetic induction. To understand the operating principles of a Rogowski coil, we first take a step back and begin with Ampere's circuital law,

$$\oint \mathbf{B} \cdot d\mathbf{l} = \mu_0 I_{\text{enclosed}}. \tag{3.1}$$

This equation shows that the closed line integral of a time-dependent magnetic field ($B(t)$) is equivalent to the product of the permeability of free space (μ_0) and the enclosed time-dependent current ($I_{\text{enclosed}}(t)$). For a cylindrical current-carrying conductor, this results in a magnetic field that is linearly proportional to the current, with r denoting the radius at which the field is be evaluated by the probe:

$$B(t) = \frac{\mu_0 I(t)}{2\pi r}. \tag{3.2}$$

The operation of a Rogowski coil is governed by Faraday's law of induction. This law states that a time-varying magnetic flux (Φ_B) passing through a closed inductive loop of wire induces an electromotive force (V_{emf}), or voltage, within the loop:

$$V_{\text{emf}} = -\frac{d\Phi_B}{dt}. \tag{3.3}$$

The magnetic flux is given by:

$$\Phi_B = \int_A \mathbf{B}(\mathbf{t}) \cdot d\mathbf{A}. \tag{3.4}$$

For a cylindrical wire loop, the induced voltage is directly proportional to the number of turns (N), the area of the loop (A), and the rate of change of current ($\frac{dI(t)}{dt}$):

$$V_{\text{emf}} \propto -NA\mu_0 \frac{dI(t)}{dt}. \tag{3.5}$$

This voltage is subsequently measured using an oscilloscope. To reconstruct the current, the signal must be integrated over time. In the case of MAIZE, the voltage signal undergoes numerical integration during post-processing. Alternatives for signal integration include using an analog RC integrator connected to the output of the Rogowski or to wind the Rogowski with a substantial number of turns. However, the substantial number of loops would render the Rogowski highly inductive, thereby impairing its ability to measure signals with high-frequency components.

A low-inductance, coaxial Rogowski coil is used on MAIZE due to its several advantages. The coil's minimal number of turns provides an excellent high frequency response, necessary to accurately measure temporal details in fast current pulses (e.g., the inductive dips that occur in current waveforms during the final stages of fast Z-pinch compression and last for less than 10 ns). Additionally, Rogowski coils are capable of accommodating high currents without experiencing magnetic saturation. They are also physically flexible and cost-effective to construct.

To determine the true current value ($I(t)$), the Rogowski coil must be calibrated using a known source. In the case of the Rogowski coil on MAIZE, it undergoes external calibration through an independent pulser. The current output from this pulser is measured with a Pearson coil, serving as a reference point. The final calibration factor for the integrated current is derived from the ratio of currents measured by the Pearson and Rogowski coils.

During experiments conducted on MAIZE, the raw voltage signal was reduced by a 30 dB power attenuator situated within a vacuum chamber. This reduces the voltage across the SMA vacuum feedthrough, thereby preventing electrical breakdown. It is critical that the signal's transmission line impedance remains consistent even when encountering attenuators and/or oscilloscope terminators. To calibrate the probe properly, the same termination impedance should be used for both the calibration process and the end-use experiment. For MAIZE calibrations and experiments, usually 50-Ω terminators are used. Any mismatch in impedance, such as measurements into a 1 MΩ input as opposed to a 50 Ω input, will result in alterations to the measured voltage by as much as a factor of two and introduce

signal reflections. Notably, the Pearson coil, which is used to provide calibrated reference measurements, typically uses a termination of 1 MΩ, whereas the Rogowski coil is terminated by 50 Ω.

3.2.1.2 B-dot Probe

Rogowski probes are effective for measuring the total enclosed current; however, B-dot (inductive) probes are used to get a more localized measurement of the magnetic field [124]. Similar to the Rogowski probe, the B-dot operates on the principle of magnetic induction, with its active region confined to the probe's tip. This localization affords several advantages, such as permitting measurements at specific points, including within the plasma volume. The B-dot probes can be fabricated with a compact form, rendering them quite flexible in terms of experimental placement. Consequently, the probe can be oriented to selectively capture and isolate individual components of the magnetic field in our experiments, including B_z or B_θ. In the experiments of this dissertation, B-dot probes were used to measure axial magnetic flux compression.

However, using B-dot probes can introduce certain challenges. The plasma can potentially impact the measurement by concealing the active region of the probe, thus effectively shielding the magnetic field. The tip of the probe is inherently delicate, and the solder junction represents a potential weak point for electrical breakdown. This issue can be mitigated by encapsulating the tip in epoxy. Furthermore, due to its typical placement in proximity to the plasma and within the load region, the probe is prone to interference from high-frequency electromagnetic noise.

3.2.2 Plasma Imaging Camera

Imaging is a powerful tool for observing the dynamics and structure of plasma. However, the quantitative interpretation and analysis of these images present challenges due to the intricate nature of plasmas. The difficulties primarily stem from the broad spectrum emitted by the plasma and the assumptions regarding plasma parameters required to derive quantitative results from the emission. Nonetheless, imaging remains invaluable for providing morphological data about the plasma, which is used extensively in this thesis. The experiments in this work utilize two imaging diagnostics that are sensitive to distinct components of the plasma's emission spectrum: a visible-light self-emission camera and an XUV emission camera. Each diagnostic method is detailed in the following subsections.

3.2.2.1 Twelve-Frame Self-Emission Camera

Optical self-emission diagnostics are a useful and simple technique to image plasma emissions within the visible spectrum. At the University of Michigan, the Invisible Vision Ultra UHSi 12/24 fast framing camera [125], is used to image plasma implosion dynamics by capturing 12 sequential time-resolved image frames. Each of these 12 frames can be set to have exposure times as low as 5 ns with an inter-frame time of 0 ns (i.e., the time duration between the end of one frame and the start of the next). The majority of plasmas generated in the MAIZE facility emit within the visible spectrum. This camera is routinely fielded on MAIZE experiments and is a primary workhorse of the laboratory and the research conducted in this dissertation.

In these experiments, the camera is coupled with a Nikon lens pair that controls the image magnification. The intensity of the photons captured by the CCD is directly proportional to both the electron density and temperature within the plasma. However, due to uncertainties associated with charge state, temperature, and density, deriving quantitative results from the images remains challenging. Despite this, the images provide substantial value in capturing the comprehensive dynamics of implosion and monitoring the bulk motion of the plasma load.

The system resolution of the camera was determined through the analysis of the modulation transfer function (MTF) curve [126]. This method is used to assess a lens's capability to convey contrast at a specific resolution from the object to the resultant image. To perform this analysis, an image of a straightedge object was captured under illumination with the lens configuration on the framing camera. The captured edge was subsequently cropped to focus on the region of interest. The edge signal was averaged along the boundary and fitted to a generalized error function, resulting in an edge spread function (ESF). Subsequently, the derivative of the ESF was computed to obtain the line spread function (LSF). Thereafter, to calculate the MTF, the Fourier transform of the LSF was applied. The point at which the MTF declines to 10% of its peak value was utilized to calculate the systematic resolution of this setup as ~ 280 µm.

3.2.2.2 XUV Emission Camera

In addition to visible-light self-emission imaging, the MAIZE facility is equipped with a time-gated, four-frame XUV pinhole camera designed for capturing higher-energy photon emissions. The assembly of the camera involves a microchannel plate (MCP), a phosphor screen, and an array of four pinholes. The four 100-µm-diameter pinholes, one for each image, are employed to separately capture emission from the plasma onto the MCP's four

quadrants. Each of the four imaging regions is biased by a 6 kV pulse provided by an external pulser. The interframe interval is configured to 15 ns between successive frames, with this timing controlled by the lengths of the output cables from the pulser.

The XUV radiation is converted from incident photons into electrons via the photoelectric effect. The primary electrons are accelerated down the MCP channels under the influence of a bias voltage, causing them to collide with the channel walls and instigate a cascade of secondary electron emissions. This process amplifies the number of electrons within the channel. Ultimately, the substantial electron bunch that emerges from the channel is collected by a phosphorescent screen, which subsequently reconverts the electrons into photons within the visible spectrum. The visible light is then captured by a Canon Rebel XTi DSLR camera. It is noteworthy that the XUV imaging assembly on MAIZE has sustained damage over its operational lifespan, resulting in cracks within the MCP that yield significant artifacts in certain regions of the images. Nevertheless, efforts were made to situate the images on the remaining viable sections of the MCP. An example of an XUV image is shown in Fig. 3.2.

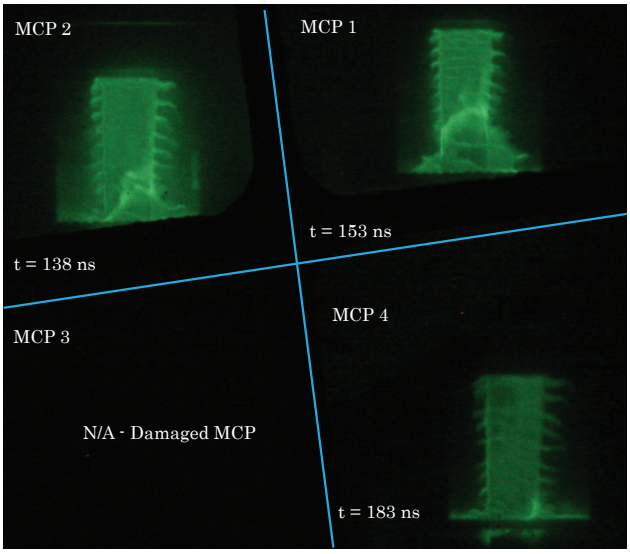


Figure 3.2: XUV images of an argon gas-puff Z-pinch imploding onto a dense central rod. The images show the formation of azimuthally correlated instability structures, characteristic of an $m = 0$ sausage instability.

The geometric resolution of the XUV imaging system is given by:

$$L_{\text{geo}} = d\left(1 + \frac{p}{q}\right), \tag{3.6}$$

where d is the diameter of the pinhole, p is the object to pinhole distance, and q is the pinhole to image distance. For MAIZE, the distances used were $p = 55$ cm, $q = 20$ cm, and $d = 100$ µm, which will produce a 375 µm resolution.

3.2.3 Laser Probing Diagnostic

Although deriving quantitative data from the self-emission images presents a challenge, laser probing can provide complementary insights into both qualitative and quantitative plasma properties, including density, temperature, velocity, and magnetic field. A notable advantage of laser diagnostics is their non-invasive nature, which facilitates the measurement of plasma parameters without significantly disturbing the plasma itself.

For this study, the laser is primarily employed to investigate the structure of the under-dense plasma through three imaging techniques: A single frame laser shadowgraphy/schlieren (backlighting/refraction angle) and interferometric (phase-difference) imaging using the 532 nm beam line. The schlieren/shadowgraphy imaging systems were mainly used to make qualitative measurements.

The MAIZE facility has an Ekspla NL122 Nd:YAG laser [127], characterized by a fundamental output at 1064 nm and a beam energy of up to 300 mJ. The system includes a frequency-doubled output at 532 nm with 125 mJ and a frequency-tripled output at 355 nm with 80 mJ. Each single pulse of this laser system has a duration of 2 ns, rendering it suitable for a number of laser probing diagnostics. Although the laser can be set up to measure plasma parameters such as temperature, velocity, and density via scattering, this application necessitates energy levels in the Joule range. The main use of this laser within the facility is to measure density properties. Although the measurement of magnetic fields via Faraday rotation is feasible [122, 123], it is not employed in the current work but is considered for future experiments.

The interaction of a laser with a plasma is governed by how an electromagnetic (EM) wave propagates through the medium. This is described by the plasma's refractive index (N), which can be derived from Maxwell's equations. We begin with Faraday's Law and Ampère's Law:

$$\nabla \times \mathbf{E} = -\frac{\partial \mathbf{B}}{\partial t} \tag{3.7}$$

$$c^2 \nabla \times \mathbf{B} = \frac{\partial \mathbf{E}}{\partial t} + \mathbf{j}/\epsilon_0, \tag{3.8}$$

where $\mathbf{E}$ and $\mathbf{B}$ are the electric and magnetic fields, $\mathbf{j}$ is the current density, ϵ_0 is the permittivity of free space, and c is the speed of light. Assume a plane wave traveling in the x-direction with an electric field of:

$$\mathbf{E} = E_0 \exp[i(\mathbf{k} \cdot \mathbf{x} - \omega t)], \tag{3.9}$$

where $\mathbf{k}$ is the wavenumber and w is the frequency. In this form, we take the Fourier analysis of Maxwell's equations (i.e. $\frac{\partial}{\partial t} \rightarrow -i\omega$ and $\nabla \rightarrow i\mathbf{k}$), yielding:

$$i\mathbf{k} \times \mathbf{E} = -i\omega\mathbf{B} \tag{3.10}$$

$$ic^2\mathbf{k} \times \mathbf{B} = -i\omega\mathbf{E} + \mathbf{j}/\epsilon_0. \tag{3.11}$$

We then take the curl ($\mathbf{k}\times$) of the first equation and multiply (ω) by the second equation. Combining the results leads to the elimination of the $\mathbf{B}$ term and results in the expression:

$$ic^2(\mathbf{k} \times \mathbf{k} \times \mathbf{E}) = -i\omega\mathbf{E} + \mathbf{j}\omega/\epsilon_0. \tag{3.12}$$

The general relationship for $\mathbf{j}$ can be expressed as the resistive form of Ohm's law:

$$\mathbf{j} = \sigma\mathbf{E}, \tag{3.13}$$

where σ is the conductivity tensor of the medium. For an isotropic medium, and applying a vector identity, the equation can be rewritten in terms of $\mathbf{E}$ as:

$$\mathbf{k}(\mathbf{k} \cdot \mathbf{E}) - k^2\mathbf{E} + \frac{\omega^2}{c^2}\mathbf{E} + i\omega\mu_0\sigma\mathbf{E} = 0. \tag{3.14}$$

The dielectric tensor is defined as:

$$\varepsilon = 1 + \frac{i}{\omega\epsilon_0}\sigma = 1 + \frac{i\mu_0 c^2}{\omega}\sigma. \tag{3.15}$$

Substituting this in gives:

$$\mathbf{k}(\mathbf{k} \cdot \mathbf{E}) - k^2\mathbf{E} + \frac{\omega^2}{c^2}\varepsilon\mathbf{E} = 0. \tag{3.16}$$

For a transverse EM wave, $\mathbf{k}\cdot\mathbf{E} = 0$. This simplifies the equation to the well-known dispersion relation:

$$\sqrt{\varepsilon} = N = \frac{kc}{\omega}, \tag{3.17}$$

where N is defined as the refractive index of the medium. This relationship is the key to understanding how light refracts, reflects, and absorbs within a plasma medium, forming the basis for the laser probing diagnostics used in this dissertation.

To find the refractive index of a plasma, we first solve for its conductivity. Let's consider a slab of cold, non-magnetized, collisionless plasma in the high frequency limit. Starting

with the electron momentum equation:

$$mn_e\left[\frac{\partial \mathbf{v_e}}{\partial t} + (\mathbf{v_e}\cdot\nabla)\mathbf{v_e}\right] = n_e q\mathbf{E}, \tag{3.18}$$

where m_e is the mass of the electron, n_e is the electron density, $\mathbf{v_e}$ is the velocity, and q is the charge. Linearizing the momentum equation to the first order gives:

$$m\frac{\partial v_e}{\partial t} = q\mathbf{E}. \tag{3.19}$$

The electric field inside a slab of plasma is described by:

$$\mathbf{E} = \frac{n_e q x}{\epsilon_0}. \tag{3.20}$$

The momentum equation can then be rewritten in the form of an ordinary differential equation (ODE):

$$m_e\frac{\partial v_e}{\partial t} = -\frac{n_e q^2 x}{\epsilon_0} \quad \rightarrow \quad \frac{\partial^2 x}{\partial t^2} + \frac{n_e q^2 x}{m_e \epsilon_0} = 0. \tag{3.21}$$

The solution to this ODE is that of a simple harmonic oscillator. The characteristic frequency of this oscillator is the electron plasma frequency:

$$w_{pe} = \sqrt{\frac{n_e q^2}{\epsilon_0 m_e}}. \tag{3.22}$$

As an oscillating wave, at frequency (ω), propagates through the plasma, the velocity of the electrons is:

$$\mathbf{v_e} = -\frac{q}{i\omega m_e}\mathbf{E}. \tag{3.23}$$

The resulting current density generated due to the electron motion is given by:

$$\mathbf{j} = n_e q\mathbf{v_e} = -\frac{n_e q^2}{i\omega m_e}\mathbf{E}. \tag{3.24}$$

This allows us to define the plasma's conductivity, from Ohm's law $\mathbf{j} = \sigma\mathbf{E}$, as:

$$\sigma = -\frac{n_e q^2}{i\omega m_e}. \tag{3.25}$$

Hence the dielectric function and the refractive index for the plasma become:

$$\varepsilon = 1 - \frac{n_e q^2}{m_e \epsilon_0}\frac{1}{\omega^2} = 1 - \frac{\omega_{pe}^2}{\omega^2} = 1 - \frac{n_e}{n_{cr}} \tag{3.26}$$

Note that in this expression, if the laser frequency ω is less than the plasma frequency ω_{pe}, then the refractive index becomes imaginary (i.e. the wave becomes evanescent and incapable of propagating through the plasma). This formulation can be rewritten in terms of the critical density associated with the laser. This critical density ($n = n_{cr}$) is the plasma density at which $\omega_{pe} = \omega$. A laser cannot propagate through a plasma if the density equals or exceeds this critical density. The expression for critical density can be written in a more practical form as:

$$n_{cr}\ [\mathrm{cm}^{-2}] \approx 10^{21}/\lambda^2_{[\mu\mathrm{m}]}, \tag{3.27}$$

where λ is the laser wavelength in µm. For the system used in this dissertation, the laser wavelength is 532 nm. This gives us a *line-integrated* critical density limit of 3.5×10^{21} cm^{-2}.

3.2.3.1 Shadowgraphy and Schlieren

Laser schlieren is a simple but powerful technique in visualizing spatial information about structure formation and density gradients within gases and plasmas [128]. The fundamental mechanism of this technique relies on the refraction of light due to a change in the refractive index (N) of the medium. The total deflection of the light rays is caused by the gradient of the refractive index that is perpendicular to the direction of the incoming rays. These rays are refracted towards regions of higher refractive index. Since $N < 1$ in plasmas and $N > 1$ in neutral gases, light rays refract as follows in these two differing media:

- In a plasma, the rays would deflect from regions of higher to lower *electron* density. This refraction is similar to a concave lens diverging the rays.
- In a neutral gas, the rays would deflect from regions of lower to higher *gas* density. This refraction is similar to a convex lens converging the rays.

For a laser propagating in the z-direction through a plasma, the total refraction ($\theta_\perp$) is the line integral of the perpendicular gradient of the refractive index:

$$\theta_\perp = \int_0^L \nabla_\perp N dz \tag{3.28}$$

$$= -\frac{1}{2n_{cr}} \int_0^L \nabla_\perp n_e dz. \tag{3.29}$$

This relation can be rewritten in terms of the electron and critical density. The resulting relation shows that schlieren systems are sensitive to the first spatial derivative of density,

whereas shadowgraphy depends on the second derivative [129].

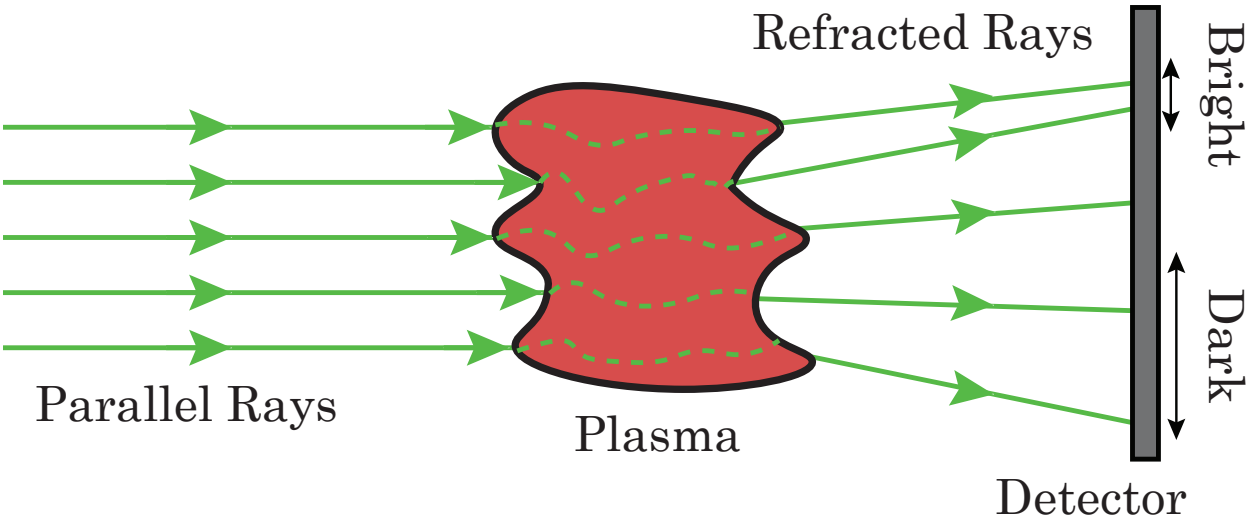


Figure 3.3: An illustration of a shadowgraphy diagnostic. A collimated probe beam of light passes through an underdense plasma, which causes the rays to refract in regions of varying electron density. This results in an image with bright and dark features (i.e., a "shadow") that corresponds to the second spatial derivative of the plasma's electron density.

Within a shadowgraphy setup (see Fig. 3.3), the probe beam propagates through the plasma and is subsequently captured directly by a detector. Variations in density within the plasma cause refraction and dispersion of the rays. Due to the pixel grid composition of the detector, these scattered rays may be collected more in certain pixels than in others, resulting in intensity modulations across the image, with some regions of the plasma appearing brighter than others. The intensity modulation

$$\frac{\Delta I}{I} = L\left[\frac{d^2}{dx^2} + \frac{d^2}{dy^2}\right]\int N dz, \tag{3.30}$$

is associated with the second derivative of the refractive index. While both schlieren and shadowgraph imaging provide insights into the electron density, extracting accurate quantitative measurements of the electron density proves challenging.

Regarding schlieren imaging, there are various setups that can be used. These setups are differentiated based on the type of spatial filter employed in the imaging system's focal plane, as shown in Fig. 3.4. These filters determine which probe rays make it to the detector. The fundamental configurations include the creation of dark images on a bright background field (i.e., "bright-field schlieren") and the creation of bright images on a dark background field (i.e., "dark-field schlieren"). To illustrate these systems, consider a laser beam traversing a

plasma object. A collection lens with a focal point is configured to relay a 1-to-1 image to the detector. Three spatial filtering options are presented:

- The simplest case is to not have a dedicated spatial filter at the focal point. This produces a dark image on a bright background field. In this scenario, both the unperturbed rays and the perturbed rays get passed through and collected by the detector, unless the refraction or absorption is significant enough that strongly perturbed rays miss the collection optic, which leaves a darkened spot on the imaging detector. This setup results in images formed by a combination of schlieren and shadowgraphic mechanisms.

- Placing an iris at the focal point produces a dark image on a bright background field. Here, the iris blocks the perturbed rays and passes the unperturbed rays onto the detector.

- Placing a beam stop at the focal point produces a bright image on a dark background field. There are many types of beam stops such as a circular beam stop and a knife edge. Both types stop the unperturbed rays and allow perturbed rays to reach the detector.

Beam stops and irises within a schlieren system can be conceptualized as spatial filters functioning in the Fourier plane. The focal plane of a collection lens contains the spatial Fourier transform of the probe rays that are scattered by the plasma. For an unperturbed probe beam, the rays converge to a singular, precise point (DC spatial component). Conversely, for a perturbed probe beam, the rays refracted by the density gradients are focused at an off-axis position (higher spatial frequencies). By introducing a filter at this plane, it becomes feasible to selectively block or transmit specific refraction angles, which correspond directly to areas of density gradient. While often used for qualitative visualization purposes, schlieren techniques can be modified to facilitate quantitative assessments. A specific approach utilizes a structured angular filter (e.g., repeating opaque and transparent rings) to accurately determine the distribution of deflection angles.

A primary advantage of qualitative schlieren imaging over interferometry is its superior dynamic range, as schlieren is limited by the collection lens, whereas interferometry is restricted by large fringe jumps at high density gradients. Nevertheless, schlieren imaging presents certain limitations. The maximum achievable refraction angle is dictated by the smallest lens within the collection optics. For instance, if the collection lens has an f-number of $f/14.8$, this corresponds to a collection angle of $3.88°$. Additionally, the number of measured points for an angular filter is limited by the number of opaque and transparent ring pairs. As the number of ring pairs increases, diffraction patterns emerge at the edges, adding

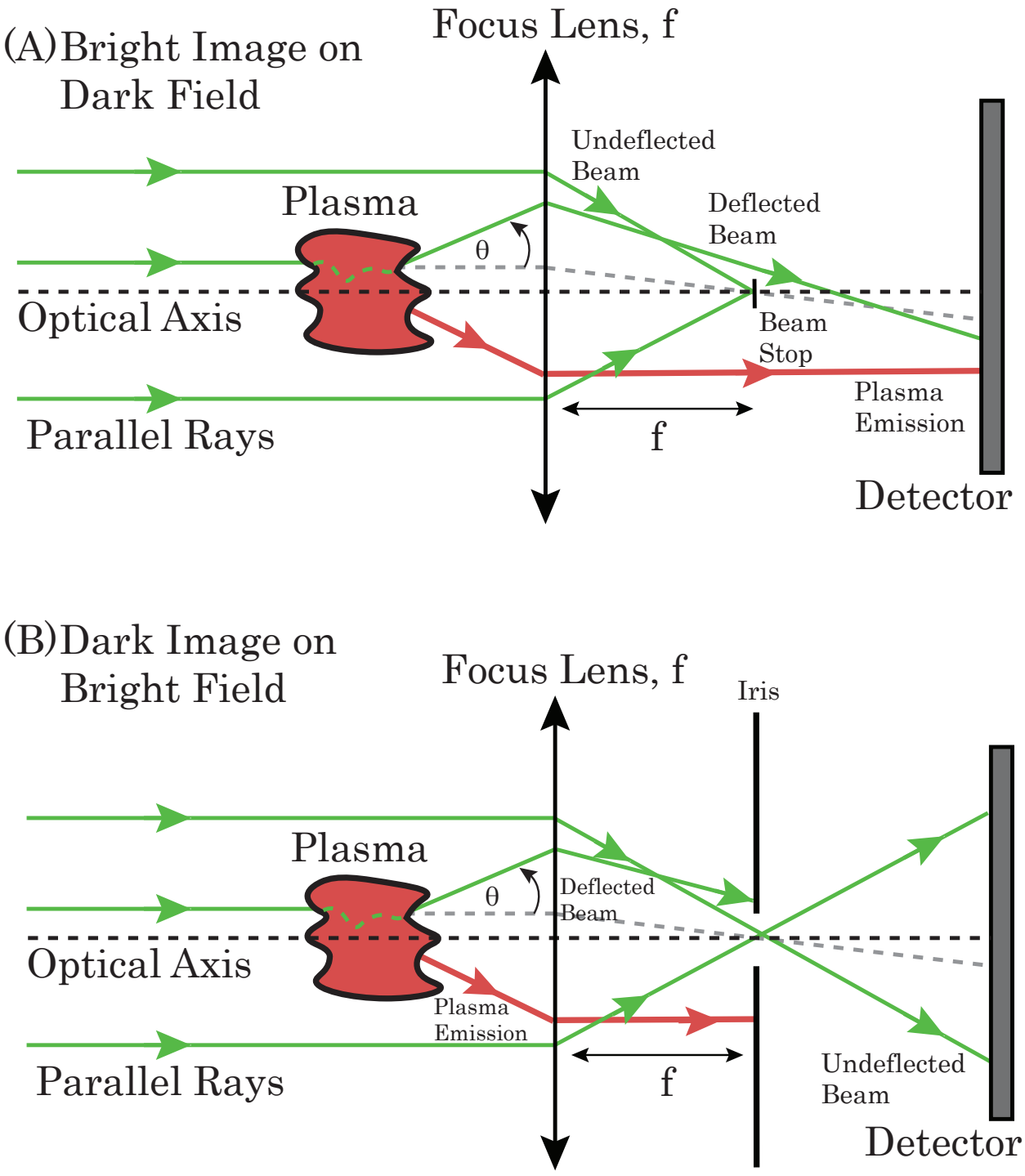


Figure 3.4: Illustration of schlieren imaging principles. A collimated probe beam passes through an underdense plasma and is focused with a single lens of focal length f. This focuses the beam to the focal length where a spatial filter separates the refracted light from the unperturbed light. The spatial filter can consist of either: (a) a beam stop (bright image on dark field); or (b) an iris (dark image on bright field). This results in an image that corresponds the first spatial derivative of the plasma's electron density.

complexity to the unfolding of density. For these reasons, interferometry is more frequently employed when the primary objective is to obtain a direct, two-dimensional density map.

Interferometry is a powerful technique for measuring plasma electron density. This technique is based on the physical principles of interference generated between dual beams, which is achieved recombining the beams after the phase of one of the beams has been perturbed by the plasma of interest. This measurement technique directly measures the phase of an object, which can subsequently be mapped to electron density. Among the various interferometry configurations available, this dissertation employs the Mach-Zehnder type interferometer. This particular imaging interferometry technique enables the acquisition of a 2-D image measurement of electron density.

3.2.3.2 Mach-Zehnder Interferometery

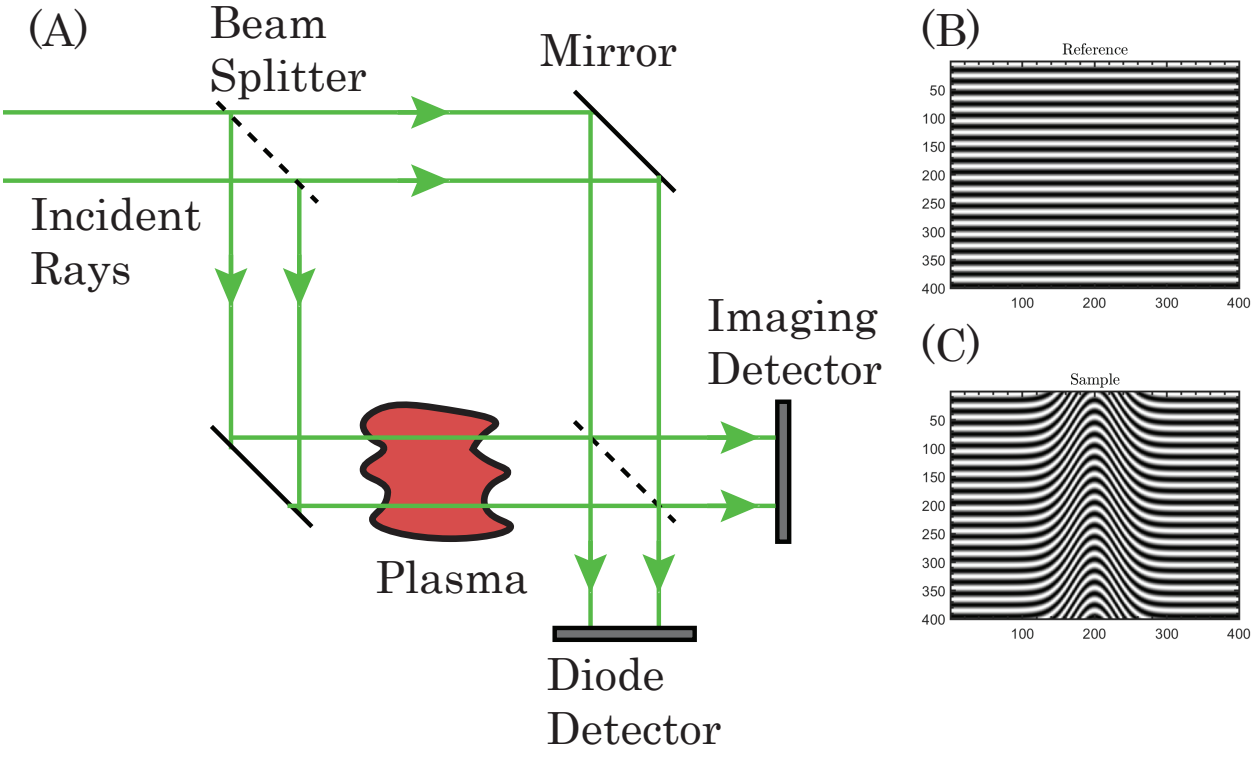


Figure 3.5: An illustration of a Mach-Zehnder interferometer and (b,c) synthetic interference pattern.(a) A collimated laser beam is split into a probe beam that passes through an underdense plasma and a reference beam. When recombined, they create an interference patter. This distortion of this pattern (fringe shift), is directly proportional to the line-integrated electron density of the plasma. A synthetic reference interferogram is shown (b), and a synthetic shot interferogram showing the fringe shift caused by a plasma object is shown in (c).

The fundamental principles of a Mach-Zehnder interferometer, as shown in Fig. 3.5, rely on splitting the probe laser beam into two distinct beams: a probe beam, which probes through the plasma object, and a reference beam, which propagates through free space over an equivalent distance. A second beamsplitter subsequently recombines these beams to form an interference pattern that is recorded by a CCD camera. This interference pattern comprises alternating bright and dark fringes, corresponding to regions of constructive and destructive interference, respectively. The quantity, density, and orientation of these fringes can be precisely controlled by adjusting the angle at which the beams recombine (at the second beamsplitter). When the probe beam passes through the plasma object, it undergoes a phase shift proportional to the line-integrated electron density. This phase shift manifests as a distortion in the fringe pattern, which can be imaged and quantitatively assessed. Through analysis of this fringe distortion, a quantitative, 2D map of the line-integrated density can be obtained.

Let's consider two propagating plane waves of the same amplitude and frequency, one wave propagates in free space (E_r) while the other propagates through a slab plasma medium (E_p):

$$E_r = E_0 \exp[i(\omega t - k_0 x)] \tag{3.31}$$

$$E_p = E_0 \exp[i(\omega t - k_p x)]. \tag{3.32}$$

The phase difference shift ($\Delta\phi_{\text{phase}}$) between the two waves passing through a plasma of length L is the difference between the phase accumulated in the plasma. This is given by the integral of the difference in their wavenumbers:

$$\Delta\phi_{\text{phase}} = -\int_0^L (k_0 - k_p)dx, \tag{3.33}$$

where k_p is the wavenumber in the plasma and $k_0 = \frac{\omega}{c}$ is the free space wavenumber. Using the relationship $k_p = \frac{\omega}{v_\phi} = k_0 N$ and the refractive index for a plasma, $N = \sqrt{1 - n_e/n_{cr}}$, the phase difference can be rewritten in terms of the density of the plasma:

$$\Delta\phi_{\text{phase}} = -\int_0^L k_0 \left[1 - \left(1 - \frac{n_e(x)}{n_{cr}}\right)^{1/2}\right] dx. \tag{3.34}$$

In the underdense limit ($n_e \ll n_{cr}$), a binomial expansion can be applied to the square root term to simplify the expression to:

$$\Delta\phi_{\text{phase}} = -\int_0^L k_0 \left(1 - \frac{n_e(x)}{n_{cr}}\right)^{1/2} dx \tag{3.35}$$

$$\approx \int_0^L k_0 \left[1 - \left(1 - \frac{1}{2}\frac{n_e(x)}{n_{cr}}\right)\right] dx \tag{3.36}$$

$$\approx \frac{k_0}{2n_{cr}} \int_0^L n_e(x) dx \tag{3.37}$$

$$\approx \frac{q^2}{2m_e\epsilon_0 c\omega} \int_0^L n_e(x) dx. \tag{3.38}$$

This final relationship is foundational for plasma interferometry. It demonstrates that, in the case of an underdense plasma, the measured phase shift is directly proportional to the line-integrated electron density. By evaluating the fringe shift from a Mach-Zehnder interferogram, it is possible to directly calculate a quantitative, 2D map of the line-integrated electron density.

The 2D phase map, $\phi(x, y)_{\text{phase}}$, obtained from interferometry is the line-integrated electron density through a 3D plasma:

$$\phi_{\text{phase}}(x, y) = \frac{\pi}{\lambda_p n_{cr}} \int_{-\infty}^{\infty} n_e(x, y, z)\, dz. \tag{3.39}$$

In the case where the plasma system is cylindrically symmetric, this function can be mathematically inverted to reconstruct the 3D, locally resolved electron density profile $n_e(r, z)$. This process enables the decomposition of the integral from Equation 3.39 into an R-Z back projection of the electron density, a procedure referred to as Abel inversion:

$$n_e(r, z) = -\lambda_p n_{cr} \int_r^{r_{max}} \frac{\partial\phi_{\text{phase}}(x, z)}{\partial x} (x^2 - r^2)^{-1/2}\, dx. \tag{3.40}$$

This technique is a 2D back projection technique that projects a line-integrated 2D map into a 3D projection. In practical experimental scenarios, the plasma source is hardly cylindrically symmetric due to numerous instabilities and deformities inherent in the plasma. Consequently, this may constrain the applicability of the inversion. Nevertheless, it continues to serve as a valuable tool for acquiring an understanding of the local electron density distribution.

CHAPTER 4

Magnetized Gas on Rod Experiment

A significant challenge in Magnetized Liner Inertial Fusion (MagLIF) is understanding the formation and seeding of instabilities that develop during the implosion phase. In particular, these implosions can develop steep helical instabilities that are not well predicted by current resistive MHD simulations. A prevailing hypothesis to account for the pronounced helical pitch angles involves magnetic flux compression occurring in low-density plasmas within the Z facility's power feed. In this context, it is postulated that such plasma is likely compressed onto the external surface of the dense MagLIF liner, potentially seeding deleterious instabilities that could compromise the structural integrity of the fusion target.

The experiments presented in this chapter were conducted on the MAIZE pulsed power facility located at the University of Michigan [60, 69]. In these experiments, MAIZE delivered a driving current pulse that rose from 0 to 500 kA in approximately 150 ns. At such current levels, generating electrode plasmas from thick metal electrodes with sufficient plasma densities to be detectable using standard diagnostic techniques remains challenging. Consequently, stripline platforms incorporating thin-foil electrodes supported by solid 3D-printed insulating material have been developed to study electrode plasma formation on MAIZE [130]. However, even with such a platform, it is still difficult to both generate *and* subsequently sweep this plasma onto an imploding liner. To address these challenges, we developed a new platform [24]—one which uses MAIZE's annular gas-puff Z-pinch system with $n_e \sim 10^{17}$–10^{18} cm^{-3} [24, 26, 121] to emulate the low-density plasma expected to be present in the MITLs on the Z facility. Using this platform, we can experimentally investigate the development of instabilities and the magnetic flux compression of a pre-embedded axial magnetic field when the low-density plasma from the gas-puff Z-pinch implodes onto a solid cylindrical target.

The key findings presented in this chapter include experimental observations of helical striations exhibiting large pitch angles within low-density plasma when a pre-embedded axial magnetic field of $B_{z0} = 0.25$–0.75 T (at $z = 10$ mm) is applied. Observations shows that the polarity of the applied axial field determines whether the helical striations are left-handed or

right-handed helices. Additionally, the magnitude of the pitch angle grows as the strength of the axial field increases. Schlieren imaging reveals that at higher axial field strengths, shorter wavelength perturbations are partially stabilized and only longer wavelength perturbations persist. Interferometry reveals that axially magnetized shots produce a larger volume of underdense plasma compared to non-axially magnetized shots, with line-integrated electron densities in the range of $\sim 10^{17}$–10^{18} cm^{-2}. Axially magnetized shots exhibit turbulent-like, complex fringe patterns, while non-axially magnetized shots show more uniform horizontal structures. The morphological difference likely stem from vertical filamentation. Measurement of the gas-puff implosion trajectory onto the central rod is shown to occur around the time of peak current, with a compressed plasma sheath thickness of approximately 1 mm. The flux compression efficiency is measured to be nearly 50%, relative to an idealized flux compression model, where an imploding thin shell with zero resistivity is assumed.

This chapter details the development and characterization of a novel experimental platform designed for studying instability development and magnetic flux compression in a low-density plasma during its implosion onto a dense cylindrical target [24]. Section 4.1 describes the experimental apparatus and the diagnostic suite used. Section 4.2 presents the primary findings, including fast-framing imagery capturing the plasma's implosion trajectory. In Section 4.3, an analysis is conducted of the overall morphology of the instabilities observed in both schlieren and self-emission images. In Section 4.4, we focus on the helical striations observed in the self-emission images, with quantification of their pitch angles under varying magnetic field strengths. In Section 4.5, the line-integrated electron density is quantified for the gas plasma both with and without a dense central target. In Section 4.6, magnetic flux compression efficiency of the gas shell is quantified using magnetic probe measurements. Finally, Section 4.7 provides a summary of these findings and discusses their implications for understanding instability seeding in extremely high current density liner implosions.

4.1 Experiment and Diagnostic Setups

The experimental load region, illustrated in Fig. 4.1, is comprised of a singular annular gas-puff (supplied by a fast-valve coupled to a nozzle), a central rod, an exit mesh, and six return-current posts. To minimize the overall load inductance—an essential parameter for the MAIZE device—this configuration underwent modification from its previous design. The original gas-puff system [121, pp. 22–25], [26] facilitated the generation of two independent annular gas shells through two independent nozzles. These nozzles can pose challenges as they introduce additional inductive pathways for the current in the absence of gas within them.

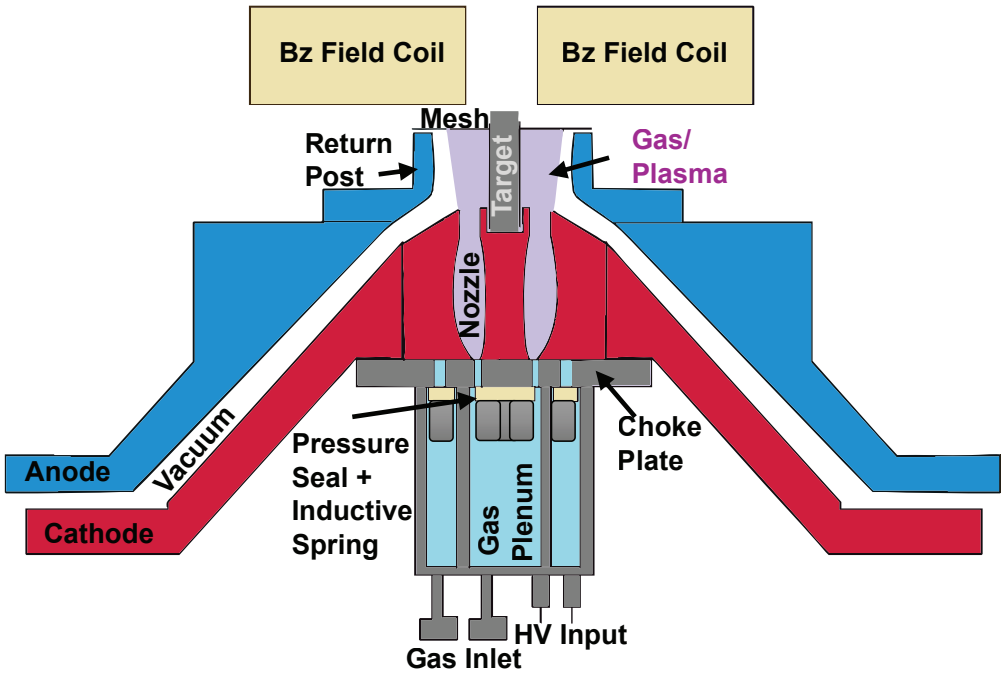


Figure 4.1: Illustration of the experimental setup and the gas-puff hardware assembly.

To reduce the inductance of this hardware, the nozzle insert was redesigned to incorporate a solid-metal-filled outer nozzle. Additionally, the radius of the six return-current posts was reduced down to 32 mm using an anode extension (see Fig. 4.1). These alterations resulted in a low-inductance load configuration tailored for optimization within the MAIZE facility. The details of the experimental load configuration are further illustrated in Fig. 4.2.

The gas-puff plenum was filled with -2 psig (17 µg/cm^{-3}) of argon gas. The gas was ejected from the plenum, through the single (inner) nozzle, into the 20-mm-tall AK gap, facilitated by an inductive piston. The nozzle is positioned at the bottom (cathode) side of the MAIZE load region. The nozzle exit has an outer radius of 10 mm and an inner radius of 4.7 mm. MAIZE is fired 700 µs after gas release to ensure that the gas has completely traversed the AK gap. To permit the escape of gas on the anode side and avert any gas accumulation within the AK gap, a stainless steel anode mesh, featuring a grid spacing of 1 mm $\times$ 1 mm, is situated above the gas-puff.

A 3-mm-radius central rod was placed on axis to serve as the target for the imploding plasma. Two types of rods were employed to achieve distinct measurement objectives. The cross-sectional views and photographs of the targets are shown in Fig. 4.3. Most of the experiments used a copper central rod to allow compression of the axial field onto a stationary conductor that is thicker than the electrical skin depth. This configuration was selected to emulate MagLIF liners, which are also electrically thick to the driving current on the

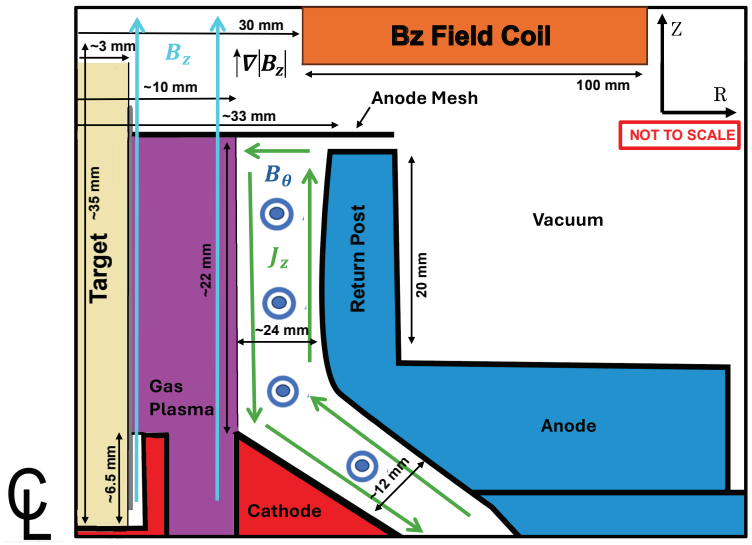


Figure 4.2: Detailed cross-section of the experimental load. The main current (green) flows upward along the anode surface (blue) and return-current posts (blue), downward through the gas plasma (purple), and back to its source along the cathode surface (red). The resulting azimuthal magnetic pressure implodes the plasma, compressing the pre-embedded axial magnetic field (cyan) generated by the axial field coil (orange). The imploding low-density plasma then collides onto the central target (beige)

Z facility. For the purpose of on-axis magnetic field measurements, the copper rod was replaced with a hollow dielectric target that housed an axial B-dot probe. This setup enabled the compressed field to penetrate to the central axis, thus permitting measurements of the compressed axial field.

The B-dot probes used for these experiments were custom built from semi-rigid copper coaxial cable, having an outer diameter of 0.02 inches and a length of ∼10–15 mm. Variations and configurations of these B-dot probes are shown in Fig. 4.4(a). The probe tip was fabricated by stripping the coaxial cable ends to expose the central conductor and its dielectric insulation. Subsequently, the inner conductor was carefully wound one to two times around the dielectric and soldered to the outer conductor, thus creating an inductive loop. For the measurement of the axial magnetic field, the loop area was oriented perpendicular (normal) to the probe axis. Finally, the tip of the tube was potted with a ceramic material and wrapped with a thin layer of kapton tape to provide electrical insulation and durability, as shown in Fig. 4.4(b).

The B-dot probe was calibrated ex situ using a custom-built test stand. This test stand consisted of a calibration coil driven by an independent pulser, as shown in Fig. 4.4(c). The calibration coil, constructed from a metal wire wound around a 3D-printed plastic housing,

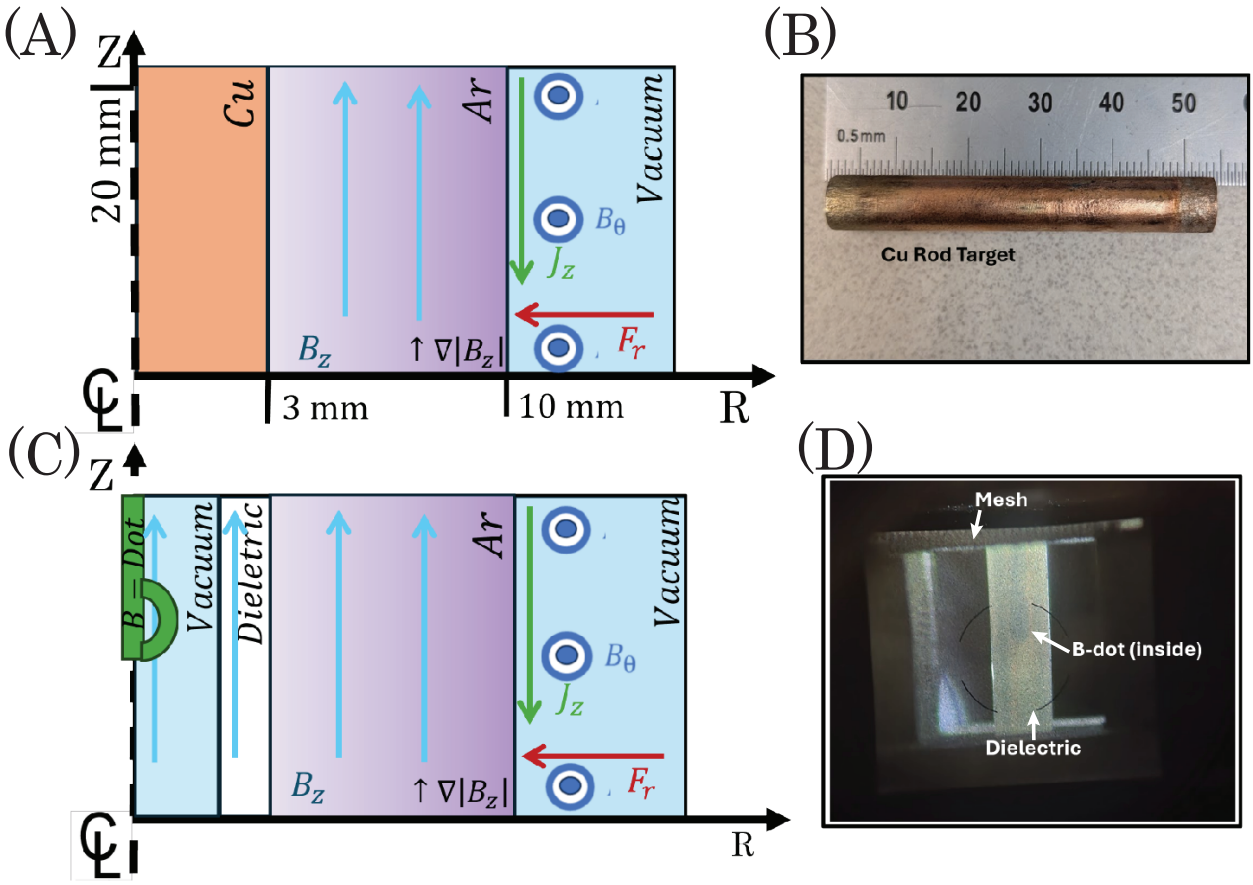


Figure 4.3: Cross-sections and corresponding photographs of the two targets used in the experiments. (a) Cross-section of the solid copper rod experiment. (b) Photograph of the solid copper rod target. (c) Cross-section of the experiment with a dielectric tube housing a B-dot probe. (d) Photograph of the dielectric tube with a B-dot probe inserted, where the dielectric tube has been installed in the MAIZE load region. Both target types have a radius of approximately 3 mm and a total height of 50 mm. Approximately 20 mm of this height is positioned within the load region, where it becomes surrounded by an argon gas shell upon gas injection

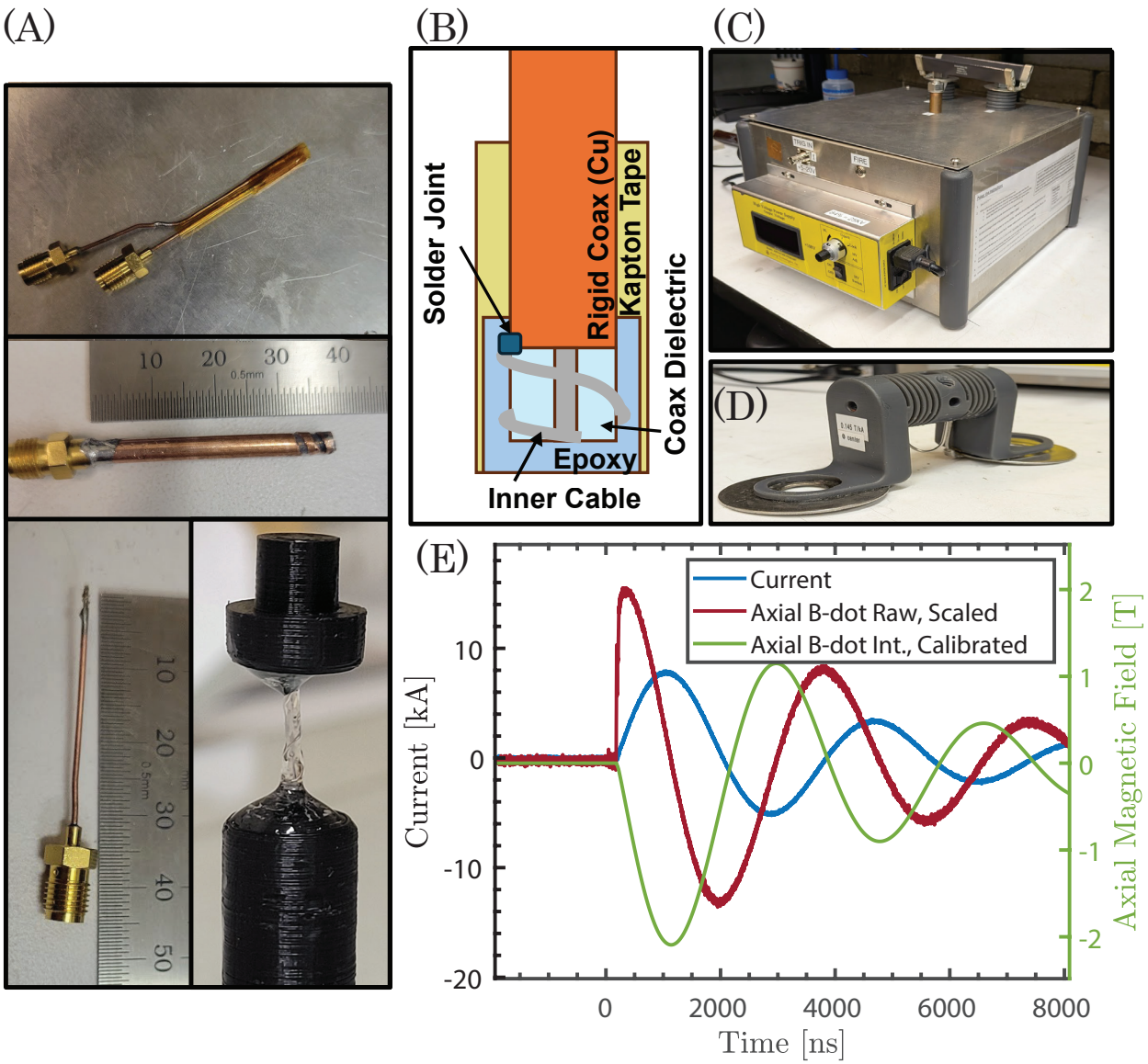


Figure 4.4: (a) Photographs of various B-dot probes constructed for this work. (b) A schematic of the final B-dot probe design. (c) The calibration pulser used. (d) The calibration coil used for ex-situ calibration of the B-dot probes. (e) A plot of the calibration waveforms from the pulser with the calibration target, showing the pulser current (blue), the B-dot probe's raw voltage (red), and the final calibrated magnetic field trace (green).

produces a central magnetic field factor of 0.145 T/kA, as shown in Fig. 4.4(d). The pulser stores ≈75 J within three 80-nF, 100-kV capacitors, each charged to 25 kV. The pulser delivers an underdamped current to the coil. The current is measured with a Pearson coil while the B-dot probe voltage response is recorded simultaneously, as shown in Fig. 4.4(d). The current pulse had a rise time of ∼1 µs and peak current of 6.8 kA, corresponding to a peak magnetic field strength of approximately 1 T. By comparing the probe's voltage signal with the known magnetic field, a calibration factor was determined.

The load was pre-magnetized with an axial field using a single 80-turn coil placed on top of the anode mesh. The coil was isolated from the mesh by a thin polycarbonate sheet, as shown in Fig. 4.5(a). The coil operation was driven by an independent capacitor bank with a capacitance of 1.2 mF and a current rise time of 2 ms. Discharge of the MAIZE generator occurred when the coil attained its peak current, aligning with the coil's peak field strength, as shown in Fig. 4.5(d). This long discharge time allowed the axial magnetic field to uniformly diffuse through the metallic load hardware prior to the main implosion.

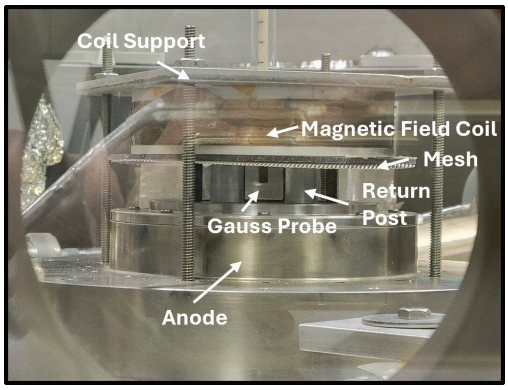
This setup uses the fringe field of the axial magnetic field (B_z) coil (i.e., the field that exists below the bottom edge of the solenoid winding). This approach was necessary because the coil's inner radius was too small to fit around the return-current structure. The variation in the peak axial field strength as a function of height is measured using a gaussmeter, as shown in Fig. 4.5(b). The relationship is approximately linear across the AK gap, as shown in Fig. 4.5(c).

For these experiments, time-resolved images of the visible-light self-emission from the imploding plasma were captured using the fast 12-frame camera. Each frame was exposed for a duration of 5 ns, with a temporal separation of 33 ns between successive frames.

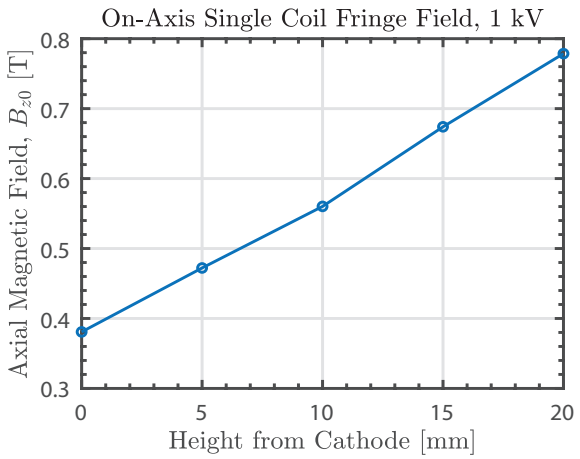
A comprehensive suite of laser-based diagnostics, including schlieren imaging, shadowgraphy, and interferometry, was implemented to visualize the structural characteristics of the gas shell and plasma. All three diagnostics were sourced by a single 2-ns, 532-nm probe beam from an Nd:YAG laser, which was situated in a climate-controlled room to maintain operational stability. The configuration of the optical setup is shown in Fig. 4.6.

Significant beam conditioning was necessary to achieve a high-quality beam. The initial beam, with a diameter of approximately 5 mm and exhibiting spatial aberrations, was relayed to the experimental area and expanded to ≈25 mm using a 5× Keplerian telescope expander. This expander consists of lenses with focal lengths of 30 mm and 150 mm. A 100-µm-diameter pinhole was located at the focal spot between the beam expander optics. This pinhole functioned as a spatial filter to improve the beam quality. An iris was then used to aperture the beam, maintaining a clean and circular profile. After conditioning, an 80:20 beam splitter divided the beam into two paths. The higher-intensity probe beam was directed

(A)



(B)



(C)

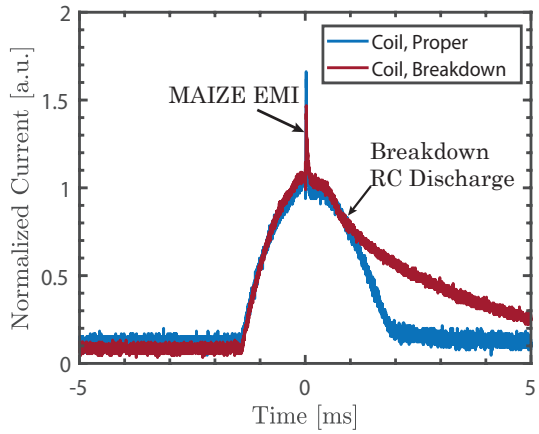


Figure 4.5: (a) A photograph of the ex-situ measurement of the axial field. In this image, a gauss probe is used to measure the peak axial field of the pulsed coils at $r = 0$. (b) A plot of the axial magnetic field strength as a function of height. Here, $z = 0$ mm is the cathode height, while $z = 20$ mm is the height of the anode mesh. The values plotted for each height are the values found on axis, at $r = 0$. (c) A current waveform from the axial field coil, measured with a current viewing resistor (CVR). The blue current trace shows a proper shot with the coil. Note that the sharp spike at the peak of the current trace is due to electromagnetic interference (EMI) from MAIZE discharging on a 100-ns time scale. This confirms that MAIZE fires at the peak magnetic field generated by the coils. The red current trace shows a fault discharge where the coil breaks down and shorts to the chamber of MAIZE, resulting in an RC decay after the discharge of MAIZE.

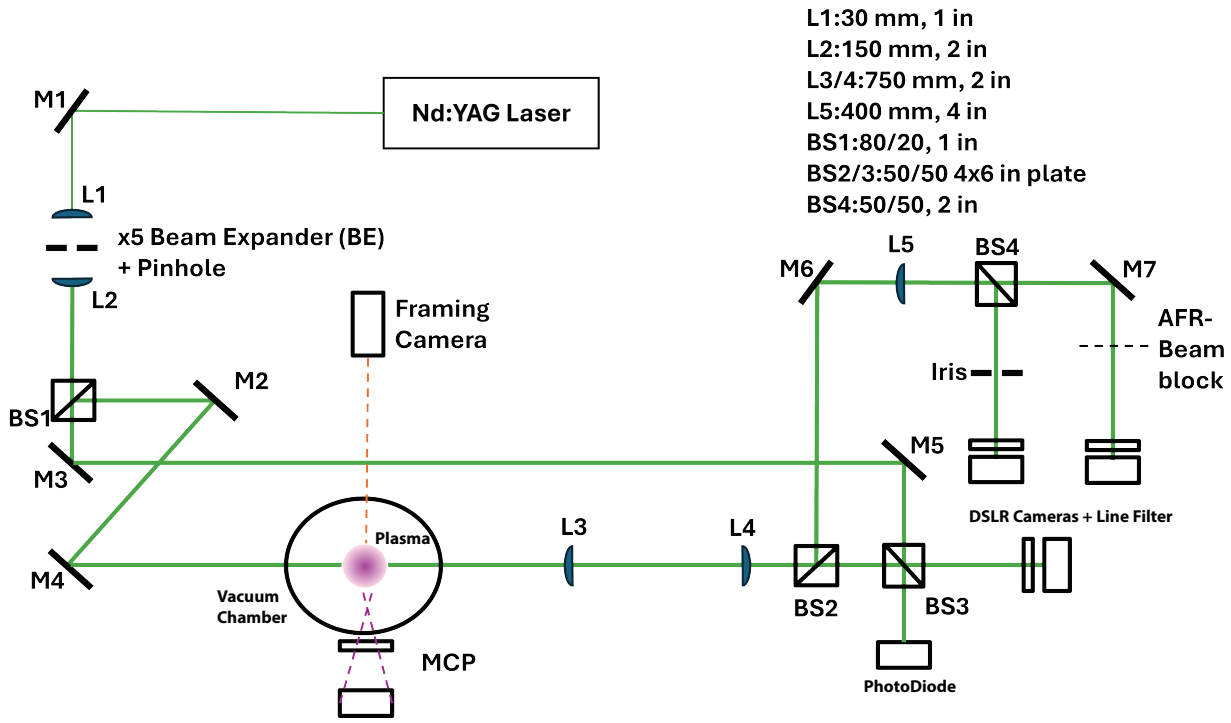


Figure 4.6: Schematic of the optical laser probing diagnostic setup. The laser beam (green) is expanded and filtered before an 80/20 beam splitter splits the beam into a reference beam and a probe beam. The probe beam is transported into the vacuum chamber, probes the plasma, and is collected by a 4f imaging telescope, while the reference beam travels concurrently through in free space. For interferometry, a portion of the probe beam is recombined with the reference beam to form an interferometric image that is captured by a DSLR camera. The rest of the probe beam is used for backlighting, where it is split to simultaneously form a dark field and bright field schlieren image.

through the plasma within the vacuum chamber. The lower-intensity reference beam was routed around the vacuum chamber for interferometry.

After passing through the plasma, the beam and image were collected and relayed using a 4-f telescope with a focal length of 750 mm and a collection angle of 3.8°. The image and beam were relayed onto the collection optics table. Here, the probe beam underwent further division for separate diagnostic applications.

For interferometry, a portion of the probe beam was diverted and subsequently recombined with the reference beam. The resulting interference pattern was imaged onto a Nikon DSLR camera.

The remaining beam segment served as a timing fiducial. The light from this timing fiducial was collected with a fast photodiode. The signal from the photodiode was used to understand and synchronize the timing of the probe laser diagnostics relative to the MAIZE current pulse.

For the laser backlighting line, an additional lens, with a 400-mm focal length and a 4-inch diameter, was used to relay the image via a 50:50 beam splitter into a shadowgraphy/schlieren camera. Within the shadowgraphy line, an iris was positioned at the focal point of the final imaging lens. This configuration impedes light that undergoes significant refraction due to the plasma while permitting unperturbed rays to reach the detector. This produces a dark image on a bright background field (see Fig. 3.4).

The schlieren line incorporated an angular beam stop, repurposed to serve as a 500-µm-diameter beam stop, positioned at the final unperturbed focal spot to establish a bright schlieren image on a dark background field (see Fig. 3.4). All three DSLR cameras were equipped with neutral density (ND) filters for intensity control and 532-nm line filters to reject unwanted plasma self-emission. The spatial resolution of the imaging system was evaluated utilizing a 1951 USAF Resolution Test Target. The resulting system resolution was found to be approximately 14.25 line pairs per mm (lp/mm), which is equivalent to about 35 µm. However, the resolution depreciates over the duration of the experimental campaign due to vibrations created during a shot (which slightly wiggles the collection lens), and due to the environment of the lab (oil and dust vapors naturally occur in pulsed power environments, which can collect on optics).

4.2 Implosion Trajectory

In Fig. 4.7(a), we present visible-light self-emission images collected from the fast 12-frame camera. These data reveal a conical shape to the imploding plasma sheath. This "zippering" effect is well known in the gas-puff Z-pinch community and is generally undesirable [131]. In

Fig. 4.7(a), the zippering persists until maximum compression occurs along the central rod. Note that in the first two frames of Fig. 4.7(a), a very dim plasma is present; these frame times correspond to a drive current of about 300–400 kA [see Fig. 4.7(b)].

The outer radial edge of the imploding plasma sheath is determined using an automated MATLAB script. Each image is first contrast enhanced and smoothed using a 5 pixel × 5 pixel (corresponding to 140 µm × 150 µm) median filter. The images are then binarized using a threshold intensity of 0.15 times the maximum intensity found in the image. A horizontal lineout is then taken across the binarized image to determine the outer radial edge of the plasma sheath.

In Fig. 4.7(b), the outer radial edge of the plasma sheath is plotted as a function of time for three different axial locations. Each radial value plotted is the average sheath radius taken over a 5-mm-tall window that is centered on the axial location indicated: $z = 2.75$ mm (green), $z = 9.5$ mm (blue), and $z = 16.5$ mm (purple). These three trajectories help quantify the differences in implosion timing of the plasma sheath from top to bottom (anode to cathode). Near 200 ns, the top of the sheath is at a radial position of $r \approx 7$ mm, the mid-height is at $r \approx 5$ mm, and the bottom has already collapsed onto the central rod with a plasma outer radius of $r \approx 4$ mm. The time difference between the top and bottom of the sheath collapsing onto the rod is approximately 60 ns. At peak compression along the rod, the thickness of the plasma sheath is about 0.5 mm. The plasma sheath then decompresses back out to a thickness of about 2 mm. The sheath thickness is quite uniform axially along the surface of the rod, despite the conical shape of the imploding sheath. The full compression of the plasma occurs at about 260 ns, which is approximately 110 ns after peak current.

4.3 Instability Evolution and Stabilization

In Fig. 4.8, the outer edge of the imploding plasma sheath has been traced (blue line) using the edge-detection method described in Sec. 4.2. For this non-premagnetized case (i.e., $B_{z0} = 0$), the dominant instability structure is azimuthally symmetric ($m = 0$). The $m = 0$ structure has been determined from the full-view images of this shot [e.g., Fig. 4.11(a)], where the striations are observed to be horizontally oriented. Using the traced edges in Fig 4.8, the instability amplitude is taken as the average radial distance between the peaks and the troughs. The instability wavelength is taken as the average axial distance between consecutive peaks. At $t = 197$ ns, the instability amplitude is about 0.14 ± 0.09 mm and the wavelength is 0.9 ± 0.3 mm. As the plasma collapses onto the central rod (around $t = 230$ ns), the instability structure transitions quickly, growing to an amplitude of about 0.6 ± 0.2 mm

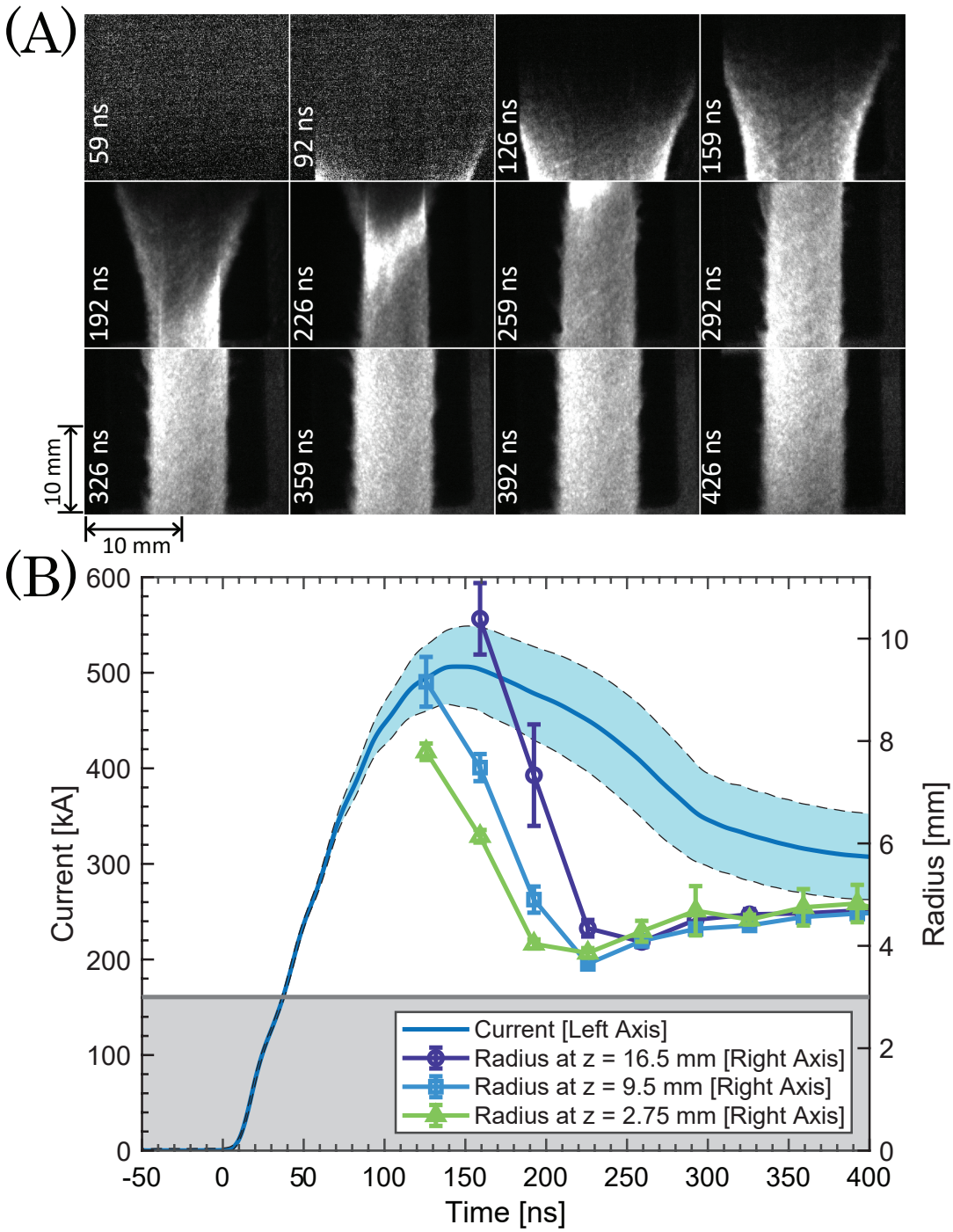


Figure 4.7: (a) Representative visible-light self-emission images from an experiment with $B_{z0} = -0.75$ T at $z = 10$ mm. The field of view in each image is 21 mm $\times$ 21 mm. (b) The average drive current and its standard deviation over 17 shots, which includes shots with and without an applied B_{z0}. Also plotted are the implosion trajectories for three different axial heights: $z = 2.75$ mm (green), $z = 9.5$ mm (blue), and $z = 16.5$ mm (purple). The center rod is represented by the shaded gray area. From bottom to top, the imploding sheath impacts the rod over the time period of 194–260 ns.

and a wavelength of 1.6 ± 0.3 mm.

The data in Fig. 4.8 also reveal mode-merger events occurring during the time period of $t = 230$–297 ns, at axial positions of $z = 0$–6 mm. A mode-merger event is where two or more shorter-wavelength structures merge into a single longer-wavelength structure. Mode-merger events have been observed previously in thin-liner implosions [17]. We also note here that the plasma appears to drift in the upward ($+z$) direction (from cathode to anode). The axial velocity is taken as the change in axial position of a given instability peak over the interframe time period. For the time period $t = 263.6$–363.6 ns, shown partially in Fig. 4.8, the peaks of the instability structure are well defined and give an average axial velocity of 21 ± 9 µm/ns.

In Fig. 4.9(a–d), we present schlieren imaging data for four different cases: $B_{z0} = 0$, $B_{z0} = +0.25$ T, $B_{z0} = +0.5$ T, and $B_{z0} = +0.75$ T (where these B_{z0} values are the fringe field values taken at $z = 10$ mm). All four images were taken around the same time of $t \approx 238$ ns, which is after the entire height of the plasma sheath has collapsed onto the rod. The tracked boundaries are shown in green. The instability amplitudes, A, were taken as $2\sqrt{2}\sigma$, where σ is the standard deviation in the plasma radius. Using this definition, we found $A = 1.5$ mm, 1.6 mm, 1.5 mm, and 0.8 mm for $B_{z0} = 0$, +0.25 T, +0.5 T, and +0.75 T, respectively. The instability wavelengths in the axial direction, λ_z, were characterized two different ways, where both ways made use of discrete Fourier transforms (DFTs). The first method used the DFT power spectra directly, taking the largest peak in each spectrum as the dominant wavelength. These spectra are shown in Fig. 4.9(e) and gave $\lambda_z = 3.1$ mm, 5.0 mm, 5.0 mm, and 6.9 mm for $B_{z0} = 0$, +0.25 T, +0.5 T, and +0.75 T, respectively. The second method used each DFT power spectrum as an energy distribution function, which could be characterized by its mean value (mean wavelength). With this description, 50% of the total fluctuation energy is carried by wavelengths below the mean value, and 50% of the total fluctuation energy is carried by wavelengths above the mean value. Using this method, we found $\lambda_z = 4.2$ mm, 4.5 mm, 4.8 mm, and 6.5 mm for $B_{z0} = 0$, +0.25 T, +0.5 T, and +0.75 T, respectively. These results are plotted with their uncertainties (error bars) in Fig. 4.9(f).

The analyses in the previous paragraph suggest that higher B_{z0} cases tend towards larger λ_z and smaller A. However, as noted in Refs. [116, 117], images like those presented in Fig. 4.9 are 2D projections of 3D objects. The full instability amplitude is only observable by non-penetrating imaging diagnostics in the case of an azimuthally symmetric ($m = 0$) structure. For helical structures, the spikes partially obscure the camera's view of the troughs (bubbles). This causes the observed instability amplitudes, A_{obs}, to be smaller than the true instability amplitudes, A_{true}. To quantify the obstructed view effects, a 3D geometric

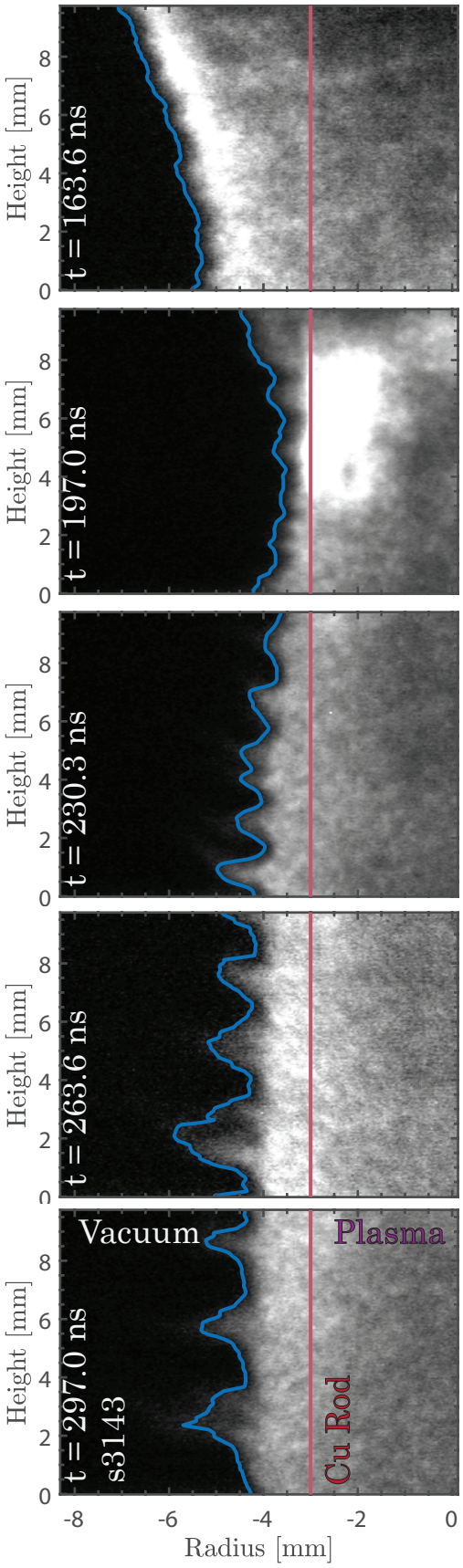


Figure 4.8: Visible-light self-emission images of the $B_{z0} = 0$ experiment as the conical plasma sheath compresses onto the central rod. The plasma boundary was tracked for each image and is indicated by the blue lines, while the red line represents the initial radius of the copper rod. These images show a notable change in the instability amplitude past 230 ns, when the process transitions from implosion onto the rod to explosion away from the rod. These images also show the instability structures evolving from shorter wavelengths to longer wavelengths over time (i.e., the so-called "inverse cascade") due to mode merger events, and an upward axial drift in the plasma structure (in the $+z$ direction).

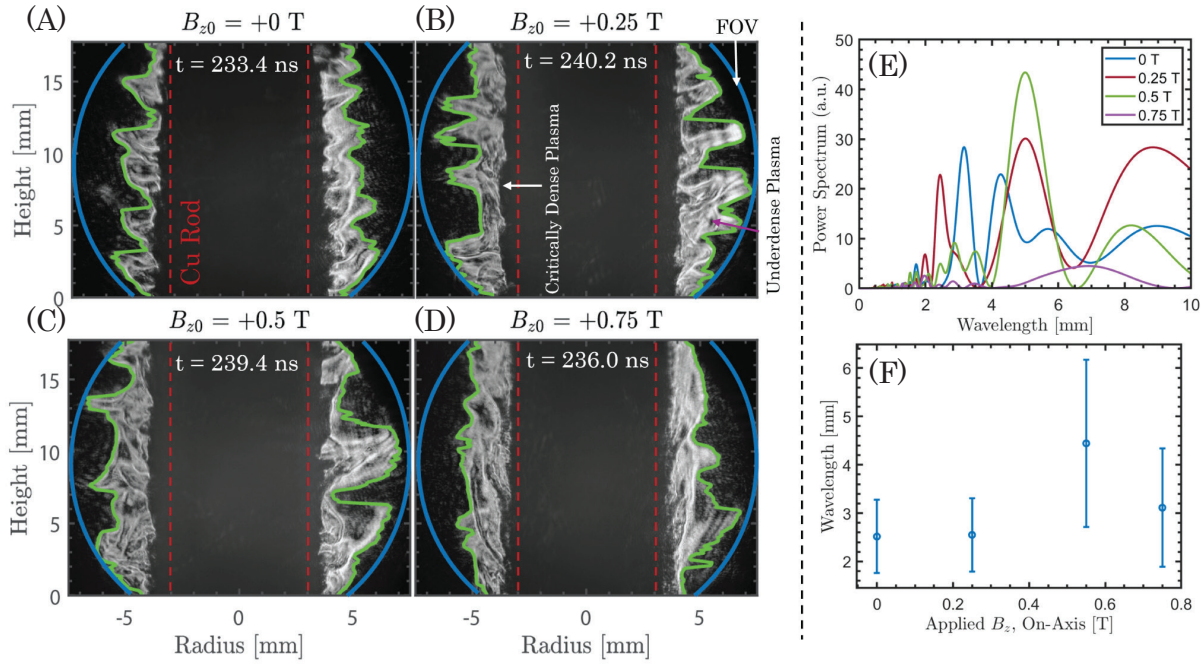


Figure 4.9: Schlieren images taken after peak compression onto the rod for four cases: (a) $B_{z0} = 0$; (b) $B_{z0} = +0.25$ T; (c) $B_{z0} = +0.5$ T; and (d) $B_{z0} = +0.75$ T. These B_{z0} values are for the fringe field at $z = 10$ mm. The plasma boundary was tracked for each image and is indicated by the green lines. The initial radius of the copper rod is indicated by the dashed red lines. (e) A plot of the power spectra of the schlieren boundaries. The colors of blue, green, red, and purple correspond to B_{z0} values of $0, +0.25, +0.5$, and $+0.75$ T, respectively. Stabilization of shorter wavelength modes is observed as $|B_{z0}|$ is increased. (f) A plot of the dominant wavelength of the schlieren images. Larger wavelengths tend to become more dominant as $|B_{z0}|$ is increased.

model with cycloidal perturbations (sharp cusps) was developed (see Fig. 4.10). This model is similar to that shown in Ref. [116, pp. 64–74] and mentioned in Ref. [117]. The model presented herein (Fig. 4.10) consists of a cylindrical surface with a radius of 5 mm, perturbed with a single mode. Various single modes were tested, including helical pitch angles that spanned from $\phi = 0°$ (i.e., an azimuthally symmetric, $m = 0$ case) to $\phi = 50°$ (i.e., a steep helical case); $\lambda_z = 1$ mm, 3 mm, or 5 mm; and $A_{\text{true}} = 1$ mm or 2 mm, where A_{true} in this cycloidal model is the full bubble-to-spike radial distance. These parameter ranges were chosen because they are similar to those observed in the experimental data. In particular, for $\phi = 30°$ and $\lambda_z = 3$ mm, the ratio $A_{\text{obs}}/A_{\text{true}}$ is 0.92 and 0.37 for $A_{\text{true}} = 1$ mm and 2 mm, respectively. In principle, we could apply such corrections to our experimentally observed instability amplitudes, A. However, doing so is difficult to justify for the data presented herein, since the corrections become exceedingly large and unreliable for the large A and ϕ values presented in this study. It is even more difficult to justify given that the instability structures observed in this study are not truly cycloidal or single modes. Therefore, due to the non-penetrating diagnostic limitations, it is difficult to quantify with certainty the degree to which the instability structures were stabilized by B_{z0} in these experiments.

4.4 Helical Striation

In these experiments, helical striations were observed for all cases with $B_{z0} \neq 0$. This is shown in Fig. 4.11, where visible-light self-emission images are presented for three cases: $B_{z0} = 0$, $B_{z0} = +0.75$ T (at $z = 10$ mm), and $B_{z0} = -0.75$ T (at $z = 10$ mm). The three frames presented in Fig. 4.11 were chosen because they were close to the same radius during the implosion. These data show very clearly that an applied axial field produces large helical pitch angles even when the applied axial field ($|B_{z0}| < 1$ T) is much smaller than the peak implosion-driving azimuthal field ($B_\theta \approx 30$ T). The peak azimuthal field comes from

$$B_\theta = \frac{\mu_0 I}{2\pi r}, \tag{4.1}$$

where $I \approx 500$ kA is the peak implosion-driving current, and $r \approx 3$ mm is the minimum possible plasma radius (i.e., the rod radius).

From Fig. 4.11, the orientation of the striations indicates that the $B_{z0} = 0$ case produced $m = 0$ structure (horizontal striations), while the two $B_{z0} \neq 0$ cases produced $m \geq 1$ structure (diagonal striations). Note that both the front and back sides of the plasma shell are observable to the fast framing camera in regions where the view of the back side is not obstructed by the central rod, indicating that the plasma is optically thin to visible-

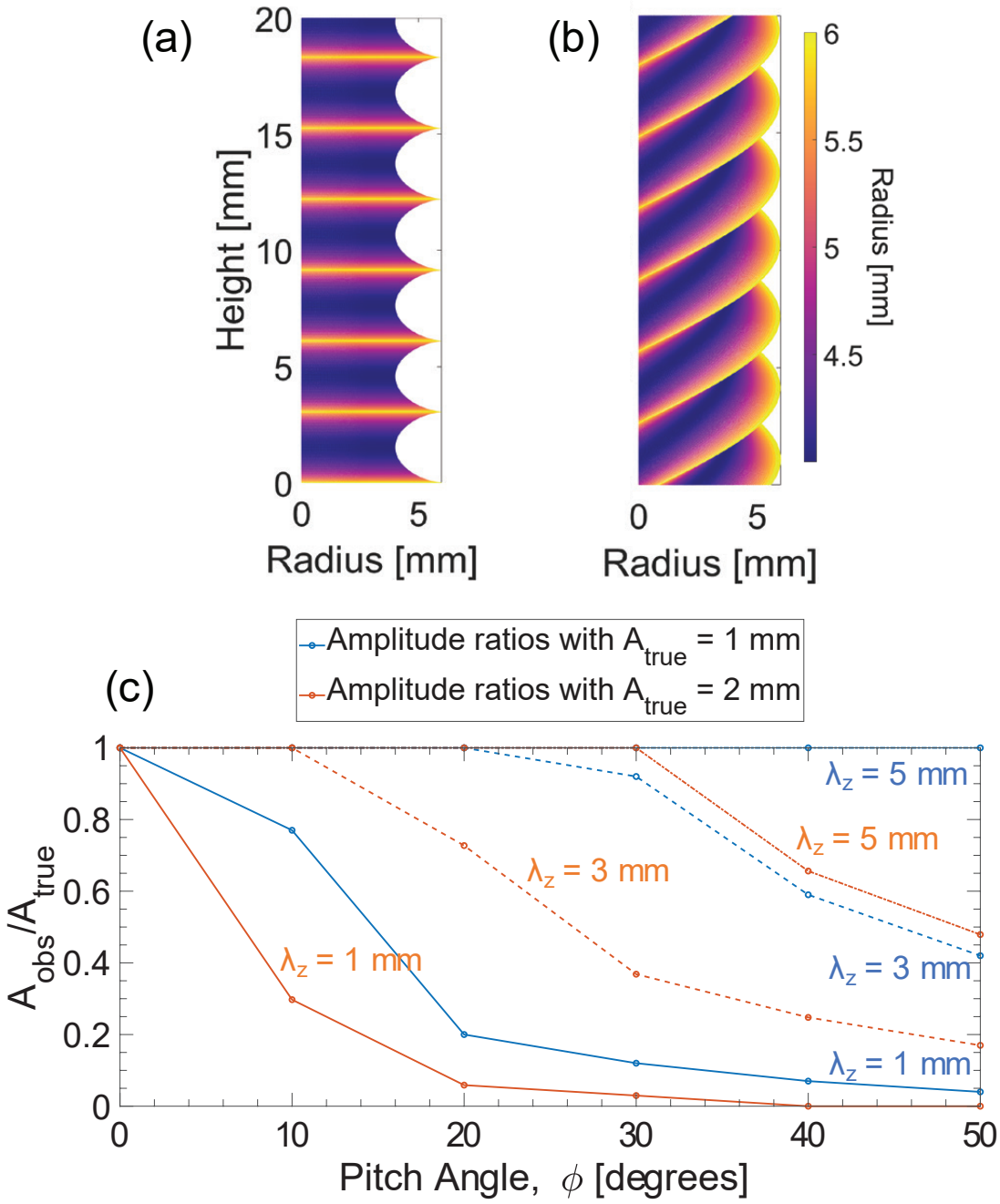


Figure 4.10: Analysis of the obstructed viewing effects that occur when attempting to observe helical instability troughs side-on with non-penetrating imaging diagnostics. (a,b) 2D views of 3D models of single-mode cycloidal perturbations. The pitch angle in (a) is $\phi = 0°$ (i.e., an azimuthally symmetric, $m = 0$ case), while in (b) it is $\phi = 30°$ (i.e., a steep helical case). In both cases, the true bubble-to-spike amplitude is 2 mm and the axial wavelength is 3 mm; however, in the helical case, the observed amplitude trough is not nearly as deep as in the $m = 0$ case, which shows the true depth of the perturbation. (c) The ratio of the observed instability amplitude (A_{obs}) to the true instability amplitude (A_{true}) for various ϕ, A_{true}, and λ_z.

light self-emission. This results in images with diagonal helical striations going in only one direction immediately in front of the rod and in two opposing directions (forming a cross-hatch pattern) in the image regions just to the left or right of the rod. We note that the cross-hatch patterns produced on MAIZE are similar to the cross-hatch patterns produced in penetrating radiography experiments with $B_{z0} \geq 7$ T on the Z facility [14, 15]. From the direction of the striations immediately in front of the rod, the handedness of the helical instability structure can be determined. With $B_{z0} > 0$, the helical instability structure is left-handed relative to the z axis. With $B_{z0} < 0$, the helical instability structure is right-handed relative to the z axis. In both cases, the handedness matches that of the global magnetic field.

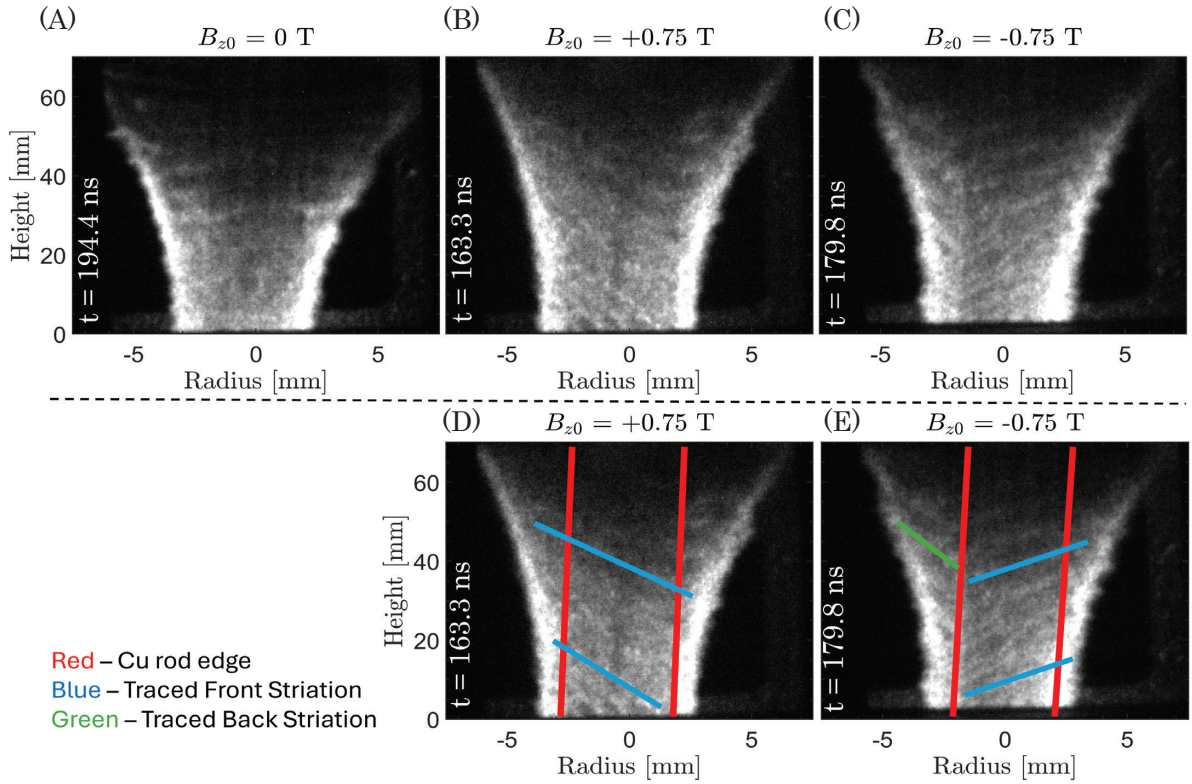


Figure 4.11: Visible-light self-emission images taken as the imploding plasma sheath approaches the central rod for three different cases: (a) $B_{z0} = 0$; (b) $B_{z0} = +0.75$ T (at $z = 10$ mm); and (c) $B_{z0} = -0.75$ T (at $z = 10$ mm). With $B_{z0} > 0$, the helical instability structure is left handed relative to the z axis. With $B_{z0} < 0$, the helical instability structure is right handed relative to the z axis. (d,e) A sample of the striation tracing. Striations traced along the front surface are marked in blue. Striations traced along the back surface are marked in green. The left and right edges of the rod are marked in red.

The helical striations were traced manually to determine the pitch angles presented in Fig. 4.12. In this figure, four different shots are presented. Three of these shots used a

copper rod, while one shot used a dielectric rod. Solid and dashed lines with the same color are from the same shot, but at two different times. The earlier times are from when the plasma near the bottom of the image is at a smaller radius than the plasma near the top of the image (i.e., while the zippering process along the rod is still in progress). The later times are from after the zippering process has completed. These data show how the pitch angles vary as a function of height. They also show how the pitch angles increase as the radii decrease. For example, for the $B_{z0} = -0.75$ T case at $z = 14$ mm and $t = 173$ ns, the measured plasma radius is $r \approx 7$ mm, and the measured pitch angle is around $20^\circ \pm 3^\circ$. By $t = 307$ ns, for this same height of $z = 14$ mm, the plasma has fully collapsed onto the central rod with an outer plasma radius of $r \approx 4$ mm, and the pitch angle has increased to nearly $40^\circ \pm 4^\circ$.

Increasing pitch angles with decreasing plasma radii is consistent with the phenomenon of pitch locking (or conservation of pitch) [14–16]. With this phenomenon, since the pitch is constant, the pitch *angle* must increase to accommodate the decrease in the plasma radius as the sheath implodes. Throughout our imaging data, where the conical plasma sheath is observed, steeper pitch angles are present near the bottom of the imploding sheath, where the plasma radii are smaller [e.g., see Figs. 4.11(b)–4.11(e) and Fig. 4.13]. Thus, as the plasma sheath implodes, the helical striations (which are initially more horizontally oriented) begin to steepen. The steepening persists until the implosion stagnates on the central rod, at which point the steepening ceases, and the pitch angle remains constant. The constant pitch angle post stagnation onto the rod can be seen, for example, via the blue curves in Fig. 4.13(c), for $z = 2$–4 mm, where the bottom of the plasma has already fully stagnated onto the rod prior to the earlier frame time of 173 ns. Thus, comparing the earlier and later frame times, we see that the pitch angle remains relatively constant, measuring $35^\circ \pm 3^\circ$ at $t = 173$ ns, and $34^\circ \pm 4^\circ$ at $t = 307$ ns. The observation of pitch locking raises the important question of when in the current pulse does the pitch become locked in? This remains an open question that could be addressed in the future.

From the post-stagnation (late-time) imaging data, the final pitch angles were larger for larger $|B_{z0}|$. Additionally, we observed larger increases in the final pitch angles over the higher field range of $|B_{z0}| = 0.5$–0.75 T than over the lower field range of $|B_{z0}| = 0.25$–0.5 T. For example, for the data points closest to $z = 10$ mm, the final pitch angles for $|B_{z0}| = 0.25$ T, 0.5 T, and 0.75 T were $23^\circ \pm 4^\circ$, $25^\circ \pm 3^\circ$, and $39^\circ \pm 4^\circ$, respectively.

Because our pre-applied axial field was a fringe field and thus a function of axial position [i.e., $B_{z0} = B_{z0}(z)$], the final pitch angles (i.e., the pitch angles persisting post stagnation onto the central rod) were also a function of z. This is illustrated in Fig. 4.12, where the solid black lines represent the scaling trends expected for the final (late-time) pitch angles

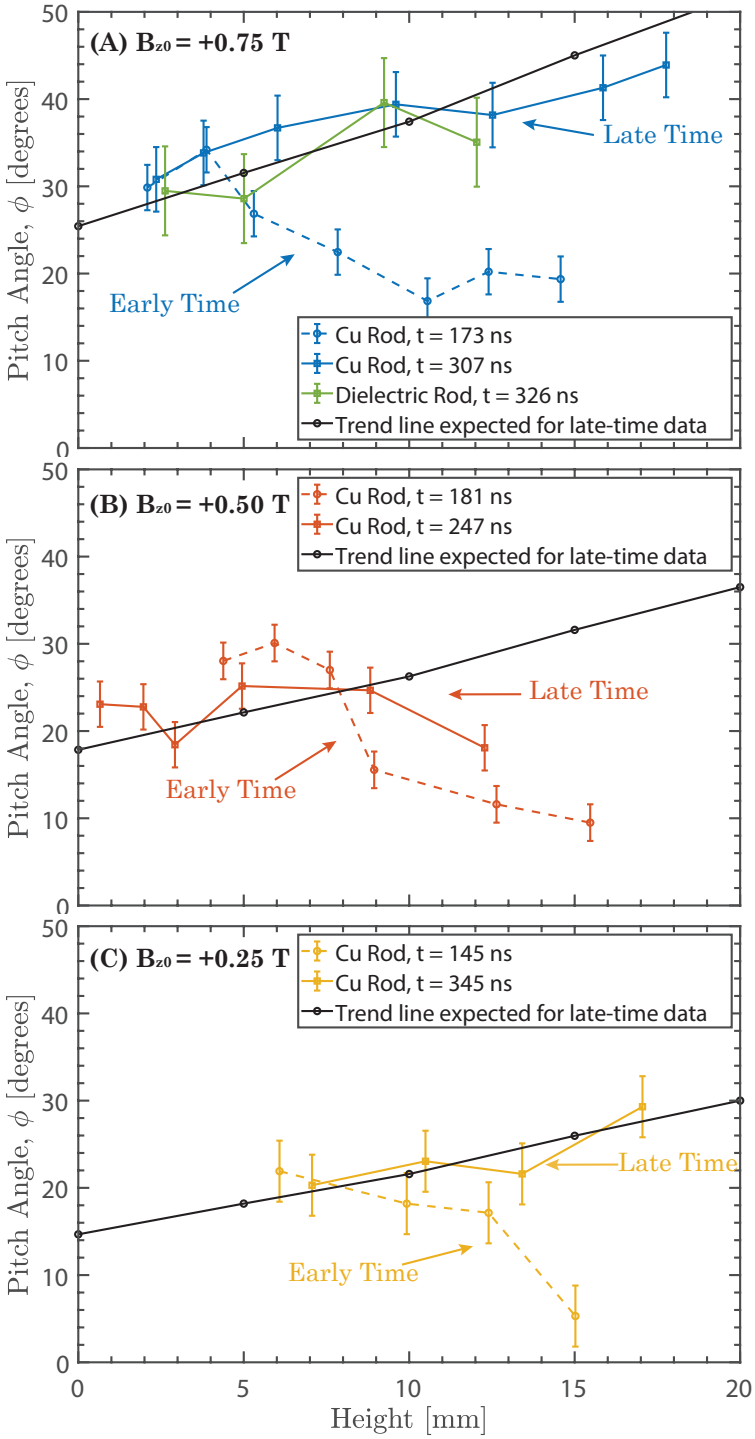


Figure 4.12: Measured helical pitch angles along the height of the plasma at various times during the implosion for the three different applied axial magnetic field strengths tested: (a) $B_{z0} = -0.75$ T, (b) $B_{z0} = -0.5$ T, and (c) $B_{z0} = -0.25$ T. Solid and dashed lines with the same color are from the same shot, but at two different times. The earlier times (dashed lines) are from when the plasma near the bottom of the imploding plasma sheath is at a smaller radius than the plasma near the top of the sheath (i.e., while the zippering process along the rod is still in progress). The later times (solid lines) are from after the zippering process has completed. The green line in (a) represents the case where a dielectric rod was used instead of a copper rod. The black solid lines represent the scaling trends expected for the late-time (final) pitch angles when accounting for the axial variation in B_{z0}. Note that $B_{z0} = B_{z0}(z)$ because the fringe field (i.e., the field below the applied magnetic field coil) was used in these experiments.

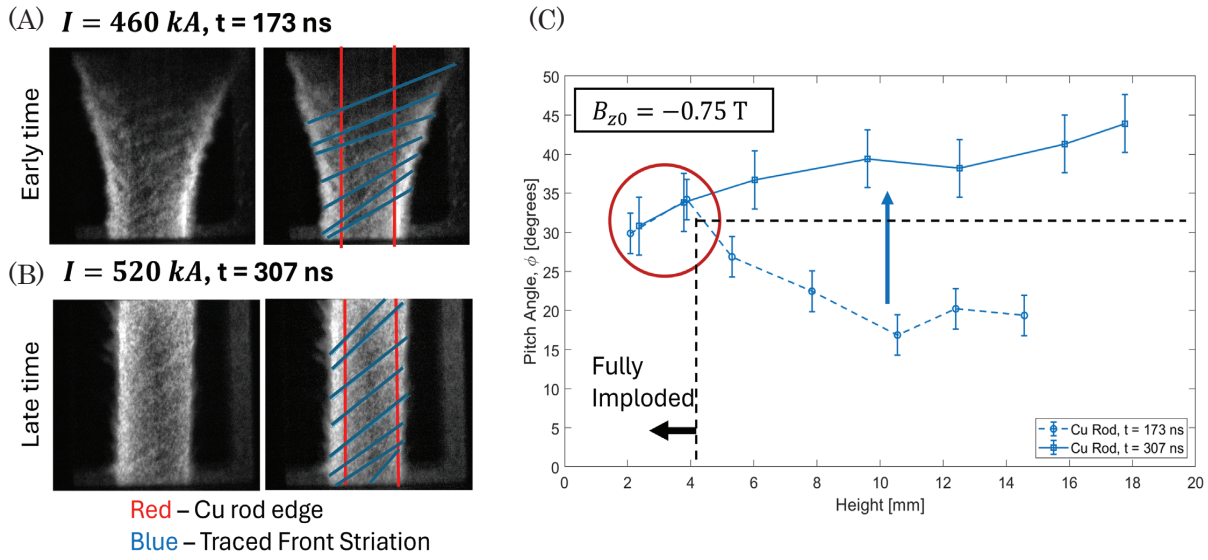


Figure 4.13: Visible-light self-emission images taken as the imploding plasma sheath approaches the central copper rod for an axial magnetization of $B_{z0} = -0.75$ T (at $z = 10$ mm) and at time (a) $t = 173$ ns and (b) $t = 307$ ns. Striations traced along the front surface are marked in blue. The left and right edges of the rod are marked in red. (c) A plot of the traced instability pitch angles as a function of height. The dashed blue line shows the pitch angles earlier in the implosion ($t = 173$ ns), while the solid blue line shows the late time pitch angles ($t = 307$ ns). The dashed black line separates regions of fully imploded plasma from in-flight imploding plasma. Note that the pitch angles within the red circle are constant from the early to late times, since the plasma had already fully imploded by the earlier time of $t = 173$ ns. By contrast, for heights >4 mm, the pitch angles increased from the early to late times, since the plasma was still imploding (zippering). Also note that the final (fully imploded) pitch angles were larger for higher axial positions. This occurred because the initial axial field (B_{z0}) was stronger at higher axial positions. The field was stronger at higher axial positions because the axial field coil resided above the target, and thus it was the coil's fringe fields that were applied to the target.

when accounting for the axial variation in B_{z0}. These trend lines (solid black lines) fit the late-time data (solid colored lines) reasonably well for the $B_{z0} = -0.25$ T and -0.75 T cases, while the agreement is marginal for the $B_{z0} = -0.5$ T case. Note that the early-time experimental data (dashed lines) are not expected to agree with the late-time trend lines (solid black lines) because the early-time data is still in the process of zippering, with an implosion radius that varies with axial position, whereas the late-time trend lines assume that all of the plasma has collapsed onto the rod and thus the plasma radius does not vary with axial position.

Our experiments with a dielectric rod [solid green line in Fig. 4.12(a)] also produced large helical pitch angles, similar to those that formed when using the copper rod. This is interesting because flux compression onto the copper rod should amplify the applied axial field more than in the case of the dielectric rod, since the field can slip through to the axis in the case of the dielectric rod. This may be evidence to suggest that the pitch of these helical structures is locked in and conserved very early in the current pulse, when the magnitudes of B_z and B_θ are similar.

In Fig. 4.14, we present visible-light self-emission images of an argon gas-puff Z-pinch imploding without a center rod, which allows the implosion to stagnate on axis. The images taken prior to stagnation clearly show the steep crosshatch pattern of the helical modes, since the back side of the plasma shell is now fully visible (i.e., it is no longer obstructed by a central rod). An interesting observation here is that vertical filaments appear early in time and persist throughout the implosion (simultaneously with the helical striations), but these vertical filaments only appear in cases where an axial magnetic field is applied (in this case, $B_{z0} = +0.5$ T). Presumably, the bright structures shown in the images represent regions of high current density. One possible explanation for the vertical filamentation may be the axial magnetic field promoting vertical gas breakdown channels to the sharper parts of the metallic anode mesh. These fascinating phenomena and others could be the subjects of future studies.

4.5 Electron Density Measurements

In these experiments, side-on measurements of line-integrated electron density were conducted on the target using the Mach-Zehnder interferometer and a Nikon DSLR camera. Measurements were performed for two primary targets: a gas-puff imploding onto a copper rod and a gas-puff imploding onto a bare axis without a rod. Each configuration was studied with and without an applied axial magnetic field.

Presented in Fig. 4.15 are the interferometric results for gas on a copper rod target with

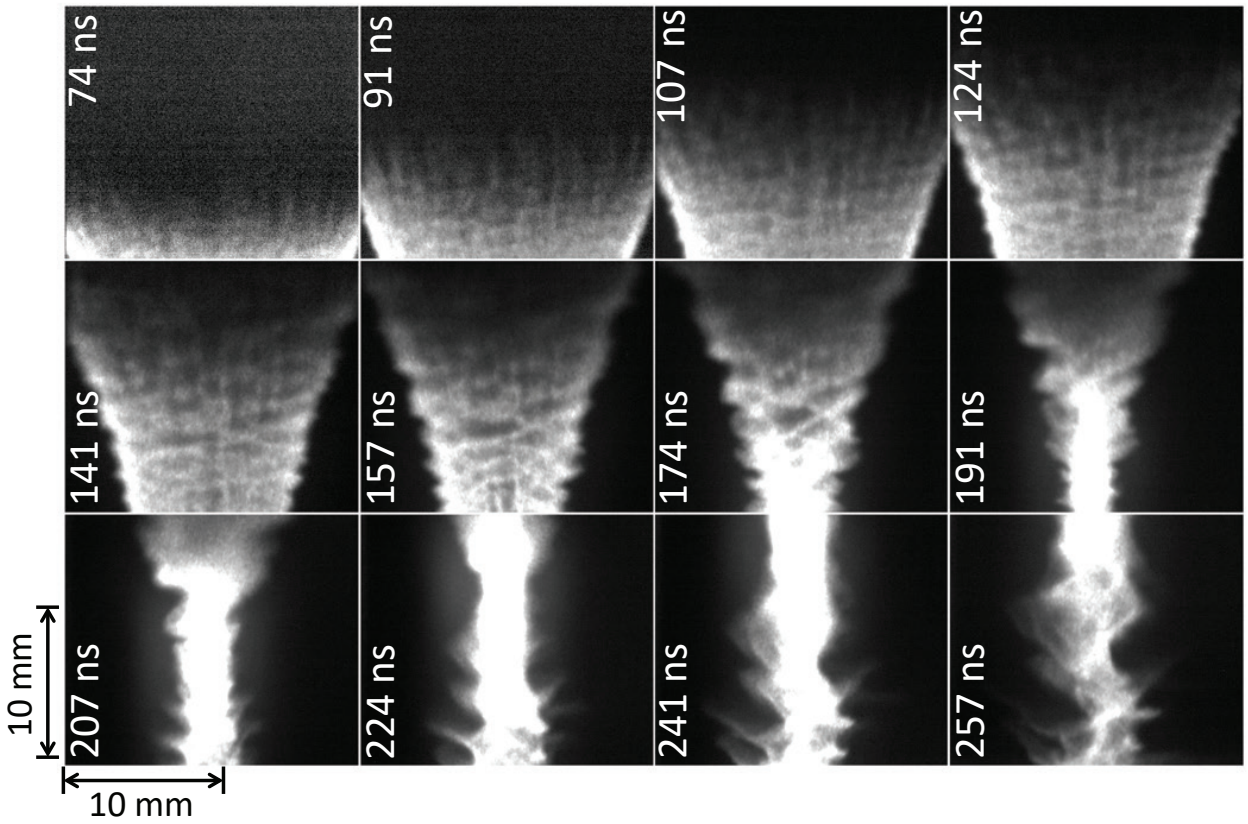


Figure 4.14: Visible-light self-emission images of an argon gas-puff Z-pinch imploding without a central rod. The axial magnetic field value applied was $B_{z0} = +0.5$ T. Note the simultaneous presence of both vertical filaments and helical striations. The vertical filaments are present only in shots with B_{z0} applied.

[Fig. 4.15(a–c)] and without [Fig. 4.15(d–f)] an axial magnetic field ($B_{z0} = -1$ T). The images were taken approximately at the same time ($t \approx 334$ ns), after the gas plasma had impinged onto the central rod. The images in the left column depict the reference interferogram without plasma, whereas the central column presents the interferogram with plasma. The final right column provides the line-integrated electron density, $\langle n_e L \rangle$. The initial radius of the copper rod is marked with a red line.

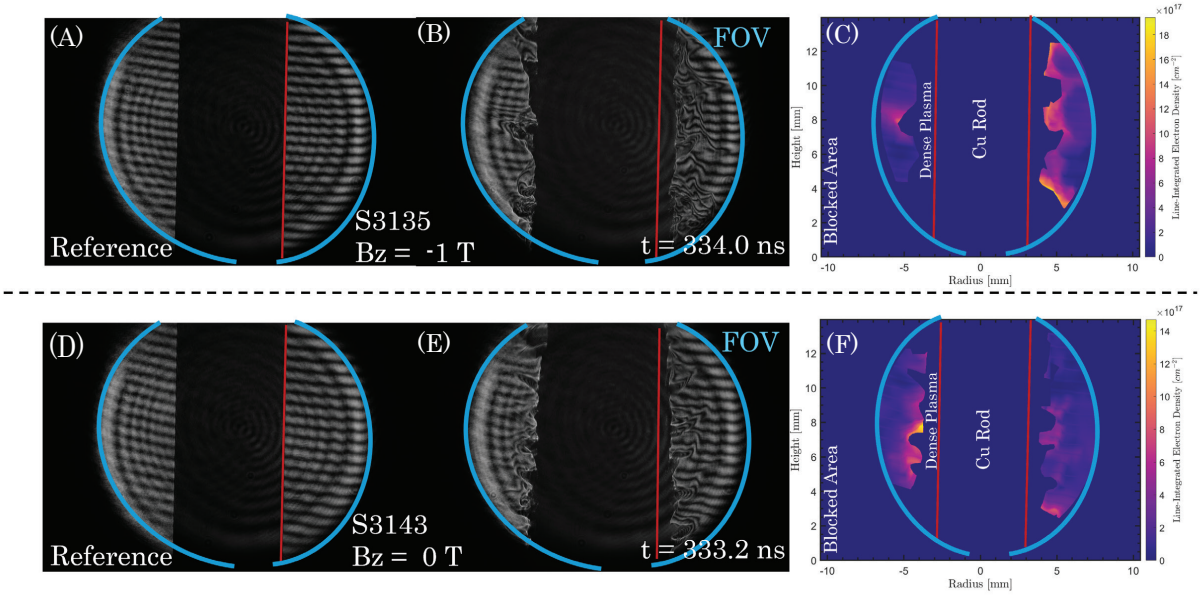


Figure 4.15: Interference images taken of the plasma sheath stagnating onto a central copper rod. **Top Row** (shot 3135, $B_{z0} = -1$ T): (a) Reference interferogram before the shot. (b) Shot interferogram taken at $t = 334.0$ ns. (c) The resulting reconstructed map of the line-integrated electron density. **Bottom Row** (shot 3143, $B_{z0} = 0$ T): (d) Reference interferogram before the shot. (e) Shot interferogram taken at $t = 333.2$ ns. (f) The resulting reconstructed map of the line-integrated electron density. The boundary of the copper rod is indicated with a red line while the field of view (FOV) is marked in blue.

The interferograms were processed as follows. First, the reference and shot interferograms were imported into an image editing software (Photoshop). The regions with a blocked view were covered with a gray mask to ensure that the area was not part of the image processing. Next, the fringes were manually traced using the image editing software. The results of the tracing produce a binarized image of the fringe location which was then imported into the MAGIC2 code. In the code, the fringes are labeled so that the background fringe was matched with the corresponding fringe in the shot image. The labeled fringes were then interpolated to produce a 2D phase map. By subtracting a reference phase map from the

shot phase map, a final phase-difference map was generated. To obtain an absolute phase map, a region of zero-fringe shift must be present in the shot interferogram; this corresponds to an area of zero electron density. If the region of zero fringe shift is not available, the relative fringe shift is measured with respect to the minimum fringe shift. This is known as the"zeroing error", since the true zero is not known. An additional source of uncertainty comes from visually identifying the minima and maxima of the fringes during the manual tracing process. This tracing process is accurate to approximately 1/5 of a fringe separation; thus, the lower detectable limit for this process is $\sim 10^{16}$ cm^{-3}.

Alternative analysis methods were explored, but they proved to be less reliable than manual tracing for this set of images. One alternative method is to use an automated fringe tracker to trace the minima and maxima of the bright and dark fringes, respectively. An automated fringe tracker performs well on the clean reference fringes but struggles to follow the complex fringe distortions created by the plasma. Another method that was attempted was to use a 2D Fourier transform to calculate the phase map. This method requires a significant amount of image filtering to obtain a clean fringe image. A major challenge in this method arises with phase unwrapping after inverse Fourier filtering. This generates disjointed jumps in the phase, which require a complex unwrapping algorithm to correct. Additionally, this method struggles with large density jumps near critical density regions. Nevertheless, this method works well with small phase shifts under 2π.

Observed in the $\langle n_e L \rangle$ map [in Fig. 4.15(c)] is a layer of critically dense plasma $\approx$ 1–1.5 mm thick on the surface of the central rod, surrounded by peripheral plasma $\sim 10^{17}$–10^{18} cm^{-2}. This dense layer corresponds to the opaque black region in the raw interferogram within the field of view (FOV). Notably, there are regions where an underdense plasma exists just outside the dense plasma. However, the fringes produced in this region are too complex to analyze. Only the fringes where we can confidently see a start and an end are measured and traced. Taking radial lineouts of the electron density at heights h = 11 mm, 10 mm, 8 mm, and 7 mm, we find that the peripheral plasma decays from a peak $\langle n_e L \rangle \approx 10$–$12 \times 10^{17}$ cm^{-2} down to 1–2$\times 10^{17}$ cm^{-2}, as shown in Fig. 4.16. At $h = 11$ mm and 8 mm, these correspond to locations with instability finger structures, while $h = 10$ mm and 7 mm correspond to bubble structures. The bubbles measure a larger line-integrated electron density of $\langle n_e L \rangle \approx 10 \times 10^{17}$ cm^{-2}, while the fingers measure $\langle n_e L \rangle \approx 6 \times 10^{17}$ cm^{-2}. The lower peak line-integrated density from the fingers suggests that these structures have a steeper density gradient compared to the broader bubbles. In all cases, the underdense plasma layer was approximately 0.5–1.5 mm thick.

The non-axially magnetized shot in Fig. 4.15(f) shows a similar density profile as the axially magnetized case. Radial lineouts at various heights (h = 6–9 mm) show the peripheral

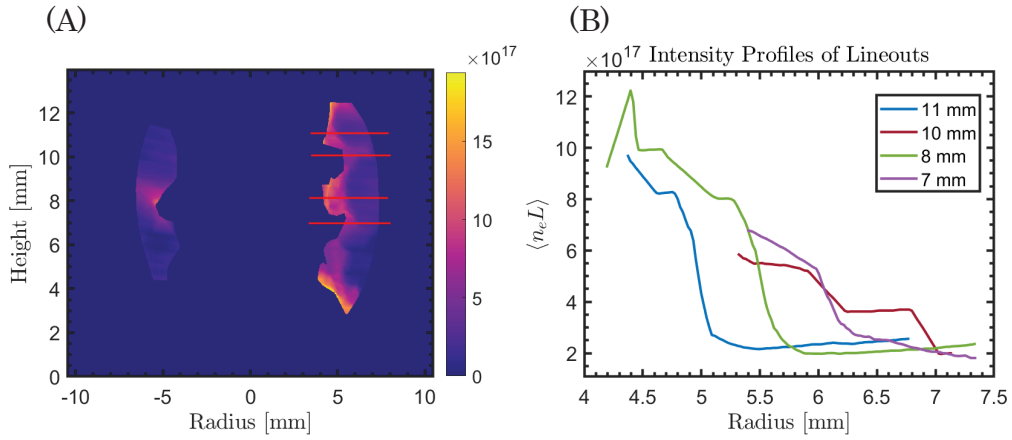


Figure 4.16: (a) Line-integrated electron density map of shot 3135 with $B_{z0} = -1$ T. The red lines denote the regions of the lineouts. (b) The resultant lineouts at various axial locations to illustrate the density of the peripheral plasma.

plasma decaying from a peak line-integrated electron density of $\langle n_e L \rangle \approx 6\text{–}8 \times 10^{17}$ cm^{-2} down to 1×10^{17} cm^{-2}. The underdense plasma near the bubbles and fingers has a similar peak density of $\langle n_e L \rangle \approx 6\text{–}8 \times 10^{17}$ cm^{-2} with a gradient layer of approximately 0.5–1.5 mm thick. A noticeable difference was observed when the raw interferogram of the axially magnetized shot was compared to that of the non-axially magnetized shot. The magnetized shot retained a larger area of observable fringes than the non-axially magnetized shot, suggesting it produced a larger volume of underdense plasma. However, these additional fringe regions in the axially magnetized case were often too complex to analyze quantitatively, even with the manual tracing method.

To characterize the gas shell prior to stagnation, line-integrated electron density measurements were performed without a central rod. This configuration provides a larger, unobstructed view, allowing for a clearer measurement of the pre-stagnation plasma density and perturbation structures. Measuring these initial conditions is important in determining the impact of the gas plasma on seeding instabilities in a liner target.

Presented in Fig. 4.17 are the interferometric results for a gas-puff Z-pinch during the implosion [Fig. 4.17(a-c)] and at stagnation [Fig. 4.17(d-f)]. The images were taken at times $t \approx 139.9$ ns and $t \approx 222.7$ ns during the early implosion and stagnation, respectively. The dark region within the FOV of the shot interferogram is the dense plasma that the laser cannot penetrate. In the surrounding areas close to the dense plasma, the fringe structure, while visible, is too complex to analyze.

In the pre-stagnation data, the imploding gas-puff Z-pinch exhibits an axial gradient in the $\langle n_e L \rangle$, this is shown in Fig. 4.17(a–c). This is a result of the "zippering" effect

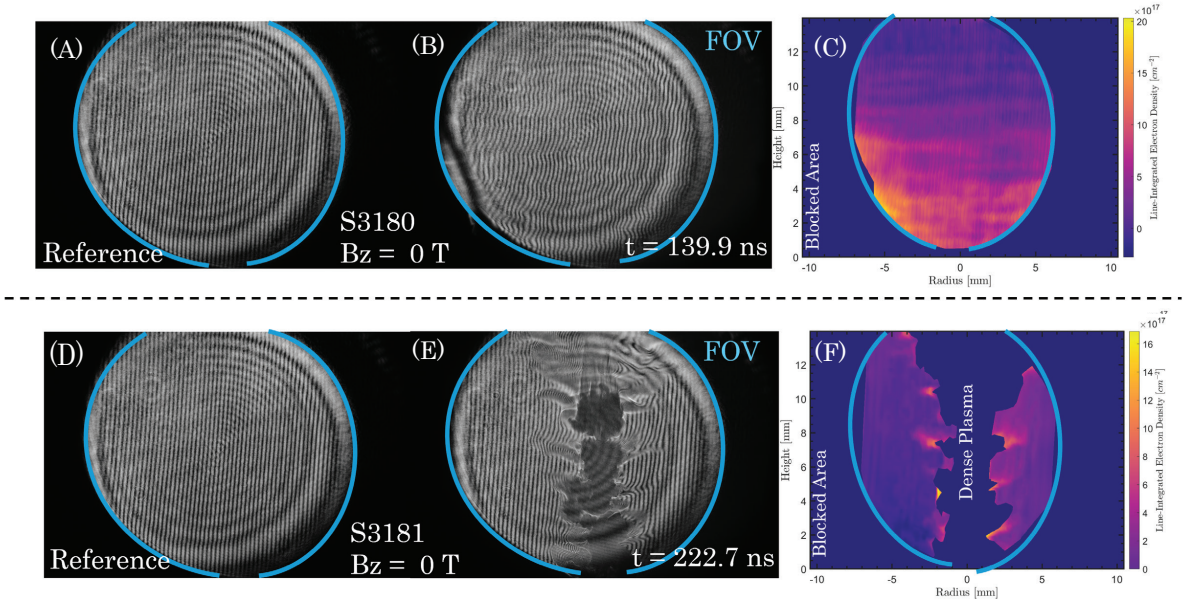


Figure 4.17: Interference images taken of the non-axially magnetized gas-puff plasma at stagnation without a central rod on axis. **Top Row** (shot 3181, $B_{z0} = 0$ T): (a) Reference interferogram before the shot. (b) Shot interferogram taken at $t = 139.9$ ns. (c) The resulting reconstructed map of the line-integrated electron density. **Bottom Row** (shot 3180, $B_{z0} = 0$ T): (d) Reference interferogram before the shot. (e) Shot interferogram taken at $t = 222.7$ ns. (f) The resulting reconstructed map of the line-integrated electron density. The field of view (FOV) is marked in blue.

that is inherent to the gas-puff system, where the bottom of the gas shell implodes before the top. Radial lineouts taken from this at heights of 1 mm, 4 mm, 8 mm, and 12 mm illustrate this density gradient, as shown in Fig. 4.18. At the top of the shell, $h = 12$ mm, the measured line-integrated density is close to zero, though this is subject to a zeroing uncertainty since the phase is measured relative to the minimum shift. Moving down the shell, the density increases to approximately $\langle n_e L \rangle \approx 7 \times 10^{17}$ cm^{-2} for $-2 \leq r \leq 2$ mm. For $r \leq -5$ mm, closest to the edge of the plasma sheath, the density increases to a peak of $\sim 16 \times 10^{17}$ cm^{-2}. In addition to the axial density gradient, the electron density map reveals azimuthally correlated structures that are characteristic of the sausage instability ($m = 0$).

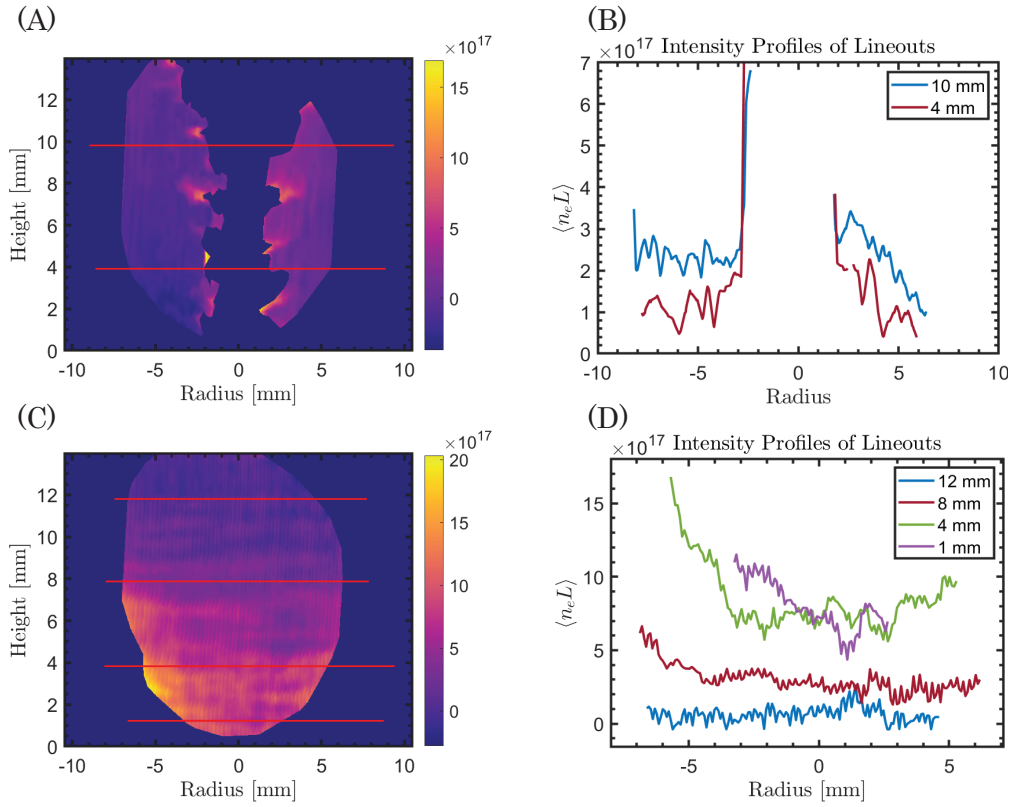


Figure 4.18: (a) Line-integrated electron density map of shot 3181 at stagnation. The red lines denote the lineout regions. The axial field was not applied on this shot ($B_{z0} = 0$ T). (b) The resultant lineouts at various axial locations to illustrate the density of the peripheral plasma. (c) Line-integrated electron density map of shot 3180 during implosion. The red lines denote the lineout regions. The axial field was not applied on this shot ($B_{z0} = 0$ T). (d) The resultant lineouts at various axial locations to illustrate the internal density.

At stagnation, the plasma starts to bend and pinch at various locations, forming blobs of dense plasma with approximately 2 mm radii. Although the laser can probe through regions close to the pinch, the fringe structure becomes unresolvable, preventing quantitative

analysis in this region. However, the surrounding peripheral plasma can still be mapped. Taking radial lineouts shows a peak line-integrated electron density $\langle n_e L \rangle \approx 3 \times 10^{17}$ cm^{-2} at the edge of the dense plasma. This density rapidly decays over a radial distance of about 2 mm, suggesting that most of the plasma is confined within the dense region.

Presented in Fig. 4.19 are the interferometric results for an axially magnetized ($B_{z0} = -0.5$ T) gas-puff Z-pinch during implosion [Fig. 4.19(a-c)] and stagnation [Fig. 4.19(d-f)]. The images were taken at times $t \approx 139.9$ ns and $t \approx 229.1$ ns.

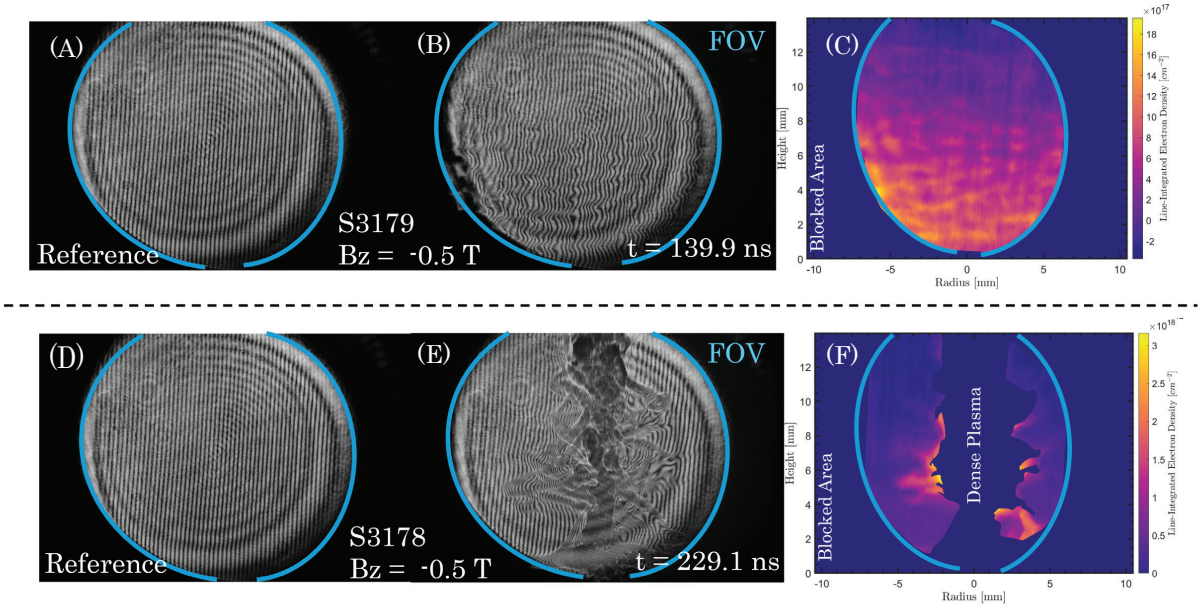


Figure 4.19: Interference images taken of the axially magnetized gas-puff plasma at stagnation without a central rod on axis. **Top Row** (shot 3178, $B_{z0} = -0.5$ T): (a) Reference interferogram before the shot. (b) Shot interferogram taken at $t = 139.9$ ns. (c) The resulting reconstructed map of the line-integrated electron density. **Bottom Row** (shot 3179, $B_{z0} = -0.5$ T): (d) Reference interferogram before the shot. (e) Shot interferogram taken at $t = 229.1$ ns. (f) The resulting reconstructed map of the line-integrated electron density. The field of view (FOV) is marked in blue.

Horizontal lineouts of the electron density reveal a peak line-integrated density of approximately 12×10^{17} cm^{-2} at $r = 0$ mm and $h = 1$ mm, as shown in Fig. 4.20. The edge of the plasma sheath measures a line-integrated electron density of approximately 20×10^{17} cm^{-2} at $r = -6$ mm. The axial density gradient is slightly higher but similar to the unmagnetized shot; this is shown in the lineouts taken at h=1 mm, 4 mm, 8 mm, and 12 mm. A notable feature of the axially magnetized shots is the presence of vertical filaments, as shown in both Fig. 4.14 and 4.19. By comparing the interferometric image with the self-emission images,

we find that the bright emission corresponds to regions of higher line-integrated electron density. As the density increases, so does the self-emission intensity. A question that arises is whether the vertical filaments reside on the surface of the plasma sheath or within the internal volume; this could be a subject for future experiments.

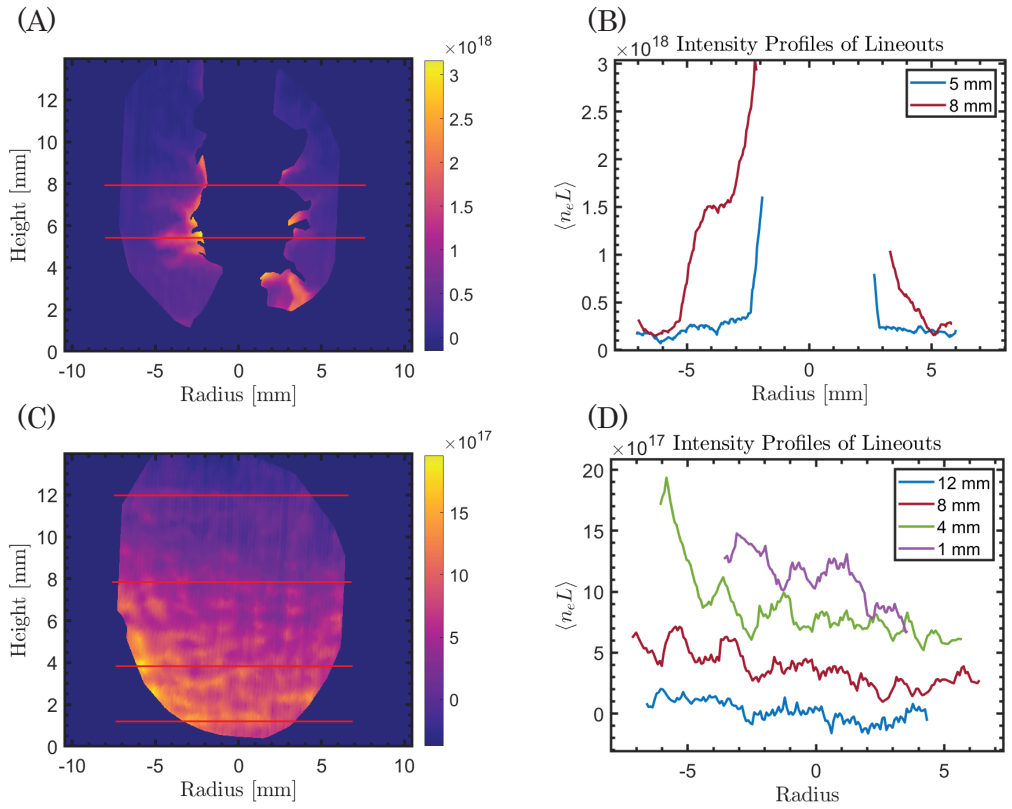


Figure 4.20: (a) Line-integrated electron density map of shot 3178 with $B_{z0} = -0.5$ T at stagnation. The red lines denote the lineout regions. (b) The resultant lineouts at various axial locations to illustrate the density of the peripheral plasma. (c) Line-integrated electron density map of shot 3179 during implosion. The red lines denote the lineout regions. The initial applied axial field was $B_{z0} = -0.5$ T for this shot. (d) The resultant lineouts at various axial locations to illustrate the internal density.

The stagnation structure of the axially magnetized shot is notably different from that of the unmagnetized shot. Instead of forming discrete necks and pinches, the internal structure appears more eruptive and chaotic. The center appears to be less dense than the unmagnetized shot, as the laser is able to penetrate and refract through the cracks and voids in the stagnation column. Furthermore, there is a larger amount of surrounding peripheral plasma. Horizontal lineouts reveal a line-integrated density of $\langle n_e L \rangle \approx 1\text{–}3 \times 10^{18}$ cm^{-2}. The majority of the plasma is confined within a radius of 5 mm.

Fig. 4.21 shows a modified bright field schlieren image of the imploding gas-puff with and

without an axial magnetic field. The schlieren images correspond to the previous interferometric images of the gas-puff Z-pinch. The bright regions shown in these images are areas with strong density gradients. Without the axial magnetic field, shown in Fig. 4.21(a), there are horizontal bands in the schlieren image. For the modified schlieren with a ring and center beam block, the horizontal bands indicate that the density gradient fluctuations are primarily in the axial direction. For the non-axially magnetized shot, the schlieren image reveals that the plasma structure is dominated by gradient fluctuations in the axial direction, which is consistent with a strong contribution from the $m = 0$ mode. By contrast, in the axially magnetized case, shown in Fig. 4.21(b), the structures appear to be more turbulent, with discrete blob-like features. This morphology may be related to the vertical filamentation observed in other diagnostics when an axial magnetic field is applied.

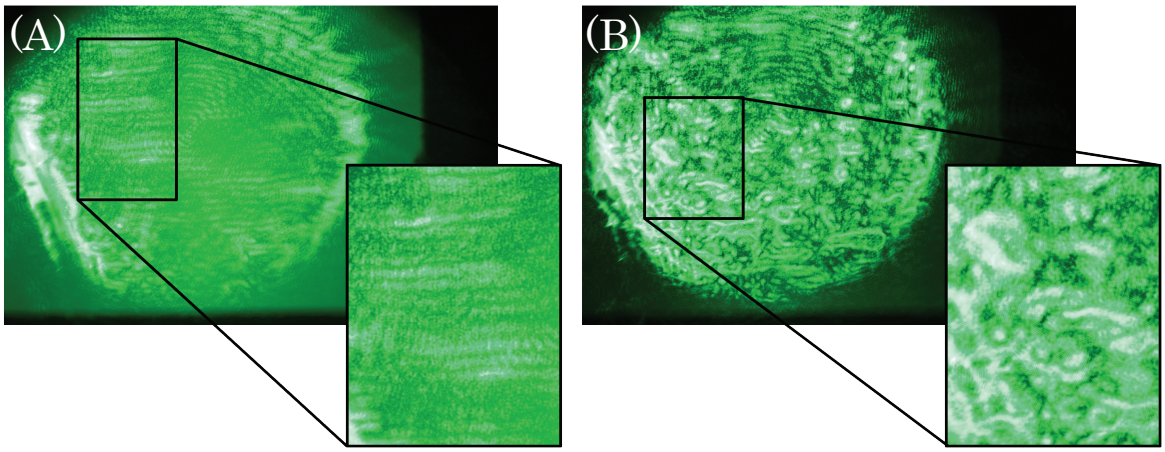


Figure 4.21: Schlieren images of an imploding gas-puff plasma for two cases: (a) without an applied axial magnetic field ($B_{z0} = 0$); and (b) with an applied axial magnetic field ($B_{z0} = -0.5$ T). Note the structural differences inside the plasma medium. For the case with $B_{z0} = 0$, the plasma structure is dominated by horizontal bands, which is consistent with a strong $m = 0$ presence. Conversely, the axially magnetized case shows a more complex structure, with significant density fluctuations in both the axial and radial directions.

4.6 Axial Magnetic Flux Compression

Magnetic flux compression measurements are presented in Fig. 4.22. Here, the initial axial field was $B_{z0} = -0.75$ T at $z = 10$ mm. Additionally, a dielectric rod was used (instead of a metal rod) to house a B-dot probe and enable $B_z(t)$ measurements on axis. At peak compression ($t = 225$ ns), the B-dot probe measured an axial field strength of $B_z(t) =$

-2.6 ± 0.5 T.

The ideal flux compression curve in Fig. 4.22 comes from a model where all of the axial magnetic flux is conserved inside of an imploding thin shell—i.e., the thin shell is assumed to have zero resistivity. The evolution of the axial magnetic field is then calculated using:

$$B_{z,\text{ideal}}(t) = B_{z0}\left[\frac{r_0}{r(t)}\right]^2, \tag{4.2}$$

where $r_0 = 10$ mm is the initial radius of the thin shell, and $r(t)$ is the radius of the thin shell during the implosion. The $r(t)$ values are taken from the visible-light self-emission images at $z = 10$ mm.

From Fig. 4.22, we see that the measured $B_z(t)$ waveform is approximately 50% of the ideal flux compression waveform. The overestimate of the ideal model is at least partially due to the fact that the real plasma shell has finite resistivity. This allows $B_z(t)$ to diffuse through the shell wall and leak out of the compressed plasma regions. Another possible explanation is that plasma could have formed on the outer surface of the dielectric rod, due to either precursor plasma accumulating on the rod or dielectric breakdown occurring over the surface of the rod. Plasma along the surface of the rod could then shield the B-dot probe inside the rod from the compressed axial field outside the rod. (Note that by "precursor plasma", we mean a low-density plasma that fills the region of space between the outer surface of the dielectric rod and the inner surface of the imploding plasma sheath.)

In Fig. 4.22, the dB/dt curve has two observable peaks. The first peak occurs when the imploding plasma shell is still in flight, at a radius of 5.5–9.5 mm. Thus, it is possible that this first peak is due to a shock wave being launched ahead of the imploding plasma sheath into a precursor plasma, where $B_z(t)$ is frozen into this precursor plasma. We note that similar phenomena were observed in Ref. [117]. The second peak occurs at the point where all of the plasma has been compressed onto the rod. We note that just after peak compression, the dB/dt signal hangs on a nearly constant positive value and does not return to zero for a very long time (∼800 ns). This is much longer than the driving current pulse on MAIZE. It is suspected that the probe has thus failed as a result of the implosion compressing the probe on axis and/or a stream of plasma bombarding the signal cable above the anode mesh. Another possible explanation is that the flux in the B-dot probe simply continues to increase due to diffusion of the axial field from the plasma volume into the hollow dielectric rod. This may be possible as the plasma persists beyond $t = 600$ ns. Simulations could help resolve these questions, as could additional dB/dt measurements, preferably with differential B-dot probes instead of single-ended B-dot probes.

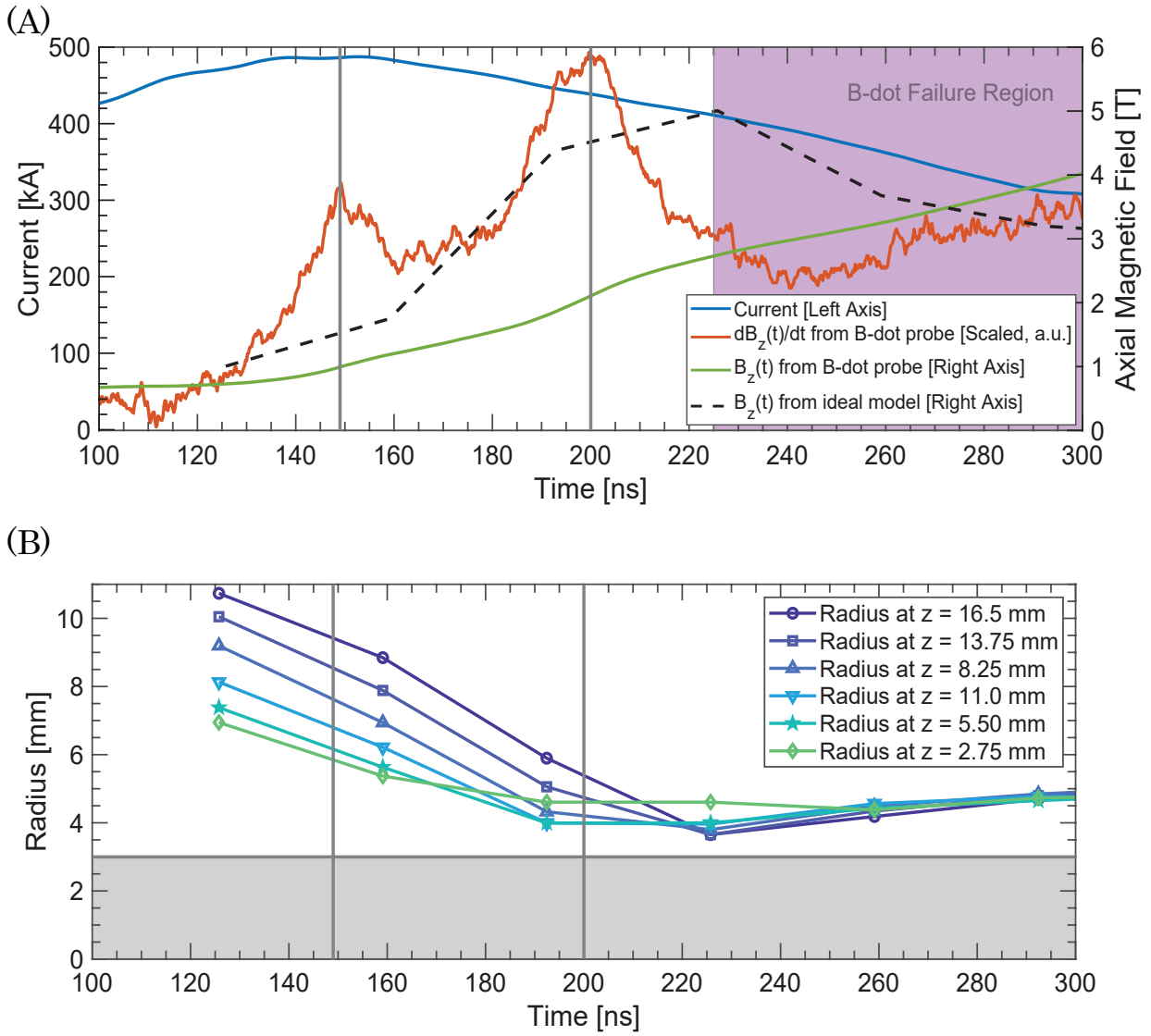


Figure 4.22: (a) Magnetic flux compression measurements on shot 3151. Plotted is the MAIZE drive current (blue); the scaled dB_z/dt waveform measured by the B-dot probe (orange); the measured axial magnetic field, $B_z(t)$ (green); an ideal flux compression waveform (dashed black), calculated using $|B_{z0}| = 0.75$ T and the measured plasma radius, $r(t)$, at $z = 10$ mm; and the probe failure region (purple shading). (b) Plasma trajectories for the same shot at various axial locations. The grey shaded area represents the central rod. In both (a) and (b), the vertical black lines indicate times of peak dB/dt.

4.7 Chapter 4 Summary

The experimental results presented in this chapter have demonstrated a newly developed platform to study instability development and magnetic flux compression in a low-density plasma as the plasma implodes onto a dense cylindrical target. Two configurations were examined, one with a copper central rod and the other with a dielectric central rod, both of which were used in conjunction with an argon gas shell. The trajectory of the imploding plasma shell was characterized for this configuration, and it was found that the plasma fully compressed onto the center rod over a time range of t = 194–260 ns, due to a zippering effect. Even though zippering occurred, the final compression of the plasma was relatively uniform over the surface of the central rod. The results of this characterization will be useful for the next two sections.

Well-defined helical instabilities with large pitch angles were observed when the load region was pre-magnetized with an axial field of $|B_{z0}| = 0.25$–0.75 T (at $z = 10$ mm). The direction of the helices is determined by the polarity of the applied axial field. With $B_{z0} > 0$, the helices are left-handed. With $B_{z0} < 0$, the helices are right-handed. In both cases, the handedness matches that of the global magnetic field. The pitch angles were found to be significantly larger in the $|B_{z0}| = 0.75$ T case than in the $|B_{z0}| \leq 0.5$ T cases. This might indicate a discontinuous jump to a higher azimuthal mode number in the $|B_{z0}| = 0.75$ T case, similar to what has been reported in previous studies [16]. The final pitch angle obtained (after full compression of the plasma onto the central rod) seems to trend with $|B_{z0}|$. The results show evidence of pitch locking early in the current pulse.

Side-on laser probing measurements show that as the plasma implodes onto the central rod, it compresses into a critically dense layer that is approximately 1–1.5 mm thick. This relatively dense layer is surrounded by a low-density peripheral plasma with a density of $\sim 10^{17}$–10^{18} cm^{-2}, which has a gradient scale length of approximately 0.5–1.5 mm. A noticeable difference was observed when comparing the raw interferograms of the axially magnetized shots with the non-axially magnetized shots. The axially magnetized shots retained a larger area of observable fringes, indicating the production of a larger volume of underdense plasma. However, these additional fringe regions in the axially magnetized case were often too complex to analyze quantitatively, even with the application of the manual tracing method. Additionally, the axially magnetized gas-puff shots revealed structures characterized by increased turbulence and discrete, blob-like features, in contrast to the horizontally oriented structures shown in the non-axially magnetized gas-puff. This morphological difference may be related to the vertical filamentation observed in the self-emission images.

Magnetic flux compression measurements, taken on axis using a B-dot probe housed inside

a dielectric central rod, returned two interesting results. The first result is the observation of two peaks in the dB/dt curve, the origins of which are still in question. A potential answer is that the first peak is due to a shock wave being launched ahead of the imploding plasma sheath into a precursor plasma, where $B_z(t)$ is frozen into this precursor plasma. The second peak occurs at the point where all of the plasma has been compressed onto the rod. The second result is that the measured flux compression is about 50% efficient relative to an ideal flux compression model, so about half of the flux (or field) escapes the imploding plasma sheath. However, the ideal model assumes that the imploding plasma is an infinitely thin shell with zero resistivity, when in fact it is a sheath with some finite thickness and finite resistivity. Measurement of the axial magnetic field distribution within the sheath is critical to understanding the amount of flux compression that occurs. In general, numerical simulations and further experimentation will be needed to fully understand the observations reported in this section. These efforts will be the subjects of future studies.

Regarding the various hypotheses for the large helical pitch angles observed in MagLIF liner implosions, it is important to note that the experiments presented herein do not attempt to isolate the flux compression mechanism from the other proposed mechanisms. For example, the Hall interchange instability (HII) could also be present in our system, since both HII and flux compression are expected to occur in the low-density plasmas surrounding the central metal liner [91, 92]. Furthermore, the experiments reported herein focus solely on the evolution of the low-density plasma as it implodes onto the central rod while ignoring the ETI effects that may be occurring in the rod. In the next chapters, the solid central rod will be replaced with an imploding liner made from thin aluminum foil [132]. The goal of this modified platform is to observe the instability coupling (seeding) that results from the low-density gas-puff plasma imploding onto the later-imploding thin-foil liner. Together with advanced 3D Hall-MHD simulations, such experiments might be able to determine which mechanisms are dominant in seeding the subsequent liner implosion instabilities.

CHAPTER 5

Gas on Liner Experiment

5.1 Introduction

The experiments presented in this chapter explore the coupling between a low-density plasma (gas-puff) and an imploding thin-foil aluminum liner. These experiments continue the work on MAIZE without axial magnetization to isolate the hydrodynamic impact of the gas layer on the liner's implosion dynamics. The study was conducted in two parts. First, the baseline behavior of the liner-only targets was characterized. Second, a gas-puff was introduced to create a gas-on-liner (GoL) configuration. Together with the experiments from the previous chapter, this work completes a systematic investigation of the four target configurations: gas-puff only, imploding liner only, gas on a static target, and gas on an imploding target.

The primary motivation for this chapter is to experimentally understand the major instability seeding mechanism onto a liner target. The previous chapter established, using the gas-on-rod (GoR) platform, two key points: (1) a small applied axial magnetic field, relative to the azimuthal magnetic field, produces an observable steep helical instability structure inside the low-density gas-puff; and (2) this plasma shell can compress the axial magnetic field, increasing the axial magnetic field strength on the target. These findings raise two questions about the instability coupling mechanism. First, is the liner instability wavelength seeded by the direct density imprinting, where the instability structure of the impacting gas plasma is dense enough to physically perturb the solid liner? Second, is the liner instability seeded by magnetic imprinting, where the gas plasma compresses the axial magnetic field, increasing the magnetic pitch angle on the liner's surface, which in turn drives the helical instability?

To isolate the first mechanism (density imprinting), the experiments in this chapter were performed using the GoL configuration without an applied axial magnetic field. By removing the axial magnetic field, we can directly observe whether the hydrodynamic impact of the gas plasma is sufficient to seed instabilities. The fast framing camera was the primary diagnostic

used to track the instability wavelengths and target morphology as evidence of this coupling.

This chapter details the implosion of a composite target, studying the instability coupling between the low-density gas layer and a solid density metal liner. Section 5.1 describes the experimental setup and target design. Section 5.2 presents the overall implosion dynamics for liner and GoL targets. Section 5.3 covers the evolution of the instability's dominant wavelength in a liner-only and GoL targets. Additionally, we discuss the instability coupling between the gas and the liner boundary. Section 5.4 quantifies the instability amplitudes and discusses potential stabilization mechanisms. Section 5.5 discusses the current coupling and velocity measurements for these targets. Finally, Section 5.6 summarizes these findings and discusses their implications for understanding instability and implosion dynamics for thin-foil liners and GoL targets.

5.2 Experiment Setup

The experimental setup was a modification of the gas-on-rod (GoR) platform from the previous chapter. The key change was the replacement of the stationary, dense central rod with an imploding thin-foil. An illustration of the experimental setup, a cross section of the target, and the design of the thin-foil liner are shown in Fig. 5.1(a–c). The primary diagnostics for this campaign were the fast framing camera, which was used to image the plasma-liner interface, and the main Rogowski coil used to measure the drive current. Unfortunately, the laser probing diagnostic was not available at this time due to repairs.

5.2.1 Thin-Foil Targets

The targets used in these experiments were constructed in-house and are shown in Fig. 5.1(b,d). Each liner target consists of a thin aluminum foil wrapped around a 3D-printed, dumbbell-shaped dielectric structure.

The liners were fabricated with aluminum foils that had thicknesses of 400 nm, 800 nm, or 1500 nm. Aluminum was chosen for its low mass and high conductivity, which are suitable for implosions on MAIZE, and have been used successfully in previous experiments on similar-scale drivers [16, 17, 117]. These foils were purchased as 160 mm $\times$ 160 mm square sheets from Goodfellow Advanced Materials and cut to a 20 mm $\times$ 15 mm square sheet. The dumbbell structure was 3D-printed on the Formlabs Form 3 printer with the Rigid 10K resin. The material was selected for its high stiffness, which allowed the central support rod to be printed with a radius as small as 0.5 mm while maintaining the structural integrity necessary to support the larger dumbbell heads. Additionally, these structures were able to survive

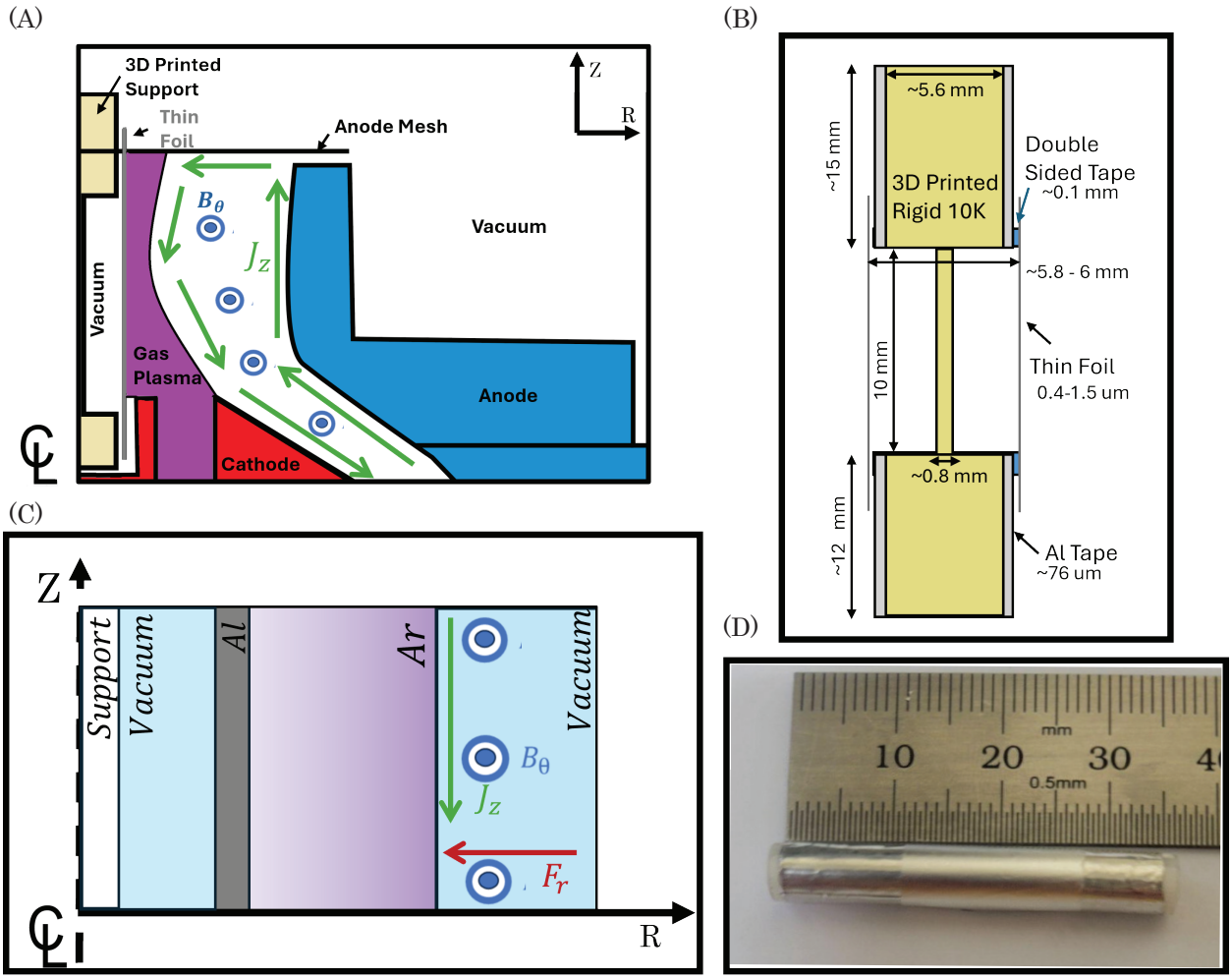


Figure 5.1: (a) Illustration of the experimental load. (b) Technical design of the thin-foil liner targets. (c) Cross-section of the GoL target. (d) Photograph of the constructed liner target with an 800-nm-thick foil.

the fabrication process and the installation of the target into MAIZE. The support rod is necessary because the foil is excessively thin to be self-supported. This requires an inner support rod to reinforce and maintain an upright orientation. The structure was designed with an inner support radius of 0.5 mm and a dumbbell head radius of 2.8–3 mm. Additionally, the support rod had to be dielectric to ensure that the drive current flowed through the aluminum foil rather than through the support. To provide an electrical connection from the anode and cathode, the dielectric heads of the dumbbell were wrapped in conductive aluminum tape. A thin layer of double-sided tape was then applied to the covered dumbbell head, and a piece of aluminum foil was carefully wrapped around it to form a 10-mm-long imploding region. The liner's initial aspect ratio is ∼1000, where the initial aspect ratio is defined as the initial radius of the liner's outer surface divided by the liner's initial shell thickness. Such a high initial aspect ratio makes the liner highly susceptible to MRTI.

These ultrathin-foil liners are electrically thin relative to MAIZE's current pulse. This means that the electrical skin depth is large compared to the shell thickness. The electrical skin depth is described by

$$\delta_{\text{skin}} = \sqrt{\frac{4\eta\tau_r}{\mu_0\pi}}, \tag{5.1}$$

where η is the resistivity of the material, τ_r is the rise time of the current pulse, and μ_0 is the permeability of free space. This is important for liner implosions because this dictates the magnetic pressure distribution on the liner target. In an electrically thick target, the drive current remains on the liner's outer surface, and all the magnetic pressure acts on the liner's outer surface. By contrast, for an electrically thin liner, with a shell thickness $\delta_{\text{wall}} < \delta_{\text{skin}}$, the current and magnetic field quickly diffuse through the liner wall at early times in the current pulse. For a current pulse rise time of $\sim$ 150 ns in MAIZE and an aluminum foil, we have $\delta_{\text{skin}} = 65.5$ µm, which is greater than the thicknesses of the foils used in this study.

For this study, argon was used as the gas species in the puff. The mass density of the gas was varied from approximately 7–14 µg cm^{-3}, linearly corresponding to a plenum pressure of −12 to 0 psig. A series of experiments was then performed to test various combinations of these gas densities with different liner thicknesses.

5.3 Implosion Trajectory

The implosion dynamics and morphology of subsequent instabilities are captured by a 12-frame visible-light self-emission camera, as shown in Fig. 5.2. This shows a collage of self-emission images of liner-only shots, where the foil thicknesses were 400 nm, 800 nm, and

1500 nm. Early in the drive current pulse, the liner is rapidly joule heated, causing it to emit visible-light and expand radially, as shown in the initial frames of Fig. 5.2. The initial emission often appears as a nonuniform speckle pattern. This is likely seeded by the electrothermal instability, which preferentially heats regions of lower resistivity on the inherently perturbed surface of the liner. The bright spots are expected to correspond to hotter regions.

Alongside ablation, current-driven instabilities become prominent on the dense liner surface. This can be seen more clearly at the edge of the liner, where the liner transitions to vacuum in the image, for example, in Fig. 5.2(a) at $t = 177.3$ ns. Since these targets are not axially magnetized, the instabilities are azimuthally correlated, which is characteristic of the $m = 0$ sausage mode. Throughout the implosion, these instabilities are observed to undergo mode mergers, where smaller wavelength instability structures merge into a larger structure in a process known as an "inverse cascade". As instabilities develop, the mass of the liner is redistributed, with mass moving from the bubble regions to the spike regions. Although the fingers of the instability are expected to contain more mass, the bubbles consistently appear brighter in the images. A plausible explanation is that, as the bubble pushes inward towards smaller radii, current density and mass density increase, leading to more intense heating and brighter emission in this region. After peak current, the magnetic pressure begins to decrease, and the thermal pressure of the liner overtakes the residual magnetic pressure, causing the liner to explode radially outward.

At the transition where the thin-foil liner meets the thicker aluminum taped support structure, the foil material is observed to explode radially outward. These regions reside above and below the imploding liner regions and are less emissive compared to the imploding liner region. As a result of the extra thickness, the material starts to expand radially outward in an elongated shape and continues to explode outward throughout the current pulse.

For the heavy liner case (where the foil thickness is 1500 nm), the overall liner is too massive to implode and mainly ablates in place. Interestingly, the instability bubbles on this heavy liner were still observed to move slightly inward, even though the bulk of the liner did not. Additionally, the large wavelength instability seems to have a slower inverse cascading rate, suggesting either a saturation limit or a slowing mechanism for the inverse cascade process. This can be seen in Fig. 5.2(c) at $t = 419$–579 ns. The saturation limit of the inverse cascade is potentially an interesting avenue for future studies.

In contrast to the heavy 1500-nm-thick foils, the 400 nm and 800 nm foils are light enough to be successfully imploded by MAIZE's drive current. Although the initial joule heating and instability seeding are similar to those of the 1500-nm-thick liner, the lighter liners then undergo a rapid acceleration radially inward towards the central support rod. During this

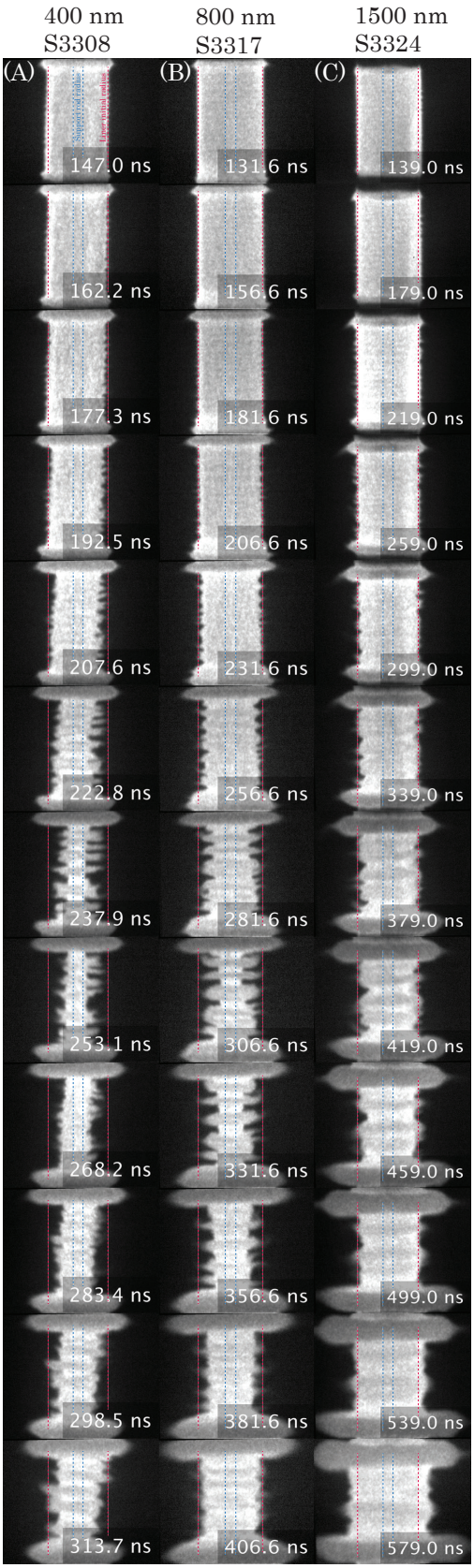


Figure 5.2: Visible-light self-emission images showing the ablation, implosion, stagnation, and explosion phases for three liner thicknesses: (a) 400 nm; (b) 800 nm; and (c) 1500 nm.

phase, the MRTI grows rapidly, developing its characteristic non-linear cusps and finger structure, as shown in Fig. 5.2(a) at $t = 237.9$ ns.

As the implosion progresses, the MRTI bubbles are the first to impact the stationary support structure while the fingers remain at larger radii. Immediately following this, the bubbles begin to explode radially outwards due to their internal thermal pressure while the fingers continue to be driven radially inwards by the magnetic pressure. This creates an inversion of the instability structure, where the initial imploding bubbles explode outward as instability fingers. This happens vice versa for the imploding fingers that turn into exploding bubbles.

In the final phase, during the explosion, the target interface should be stable to MRTI growth; however, since the current is still flowing, it is subject to the continuing development of current-driven instabilities such as $m = 0$ and $m = 1$ instabilities. The target is then eviscerated afterward.

Self-emission images of the GoL configuration reveal a vastly different implosion dynamic, as shown in Fig. 5.3. This figure shows a collage of self-emission images for a 400-nm-thick liner with various gas pressures, illustrating the differences in behavior as the gas pressure increases while the liner mass remains constant. The initial gas shell implosion "zippers" from the cathode to the anode; this process takes $\sim$ 25 ns to fully cover the imploding region of the liner. Upon colliding with the liner, it produces a bright flash of emission, likely due to the transfer of current to the aluminum foil and the rapid joule heating of the foil. A notable effect of this collision is that the pre-existing instability structure in the gas appears to be "reset" (i.e., the amplitude of the instability in the gas is disrupted where the bubbles are unable to progress further due to the presence of the dense liner, allowing the fingers to catch up). This temporarily flattens the gas plasma against the dense liner, thus decreasing the amplitude of the instability. The liner does not move immediately upon contact with the gas plasma; this can be seen in Fig. 5.3(b) at $t = 136.8$–170.1 ns, where the gas has already impinged on the liner, but the liner remains stationary. The liner begins its implosion approximately 50–70 ns after the initial gas impact.

A feature that occasionally occurs in these GoL implosions is an upward axial velocity of the instability structures, as seen in Fig. 5.4. This was also observed in the GoR experiments; however, a key difference is that in the GoL experiments, the liner and gas instability structures both move upward. The measured axial velocity from the self-emission images is $v_z \approx 5$ km/s, while the radial implosion velocity measures $v_{\text{imp}} = 10$–25 km/s. Two potential mechanisms could explain this observation. First, as the zippering gas plasma front collides with the liner at an angle, the compressed material may be pushed axially upward into the less dense, uncompressed region above it. Another plausible explanation is that the

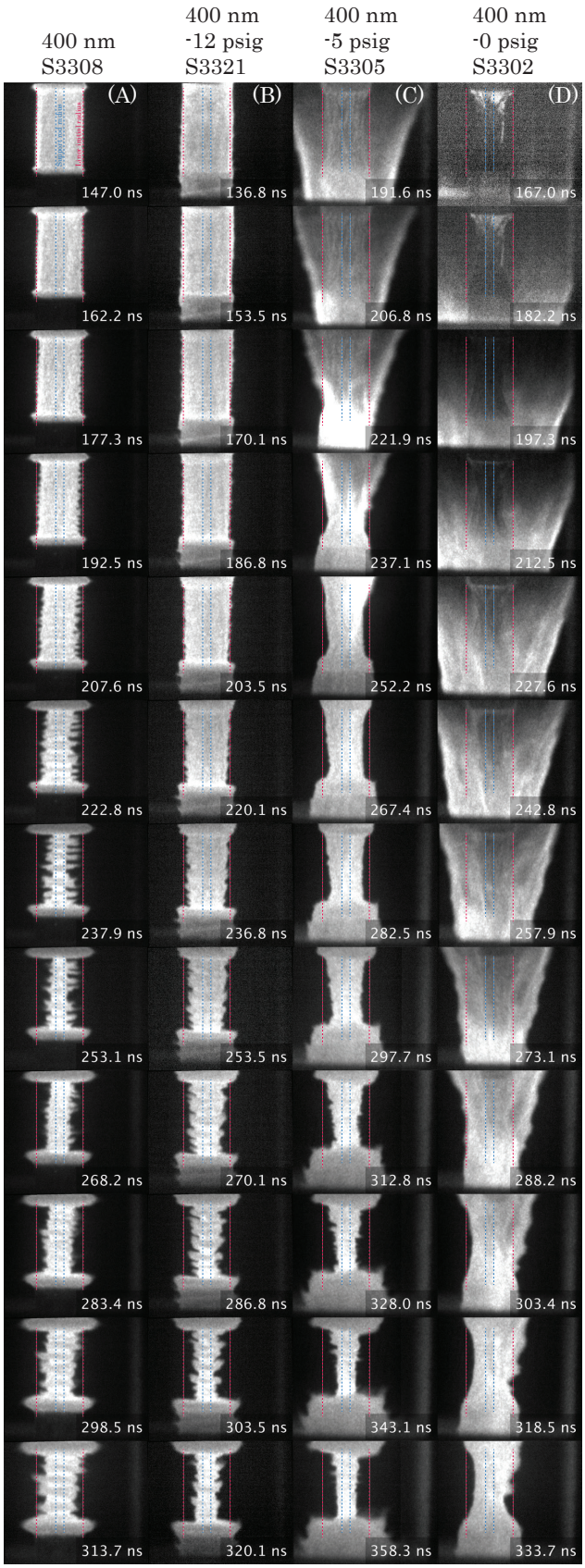


Figure 5.3: Visible-light self-emission images showing the ablation, implosion, stagnation, and explosion phases for GoL configuration using a 400-nm-thick liner at various gas pressures. The panels show: (a) no gas; (b) -12 psig; (c) -5 psig; and (d) 0 psig.

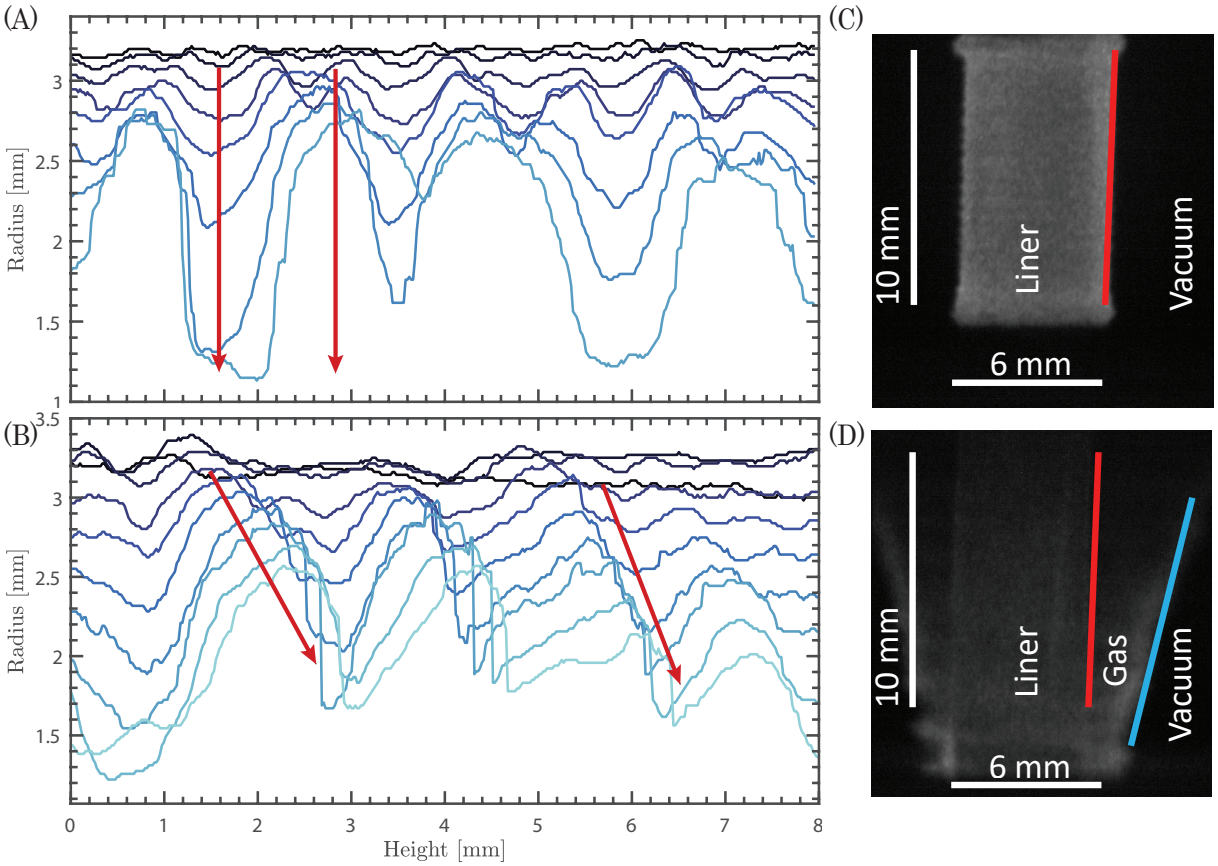


Figure 5.4: Plots of the tracked liner boundaries as a function of height for (a) liner-only targets and (b) GoL targets. The black-blue color gradient indicates increasing time during the implosion up to the time of stagnation. The red arrows highlight regions of the instability structures. Note the significant axial shift in instability structure when gas is applied compared to the liner-only targets. Visible-light self-emission image of the (c) liner-only and (d) GoL targets. The red and blue lines indicate the initial position of the liner and gas plasma, respectively.

axial drift is due to $\mathbf{E} \times \mathbf{B}$ drift, as the target plasma could be influenced by a strong radial electric field and a strong azimuthal magnetic field [133], [134, pp. 31–38]. The axial $\mathbf{E} \times \mathbf{B}$ drift results in a sheared flow—i.e., $V_z(r)$ increases with radial distance away from the liner's outer surface. This shear causes the instability fingers to drift axially upward and eventually roll over (like breaking waves).

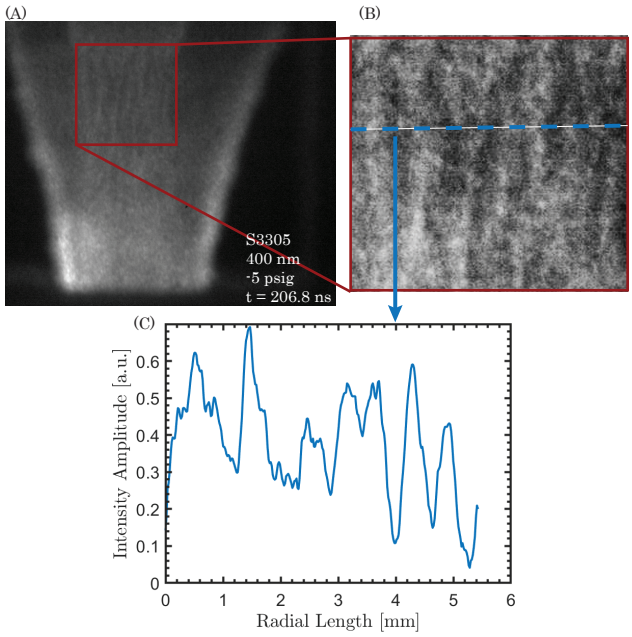


Figure 5.5: (a) Visible-light self-emission image of shot 3305 with a liner thickness of 400 nm and gas pressure of -5 psig at $t = 206.8$ ns. (b) A magnified and contrast enhanced view showing vertical filaments on the liner surface attributed to pressure buckling from the gas. (c) A plot of an intensity line-out from the self-emission images showing the perturbation structure of the buckling.

At higher initial injected gas pressures ($P_{0,\mathrm{gp}} > -5$ psig), the thin-foil liner is observed to buckle and bow radially inward prior to MAIZE firing. This occurs because the gas is injected $\sim$500 µs prior to MAIZE discharging, allowing the static gas pressure to slowly displace the light foil, as seen in Fig. 5.3(c,d). To test this hypothesis, a simple 1D equation of motion was solved for a 400-nm-thick liner at 0 psig of gas pressure over a time period of 150 µs. The setup consists of a liner interface with a set mass. On one side of the interface, there is vacuum pressure, and on the other side, there is gas pressure. This finds a radially inward displacement of ~ 0.7 mm, which is comparable to the experimentally observed displacement of ~ 1 mm, confirming the mechanism. This displacement becomes negligible for lower gas pressure ($P_{0,\mathrm{gp}} < -8$ psig) or thicker liners ($\delta_{\mathrm{wall}} > 400$ nm at a radius of 3 mm).

In addition to bowing and displacement, vertical filaments form on the surface of the liner, as shown in Fig. 5.5(a,b). This is suspected to be pressure buckling as a consequence

of the displacement. Intensity lineouts of the self-emission image show that the filaments emit brighter than the surrounding liner and have a characteristic wavelength of 0.5–1 mm, as shown in Fig. 5.5(c).

As shown in Fig. 5.6, a collage of self-emission images for liners with foil thicknesses of 400 nm, 800 nm, and 1500 nm displays the differences in behavior as the liner mass increases while the gas pressure remains constant (-12 psig). Note the difference in the instability morphology and implosion trajectory between the liner-only and GoL shots.

Liner boundaries were tracked from the self-emission images using the following process. Each raw image was converted to a double-precision grayscale format and rotated vertically. To clearly define the edge of the liner, the contrast of each frame was individually enhanced. The horizontal pixel-to-length scale was determined using the first visible image of the liner, which had a known initial radius of 3 mm. The vertical pixel-to-length scale was determined based on the known length of the imploding region, with an estimated uncertainty of ± 0.3 mm. This is due to the plasma expanding into the imploding region, from the upper and lower ends of the imploding region, where the liner is wrapped onto the underlying support structure. The enhanced images were converted to a binary image, where one represented the bright emissions and zero represented the dark regions. The zero to one transition of the image was calculated, and the position value of this transition point was taken as the boundary of the liner. Any outliers were replaced with the nearest mean if needed, and the final boundary was trimmed to include only the active imploding region.

The implosion trajectory varies significantly with the thickness of the liner, as shown in Fig. 5.7(a). This figure shows data for the 400 nm, 800 nm, and 1500 nm liner-only shots and a 400 nm GoL shot. The mean radius and the region between the instability structures were taken from the liner boundary and are denoted by a dashed line and a transparent shaded region, respectively. The uncertainty of the radius is taken as the distance between the finger and the bubble of the instability.

Initially, all liners expand radially outward from joule heating, with the thicker 1500 nm and 800 nm liner targets expanding more (radii of 3.3 mm and 3.1 mm, respectively) compared to the thinner liners. The expansion could be larger, as the images were taken starting at approximately $t = 140$ ns during the rise of the current pulse and the start of the implosion. As the magnetic pressure overtakes the initial expansion, the liner starts to accelerate radially inward. The 1500-nm-thick liner was too massive to fully implode, reaching a minimum radius of only ~ 2.9 mm before exploding back outward. by contrast, the 400 nm and 800 nm thick foils implode much further, reaching minimum radii of 2.1 mm and 1.5 mm, respectively.

A noticeable feature is that none of the liners imploded all the way to the 0.5 mm radius

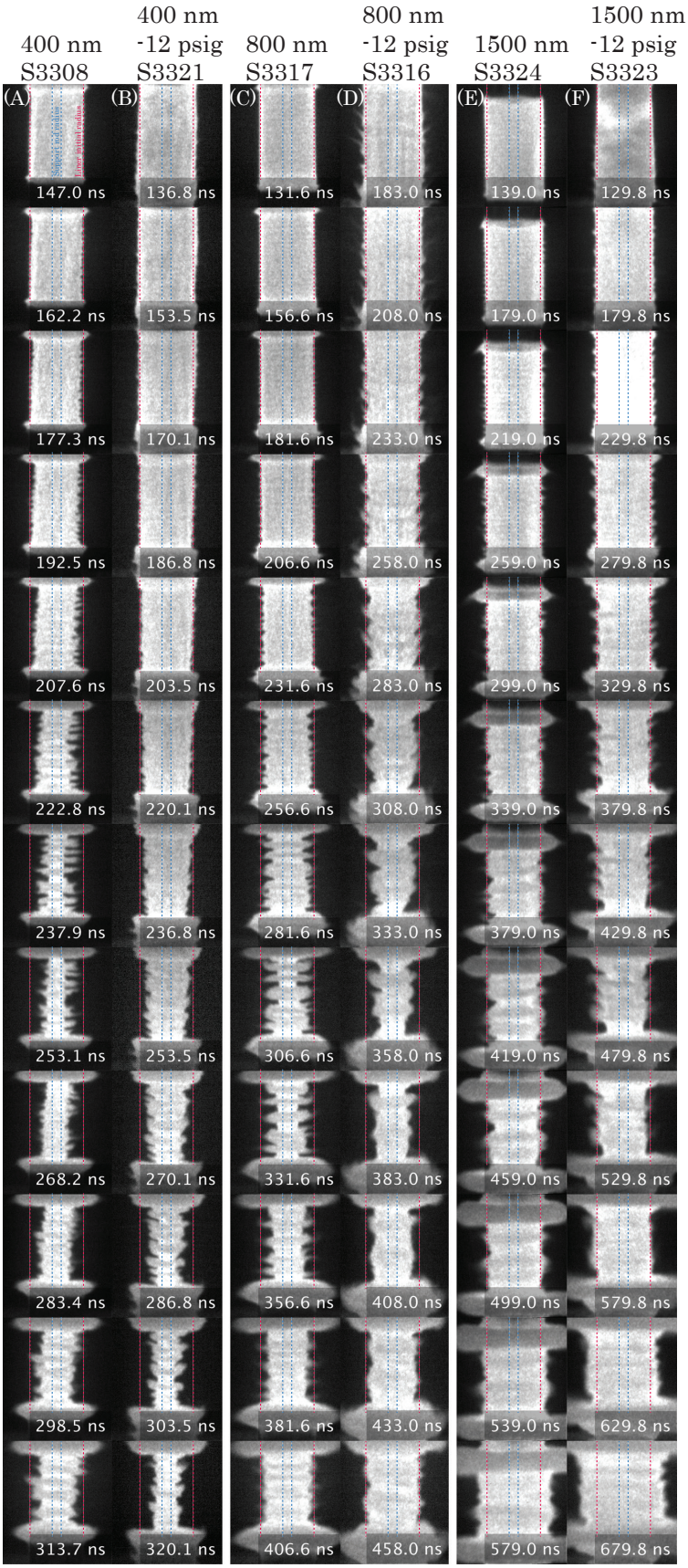


Figure 5.6: Visible-light self-emission images showing various GoL configurations. The panels show: (a) 400 nm without gas; (b) 400 nm with gas; (c) 800 nm without gas; (d) 800 nm with gas; (e) 1500 nm without gas; and (f) 1500 nm with gas. Note the impact to the instability structure and implosion dynamics with and without gas.

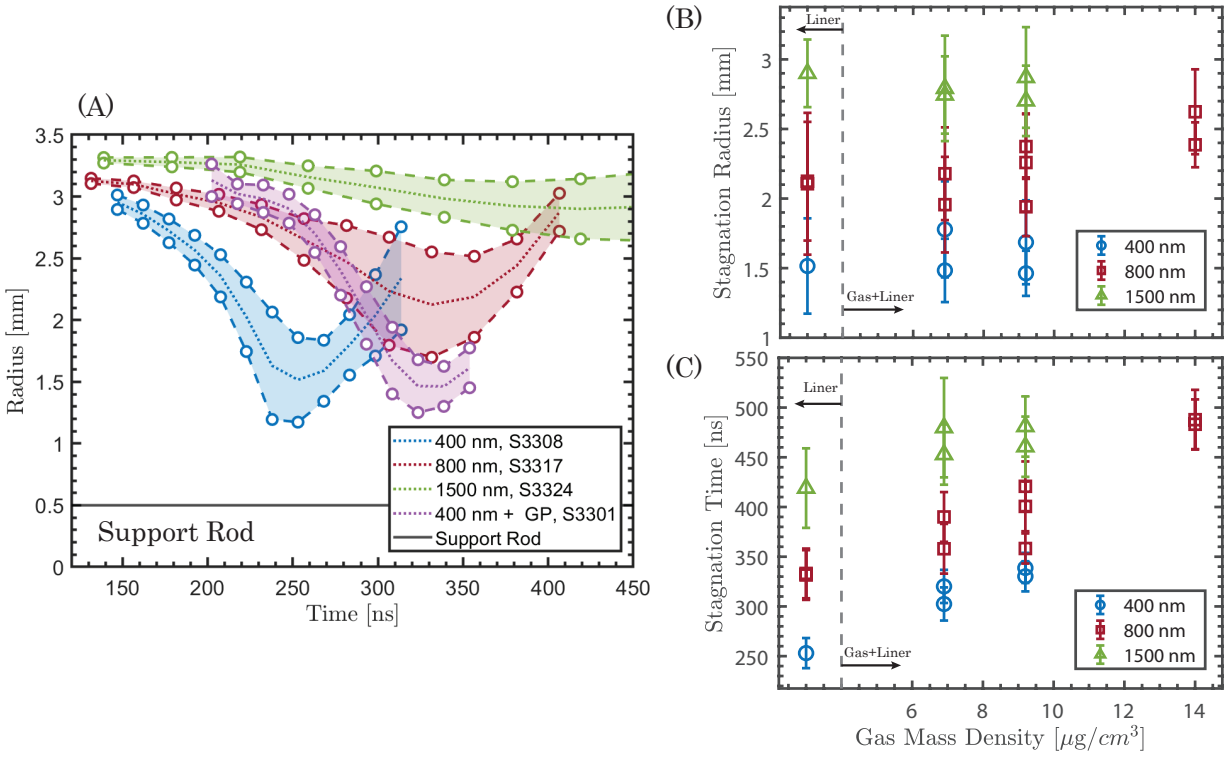


Figure 5.7: (a) A plot of the implosion trajectories for liner thicknesses of 400 nm (blue), 800 nm (red), 1500 nm (green), and a 400 nm GoL configuration (purple). The support rod radius is indicated by the solid black line. (b) A plot of the stagnation radius as a function of gas pressures. (c) A plot of the stagnation time as a function of gas pressures. Liner thicknesses of 400 nm, 800 nm, and 1500 nm are represented by the blue circle, red square, and green triangle markers, respectively. The grey dashed line separates the liner-only targets (left) from the GoL targets (right).

of the support rod. A plausible explanation is that, as the liner is joule heated and expanded, the magnetic pressure is distributed through the expanded liner material. Since the thin-foil liner is initially thinner than the electrical skin depth (δ_{skin}), its inner surface could be accelerated ahead of the bulk material and stagnate on the rod first. This early impact would create a high pressure plasma "cushion", which then stops the rest of the incoming liner at a larger radius. This was shown to be possible in previous studies, where the inner surface plasma was estimated experimentally in thin-foil implosions [117] and simulated with extended MHD [133].

Adding a gas layer to the target modifies the trajectory of the implosion, as shown by the purple trace (shot 3301) in Fig. 5.7(a). Initially, the gas collides with the liner, causing a momentary outward bounce of the gas plasma, on the order of 0.2 mm in radius. The combined gas-liner target then implodes to a minimum radius similar to that of the liner-only case. Additionally, the presence of the gas layer reduces the instability amplitude, as indicated by the smaller transparent region in Fig. 5.7(a). The GoL target stagnates approximately 80 ns later than the liner-only target. This delay means that the stagnation occurs well after peak current, during a phase when the magnetic drive pressure is decreasing.

In Fig. 5.7(b), the stagnation radius is plotted as a function of the mass of the gas injected. For the baseline cases with liner-only targets, the minimum stagnation mean radius is 1.5 ± 0.3 mm, 2.1 ± 0.5 mm, and 2.9 ± 0.3 mm for liners with foil thicknesses of 400 nm, 800 nm, and 1500 nm, respectively. Counterintuitively, adding a small amount of gas (≤ 9 µg cm^{-3}) did not necessarily increase the stagnation radius. In several cases, the GoL targets stagnated at a comparable or even slightly smaller radius. For example, an 800 nm liner-only shot stagnated at 2.1 ± 0.5 mm compared to a shot with an 800 nm liner and 7 µg cm^{-3} of gas that stagnated at 1.9 ± 0.3 mm. The mass of the gas shell, assuming a uniform distribution, is estimated to be approximately $3.7\text{–}7.4 \times 10^{-7}$ kg while the mass of a 400 nm thick liner is approximately 2×10^{-6} kg. As the gas mass increased further, the stagnation radius began to increase as expected. This can be seen in Fig. 5.7(b), as the right side of the dashed line indicates GoL shots at various pressures. A potential explanation for these results could be that the gas layer is suppressing large instability fingers, resulting in a smaller calculated mean radius. Additionally, the imploding gas delivers additional ram pressure to the liner, which may aid in compression, thus resulting in a smaller stagnation radius. Furthermore, buckling of the liner could initially displace the liner slightly inwards, which may be enough to produce a smaller stagnation radius.

The stagnation time of these targets increases with both the liner mass and the gas pressure, as shown in Fig. 5.7(c). For the baseline cases with liner-only target, the stagnation time is 253 ± 15 ns, 333 ± 25 ns, and 419 ± 40 ns for liners with foil thicknesses of 400 nm,

800 nm, and 1500 nm, respectively. Adding a gas layer further delayed the implosion. A gas mass of 7 µg cm^{-3} increased the stagnation time by approximately 50 ns compared to liner-only targets. This delay is attributed to the time required to ionize and compress the gas onto the liner prior to the liner implosion. Increasing the injected gas pressure increases the time of stagnation, as expected. The stagnation time was observed to increase linearly with the initial gas pressure. It is important to note that since the MAIZE quarter period is $\approx$ 200 ns, these later stagnation times occur well after the peak current, when the magnetic drive pressure is decreasing.

5.4 Instability Coupling

The time evolution of the instability structures, as shown in Fig. 5.8, reveals key differences between the liner-only and the GoL targets. The initial instability wavelength is likely set early in the current pulse by a combination of innate surface perturbations and electrothermal instability. As the liner accelerates inward, these seed perturbations grow via the MRTI.

A characteristic feature of the instability evolution is the inverse cascade process, also known as mode merging, where the dominant instability wavelength shifts to larger values over time. This can be seen in Fig. 5.8(a), where the red arrows denote the positions of the instability fingers and the green arrows denote the instability bubbles. In general, for a liner-only target, the instability bubble will remain a bubble in the same axial location unless a mode merger event occurs. The two neighboring instability fingers merge and absorb the instability bubble between them, forming a single larger finger structure.

The underlying physics of this mode merging is an active area of research. One hypothesis is that a magnetic pressure differential on either side of an instability finger pushes adjacent fingers together. Another explanation lies in the transition from linear to non-linear growth. In the linear regime, the growth rate of the MRTI is exponential and favors small wavelengths ($\gamma \propto \sqrt{1/\lambda}$), where γ is the growth rate and λ is the wavelength of the perturbation. As these small wavelength modes first transition to non-linear growth (algebraic growth), their growth slows, allowing larger wavelength modes, which are still growing exponentially, to overtake them and become dominant.

The evolution of instabilities in the GoL target is more complex, as shown in Fig. 5.8(b). After the initial gas instability is "reset" upon impact with the liner, a new, smaller wavelength instability appears to develop within the combined structure. A central challenge is determining where this new instability resides: on the outer gas-vacuum interface or on the inner gas-liner interface. Several scenarios could explain these observations. First, in the gas-dominated growth, the emission is solely from the gas plasma. The initial instability in

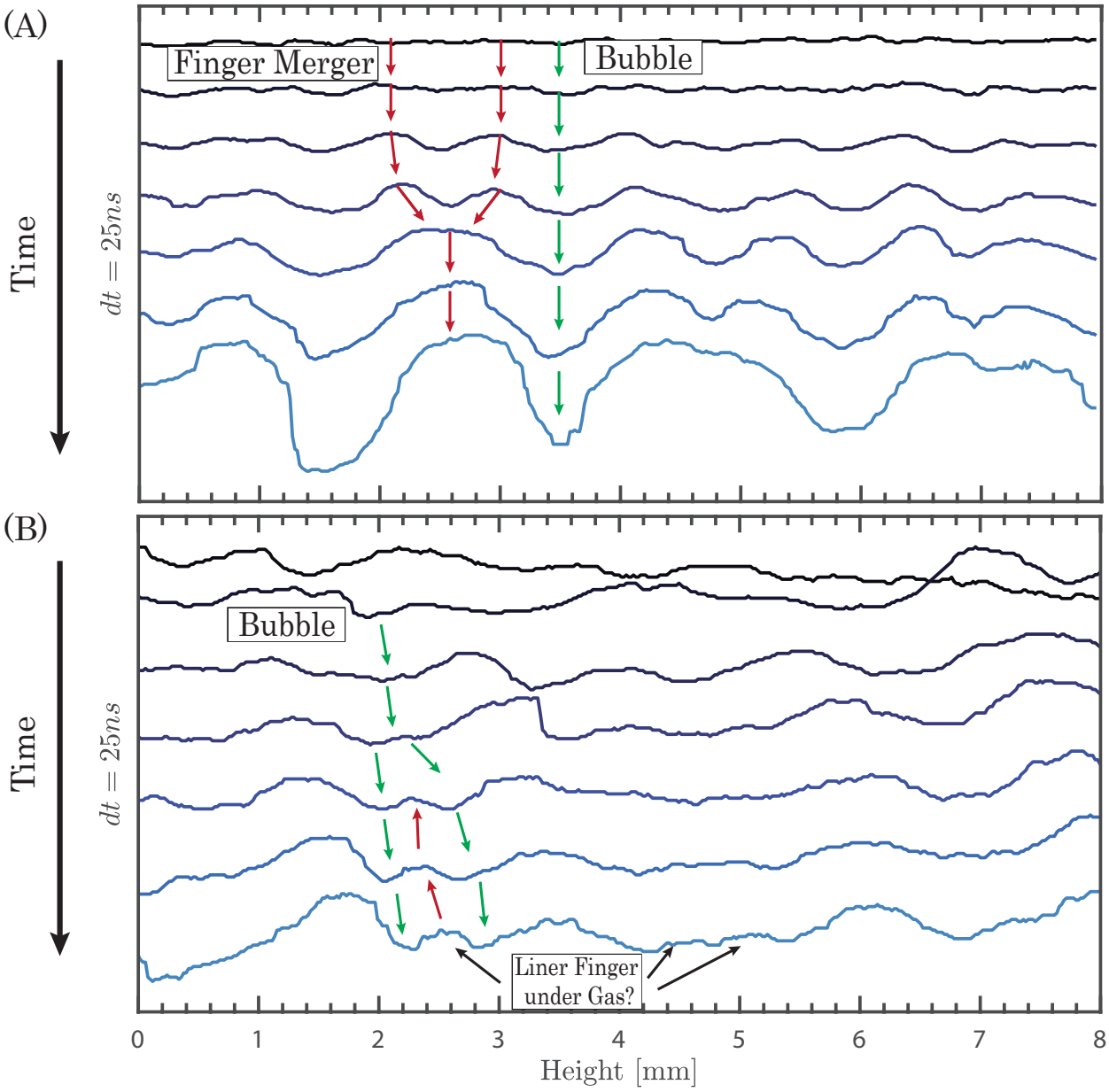


Figure 5.8: Visible-light self-emission implosion boundaries for (a) liner-only and (b) gas-on-liner targets. The tracked plasma boundaries are separated in time by 25 ns intervals as a function of height. The red and green arrows trace the evolution of the instability's finger and bubble structure through the implosion. Note that in the liner-only case, a finger merger event is observed while the bubbles stay in the same axial position, consistent with expectations. Conversely, the GoL targets display an unusual event where a new finger emerges from an existing bubble. This is suggests that the liner's instability structure may develop decoupled from the overlying gas plasma.

the gas is erased as a result of the collision with the liner, and a new instability grows from small perturbations on the gas surface. Second, the liner-dominated growth emits significantly more light compared to the gas. The observed emission is only from the liner, which grows its own instabilities independently of the gas impact. Third, in decoupled growth, both the gas-vacuum and gas-liner interfaces exhibit growing instabilities at different rates, which are observed on the self-emission camera. As the target implodes, the instability of the heavier liner eventually dominates the observed structure. An observation that supports the third scenario can be seen in Fig. 5.8(b). A unique feature in the GoL implosion is the appearance of an instability finger emerging from an existing instability bubble. This could be interpreted as a dense finger from the underlying liner instability poking through the less dense, overlying gas bubble. However, definitively distinguishing between these scenarios with a self-emission diagnostic remains a challenge. An improvement would be to use penetrating radiography. This diagnostic could distinguish between the gas and liner interfaces and help quantify any material mixing, which is difficult to infer from the self-emission alone.

Note that this target configuration resembles the core-coronal structure in wire Z-pinches, where a hot, low-density plasma surrounds a colder, denser central conductor [135]. This similarity suggests that the underlying physics in both scenarios may be related and could be a future topic of study.

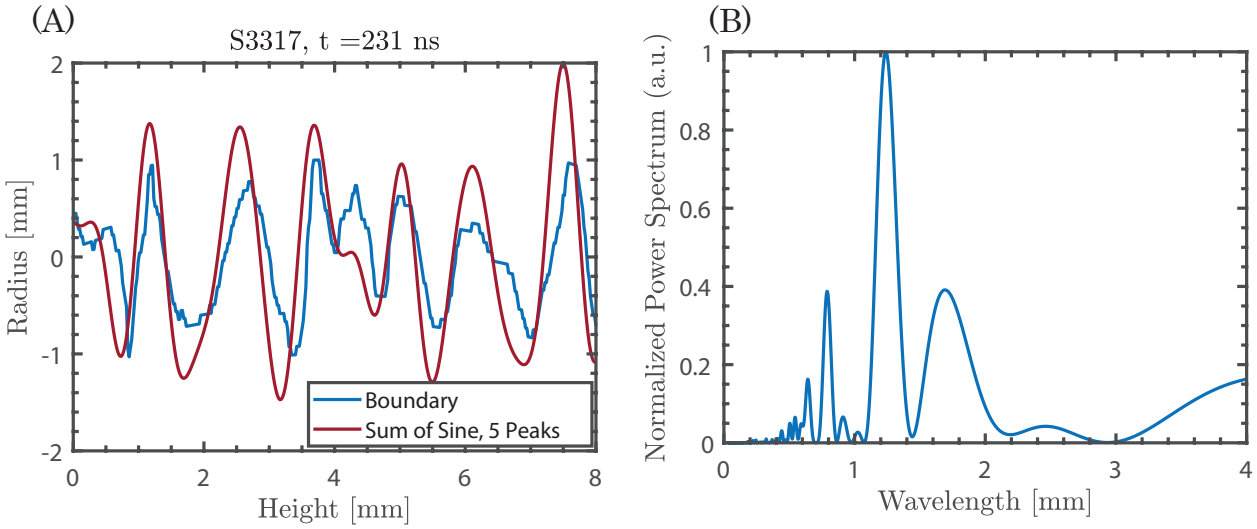


Figure 5.9: (a) A plot of the self-emission plasma boundary for shot 3317 at $t = 231$ ns, overlaid with the waveform reconstructed from the five largest peaks of the power spectra. (b) The power spectra of the same boundary.

To distinguish the dominant instability wavelengths, a time-wavelength analysis was conducted on the tracked boundaries. To isolate the oscillatory perturbation structure from the bulk material motion within the tracked boundary data, the mean radius of the tracked

boundaries was found and then subtracted from the raw data. However, the mean radius of the liner material was not constant as a function of axial position. Instead, the mean radius showed signs of bulging, curvature, and skew. To remove these low-frequency trends, the mean radius was found by fitting a second-order polynomial to the boundary data. This fitted polynomial was then subtracted from the raw boundary data to obtain a detrended oscillatory signal. The detrended signal was significantly zero-padded to access the optimal spectral resolution. The resulting signal was then processed using a Fast Fourier Transform to generate the power spectra, as shown in Fig. 5.9(b). To verify the accuracy of the power spectra and confirm that the zero-padding did not artificially include any additional wavelengths, the original signal was reconstructed by summing the five most prominent wavelengths, as shown in Fig. 5.9(a). The reconstructed waveform reasonably represents the original signal.

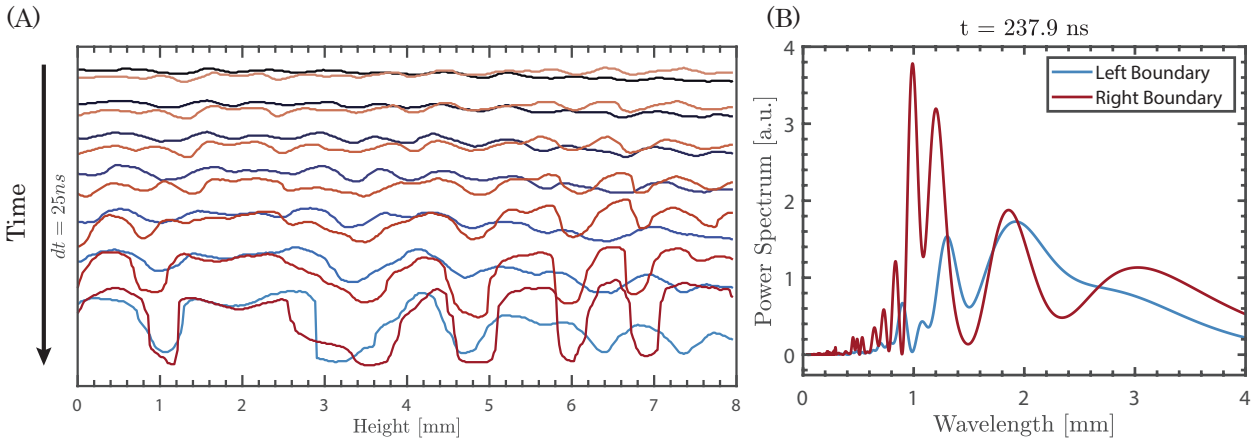


Figure 5.10: (a) A plot of self-emission implosion boundaries. Each tracked plasma boundary is separated in time by 25 ns intervals, ending at stagnation. (b) Power spectra of the left and right boundaries near stagnation. The blue and red lines indicate the left and right boundaries, respectively

It is observed that the instability structure on the left and right boundaries is not initially identical. This is likely because random surface perturbations seed a different initial wavelength spectra on either side. However, as the liner evolves over time, the instability wavelength becomes more correlated, as shown in Fig. 5.10. This suggests that perturbation information travels azimuthally around the liner, likely at the Alfvén speed [85, 136]. To increase confidence and reduce uncertainties, both the left and right boundaries from each image are utilized for analysis.

In Fig. 5.11, the liner boundaries and their corresponding power spectra are shown for liners with foil thicknesses of 400 nm, 800 nm, and 1500 nm at times up to stagnation. As the liner implodes inwards, the increasing intensity of the power spectra indicates the growth

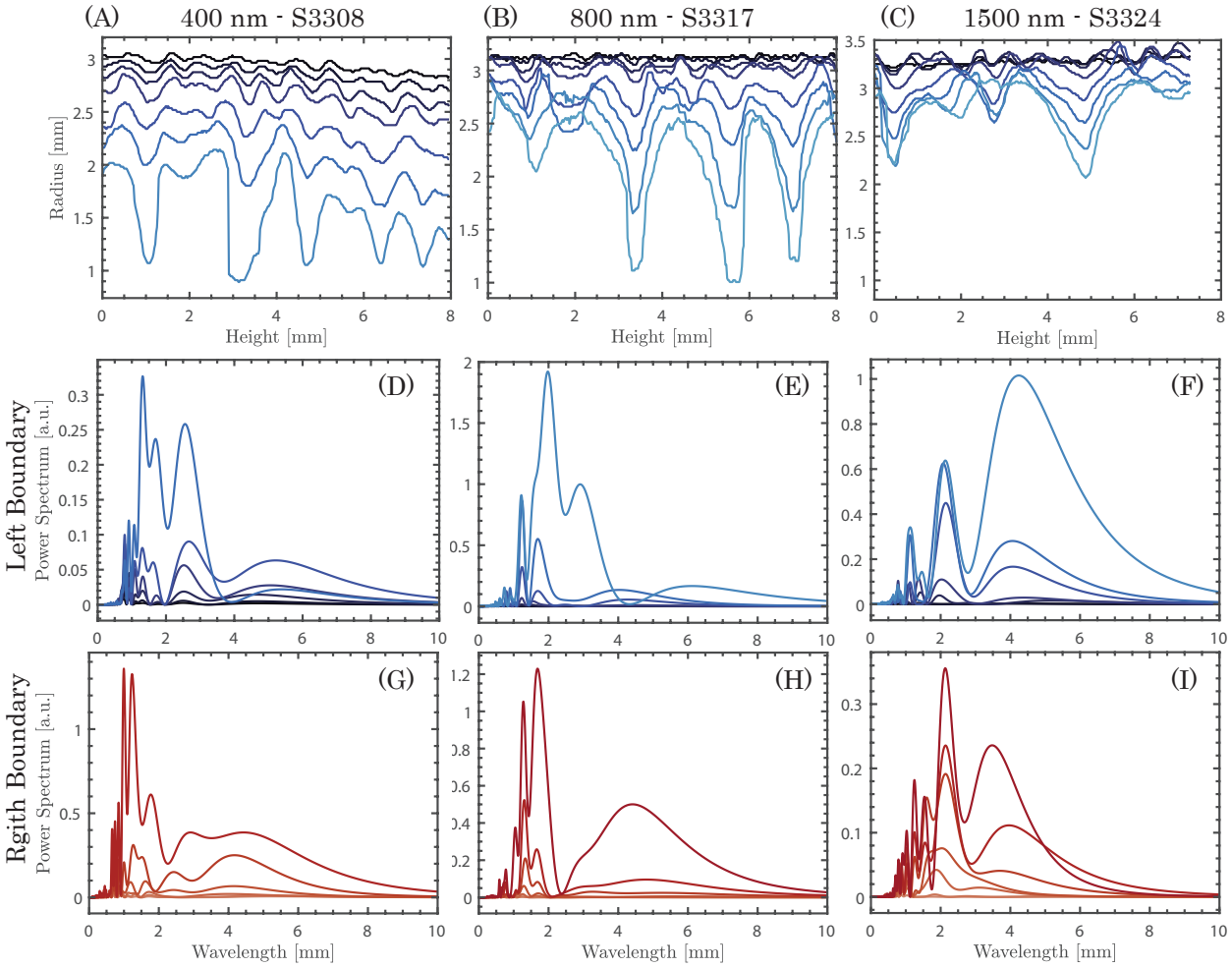


Figure 5.11: Time evolution of the imploding self-emission boundaries for liners with foil thicknesses of (a) 400 nm, (b) 800 nm, and (c) 1500 nm. The black-blue color gradient indicates increasing time during the implosion of the left boundaries up to the time of stagnation. (d–f) The power spectra of the left boundaries for liners with foil thicknesses of 400 nm, 800 nm, and 1500 nm, respectively. (g–i) The power spectra of the right boundaries for liners with foil thicknesses of 400 nm, 800 nm, and 1500 nm, respectively.

of the instability amplitude.

The spectra are normalized to the peak value at each time step to emphasize the evolution of the dominant wavelengths. The left and right boundaries, along with the corresponding normalized spectra, are shown in Fig. 5.12. Note that the plots are interpolated for visualization, as the raw data consist of twelve time points from the framing camera. The dashed line indicates the time of stagnation, separating the implosion (left) and explosion (right) phases.

Early in the implosion ($t \leq 200$ ns), the instability exhibits a broad, multi-moded spectra, typically with $\lambda \leq 1.5$ mm. This is consistent with the initial seeding of a wide range of modes from random surface perturbations. For example, the 400-nm-thick liner, at $t = 160$ ns, shows several dominant wavelengths between 0.6 mm and 1.25 mm. As the liner accelerates inward, one or two wavelengths begin to grow faster and dominate the spectra. By $t = 200$ ns, the dominant wavelengths for the 400 nm liner have shifted to 1.25 mm and 1.75 mm. This trend of the dominant wavelength shifting to larger values continues through the implosion and explosion phases.

The 1500-nm-thick liner does not significantly implode and is expected to be dominated by current-driven instabilities rather than acceleration-driven MRTI. Initially, its instability spectra are broad and composed of small wavelengths, similar to those of the thinner liners. A consistent feature is observed around $t = 200$ ns: where a dominant $\sim$2 mm wavelength mode emerges and persists until stagnation. This characteristic wavelength appears in nearly all the liner implosions in this study, regardless of liner thickness. Furthermore, the $\sim$2 mm wavelength appears for all three thicknesses at approximately $t = 200$ ns, regardless of the convergence ratio (i.e., the 800-nm-thick foil has imploded more than the 1500-nm-thick foil). The convergence ratio is defined as $CR \equiv R_0/R_{\min}$. The independence from liner thickness (and thus from acceleration) suggests that MRTI is not responsible for initially setting the dominant wavelength. However, once a perturbation wavelength is established by other means, the MRTI is expected to be the primary mechanism for driving its rapid amplification as the liner accelerates. A reasonable explanation is that the current-driven instability dictates the seeded instability, and MRTI grows the amplitude. This is supported by comparing the 400 nm and 800 nm thick liners at stagnation. The 400-nm-thick liner accelerates faster and stagnates earlier, which provides less time for non-linear evolution, such as mode merging. Consequently, the 400-nm-thick liner retains more of its small-wavelength structure at stagnation, whereas the slower imploding 800-nm-thick liner has more time for modes to merge into larger wavelengths.

Fig. 5.13 compares the power spectra of a liner-only target and a GoL target, revealing distinct differences in their instability wavelength evolution. The liner-only spectra are

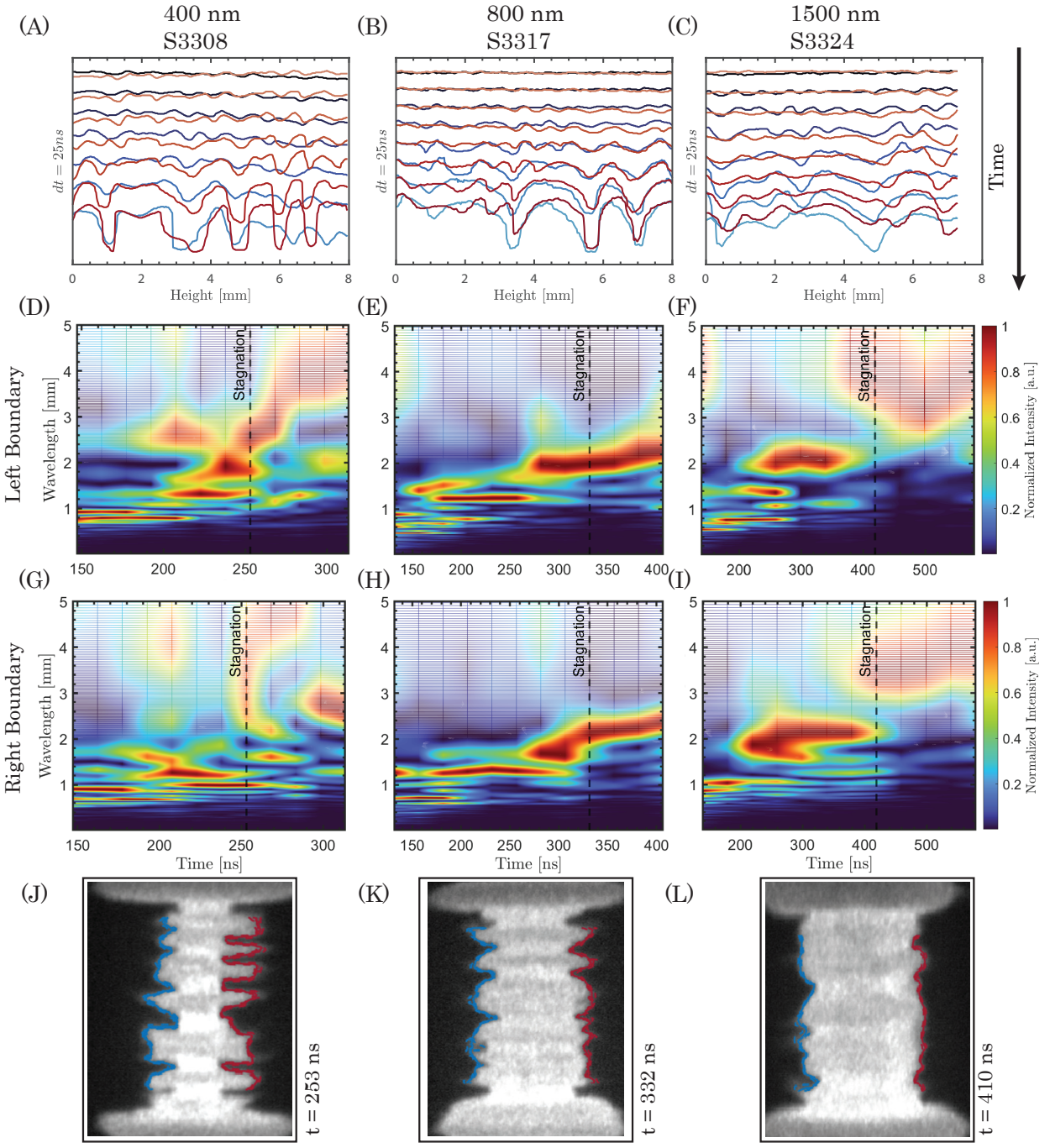


Figure 5.12: Comparison of the implosion dynamics for three liner thicknesses: 400 nm (left column), 800 nm (middle column), and 1500 nm (right column). **Top Row** (a–c): time evolution of the imploding self-emission boundaries. Each tracked plasma boundary is separated in time by 25 ns intervals, ending at stagnation. The blue and red lines indicate the left and right boundaries, respectively. **Top-Middle Row** (d–f): the time-wavelength evolution of the normalized power spectra for the left boundaries. **Bottom-Middle Row** (g–i): the time-wavelength evolution of the normalized power spectra for the right boundaries. The dashed black line indicates time of stagnation. **Bottom Row** (j–l): the corresponding self-emission images at stagnation. The overlaid blue and red lines indicate the tracked left and right boundaries, respectively.

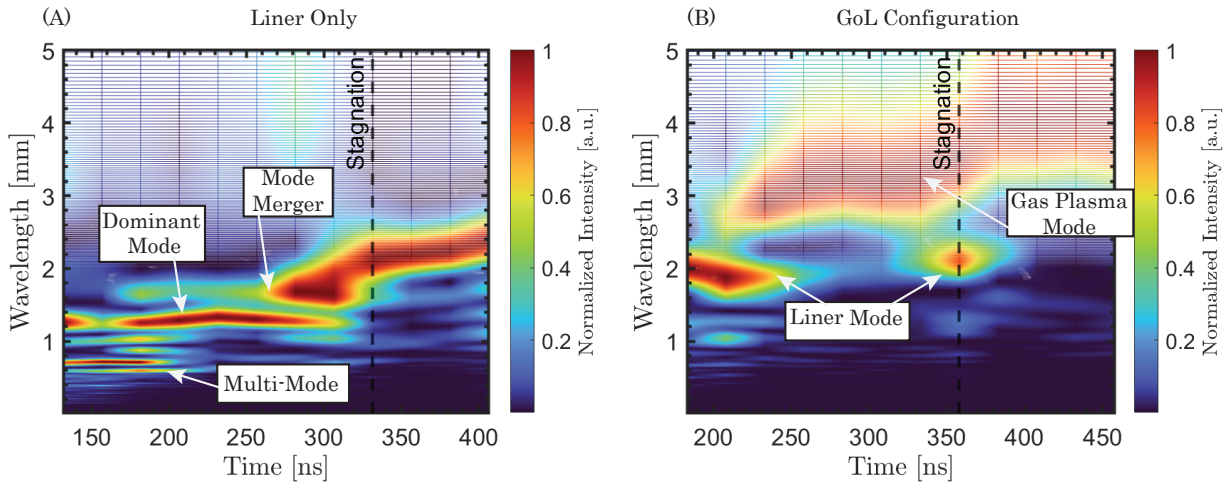


Figure 5.13: The time-wavelength evolution of the normalized power spectra for (a) liner-only and (b) gas-on-liner targets, corresponding to shots 3317 and 3318, respectively. The dashed black line indicates time of stagnation. Note the distinct features in liner-only spectra: the spectra is initially multi-moded at $t \approx 150$ ns, transitions to a single dominant mode by $t \approx 250$ ns, and then shows a mode merger event at $t \approx 300$ ns. By contrast, the GoL targets exhibit two dominant wavelengths at stagnation, $\lambda \approx 2$ mm and $\lambda \approx 3$–4 mm, which can be attributed to the dominant mode of the liner and gas plasma, respectively.

initially multi-moded at $t \approx 150$ ns. This transitions to a single dominant mode by $t \approx 250$ ns and then shows a mode merger event at $t \approx 300$ ns, increasing the wavelength. By contrast, the GoL targets exhibit two dominant wavelengths at stagnation, $\lambda \approx 2$ mm and $\lambda \approx 3$–4 mm, this can be attributed to the dominant modes of the liner and gas plasma, respectively.

The addition of a gas layer significantly alters the instability spectra, as shown in the comparison between GoL and liner-only targets in Fig. 5.14. A notable difference in the spectra is the suppression of small wavelength perturbations. The GoL targets do not exhibit the broad, small wavelength spectra ($\lambda \leq 1$ mm) that were prominent in the early-time liner-only implosions. Instead, the GoL target at lower gas pressures is dominated by a persistent wavelength of $\lambda = 1.5$–2 mm. This appears around $t = 150$–200 ns, similar to the liner-only targets, but persists for the entire implosion without merging into a larger wavelength. The lack of a large wavelength ($\lambda \geq 3$ mm) suggests that the self-emission boundary might be liner-dominated. At higher gas pressures (-10 psig), a distinctly larger wavelength instability $\lambda = 2.5$–4.5 mm appears, as shown in Fig. 5.14(f,i), and it can be part of the power spectra of the gas plasma. This behavior suggests that the measured self-emission boundary can be either liner-dominated, gas-dominated, or mixed. For example, Fig. 5.15 shows two shots with identical initial conditions (800-nm-thick liner with -12 psig of gas), and one produced a mixed spectra, while the other produced a liner-dominated spectra.

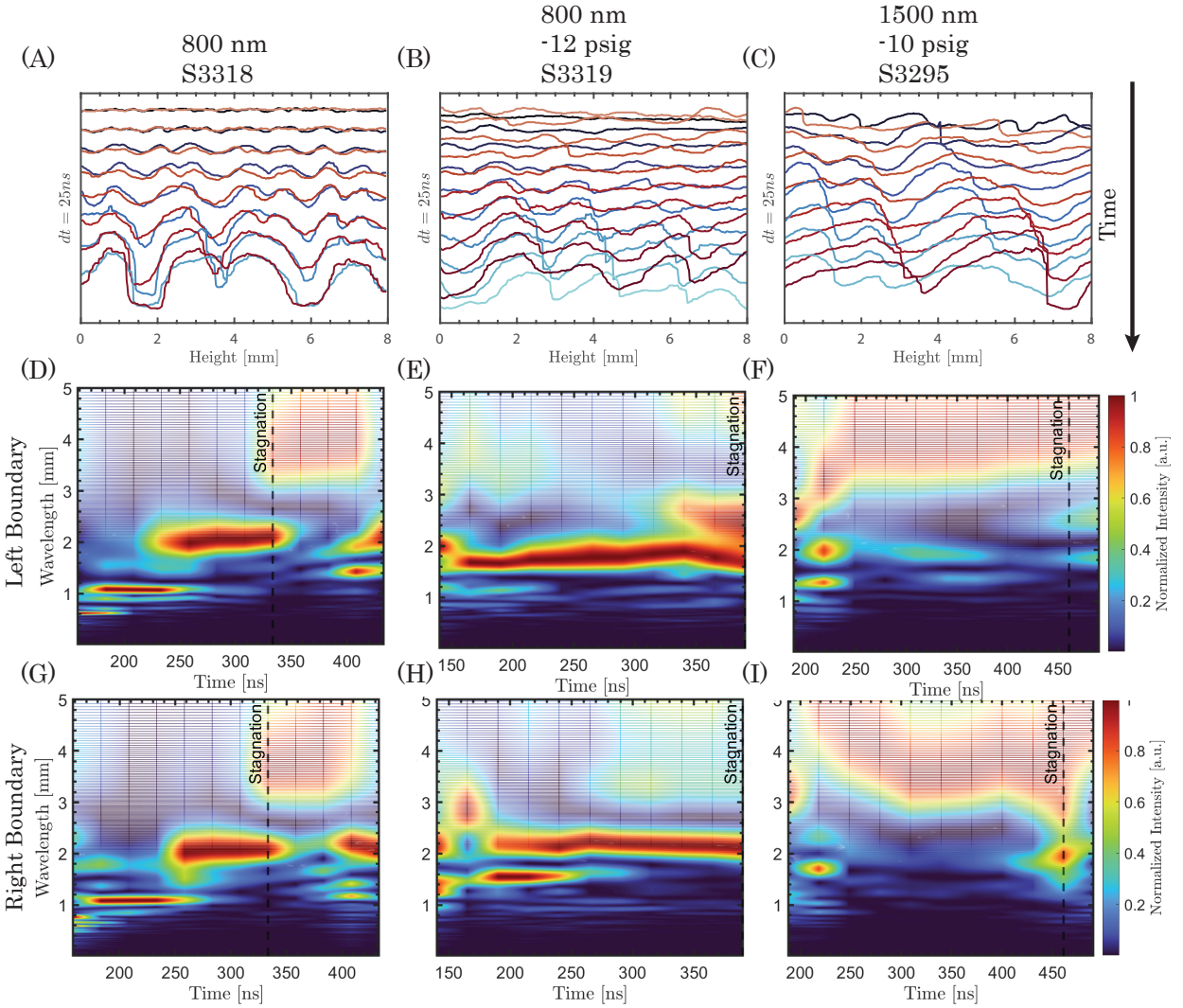


Figure 5.14: Comparison of the implosion dynamics for three GoL targets with increasing gas pressure: 800 nm (left column), 800 nm and −12 psig (middle column), and 1500 nm and −10 psig (right column). **Top Row** (a–c): time evolution of the imploding self-emission boundaries. Each tracked plasma boundary is separated in time by 25 ns intervals, ending at stagnation. The blue and red lines indicate the left and right boundaries, respectively. **Middle Row** (d–f): the time-wavelength evolution of the normalized power spectra for left boundaries. **Bottom Row** (g–i): the time-wavelength evolution of the normalized power spectra for right boundaries. The dashed black line indicates time of stagnation. Note the lack of small wavelength modes and increase in large wavelength modes as gas pressure increases.

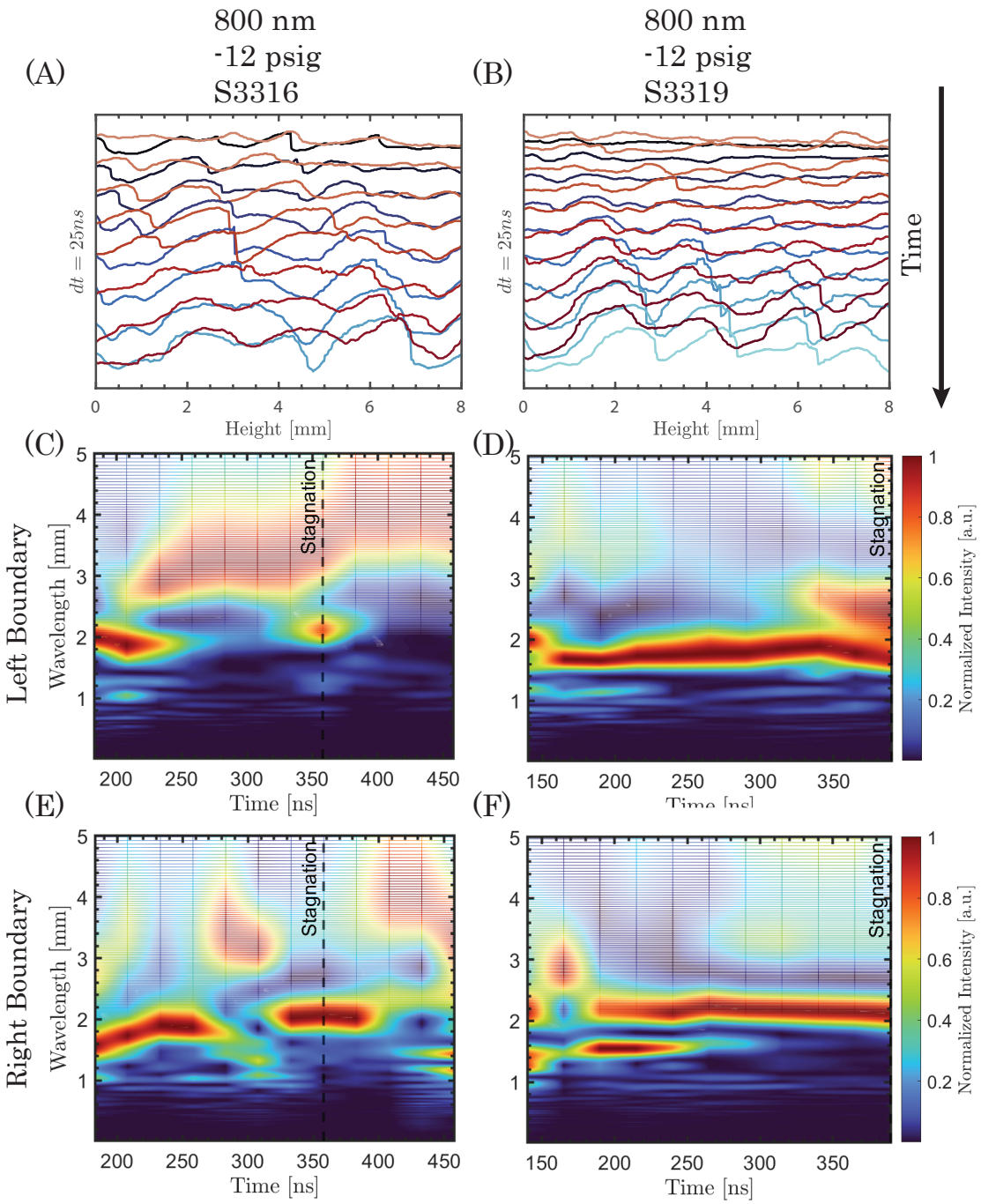


Figure 5.15: Comparison of the implosion dynamics for two similar GoL targets, both with 800 nm and −12 psig. **Top Row** (a,b): time evolution of the imploding self-emission boundaries. Each tracked plasma boundary is separated in time by 25 ns intervals, ending at stagnation. The blue and red lines indicate the left and right boundaries, respectively. **Middle Row** (c,d): the time-wavelength evolution of the normalized power spectra for left boundaries. **Bottom Row** (e,f): the time-wavelength evolution of the normalized power spectra for right boundaries. The dashed black line indicates time of stagnation. Note the absence of large wavelengths ($\lambda > 3$ mm) in the power spectra for shot 3319. This may suggest that shot 3319 is more liner-dominated than gas-dominated.

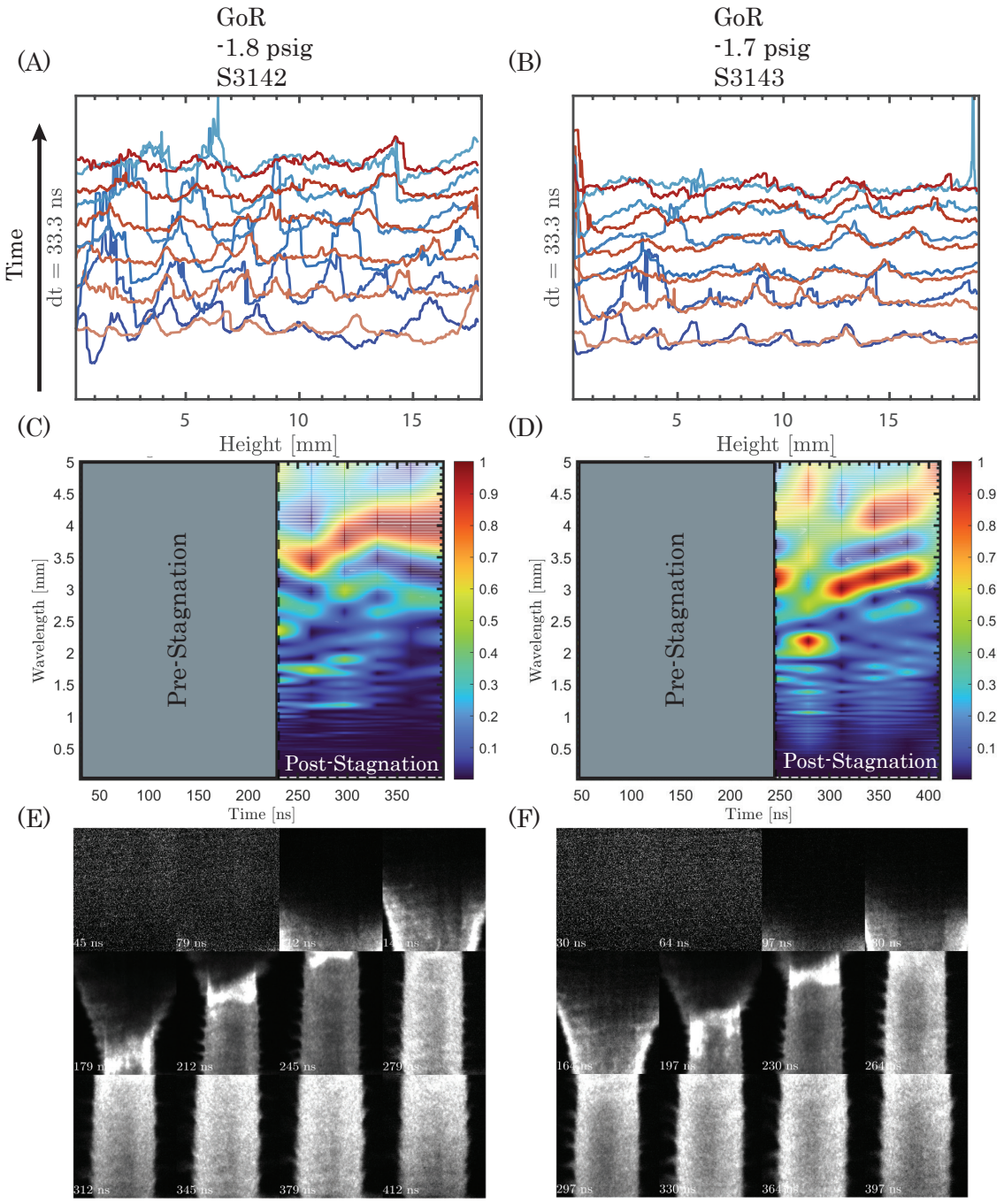


Figure 5.16: Comparison of the implosion dynamics for two similar gas-on-rod (GoR) targets, both with copper rods and −12 psig. **Top Row** (a,b): time evolution of the imploding self-emission boundaries. Each tracked plasma boundary is separated in time by 33 ns intervals, starting at post-stagnation. The blue and red lines indicate the left and right boundaries, respectively. **Middle Row** (c,d): the corresponding post-stagnation time-wavelength evolution of the normalized power spectra. The gray region is during the implosion phase. **Bottom Row** (e,f): the visible-light self-emission images of the GoR targets. Note the absence of strong small wavelengths ($\lambda < 2$ mm) in both power spectra. This suggest that the gas loads produce large wavelengths ($\lambda > 3$ mm) post-stagnation.

To further support the hypothesis that the large wavelength structures $\lambda \geq 3$ mm originates from the gas, we performed spectral analysis on gas-on-rod (GoR) experiments. In these GoR targets, the gas stagnates on the dense central rod. Spectral analysis of the post-stagnation GoR plasma reveals a distinct, large wavelength structure, as shown in Fig. 5.16. The dominant wavelengths are indeed in the range of $\lambda = 2.5$–4 mm, with a notable lack of spectral content below $\lambda \leq 2.5$ mm. In the GoL spectra, for a given material combination and drive current, the characteristic instability wavelengths that develop on the liner surface appear consistently at the same time. With this in mind, it is believed that the gas plasma also behaves similarly. The wavelengths formed at $t = 225$ ns in the GoR spectra will form at $t = 225$ ns in the GoL targets. This is consistent with the GoL data, where a large wavelength mode is also observed to emerge at this time.

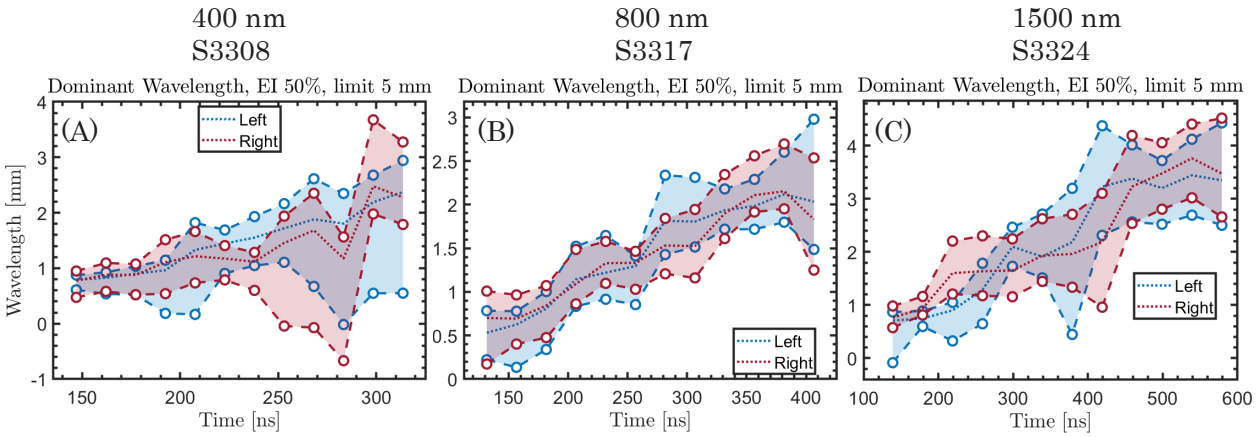


Figure 5.17: Time evolution of the dominant instability wavelength for liners with foil thicknesses of (a) 400 nm, (b) 800 nm, and (c) 1500 nm. The blue and red lines indicate the left and right boundaries, respectively.

To quantify the dominant wavelength, the power spectra were integrated, and the dominant wavelength was defined as the median of the resulting cumulative distributions (50%). The uncertainty was defined at the 25th and 75th percentiles of the cumulative distributions. Initially, at $t \approx 150$ ns, the spectral power is concentrated at short wavelengths under $\lambda \leq 1$ mm, as shown in Fig 5.17. As the implosion evolves, the dominant wavelength consistently shifts to larger values, which is characteristic of the inverse cascade. Unexpectedly, this growth continues through stagnation and well into the liner's explosion phase. This was unusual since the liner is disrupted by the collision with the support rod, yet the dominant wavelength continued to grow. Simulations confirm that the instability structure is preserved after collision with the support rod for a support rod radius of 0.5 mm [133].

A power law fit to the evolution shown in Fig. 5.17 reveals nearly linear growth, with the dominant wavelength scaling as $t^{1–1.5}$. This scaling appears to be independent of liner

mass and MRTI growth rate, since the scaling relation was similar for liners with different thicknesses. The dominant wavelengths of the instability were also found to be generally symmetric between the left and right boundaries.

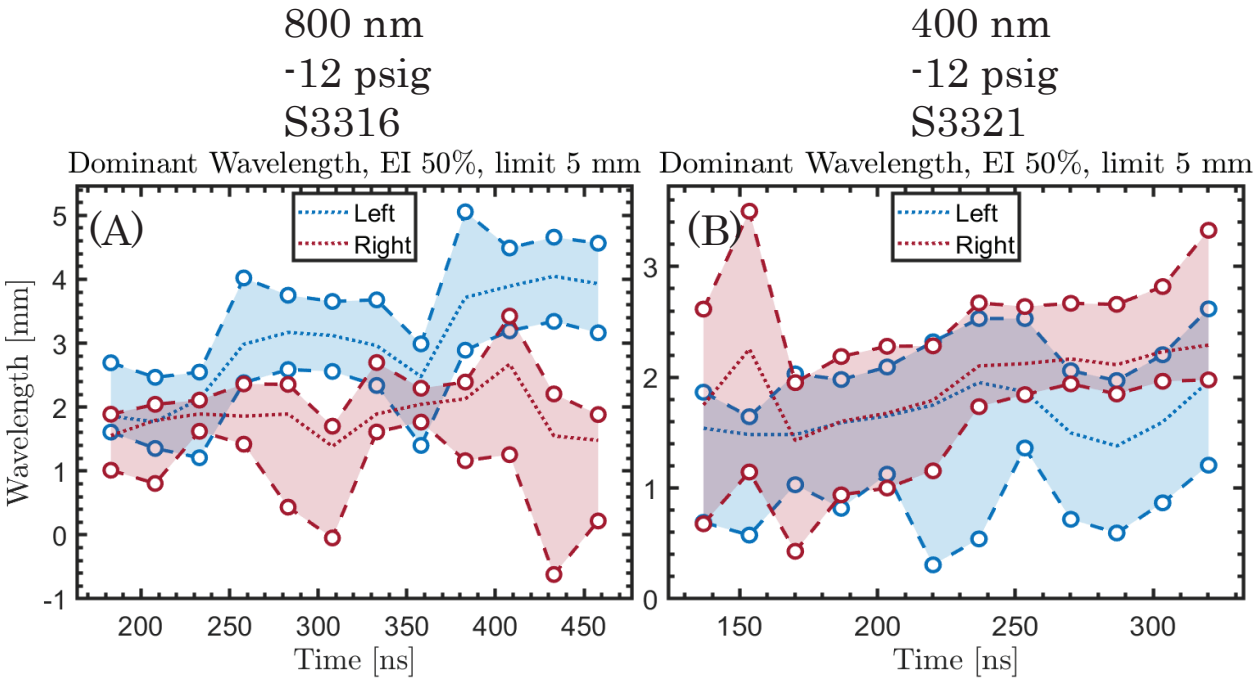


Figure 5.18: Time evolution of the dominant instability wavelength for two GoL targets: (a) 800 nm liner with −12 psig of gas; and (b) 400 nm liner with −12 psig of gas. The blue and red lines indicate the left and right boundaries, respectively.

For the GoL targets, which comprise an 800-nm-thick liner and −12 psig of gas, the dominant wavelength evolves much less than for the liner-only targets, as shown in Fig. 5.18. The dominant wavelengths lie in the range of 2–3 mm. The power spectra is also notably broad, with significant power distributed across wavelengths from 0.5–4 mm. This broad spectra is likely the result of two prominent instability modes: a larger wavelength from the gas plasma and a smaller wavelength from the liner. The lack of the inverse cascade is surprising, as the instability's dominant wavelengths remain unchanged over time.

5.5 MRTI Amplitudes

A key metric for liner performance is the instability growth, quantified by the change in perturbation amplitude during the implosion. If the amplitude grows too large, the instability can compromise the liner's integrity or even penetrate through it entirely, which would be detrimental to a fusion target. For these experiments, the instability amplitude was

calculated from the self-emission boundaries, with the peak-to-peak instability amplitude defined as $2\sqrt{2}\sigma$, where σ is the standard deviation of the boundary.

Figure 5.19 shows a comparison of the performance metrics for the liner-only targets for liners with foil thicknesses of 400 nm, 800 nm, and 1500 nm. The peak-to-peak amplitude (A_{p-p}) is shown as a function of normalized distance moved (δR), where the mean radius ($R(t)$) is normalized to the initial radius of the liner ($R(0) = 3$ mm), as shown in Fig. 5.19(c). The 1500-nm-thick liner reached a maximum amplitude of $A_{p-p} = 0.78 \pm 0.03$ mm at $\delta R = 0.02$, the 800 nm and 400 nm thick liners reached amplitudes of $1.44 \pm .0.12$ mm and 1.23 ± 0.18 mm for distances of 0.29 and 0.46, respectively. Notably, the calculated instability amplitude sometimes appears to decrease at higher convergence, as seen for the 400-nm-thick liner in Fig. 5.19(c). For this shot, the instability amplitude decreases to $A_{p-p} = 0.97 \pm 0.22$ mm as it converges further to $\delta R = 0.5$. This apparent decrease is an artifact of the analysis method. The amplitude is calculated from the standard deviation of the boundary's mean radius. At late times, near stagnation, the instability bubbles have already stagnated while the fingers are still compressing inward. As the trailing fingers "catch up" to the stagnated, stationary bubbles, the overall spread of the boundary decreases, leading to a smaller calculated amplitude and a higher convergence ratio.

Figure 5.20 shows a comparison of the performance metrics of GoL targets with a constant -10 psig of gas and liners with foil thicknesses of 400 nm, 800 nm, and 1500 nm. The calculated peak instability amplitude for the GoL targets is $A_{p-p} = 1.10 \pm 0.2$ mm, 0.99 ± 0.19 mm, and 0.76 ± 0.09 mm at a $\delta R = 0.03$, 0.28, and 0.44 for liners with foil thicknesses of 400 nm, 800 nm, and 1500 nm, respectively.

A surprising result is that the GoL targets were more stable against the MRTI compared to the liner-only targets, as shown in Fig. 5.21. A direct comparison between two 800-nm-thick liner shots at a similar convergence of $\delta R \approx 0.3$ highlights this effect. The liner-only shot (3318) reached a maximum instability amplitude of $A_{p-p} = 1.44 \pm 0.12$ mm, while the GoL shot (3310) had a smaller amplitude of 0.99 ± 0.19 mm. Furthermore, the instability amplitude decreases even further, reaching an amplitude of 0.6 ± 0.22 mm at peak convergence. This stabilizing effect is also confirmed visually in the raw self-emission images, as shown in Fig. 5.21 (b,c)

Figure 5.22 shows that increasing the gas pressure has a stabilizing effect on MRTI. All of the GoL targets exhibit smaller peak instability amplitudes compared to the liner-only targets. Furthermore, the dataset shows a trend in which increasing the initial gas pressure leads to a further reduction in the measured instability amplitude.

Several physical mechanisms could contribute to this observed stabilizing effect:

- **Smoother Density Gradient**. The gas layer creates a gradual density transition

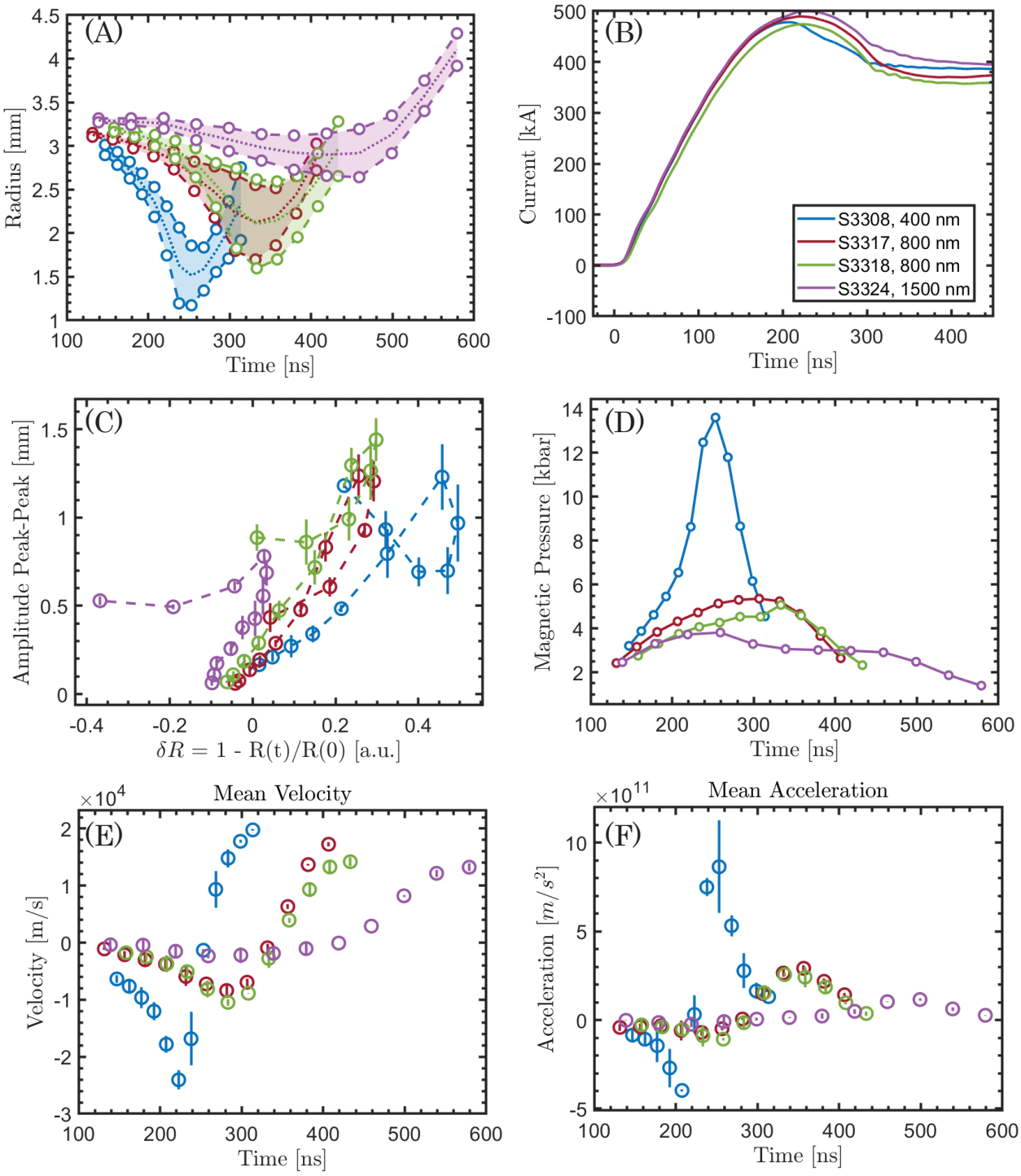


Figure 5.19: A comparison of liner-only targets with varying liner thicknesses: 400 nm (shot 3308), 800 nm (shot 3317 and 3318), and 1500 nm (shot 3324). The plots show: (a) implosion trajectories; (b) drive current waveforms; (c) instability amplitudes as a function of normalized distance moved; (d) magnetic pressures; (e) velocities; and (f) accelerations.

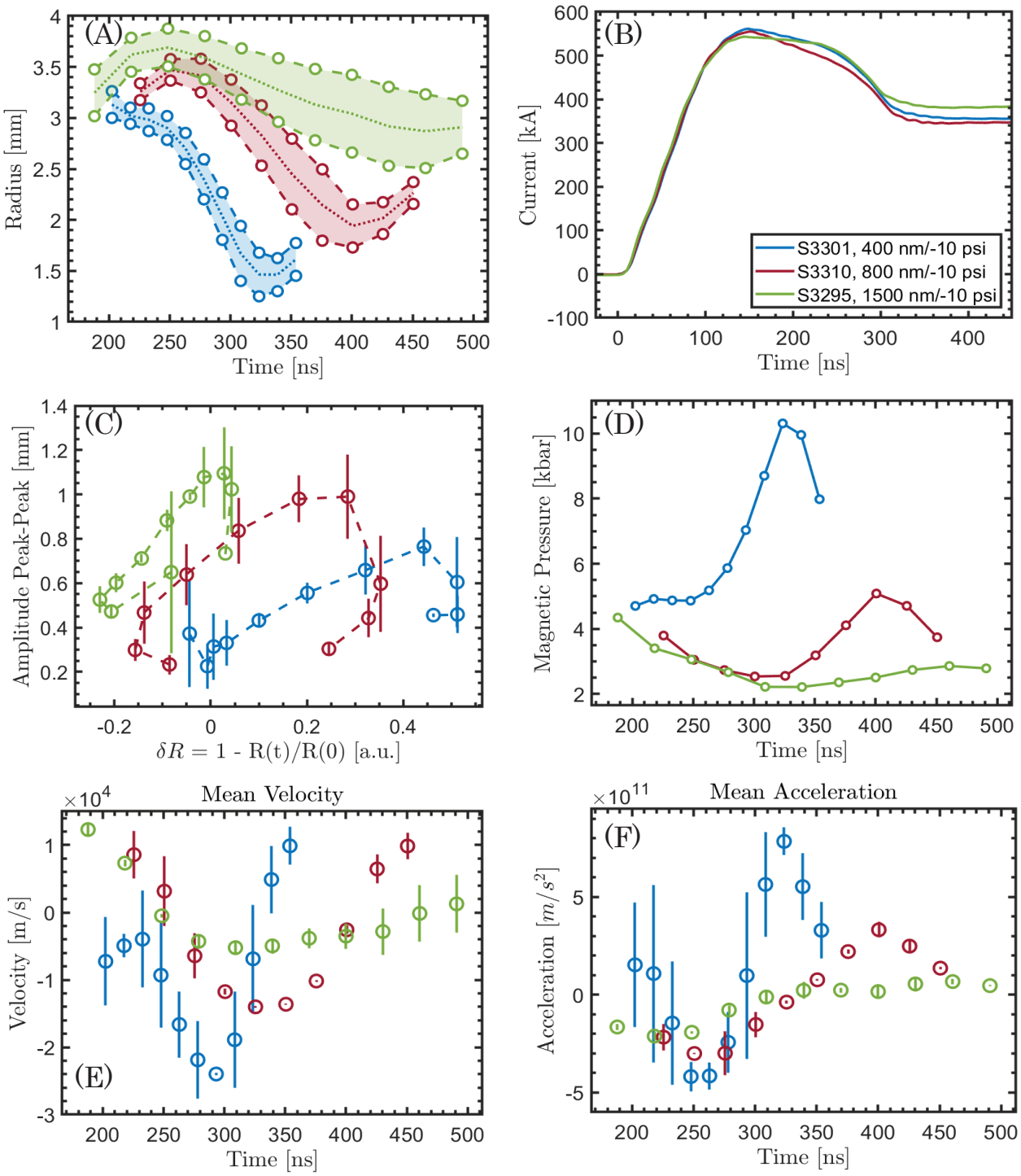


Figure 5.20: A comparison of GoL targets with constant gas pressure of −10 psig and varying liner thicknesses: 400 nm (shot 3301), 800 nm (shot 3310), and 1500 nm (shot 3295). The plots show: (a) implosion trajectories; (b) drive current waveforms; (c) instability amplitudes as a function of normalized distance moved; (d) magnetic pressures; (e) velocities; and (f) accelerations.

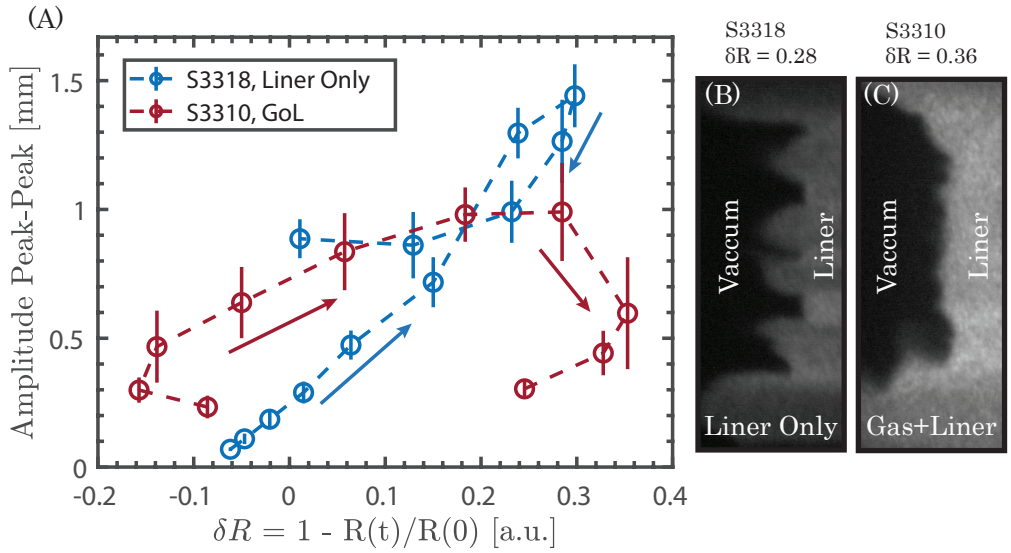


Figure 5.21: (a) Evolution of the peak-to-peak instability amplitude as a function of normalized distance moved. The blue and red curves correspond to liner-only and gas-on-liner targets, respectively. The arrows indicate the trajectory. The corresponding visible-light self-emission image for (b) liner-only and (c) GoL targets at $\delta R = 0.28$ and $\delta R = 0.36$, respectively.

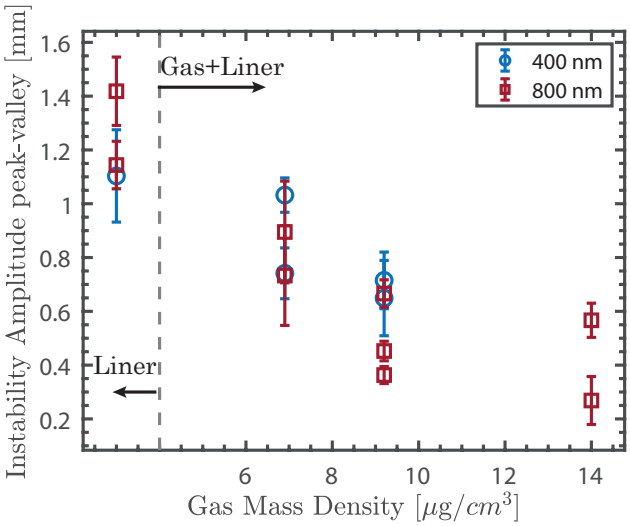


Figure 5.22: A plot of the maximum peak-to-valley instability amplitude as a function of injected gas mass density. The grey dashed line separates the liner-only targets (left) from the GoL configured targets (right). The blue circle and red square markers denote the 400 nm and 800 nm liner thickness, respectively. Note that all GoL targets exhibit smaller instability amplitude compared to liner-only targets.

from the vacuum to the dense liner, unlike the sharp interface of a liner-only target. Rayleigh-Taylor theory predicts that smoother density transitions are inherently more stable

- **Sheared Flow Stabilized**. The gas layer was measured to impart an axial velocity to the liner, creating a sheared-flow layer. This can be stabilizing if the shear is large enough to satisfy the shear flow stabilization criterion, $\frac{\partial V_z}{\partial r} \geq 0.1kV_A$, where k and V_A are the perturbation wavenumber and the Alfvén speed, respectively. We estimate these values based on the experimental parameters. Assuming a maximum axial velocity of $\Delta V_z = 5$ km/s across a 0.3 mm gas layer, the velocity gradient is $\frac{\partial V_z}{\partial r} = 1.67 \times 10^7$ s^{-1}. For the stability threshold, using the assumptions of argon gas with $Z = 8$, an electron density of $n_e = 1 \times 10^{25}$ m^{-3}, $I_{\text{peak}} = 500$ kA, and a wavelength of $\lambda = 2$ mm, the criterion is calculated to be $0.1kV_A = 2.95 \times 10^7$ s^{-1}. This preliminary calculation for our parameters suggests that the target is close to this stability threshold, making it a plausible mechanism.

- **Modulation of the Acceleration**. The gas adds mass to the target, reducing the liner's peak acceleration (g). Since the linear MRTI growth rate is $\propto \sqrt{g}$, a lower acceleration directly leads to a slower instability growth rate. Measurements of the gas layer have shown that the GoL target can have half the acceleration of a liner-only target in some shots, as seen in Figs. 5.19 and 5.20.

- **Larger Aspect Ratio**. Thicker shells (i.e., those with a smaller aspect ratio, $R/\Delta R$) are more robust to MRTI growth. A thin-foil liner typically has a very large, unstable initial aspect ratio (~ 1000). Adding a gas layer creates a much thicker combined shell with a significantly smaller and more stable aspect ratio. For example, if the gas layer adds 0.3 mm to the liner target, the resulting aspect ratio is ~ 11.

- **Bubble Filling**. Another considered hypothesis is that the gas simply fills the bubbles of the liner instability, artificially reducing the measured amplitude.

To quantify the instability growth, the instantaneous MRTI growth rate (γ) was calculated by performing an exponential fit ($A(t) \propto e^{\gamma t}$) to the instability amplitude over time. This analysis assumes that the instability is in the linear growth phase. The exponential form provides an excellent fit to the data, with a coefficient of determination $R^2 > 0.95$ for the liner-only targets and $R^2 > 0.89$ for the GoL targets, as shown in Fig 5.23(b,c). The analysis reveals that the 400-nm-thick target has a higher growth rate ($\gamma \approx 0.026$ ns^{-1}) than the 800-nm-thick liner ($\gamma \approx 0.015$ ns^{-1}). The GoL target consistently exhibits significantly lower growth rates compared to the liner-only targets, as seen in Fig 5.23(a).

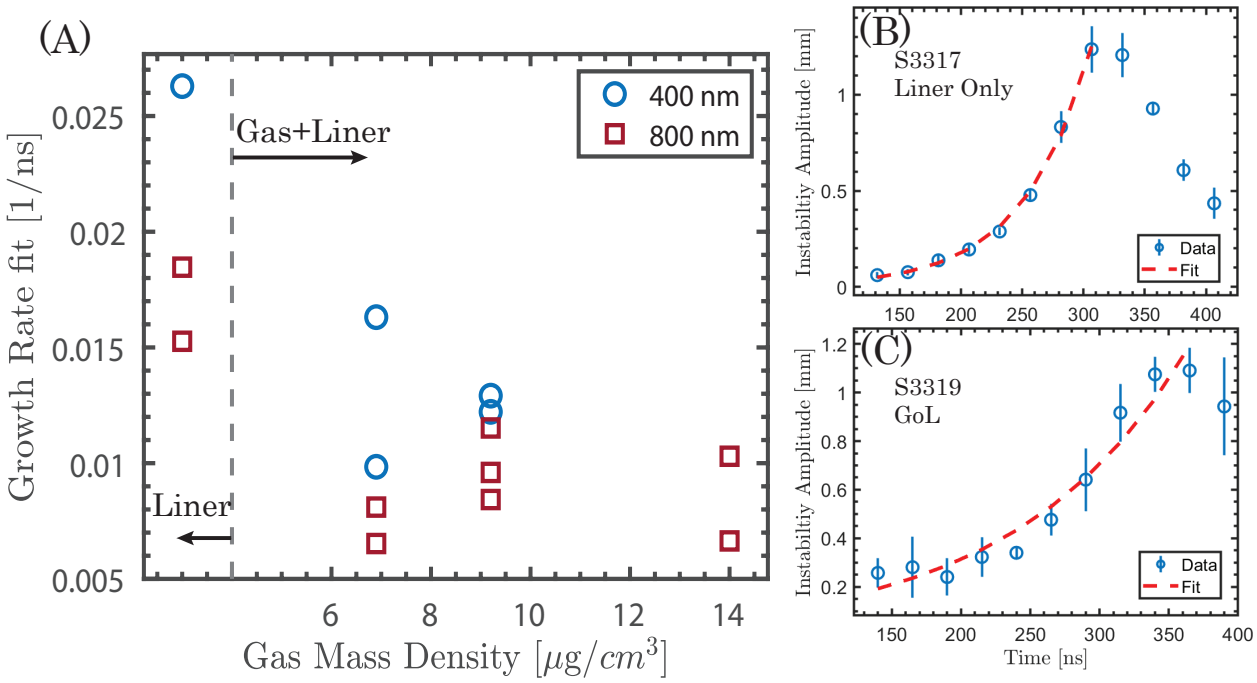


Figure 5.23: (a) A plot of the calculated growth rate as a function of injected gas mass density. The grey dashed line separates the liner-only targets (left) from the GoL targets (right). The blue circles and red squares denote liners with thicknesses of 400 nm and 800 nm, respectively. (b) Time evolution of the peak-to-peak instability amplitude for liner-only targets. (c) Time evolution of the peak-to-peak instability amplitude for GoL targets. The red curve is an exponential fit to the data. Note that the quality of fit suggests that the instability growth is in the linear growth regime.

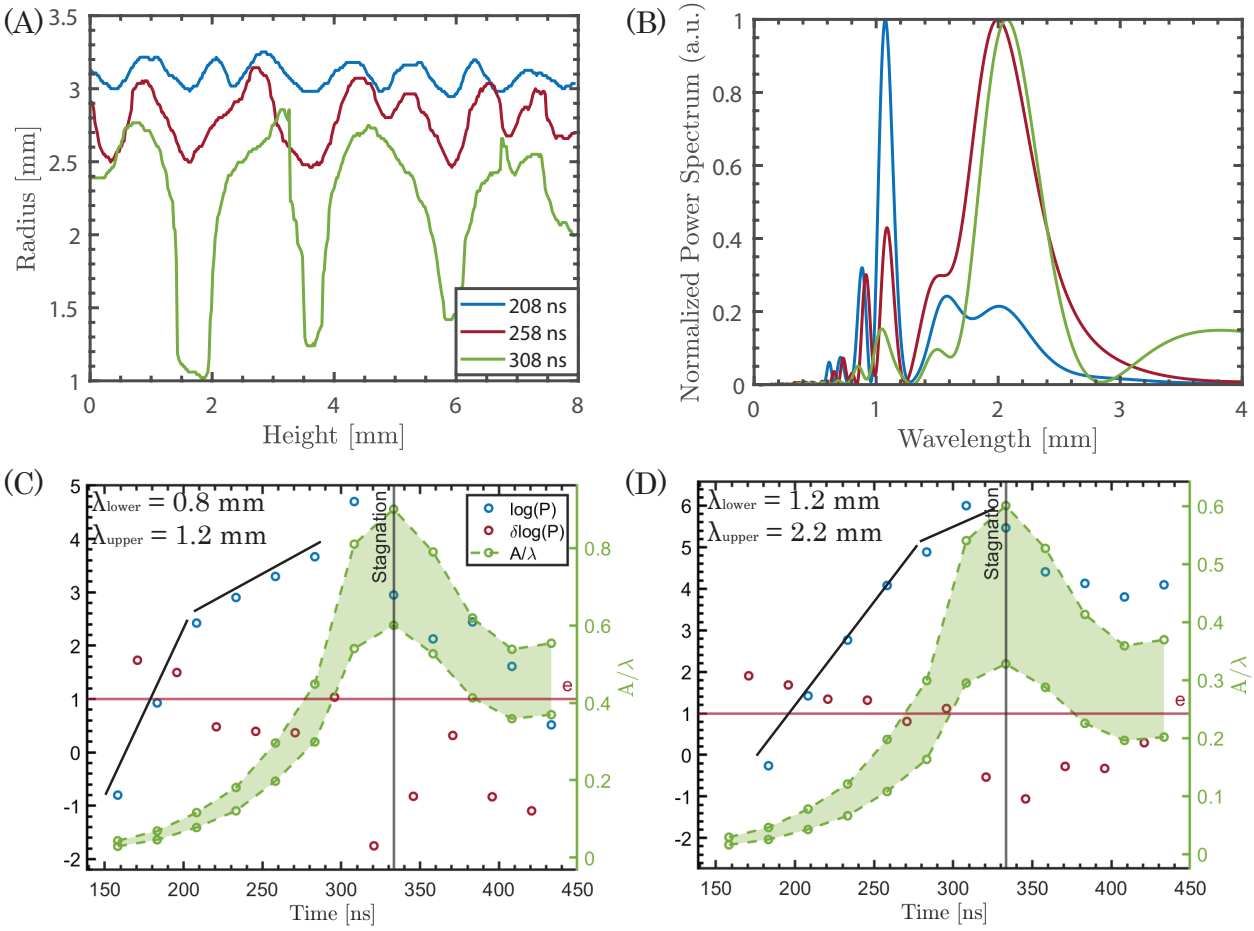


Figure 5.24: (a) A plot of self-emission boundary curves. The blue, red, and green curves denote $t = 206.6$ ns, 256.6 ns, and 306.6 ns, respectively. (b) The corresponding normalized power spectra of shot 3318. Analysis plots of the power spectra evolution for two wavelength ranges: (c) $\lambda = 0.8$–1.2 mm; and (d) $\lambda = 1.2$–1.6 mm. The log of the spectral powers are indicated by the blue markers, the differences in the logs of the integrated powers are indicated by the red markers, and the A/λ ranges are indicated by the green shaded regions. The solid red line denotes a constant value of e, and the grey line denotes the stagnation times. The solid black line estimates the slope of the linear and non-linear regions.

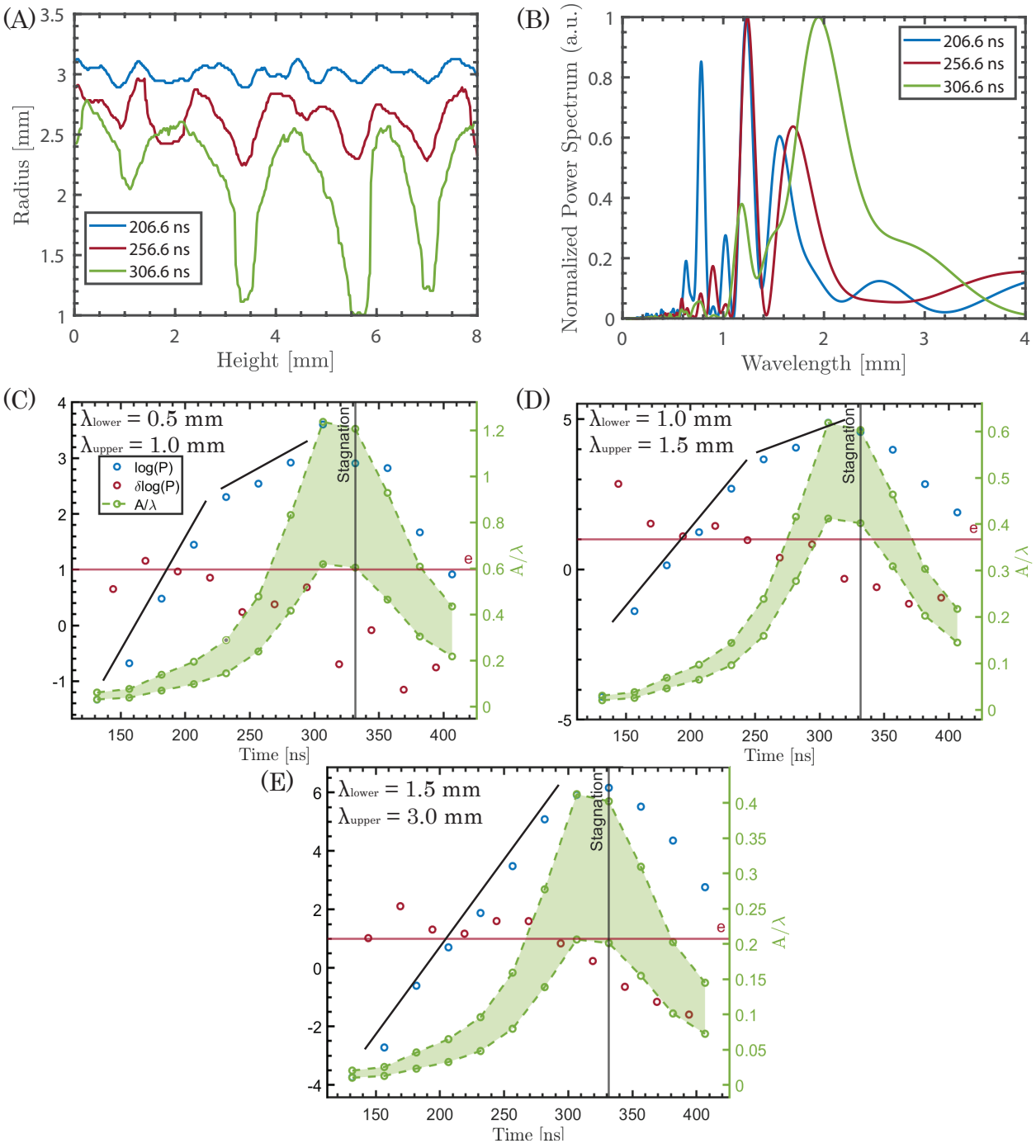


Figure 5.25: (a) A plot of selected self-emission boundary curves. The blue, red, and green curves denote $t = 206.6$ ns, 256.6 ns, and 306.6 ns, respectively. (b) The corresponding normalized power spectra of shot 3317. Analysis plots of the power spectra evolution for three wavelength ranges: (c) $\lambda = 0.5$–1.0 mm, (d) $\lambda = 1.0$–1.5 mm, and (e) $\lambda = 1.5$–3.0 mm. The log of the spectral powers are indicated by the blue marker, markers, the differences in the logs of the integrated powers are indicated by the red markers, and the A/λ ranges are indicated by the green shaded regions. The solid red line denotes a constant value of e, and the grey line denotes the stagnation times. The solid black line estimates the slope of the linear and non-linear regions.

For the liner-only targets [Fig. 5.23(b)], an exponential fit to the instability amplitude suggests that the growth remains in the linear regime for most of the implosion ($\sim$ 150 ns). This is surprising, as linear theory is typically only valid for small-amplitude perturbations, and clear non-linear signatures, such as cusps and inverse cascades, are observed in the self-emission images[e.g., see Fig. 5.6(c)].

In the laser-driven ICF community, the transition from linear to non-linear growth is often estimated to occur when the ratio of the instability amplitude to its wavelength (A/λ) exceeds a threshold of approximately 0.1–0.4 [137, 138]. Previous work in thin-foil liner implosions has shown that a recurrence of exponential growth can occur when mode merging increases the dominant wavelength (λ) rapidly enough to satisfy the ratio of $A/\lambda < 0.16$ ($kA < 1$) [17]. However, since the power spectra in this study often contain more than one dominant wavelength, a simple A/λ analysis of the entire boundary is insufficient. To investigate the growth of individual modes, we track the integrated power of each major spectral peak over time. Plotting the natural logarithm of this power as a function of time reveals whether individual modes are growing exponentially.

To quantify the transition from linear to non-linear growth, individual instability modes were tracked over time. Figure 5.24 shows this analysis for shot 3318 (an 800-nm-thick liner) where two modes, at $\lambda = 1$ mm and $\lambda = 2$ mm, were persistent. Early in the implosion ($t = 250$ ns), the 1 mm mode is dominant. As the instability evolves, a mode merger event occurs, transferring energy from the 1 mm mode to the 2 mm mode, which then dominates at later times. By tracking the integrated power of each mode on a log plot, we can identify a "knee" in the curve where the growth deviates from exponential, marking the transition to non-linear saturation. For the 1 mm mode, integrated from $\lambda = 0.8$–1.2 mm, this transition occurs at $t \approx 220$ ns, corresponding to a threshold of $A/\lambda = 0.07$–0.11. Note that the range of A/λ values is calculated from the lower and upper wavelength bounds of the integration. The larger 2 mm mode, integrated from $\lambda = 1.2$–2.2 mm, transitions later at $t \approx 283$ ns and at a higher threshold of $A/\lambda = 0.16$–0.3. The transition to non-linearity is visually confirmed by the appearance of non-linear cusp structures in the boundary image at $t = 308$ ns. By this time, the 2-mm mode is the only dominant mode and has grown to $A/\lambda = 0.3$–0.56, further supporting that the state of the instability growth is non-linear.

This analysis was repeated for a three-mode shot (see Fig. 5.25), and the transition thresholds were found to be consistent with those of the two-mode shot. The three dominant wavelengths, 0.8 mm, 1.2 mm, and 2 mm, transitioned at $A/\lambda = 0.14$–0.28, 0.1–0.14, and 0.14–0.28, respectively. These findings provide supporting evidence for the recurrence of exponential growth through mode merging. As small modes saturate and merge, energy cascades to larger wavelength modes that have a higher linear saturation amplitude, allowing

the overall perturbation to continue near-exponential growth. The transition to non-linearity generally occurred in the range of $A/\lambda \approx 0.1$–0.3.

5.6 Current Coupling

Current delivery is an important parameter in magnetically driven implosions, as the peak current determines the drive pressure. For a low impedance driver like MAIZE, the delivered current is highly sensitive to the initial load inductance.

The GoL target is shown to consistently couple more current from the generator than the liner-only targets. This is because the GoL configuration presents a lower initial inductance. In a GoL shot, the current initially flows through the large-radius gas-puff ($r_{\text{in}} \approx 10$ mm, giving $L \approx 4.8$ nH). Whereas in a liner-only shot, the current path begins at the small-radius liner ($r_{\text{in}} \approx 3$ mm, giving $L \approx 9.6$ nH). A high initial gas pressure was also observed to further increase the current coupling. This effect is evident in the current waveforms, as shown in Figs. 5.26(b) and 5.27(b). The liner-only target drew a peak current of 477 kA with a 200 ns rise time. By contrast, the GoL target drew a higher peak current of 560 kA with a faster 145 ns rise time. An unexpected feature in the GoL shots was the development of a flat-top current pulse, unlike the more sinusoidal pulse of the liner-only targets. Note that the Rogowski coil signal does not return to zero at later times, $t \geq 300$ ns. This is likely due to either the machine self-crowbarring or a flow of charged particles shielding the probe.

An unanswered question is the nature of the current partitioning in the GoL target. Before the gas fully ionizes, the current likely flows through the liner. After gas breakdown, it is unclear how the current divides between the gas plasma and the liner, which has significant implications for the magnetic pressure distribution and overall implosion dynamics. A comparison of the self-emission images suggests that, in the GoL target, the majority of the drive current initially flows through the gas plasma rather than through the liner. The primary evidence for this current partition is the observed dynamics. In the GoL shots, the gas shell implodes while the liner remains stationary for a significant period. Since the implosion is driven by magnetic pressure, this indicates that the gas carries the bulk of the current during this phase. Additionally, this conclusion is supported by the timing of thermal emission. In the liner-only shots, the liner heats up and emits light early in the current pulse. By contrast, in the GoL shots, the liner remains dark until the moment the gas collides with it. This suggests rapid heating and ionization of the liner through current switching from the gas to the liner.

Although the GoL targets draw more current, the initial magnetic pressure driving the implosion can actually be lower than in the liner-only cases [Fig. 5.26(d)]. The GoL target's

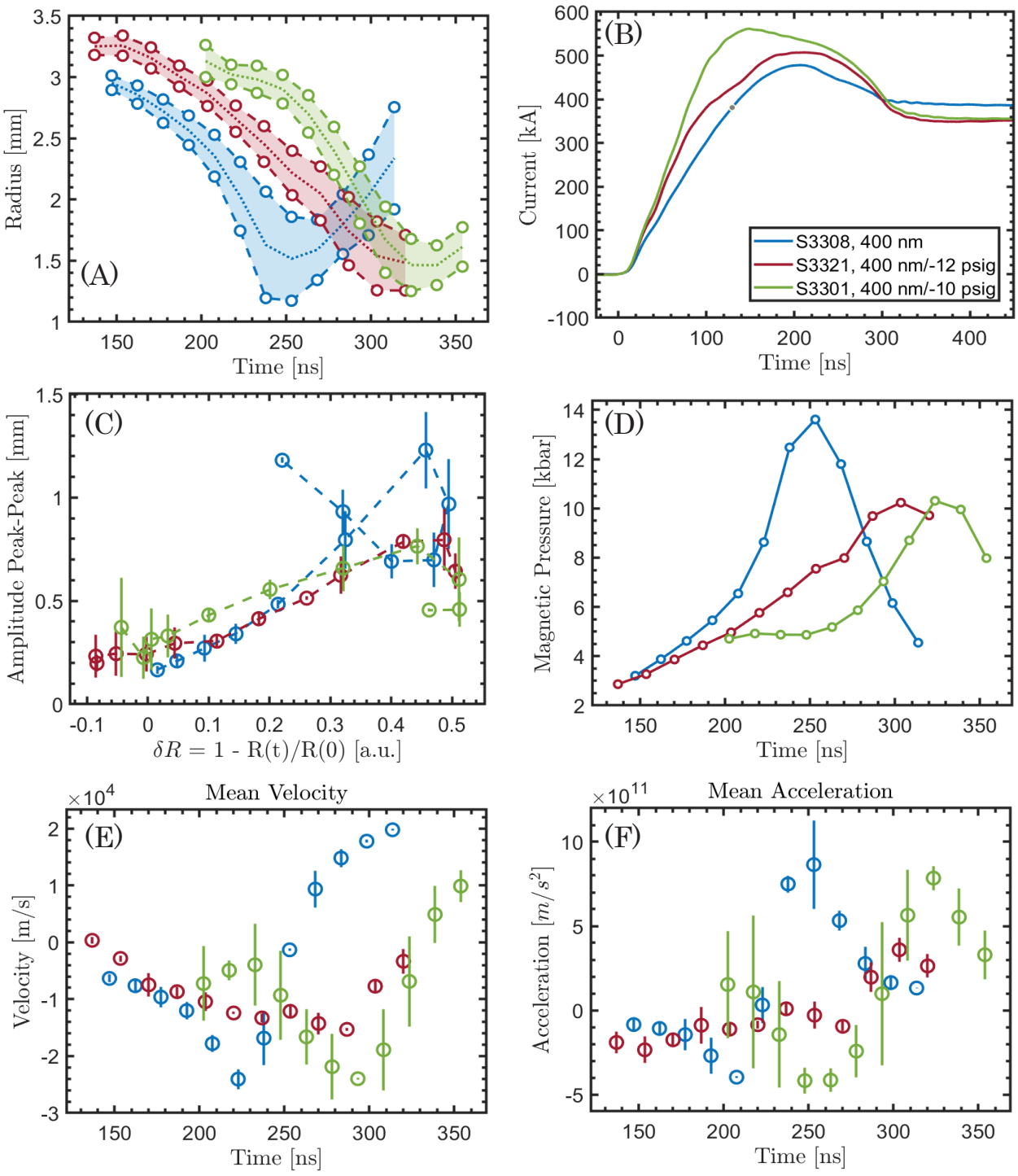


Figure 5.26: A comparison of GoL targets with constant 400 nm liner thickness and varying gas pressures: no gas (shot 3308), −12 psig (shot 3321), and −10 psig (shot 3301). The plots show: (a) implosion trajectories; (b) drive current waveforms; (c) instability amplitudes as a function of normalized distance moved; (d) magnetic pressures; (e) velocities; and (f) accelerations.

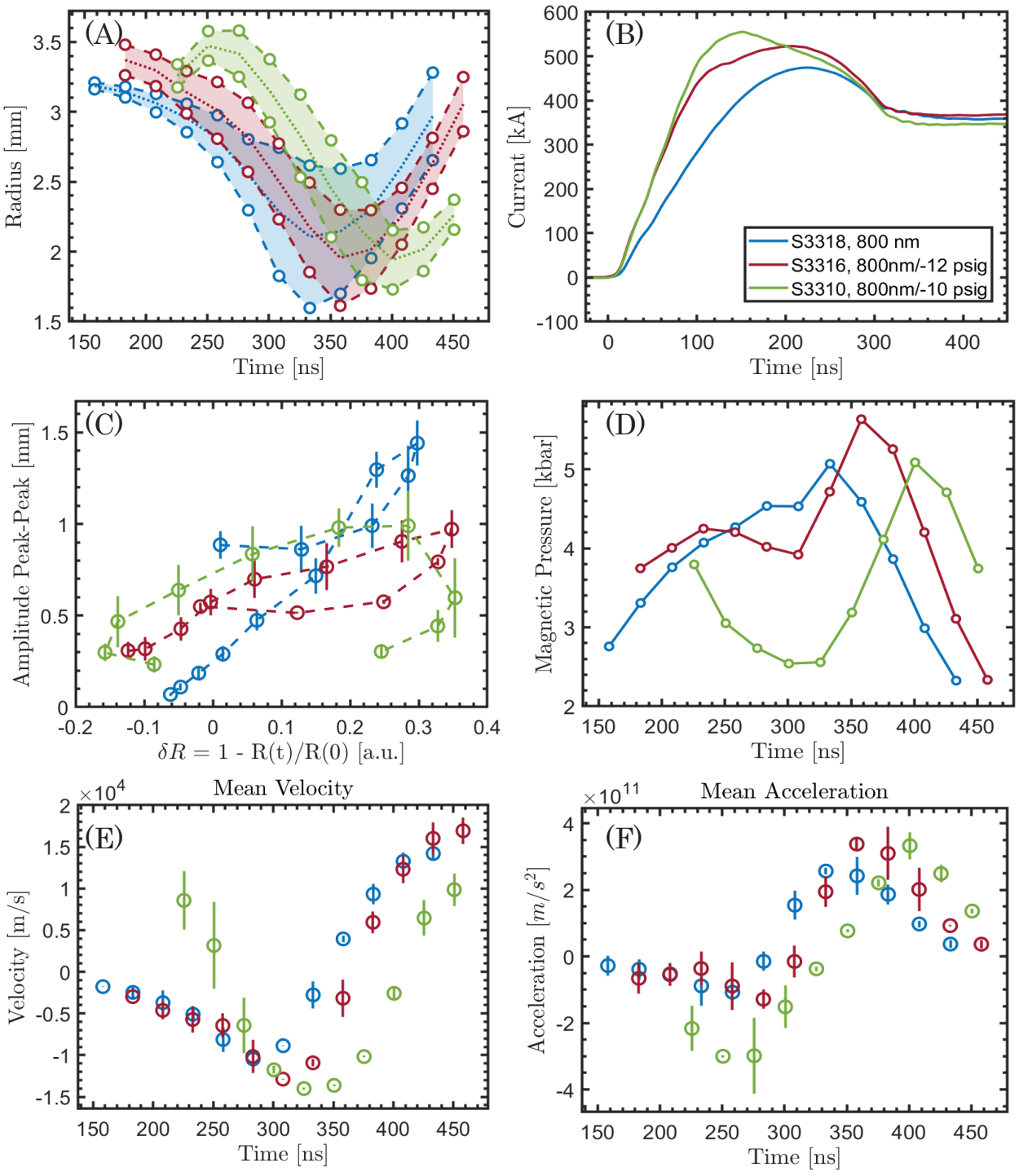


Figure 5.27: A comparison of GoL targets with constant 800 nm liner thickness and varying gas pressures: no gas (shot 3318), −12 psig (shot 3316), and −10 psig (shot 3310). The plots show: (a) implosion trajectories; (b) drive current waveforms; (c) instability amplitudes as a function of normalized distance moved; (d) magnetic pressures; (e) velocities; and (f) accelerations.

current (I) is $\approx$ 20% higher, but its initial radius (r) is three times larger. The strong dependence on radius dominates, resulting in a lower initial pressure for the GoL target ($\approx$ 10 kbar) compared to the liner-only target ($\approx$ 14 kbar) since magnetic pressure scales as $P_{\text{mag}} \propto I^2/r^2$. Furthermore, at late times ($t \geq 300$ ns), the current is crowbarring, which increases the uncertainties in this region and suggests that the actual magnetic pressure is likely even lower than the calculated values. Nonetheless, despite experiencing a lower magnetic drive pressure, the GoL targets converge just as effectively as, and in some cases even better than, the liner-only target. This strongly suggests that an additional mechanism is aiding the implosion in the GoL configuration. The most plausible explanation is that the ram pressure delivered by the impacting gas plasma provides a pressure drive that compensates for the lower magnetic pressure.

The GoL targets achieved a higher maximum implosion velocity compared to the liner-only target [Fig. 5.27(e)]. The liner-only shot reached 10.5 ± 0.6 km/s, while the -10 psig and -12 psig GoL shots reached significantly higher velocities of 14.0 ± 0.2 km/s and 12.8 ± 0.3 km/s, respectively.

However, the acceleration history provides a more complex picture. One hypothesis was that the gas layer stabilizes the liner by reducing its acceleration. The data did not support this. For example, a GoL target (shot 3316) had an acceleration history comparable to a liner-only target (shot 3318), yet its instability amplitude was $\sim$ 50% smaller, as shown in Fig. 5.27. Furthermore, another GoL target (shot 3310) had nearly twice the acceleration compared to shot 3316 but still produced a smaller instability. These results suggest that the reduced acceleration is not the dominant stabilization mechanism in these experiments. This points toward other effects, such as a smoothed density profile, that could be more important.

These results are promising for advanced target design and suggest several avenues for future research. Future optimization studies could explore the ideal parameters to maximize the final liner velocity.

5.7 Chapter 5 Summary

This chapter investigates the coupling between a low-density gas plasma and an imploding thin-aluminum-foil liner (400 nm, 800 nm, and 1500 nm). These experiments were performed without an axial magnetic field to isolate the hydrodynamic effects of the gas plasma layer on the dynamics of the liner implosion. The study was conducted in two parts: first, the baseline behavior of the liner-only target was characterized; second, a gas-puff was introduced to create a GoL configuration. The primary motivation is to distinguish between two potential instability seeding mechanisms: density imprinting and magnetic imprinting. By removing the axial magnetic field, we can directly observe whether the hydrodynamic impact of the gas plasma alone is sufficient to seed instabilities in the liner.

At lower gas pressures, GoL targets achieved stagnation radii comparable to the liner-only targets. However, it is noted that the maximum achievable convergence is constrained to $CR \sim 6$ due to the presence of the support rod, which has a radius of 0.5 mm. A significant difference, however, was the stagnation time, which was delayed by more than 100 ns for GoL targets. This delay is attributed to the time required for the current to first ionize and implode the gas shell onto the liner.

The GoL targets also coupled more current from the generator due to their lower initial inductance, since the current is initially flowing through the larger-radius gas-puff. This, however, led to a lower initial magnetic drive pressure due to the larger initial radius. Despite this lower magnetic drive, the GoL targets converged just as efficiently. This suggests that an additional mechanism is at play. It is theorized that either the additional ram pressure from the impacting gas imparts additional pressure, or the modification to the current pulse may serve as the cause, or potentially a combination of both.

Power spectra of the liner-only targets reveal that a consistent dominant wavelength of ~ 2 mm develops during the implosion. We postulate a three-stage instability process that sets the dominant wavelength. First, the electrothermal instability (ETI) seeds a broad spectra of small-wavelength perturbations on the liner surface prior to significant radial motion. Subsequently, these perturbations are subjected to current-driven instabilities and undergo mode mergers prior to any significant motion in the liner, thus increasing their wavelength. Finally, as the liner accelerates, the MRTI amplifies these seeded modes and drives further mode merger events. This procedure explains the observed dependence on liner mass. Lighter, faster-imploding liners (400 nm) stagnate earlier, providing less time for mode merging. As a result, they retain a broader, smaller-wavelength spectra. Heavier liners (800 nm) implode more slowly, allowing more time for instabilities to merge into the single, characteristic ~ 2 mm dominant mode.

The GoL targets exhibit a more complex spectra, which appears to be a mix of liner and gas modes. Often, two dominant modes exist simultaneously: a smaller wavelength mode (~ 2 mm) from the liner and a larger wavelength mode (> 3 mm) from the gas. The persistence of both spectra throughout the implosion suggests that they may either evolve independently from each other (decoupled evolution of the two interfaces), or there may be mode competition occurring between them. The nature of their interaction remains unclear without further investigation. It is noteworthy that the inverse cascade was not seen on the liner during the GoL experiments. This absence could be attributed either to the obscuring effect of the superimposed gas plasma layer or to the possibility that the layer itself inhibited the occurrence of the inverse cascade.

The dominant wavelength resulting from the mode mergers for liner-only targets grows as $t^{1–1.5}$. This growth appears to be independent of both liner mass and acceleration. This is supported by the constant rate of increase in the dominant wavelength, even when the 1500 nm liner, which was substantially heavier than the 400 nm liner, barely imploded ($g \approx 0$).

A significant finding of this chapter is that a gas layer provides a powerful stabilizing effect on an imploding liner. The GoL targets were consistently more stable against MRTI than their liner-only counterparts. This conclusion is supported by two key metrics: the GoL targets exhibited smaller peak instability amplitudes, and their calculated MRTI growth rates were significantly lower. The data also provided an important insight into the stabilization mechanism. Several effects are likely at play (such as a smoothed density profile or a decreased aspect ratio), the analysis showed that reduced acceleration is not the dominant cause of the observed stability.

CHAPTER 6

Magnetized Gas on Liner Experiment

The experiments presented in this chapter examine the magnetic imprinting of helical instabilities on a magnetized gas-on-liner (MGoL) target. Preceding chapters have established that the gas plasma shell produces an observable steep helical instability structure when a relatively small axial magnetic field is applied compared to the azimuthal magnetic field. This plasma shell is capable of compressing the axial magnetic field, leading to the development of distinct modes in the gas plasma. The gas-on-liner (GoL) experiments established that the wavelength emerging from the liner is shorter than that of the gas. This observation suggests that density imprinting from the gas may not be a significant influence. The investigation of fully integrated MGoL targets aims to determine whether the helical pitch angle of the compressed gas plasma increases the instability pitch angle formed on the liner via magnetic imprinting. The fast framing camera and laser backlighting were the primary diagnostics used to track the instability wavelengths and target morphology as evidence of this coupling.

This chapter details the implosion of an axially magnetized composite target, studying the development of helical modes in a solid density metal liner from magnetic imprinting. Section 6.1 describes the experimental setup and choice of the target. Section 6.2 presents helical mode coupling onto the liner. In Section 6.3, we cover the implosion dynamics of the MGoL configuration for increasing axial magnetic field strengths. In Section 6.4, the results of laser probing are detailed. Finally, Section 6.5 summarizes these findings and discusses their implications for understanding instability seeding from a magnetized low-density plasma onto an imploding thin metal liner.

6.1 Experiment Setup

In this experimental setup, the configuration from Chapter 5 was used, with the addition of a fringe axial magnetic field generated by the axial field coil, as shown in Fig. 6.1. The

magnetic field strength was varied within the range of 0–0.75 T in a single direction. For the liner material, a 400-nm-thick liner was used, given its good results in the gas-on-liner (GoL) experiments. The dimensions and construction of the targets remained consistent with those detailed in Chapter 5. However, due to the curing shrinkage of the support material, the outer radius of the liner was slightly reduced to approximately 2.8–3 mm. The operational gas pressure was −12 psig and −8 psig, as these values minimized the deformation of the liner target to an acceptable degree. Within this campaign, we evaluated target performance and instability seeding for MGoL in contrast to an axially magnetized liner-only target. The diagnostics fielded included those previously mentioned in Chapter 5, with the addition of a laser probing diagnostic to attempt to probe through the gas plasma.

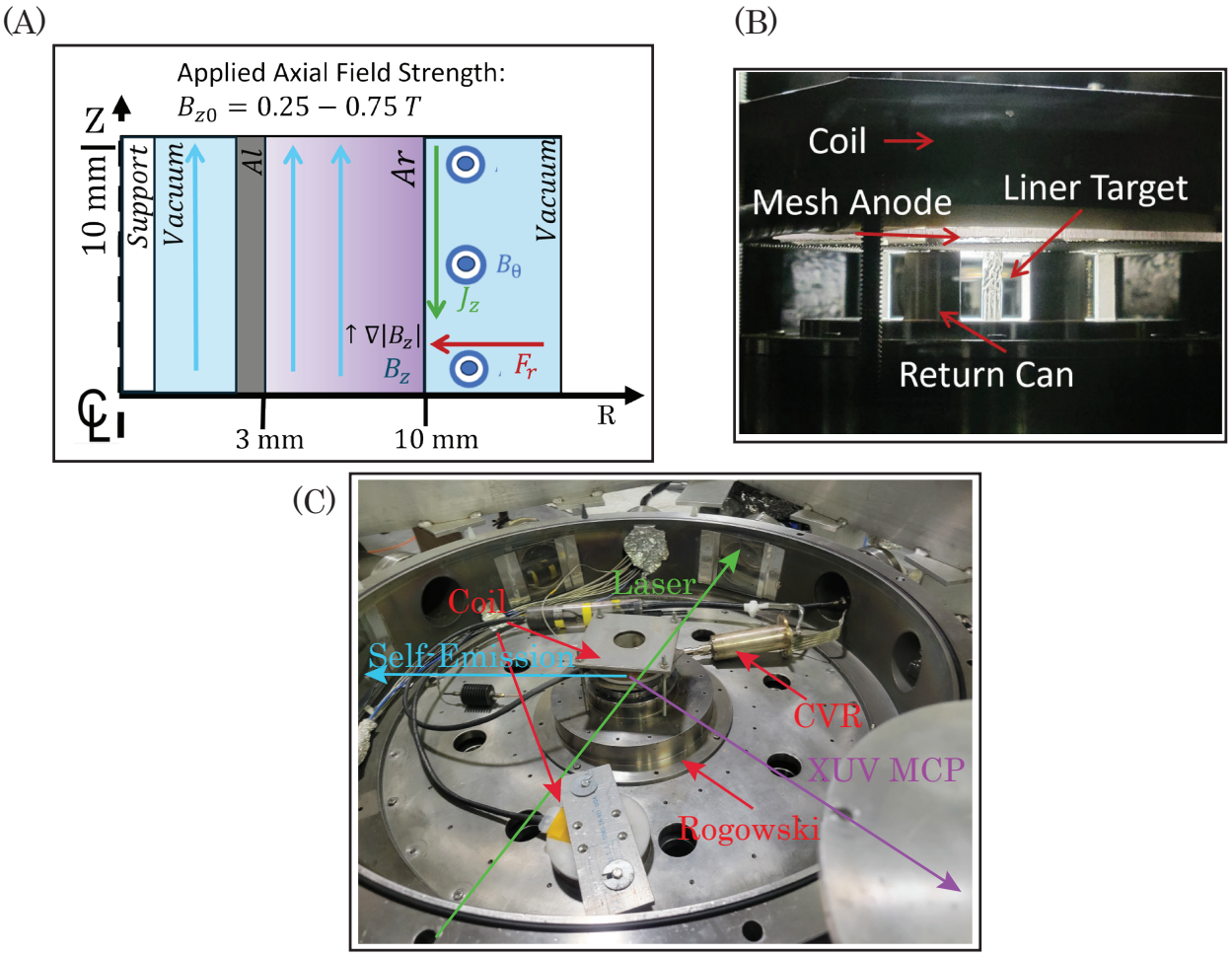


Figure 6.1: (a) Cross-section of the MGoL target. (b) Photograph of a target installed in MAIZE's central load region. (c) An overview of the MAIZE vacuum chamber with the primary diagnostics labeled.

6.2 Helical Mode Coupling

To analyze the helical modes, raw images are imported and subsequently cropped to focus on the specific regions of interest. Each image undergoes individual contrast adjustment and is processed through a Gaussian filter with a 3 pixel × 3 pixel box. The image is then finally passed through an unsharpen filter with a 20-pixel radius and a sharpening magnitude of 10 pixels. This sequence of processing prepares the image for helical pitch angle analysis. The research focuses on examining front-facing instabilities, characterized by the dark and bright emissions from the liner, as shown in Fig 6.2. Helical pitch angles are traced using a processing script (see appendix B), which identifies either darker or brighter pixels across a specified set of data points; in this study, an N of 100 was used. The script searches for the next bright or dark point within a 3-pixel box from the initial position, moving from left to right. Each helical trace within the image frame is fitted using a first-order polynomial approximation. The arctangent of the slope derived from this fit is considered the pitch angle for the respective striation. The mean value of these pitch angles is interpreted as the helical pitch angle at a particular frame or time. The associated uncertainty is calculated as the standard deviation of the pitch angles divided by the square root of their count, which is equivalent to the standard error of the mean.

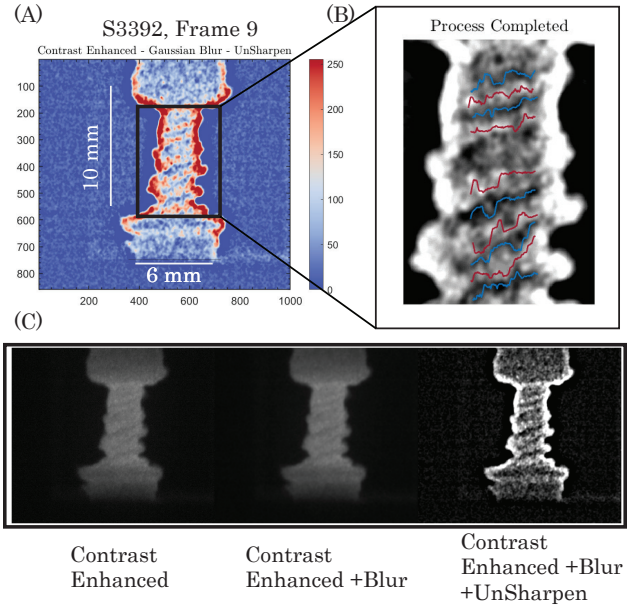


Figure 6.2: (a) A processed image of frame 9 (t =322 ns) of shot 3392 for an MGoL target. (b) The result of the automated tracing algorithm, identifying the dark (blue) and bright (red) helical striations. (c) Intermediate steps in the image processing, including contrast enhancement, Gaussian blurring, and an unsharp mask filter.

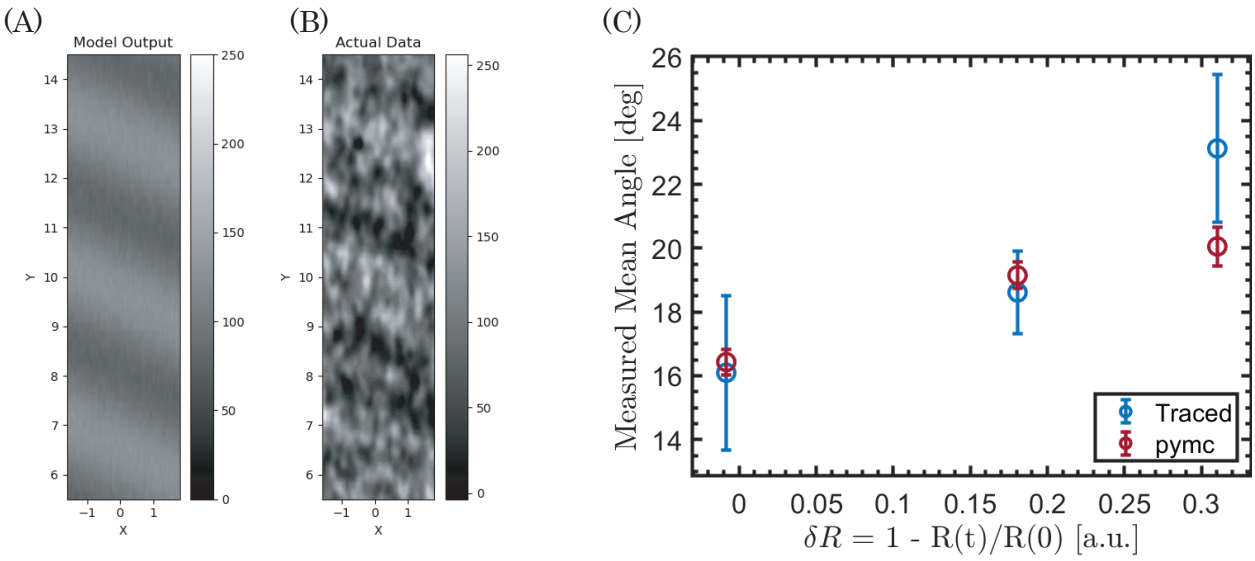


Figure 6.3: (a) A synthetic image of the instability, reconstructed from the results of the Bayesian analysis. (b) The corresponding trimmed and processed self-emission image used as the input for the analysis. (c) A plot of the resultant helical pitch angle as a function of normalize distanced moved, comparing the results from the direct tracing method with the more robust Bayesian approach.

Additionally, to provide a more robust measurement of the helical pitch angles and their uncertainty, we modeled the two-dimensional image data using a Bayesian framework with the PyMC library, as shown in Fig. 6.3. The data were modeled as a sinusoidal plane wave, described by the following:

$$I(X,Y) = A_0 + A\sin\left[\frac{2\pi}{\lambda}(Y\cos\theta + X\sin\theta) + \phi\right], \tag{6.1}$$

where A_0 is the background intensity, A is the self-emission intensity, λ is the wavelength, θ is the angle of wave propagation, ϕ is the phase offset, and X and Y are the spatial coordinates. The likelihood of the observed data was assumed to follow a Laplace distribution, where the mean was defined by the model $I(X,Y)$ with a noise level of σ. The priors for the model were chosen to have a uniform distribution over ranges informed by experiments. The posterior distribution for the model was estimated using the No-U-Turn Sampler (NUTS), a gradient-based Markov Chain Monte Carlo algorithm. The analysis was performed by running 8 parallel chains, with each chain generating 5000 samples from the posterior distribution. The pitch angle derived from the Bayesian methodology closely aligns with that obtained through the intensity tracing algorithm while showing reduced uncertainty in comparison. This highlights the strength of the Bayesian approach. Nevertheless, the model presumes a single dominant wavelength, thereby constraining its capacity to represent the initial development

of multi-modal instability. Future work should develop a novel model that accommodates multiple wavelengths.

In the visible-light self-emission images, the development of instabilities in various liner configurations can be observed, as shown in Fig. 6.4. During the implosion process of the liner, it becomes evident that detecting the front-facing striations is challenging until the target nears stagnation, at which point the fingers and bubbles begin to emit at contrasting intensities. However, at post-stagnation, the presence of helical instabilities is apparent in both the axially magnetized liners and the MGoL target. It is postulated that the striations of the magnetized liner are not initially visible due to the small wavelength and broad nature of the initial perturbations, which lead to a blurring effect in the emission contrast. The MGoL target presents additional challenges due to the emission of the gas layer on top of the liner. With an increase in the magnetic field strength for the MGoL target, these striations are absent. This absence indicates that the instabilities are effectively mitigated, as evidenced by the smooth interface observed at the boundary between the target and the vacuum.

Despite the inability to observe the front-facing striations at the initial radius preceding the implosion, the helical pitch angle during the explosion is visible. It is postulated that pitch-locking persists throughout the trajectory from implosion to explosion. Given this condition and the requirement for pitch conservation as the radius evolves, it is anticipated that the pitch angle prior to implosion corresponds to the pitch angle of the exploding liner upon reaching the same radius.

From the front-facing striation tracing, we observe that the application of a $B_{z0} = 0.25$ T magnetic field to the GoL targets results in the formation of pronounced helical pitch angles on the liner surface, as shown in Fig. 6.5. Notably, the majority of these pitch angle measurements were taken near stagnation or during the explosion phases. The mean measured pitch angle is plotted as a function of normalized distance moved (δR), as the pitch angle is anticipated to be $\propto \arctan(m/kR)$. At approximately the initial radius of 3 mm ($\delta R \approx 0$), the pitch angle was recorded as $\approx 16^\circ \pm 2^\circ$. This increased to a pitch angle of $\approx 27^\circ \pm 5^\circ$ at $\delta R \approx 0.4$. Upon further enhancement of the axial magnetic field applied ($B_{z0} = 0.5$ T) to the MGoL target, we observe an increase in the pitch angle measured at $\approx 36^\circ \pm 3^\circ$ at $\delta R \approx 0.15$. These sets of measured pitch angles appear to be inversely proportional to the radius, which is consistent with pitch locking.

Part of this investigation compares liner-only target performance with MGoL target performance. Here, the liner-only target used $B_{z0} = 0.75$ T, while the MGoL target used $B_{z0} = 0.25$ T. For the liner-only targets, the mean pitch angles at $\delta R \approx 0.3$ were calculated to be $\approx 8^\circ \pm 1^\circ$, which is lower than those in the MGoL targets, despite the initially applied

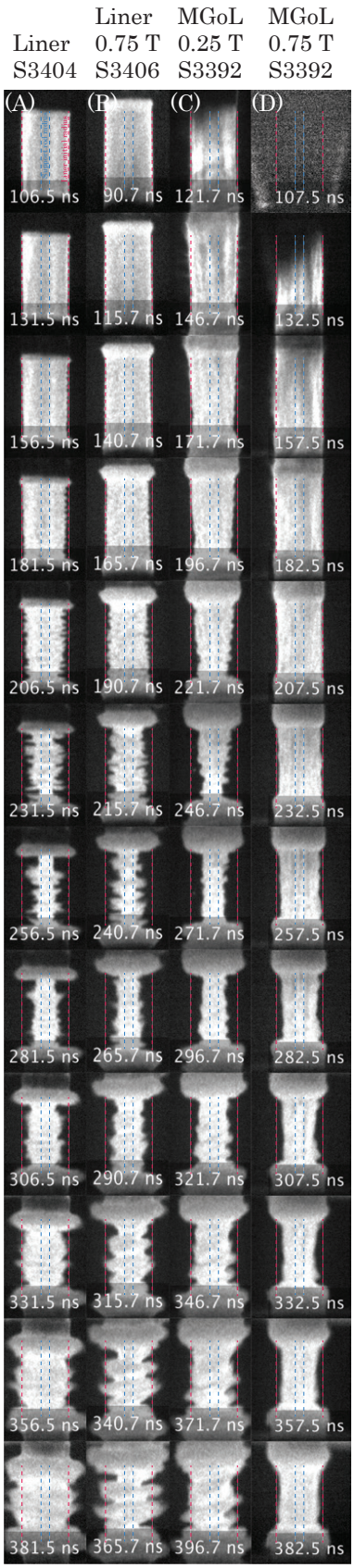


Figure 6.4: Visible-light self-emission images showing the implosion, stagnation, and explosion phases for various liner targets. The panels show: (a) $B_{z0} = 0$ liner-only; (b) $B_{z0} = 0.75$ T liner-only; (c) $B_{z0} = 0.25$ T and -12 psig MGoL; and (d) $B_{z0} = 0.75$ T and -12 psig MGoL. Note the pronounced helical structures as the liner explodes radially outwards.

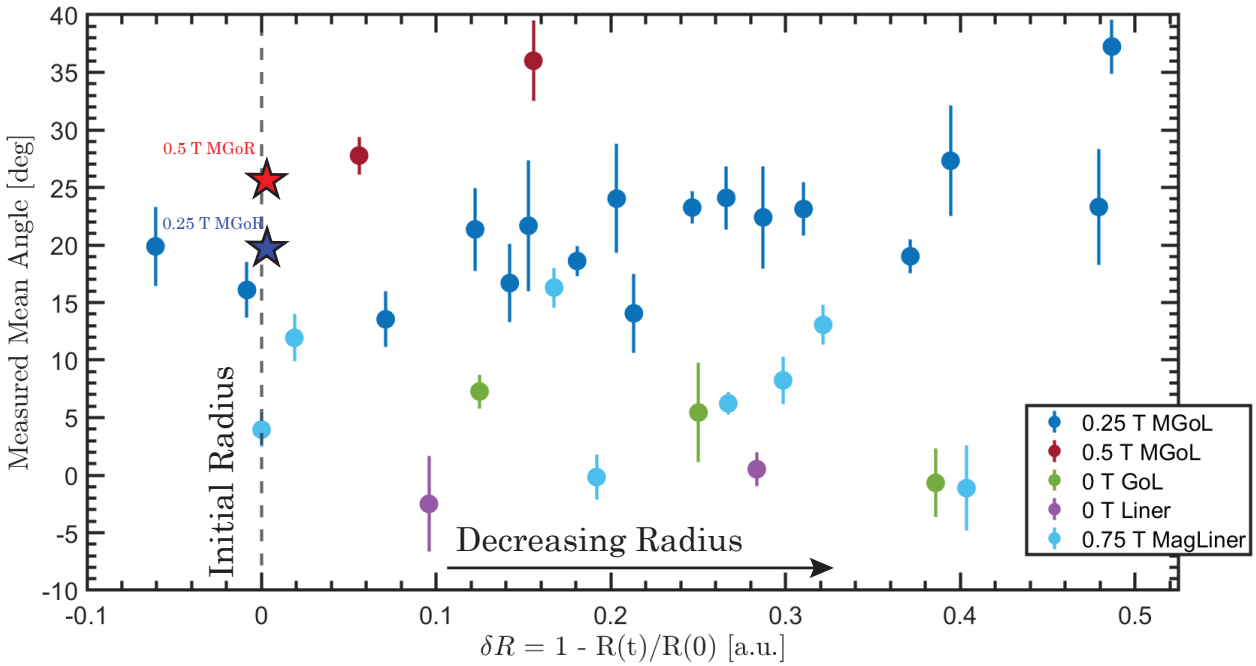


Figure 6.5: Measured instability pitch angles for various target configurations as a function of normalized distance moved. The targets include $B_{z0} = 0$ liner-only (purple), $B_{z0} = 0.75$ T liner-only (cyan), $B_{z0} = 0$ GoL (green), $B_{z0} = 0.25$ T MGoL (blue), and $B_{z0} = 0.5$ T MGoL (red). The larger positive x-axis values correspond to a smaller implosion radius, and the dashed black line indicates the initial 3 mm radius. The star markers represent data from the MGoR experiments, with applied axial magnetic field of $B_{z0} = 0.25$ T (blue) and $B_{z0} = 0.5$ T (red), showing the final instability pitch angle of the gas as it stagnated onto the solid rod. Notably, the stagnated pitch angle of the gas in the MGoR experiments is very similar to the initial pitch angle measured on the liner in the MGoL experiments when B_{z0} is the same for both cases.

field being three times greater in the liner-only targets. The decision to use a 0.75 T field for the liner-only target was due to the observed measurements from the magnetized gas-on-rod (MGoR) experiments, which determined a B_{z0} compression ratio of ∼2.5–3. Thus, in order to compare a MGoL target with $B_{z0} = 0.25\ T$, it is necessary for the liner-only target to have an axial magnetic field within 0.63–0.75 T. However, these results should be interpreted cautiously, as the measurement captured axial magnetic flux on-axis, which accounted for only 50% of the predicted compressed field based on the outer boundary of the gas plasma. It is possible that a higher magnetic field is compressed onto the surface of the liner. Nevertheless, the compression of an axial magnetic field from a gas plasma onto a solid metallic liner increases the pitch angle of helical striations on the surface of the liner. In this context, the ratio of the applied axial magnetic field to the peak azimuthal magnetic field is $b \sim 0.0075$ at $r = 3$ mm. Assuming 100% flux conservation, the resultant compressed axial magnetic field would be 1.52 T, which remains severely insufficient to explain the helical pitch angles observed in the plasma, $\phi_{\text{plasma}}(t)$. For $\phi_B = arctan[B_z(t)/B_\theta(t)]$ to be equal to $\phi_{\text{plasma}}(t)$, the flux-compressed axial field, $B_z(t)$, would need to be approximately 11 T.

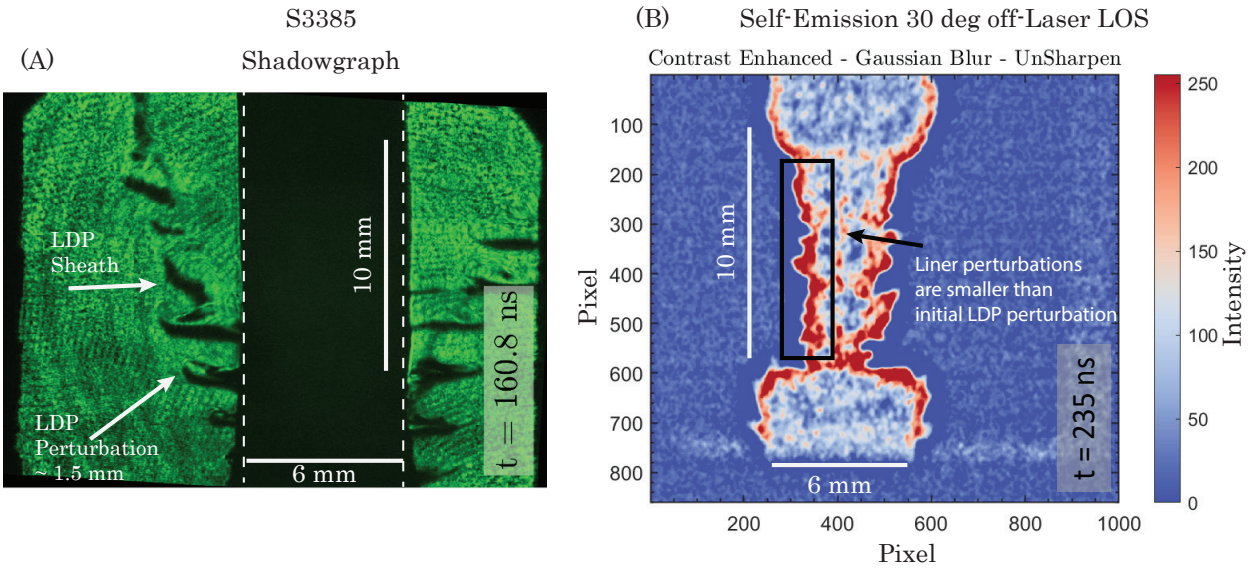


Figure 6.6: (a) Shadowgraph of an imploding gas plasma beginning to impact the thin-foil liner. (b) A self-emission image of the liner from the same shot, taken approximately 75 ns later from a 30° viewing angle off of the laser line of sight (LOS). The initial perturbation wavelength in the gas plasma (≈ 1.5 mm) is larger than the resulting perturbation wavelength observed on the liner.

Upon revisiting the MGoR experiments, the pitch angle of the imploding gas sheath was tracked, and it was observed that the pitch angle at which the sheath impacts the target closely aligns with the initial pitch angle formed on the liner in the MGoL experiments.

Specifically, for the MGoR experiments with $B_{z0} = 0.25$ T and 0.5 T, the measured pitch angles at impact with the rods are $\approx 20°$ and 25°, respectively. For the MGoL experiments with a field strength of $B_{z0} = 0.25$ T, the pitch angle at $r = 3$ mm measures $\approx 20°$. This observation is noteworthy, as the wavelength of the instabilities on the liner is smaller compared to that of the gas plasma, as identified in the preceding chapter. This phenomenon becomes more apparent with the aid of laser backlighting, as shown in Fig. 6.6, which presents data from a MGoL experiment. In Fig. 6.6(a), the shadowgraph shows the gas plasma sheath imploding onto the liner with a perturbation wavelength of approximately 1.5 mm. Subsequently, after ≈75 ns, the liner starts imploding [Fig. 6.6(b)], and the perturbation wavelength is smaller [compare Figs. 6.6(a) and 6.6(b)].

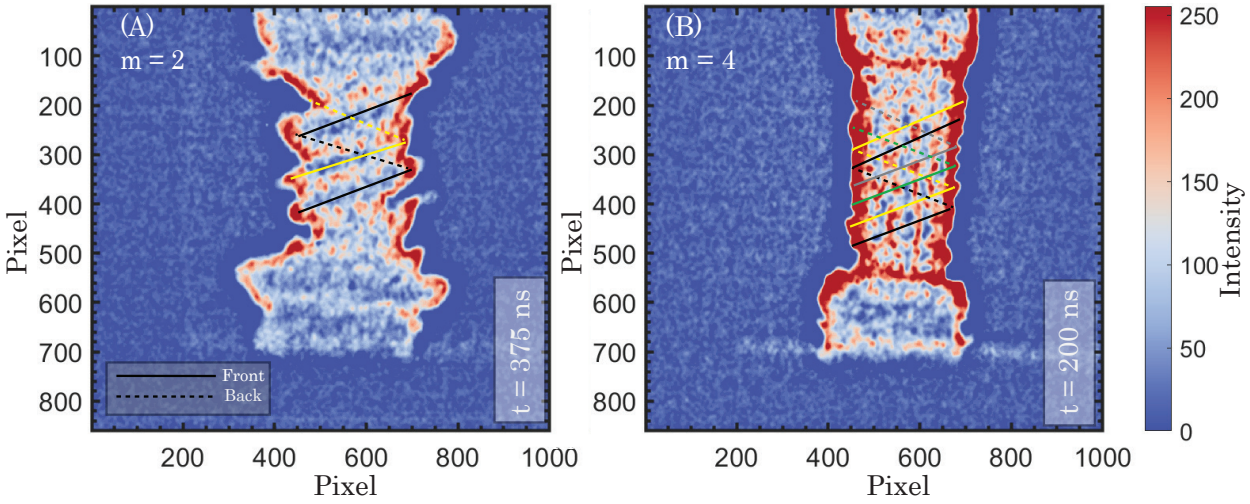


Figure 6.7: (a) A self-emission image of a MGoL target late in the explosion phase ($t = 375$ ns). The front-facing helical striations (solid lines) are clearly visible, which allows us to infer the approximate location of the back-facing helical striations (dashed lines) using simple connectivity arguments. (b) The same shot at a much earlier time ($t = 200$ ns). Although the striations are not visible on either surface in (b), the instabilities at the left and right edges of the image left and right edges of the image must connect. The overlaid lines in (b) show the inferred path of these striations, with the pitch angle determined by assuming pitch locking from the later-time measurements shown in (a).

To explain the underlying mechanisms, we postulate that the pitch is both transferred to and conserved within the liner. The pitch is $p = \lambda_z m$, where λ_z axial projection of the perturbation wavelength, and m represents the azimuthal mode number. If the pitch is conserved from the gas layer to the liner target, yet λ_z varies, then m must vary as well to compensate. Due to the smaller λ_z within the liner region, an increase in the m is required. To characterize m, we use the tracked helical striations along the front surface and assume a connection of the back-facing striations at an identical pitch angle. It was observed that near

stagnation, for a MGoL target with $B_{z0} = 0.25$ T, the azimuthal mode number is $m = 2$, as shown in Fig. 6.7.

It is reasonable to assert that an inverse cascade also occurs within the imploding liner of the MGoL configuration. Should this be the case, both λ_z and m must change together when mode merger events occur. For example, during stagnation, with $\lambda_z = 2$ mm and $m = 2$, tracing the cascade to an earlier time when $\lambda_z = 1$ mm necessitates $m = 4$ to conserve p. Notably, we observe wavelengths as minimal as $\lambda_z = 0.5$ mm, indicating the potential presence of at most $m = 8$ modes at the initiation of the liner implosion. Previous experimental studies have assessed the azimuthal mode number in axially magnetized foil experiments [16, 17] and have demonstrated that an increase in the axial magnetic field from 1 to 2 T consequently increases the azimuthal mode number from $m = 4$ to $m = 2$. Our MGoL experiments, by contrast, produced $m = 2$ by using $B_{z0} = 0.25$ T. This phenomenon is intriguing since it implies that either: (1) the development of the azimuthal mode is influenced by the gas layer; or (2) the gas layer compresses the B_{z0} to an extent equivalent to 1–2 T. On the second point, the striation pitch angles that we measured (20–35°) were significantly larger than the pitch angles presented in [16] (4–12°).

6.3 Implosion Dynamics

Following the successful performance results obtained from the GoL targets, we seek to further evaluate their performance under the influence of an applied axial magnetic field.

Figure 6.8 shows a collage of plots of various implosion performance metrics. We compare MGoL targets with a constant liner thickness of 400 nm, −12 psig of gas, and varying $B_{z0} = 0$–0.75 T to a 400-nm-thick liner-only target with $B_{z0} = 0.75$ T. First, consider the plots displaying stagnation radii [Fig. 6.8(a)] and stagnation times [Fig 6.8]. The stagnation radius in this context refers to the point at which the instability *bubble* attains the minimum radius of implosion. The findings indicate that the stagnation radius increases from ≈ 1.4 mm to ≈ 2.2 mm at axial magnetic fields of $B_{z0} = 0$ and 0.75 T, respectively. We speculate that the larger stagnation radius is attributable to the enhanced axial magnetic pressure introduced within the liner as a consequence of the interaction between the gas and the liner. This pressure may be adequate to provide a back pressure that prevents further compression. Notably, there was no observed increase in the stagnation radius at $B_{z0} = 0.25$ T. Any further increase in the axial magnetic field at this point results in an increased stagnation radius (i.e., reduced convergence). By contrast, the axially magnetized liner-only target demonstrated a stagnation radius of ≈ 1.5 mm, which is slightly larger than that of the unmagnetized GoL target. As for stagnation time, the magnetized liner exhibited earlier

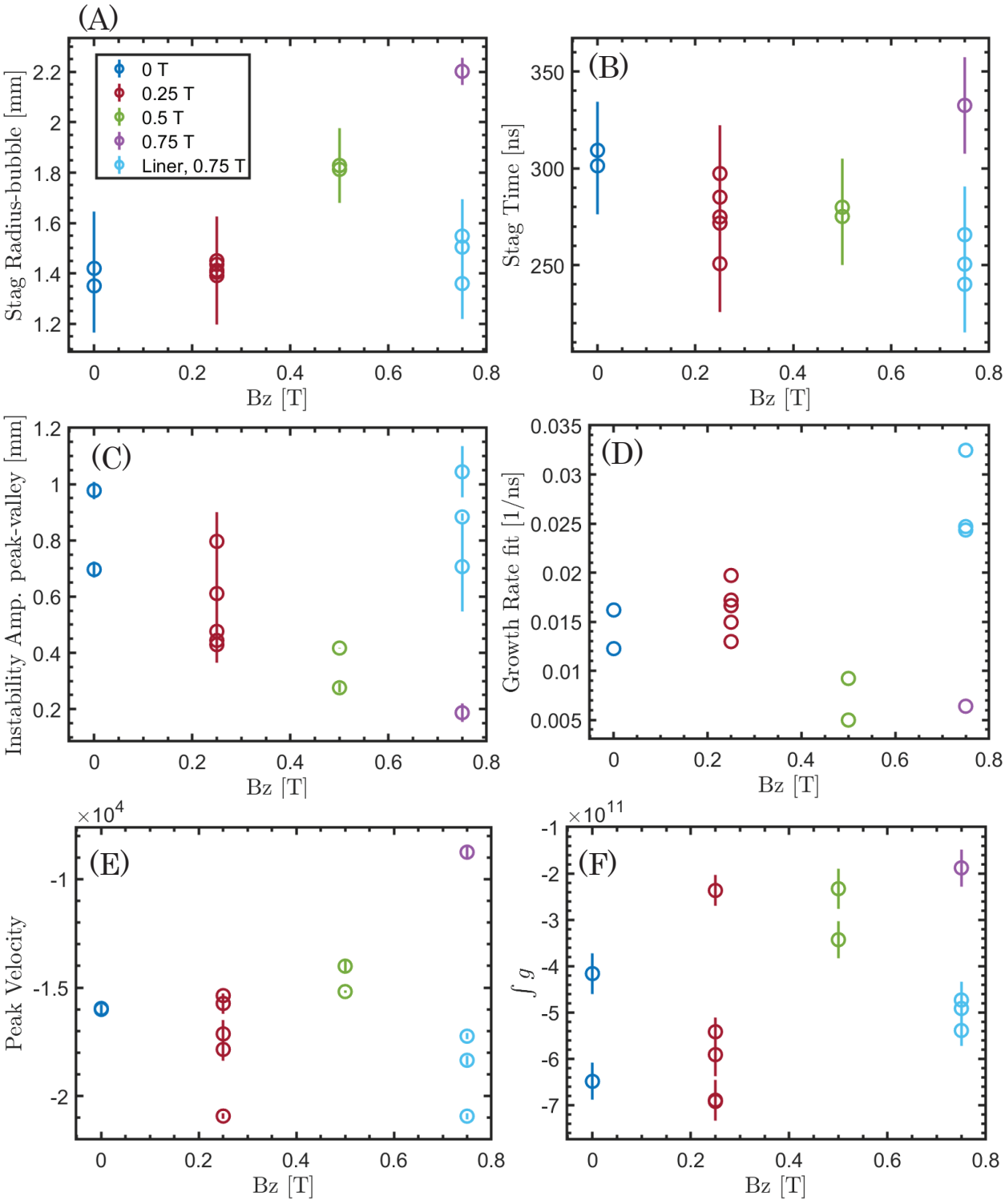


Figure 6.8: A collage of plots showing: (a) stagnation radii; (b) stagnation times; (c) peak-to-peak instability amplitudes; (d) instability growth rates; (e) peak target velocities; and (g) peak cumulative accelerations as a function of applied axial magnetic field. Across this dataset, the foil thickness (400 nm) and gas pressure (−12 psig) were held constant. Note that the cyan markers denote axially magnetized liner-only targets while the rest are MGoL targets.

stagnation, at $t \approx 250$ ns, whereas the unmagnetized GoL target stagnated at 300 ns, a result consistent with those reported in Chapter 5. Notably, the stagnation time for $B_{z0} = 0.25$–0.5 T occurred earlier, at $t \approx 275$ ns, while for $B_{z0} = 0.75$ T, it occurred later, at $t \approx 330$ ns.

Figure 6.9 presents data from MGoL targets, where the applied axial magnetic field was varied over the range of $B_{z0} = 0$–0.75 T. Across this dataset, the foil thickness (400 nm) and gas pressure (−12 psig) were held constant. It is observed that increasing the applied axial magnetic field does not significantly alter the current drawn, which was ≈ 500 kA. However, the magnetic pressure is lower for $B_{z0} = 0.5$–0.75 T compared to $B_{z0} = 0$–0.25 T, with the peak magnetic pressure reaching 11.6 kbar.

On the same figure [Fig. 6.9(e)], the peak velocity generally decreased as the axial magnetic field was increased. For example, the MGoL target with $B_{z0} = 0.25$ T reached an average peak velocity of $v_p \approx 16$ km/s. When the field was increased to $B_{z0} = 0.75$ T, the peak implosion velocity decreased by nearly half to $v_p \approx 8.7$ km/s. This trend shows that the magnetic field pressure provides significant back pressure against the implosion. While the liner-only target was the fastest, it is notable that some MGoL shots with a low magnetic field ($B_{z0} = 0.25$ T) still reached high velocities, comparable to the liner-only case with $v_p \approx 21$ km/s.

Figure 6.10 presents a compilation plot comparing three target types: (1) an unmagnetized GoL target; (2) an MGoL target (with $B_{z0} = 0.25$ T); and (3) a magnetized liner-only target (with $B_{z0} = 0.75$ T). Across the dataset, the foil thickness was held constant (400 nm). For the shots with gas, the pressure was set to −12 psig. Of particular interest is the observation that the velocity and acceleration of the MGoL targets closely resemble those of the axially magnetized liner-only target.

Stabilizing the MRTI growth is helpful for maintaining liner integrity. The experiments detailed in the previous chapter demonstrated that a gas plasma layer mitigates MRTI growth in comparison to a liner-only target. It is expected that the addition of an axial magnetic field to GoL targets will further decrease MRTI growth, and the experiments reported herein have shown this to be true. Specifically, the application of an axial magnetic field of $B_{z0} = 0$ resulted in an instability amplitude of $A_{p-p} = 0.8 \pm 0.1$ mm. An axial magnetic field of $B_{z0} = 0.25$ T yielded an instability amplitude of $A_{p-p} = 0.6 \pm 0.2$ mm, while a field of $B_{z0} = 0.5$ T produced an amplitude of $A_{p-p} = 0.3 \pm 0.1$ mm. Similarly, an axial magnetic field of $B_{z0} = 0.75$ T led to an instability amplitude of $A_{p-p} = 0.2 \pm 0.1$ mm. By contrast, an axial magnetic field of $B_{z0} = 0.75$ T applied to a liner-only target resulted in an amplitude of $A_{p-p} = 0.9 \pm 0.2$ mm. These findings are significant, indicating that the MRTI amplitude for MGoL targets is considerably reduced compared to previous configurations. Moreover, the application of $B_{z0} = 0.75$ T to a MGoL target reduced the instability amplitude by

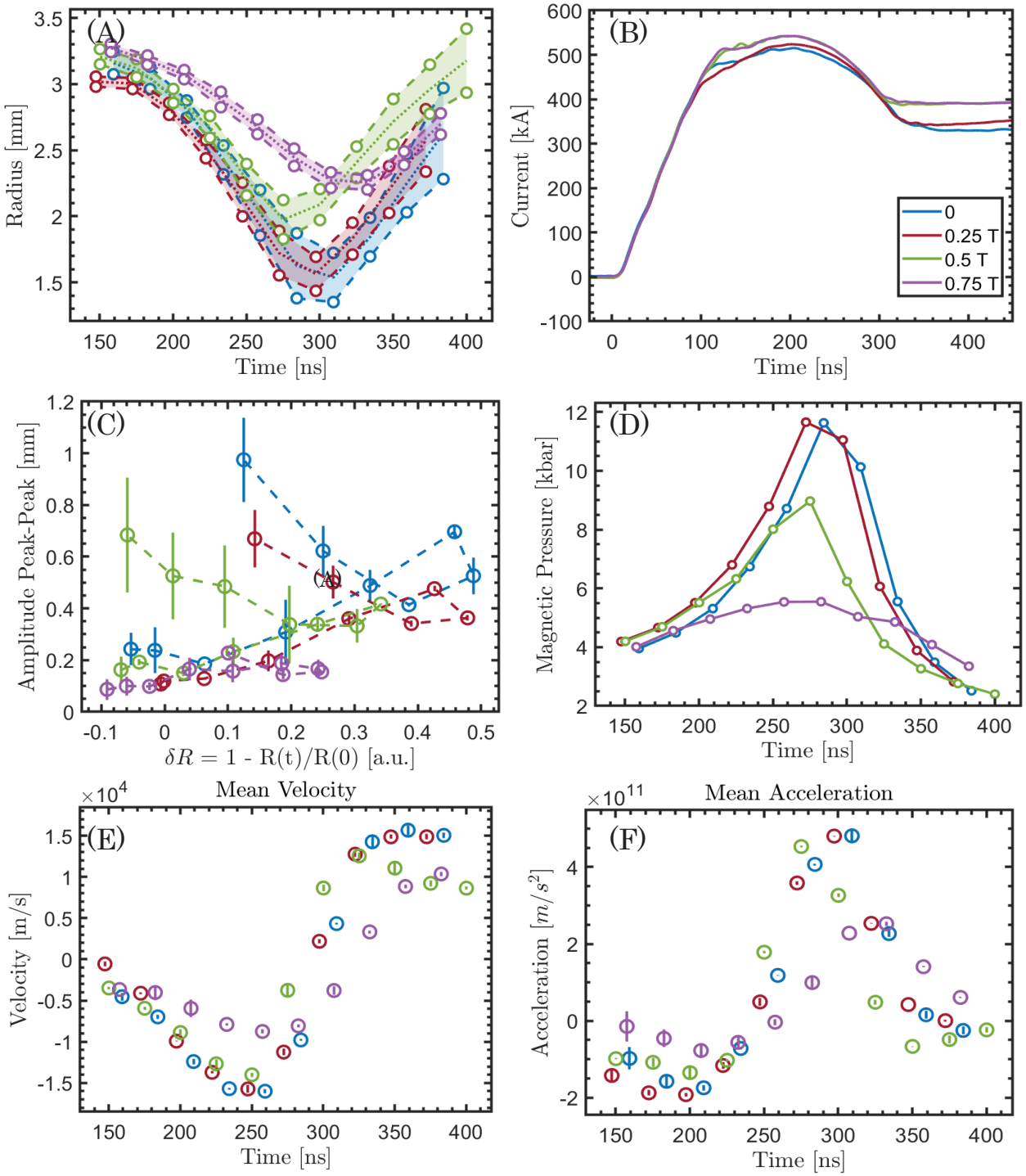


Figure 6.9: Collage of plots showing: (a) implosion trajectories; (b) drive current waveforms; (c) instability amplitudes as a function of normalized distance moved; (d) magnetic pressures; (e) velocities; and (f) accelerations. The plots compare MGoL targets with increasing axial magnetic field strength: $B_{z0} = 0$ (shot 3403, blue); $B_{z0} = 0.25$ T (shot 3399, red); $B_{z0} = 0.5$ T (shot 3394, green); and $B_{z0} = 0.75$ T (shot 3393, purple). Across this dataset, the foil thickness (400 nm) and gas pressure (-12 psig) were held constant.

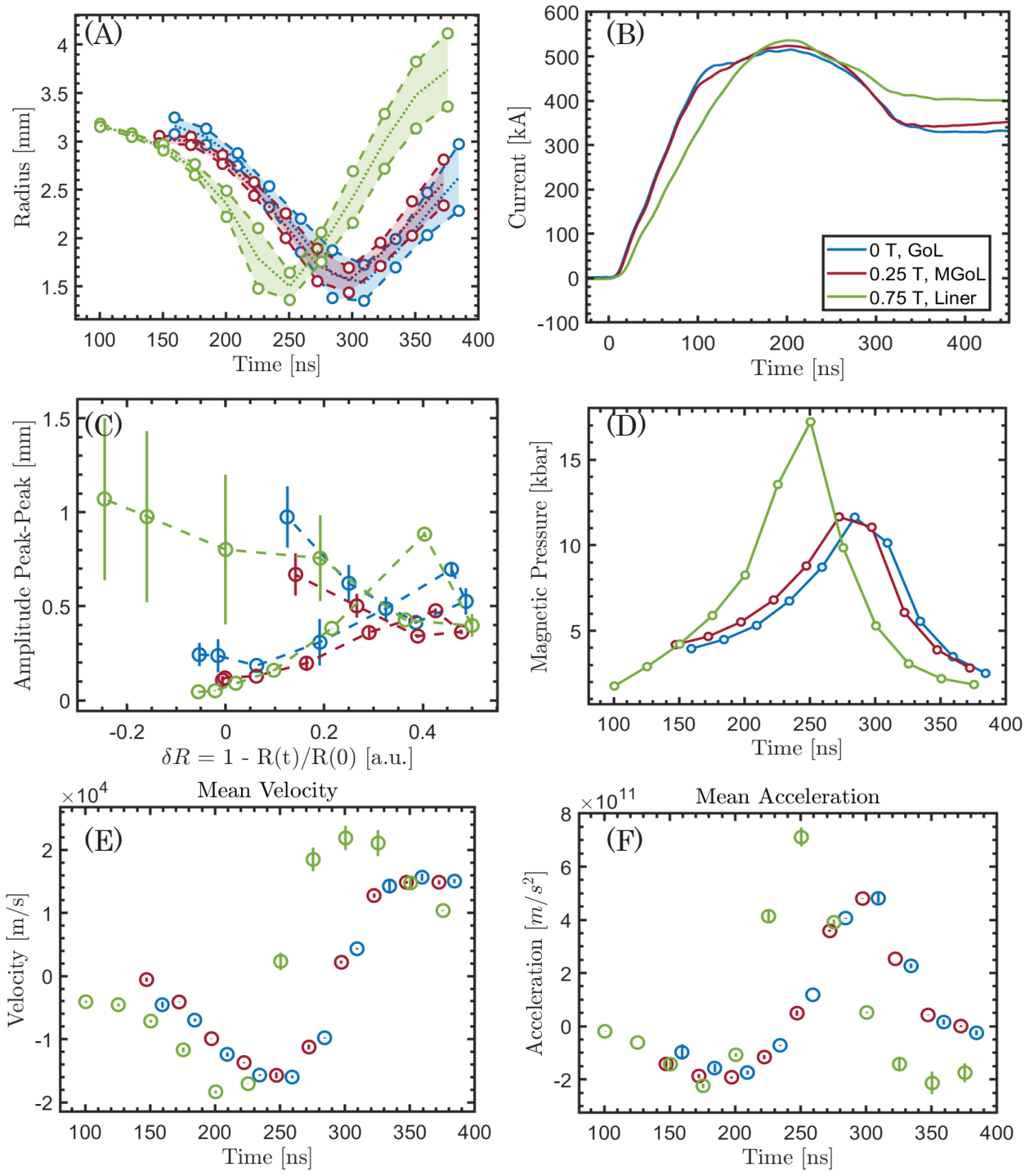


Figure 6.10: Collage of plots showing: (a) implosion trajectories; (b) drive current waveforms; (c) instability amplitudes as a function of normalized distance moved; (d) magnetic pressures; (e) velocities; and (f) accelerations. The plots compares: $B_{z0} = 0$ GoL target (shot 3403, blue); a $B_{z0} = 0.25$ T MGoL target (shot 3399, red); and a $B_{z0} = 0.75$ T liner-only target (shot 3407, green).

nearly a factor of five in comparison to a $B_{z0} = 0.75$ T liner-only target. However, it is noteworthy that the stagnation radius was less favorable for the 0.75 T MGoL target compared to the 0.75 T liner-only target. Nevertheless, the 0.25 T MGoL targets achieved convergence comparable to the 0.75 T liner-only targets, but with approximately half the instability growth.

These competing effects between the stability of MRTI and implosion velocity suggest that an optimal configuration may exist. The implosion performance of the magnetized liner-only and MGoL targets is shown in Table 6.1. While the $B_{z0} = 0.75$ T MGoL target was the most stable, its convergence was poor. However, the $B_{z0} = 0.25$ T MGoL target achieved a convergence comparable to the $B_{z0} = 0.75$ T liner-only target, but with half the instability amplitude. This indicates that a modest axial magnetic field, combined with an outer gas layer, can provide a more favorable outcome than simply using a very high axial magnetic field on a liner alone.

Table 6.1: Implosion performance for Liner and MGoL configurations.

	Liner	MGoL			
Liner thickness (nm)	400	400	400	400	400
Plenum pressure (psig)		-12	-12	-12	-12
Axial magnetic field (T)	0.75	0	0.25	0.5	0.75
Min. stagnation radius (mm)	1.47 ± 0.08	1.38 ± 0.15	1.42 ± 0.06	1.82 ± 0.09	2.20 ± 0.05
Stagnation time (ns)	252 ± 14	305 ± 18	276 ± 11	278 ± 18	333 ± 25
Peak velocity (m/s)	$(-1.88 \pm 0.1) \times 10^4$	$(-1.60 \pm 0.15) \times 10^4$	$(-1.74 \pm 0.2) \times 10^4$	$(-1.46 \pm 0.14) \times 10^4$	$(-8.76 \pm 0.28) \times 10^3$
Cumulative acceleration (m/s^2)	$(-5.01 \pm 0.23) \times 10^{11}$	$(-5.33 \pm 0.30) \times 10^{11}$	$(-5.50 \pm 0.18) \times 10^{11}$	$(-2.88 \pm 0.30) \times 10^{11}$	$(-1.88 \pm 0.40) \times 10^{11}$
MRTI Amplitude (mm)	0.88 ± 0.06	0.84 ± 0.02	0.55 ± 0.03	0.35 ± 0.01	0.19 ± 0.03

6.4 Laser Probing Results

We used laser probing to investigate the underdense gas plasmas and their interaction with the dense liner, providing a clearer view of the liner underneath. We use the same optical setup as that presented in Chapter 4, which was able to probe through the underdense plasma.

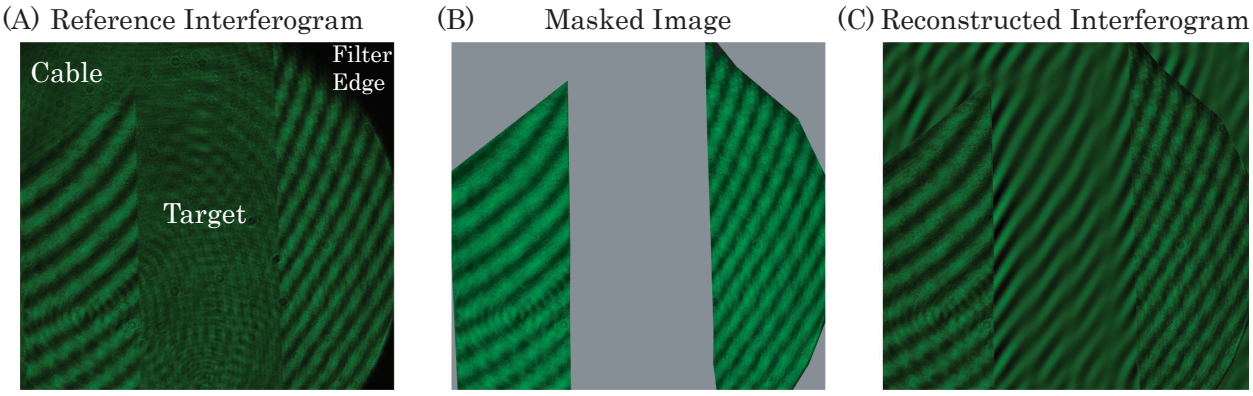


Figure 6.11: The reconstruction process for the reference interferogram. (a) The original interferogram with the central region obscured by the target. (b) The obscured region is masked in gray. (c) The final image after the masked area has been filled with a synthetically generated fringe pattern.

A challenge in interferometric analysis is that the imploding target blocks the view of the reference fringes in the central region. To address this, synthetic reference fringes were generated using the following procedure. The initial reference interferogram was processed to isolate the existing fringe pattern from the central region by masking the blocked region with a gray mask. A MATLAB script was used to separate the gray and fringe regions. The subsequent fringe image was Fourier Transformed to obtain the frequency of the fringes. In the resulting frequency space, the dominant spatial frequency (corresponding to the fringe spacing and orientation) was manually selected. An ideal synthetic fringe pattern was generated by performing an inverse FFT using only this single dominant frequency. This synthetic pattern was then used to fill the gray masked region of the original reference image, creating a complete reference interferogram. It should be noted that the fringe pattern is curved to measure both horizontal and vertical density gradients. This curvature provided additional difficulties in the reconstruction since the space was non-uniform. Nonetheless, we achieved a satisfactory approximation. The central liner region is of primary interest, and in this area, particular attention was given to ensure that the fringes were closely aligned with the actual data, as shown in Fig. 6.11.

The interferometric data show that increasing the applied axial magnetic field strength

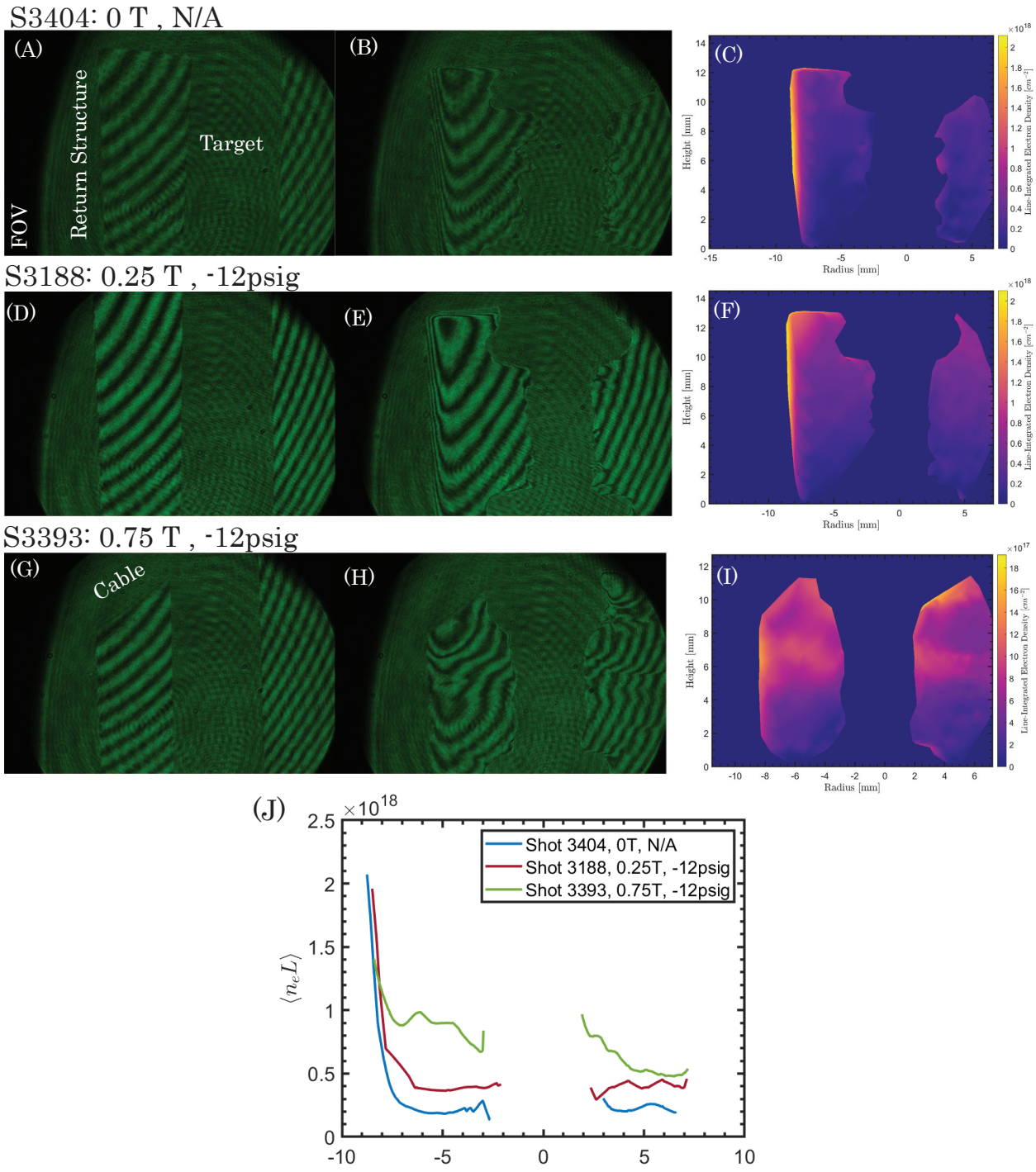


Figure 6.12: Comparison of interferometry results for a liner-only target and MGoL targets. Each row shows a single shot with the **top row** (a–c) representing a liner-only target (3404). The **middle row** (d–f) represents an MGoL target with $B_{z0} = 0.25$ T. The **bottom row** (g–i) represents an MGoL target with $B_{z0} = 0.75$ T. Each column represents the (left) reference interferogram, (center) shot interferogram, and (right) reconstructed areal density map. (j) A plot comparing radial lineouts of the line-integrated density for each case.

increases the background line-integrated electron density. Figure 6.12 shows lineouts at $h \approx 8$ mm for a non-magnetized liner-only target and MGoL targets with $B_{z0} = 0.25$ and 0.75 T. Notably, the liner-only target had no measurable peripheral plasma. By contrast, the MGoL shots measured an $\langle n_e L \rangle \approx 0.4$ and 0.8×10^{18} cm^{-2} for $B_{z0} = 0.25$ and 0.75 T, respectively. On the left edge, a significant density increase to $\langle n_e L \rangle \approx 2 \times 10^{18}$ cm^{-2} is observed. This increase corresponds to imaging the edge of the return structure, which is approximately 33 mm away from the target. The density measurements are notably similar across the three shots, suggesting that the peripheral plasma may not extend to the return-current structure, implying that the plasma observed at the return-current structure likely originates from the return-current structure itself. The observation of this locally generated electrode plasma on a sub-1-MA machine like MAIZE suggests that similar phenomena may occur in multi-MA facilities like the Z machine.

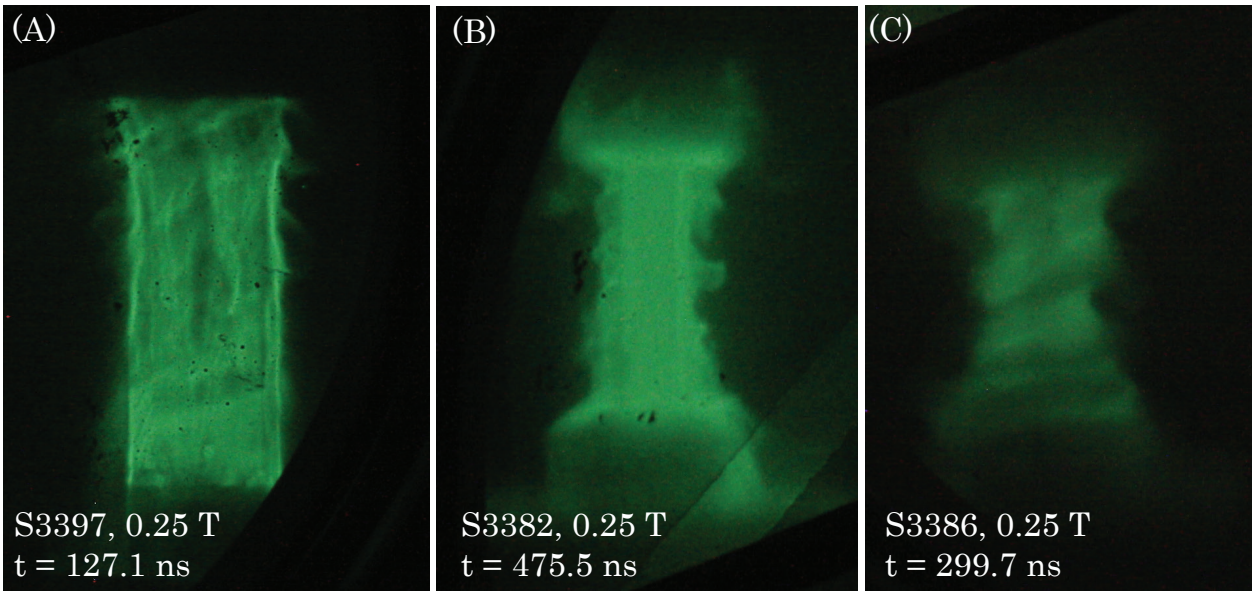


Figure 6.13: XUV images of a MGoL target at different stages. (a) The initial impact of the gas plasma onto the liner. (b) A later-time image showing a potentially stable liner column persisting underneath the surrounding gas plasma. (c) Helical features are visible during the liner's explosion phase.

In Fig. 6.13, XUV emission images are presented that show significant emissions upon the impact of gas plasma with the liner, similar to the observations captured by the framing camera. In Fig. 6.13(a), we present an image of an MGoL target with $B_{z0} = 0.25$ T at an early time (when the gas impacts the liner) to investigate the potential density imprinting of instability structures. The instability structures within the gas are not easily identifiable in the XUV images. This observation may indicate a lack of density variations, suggesting

that density imprinting may not play a significant role. In Fig. 6.13(b) XUV image reveals a fainter peripheral plasma surrounding a brighter, stable column, possibly indicating a more stable liner beneath the gas plasma. Occasionally, helical modes are observable in the explosion data, as depicted in Fig. 6.13(c).

6.5 Chapter 6 Summary

This chapter investigates the magnetic imprinting of helical instabilities in a magnetized gas-on-liner (MGoL) target. These experiments were performed with an axial magnetic field. The main motivating question is, in a fully integrated MGoL target, do the helical structure and the compressed magnetic field originating from the gas imprint a more pronounced helical instability onto the liner. The results confirm this hypothesis.

In magnetized liner-only and MGoL implosions, helical structures become visible at stagnation and are clearly visible during the explosion phase. Assuming that the instability pitch is conserved early during the implosion, the visible pitch angles on the exploding liner can be used to infer pitch angles during the implosion. The key results show a liner-only target with a strong axial magnetic field ($B_{z0} = 0.75$ T) produced pitch angles of only $\approx 8 \pm 1°$. By contrast, an MGoL target with a much weaker axial magnetic field ($B_{z0} = 0.25$ T) produced significantly steeper pitch angles of $\approx 16 \pm 2°$ at a similar radius. The investigation reveals that the steep pitch angles observed in the MGoL targets are similar to the pitch angles characteristic of the gas plasma upon its interaction with the liner. Despite the apparent absence of perturbation wavelength transfer from the gas to the liner, it is reasonable that the pitch angle is nonetheless transferred from the gas to the liner. We are hesitant to conclude that the pitch angle observed in the liner is attributable to magnetic imprinting from the enhanced axial magnetic field without directly measuring the axial magnetic field strength on the liner surface. Additionally, the laser backlighting data further supports that density imprinting may play a minor role in seeding instabilities.

While adding an axial magnetic field enhances helical instabilities, it also has a significant impact on the overall implosion performance. Most notably, the MGoL targets provide a significant stabilizing effect against MRTI. The measured instability amplitude systematically decreases with increasing axial magnetic field (B_{z0}) from ≈ 1 mm to ≈ 0.2 mm with $B_{z0} = 0$ and $B_{z0} = 0.75$ T, respectively. By contrast, the axially magnetized liner-only target produced has an instability amplitude of ≈ 0.8–1 mm with $B_{z0} = 0.75$ T. This stability comes at the cost of convergence. The increased axial magnetic pressure is suspected to provide an internal resistance to the driving pressure, causing the stagnation radius to increase with the applied axial magnetic field (from a stagnation radius of ≈ 1.4 mm to ≈ 2.2 mm with $B_{z0} = 0$ and 0.75 T, respectively). Consequently, the peak implosion velocity generally decreases as the axial magnetic field increases.

The interplay between the stability of MRTI and implosion velocity suggests the potential existence of an optimal configuration. Although the $B_{z0} = 0.75$ T MGoL target was the most stable, its convergence was poor. By contrast, the $B_{z0} = 0.25$ T MGoL target achieved a

convergence on par with the $B_{z0} = 0.75$ T liner-only target, but with approximately half the instability growth. This observation underscores that a modest axial magnetic field, in conjunction with an outer gas layer, may yield a more favorable outcome than the application of an excessively high axial magnetic field on a liner alone.

Interferometry data reveal that the amount of peripheral plasma surrounding the target increases with the applied axial magnetic field (from a line-integrated density of $\approx 1.5 \times 10^{18}$ cm^{-2} to $\approx 6 \times 10^{17}$ cm^{-2} with $B_{z0} = 0$ and 0.75 T, respectively). XUV images confirm the presence of a helical mode during the explosion.

CHAPTER 7

Concluding Remarks

The central motivation of this dissertation was to experimentally investigate the physical mechanism responsible for seeding steep helical instabilities in MagLIF targets. It is hypothesized that the imprinting of instabilities from a low-density plasma compressing the axial magnetic field was the origin of enhanced helical modes on MagLIF targets. To investigate this, we conducted reduced-scale experiments on the MAIZE pulsed power facility (1 MA, 200 ns) to simulate the environment anticipated in MagLIF experiments on the Z facility (20 MA, 100 ns). An experimental platform was developed to inject an axially magnetized annular gas-puff plasma, which subsequently imploded onto a dense central target, mimicking the desorbed low-density plasmas present in the MITL power feeds of the Z facility.

The first experiments examined the implosion of an axially magnetized annular gas plasma onto central metal rod and a hollow dielectric rod. It was observed that this axially magnetized gas-puff plasma was able to generate steep helical structures in the plasma sheath for a small magnetic field ratio ($B_{z0}/B_{\text{peak}} \approx 0.0075$–$0.023$). These steep helical structures scale with increasing B_{z0}. The angle of the helical structures remained constant when the radius was fixed, indicating the occurrence of a phenomenon known as "pitch locking." Furthermore, it was determined that the gas plasma has the capacity to compress the axial magnetic field, with the measured axial flux compression being approximately 50% efficient relative to an ideal flux compression model. Side-on interferometry yielded measurements of a surrounding peripheral plasma with a line-integrated electron density of approximately 10^{17}–10^{18} cm^{-2}, and with a gradient layer thickness of approximately 0.5–1.5 mm.

The second experiment studied the coupling between low-density plasma (gas-puff) and an imploding thin-foil aluminum liner. The primary motivation was to distinguish between two potential instability seeding mechanisms: density imprinting and magnetic imprinting. By removing the axial magnetic field, we can directly observe whether the hydrodynamic impact of the gas plasma alone is capable of seeding instabilities on the liner. Power spectra of the liner-only targets reveal that a consistent dominant wavelength of ≈ 2 mm develops

during the implosion. We postulate a three-stage instability process that sets the dominant wavelength. First, the electrothermal instability (ETI) seeds a broad spectrum of small-wavelength perturbations on the liner surface prior to significant radial motion. Subsequently, these perturbations are subjected to current driven instabilities and undergo mode mergers prior to any significant motion in the liner, thus increasing the perturbation wavelength. Finally, as the liner accelerates, the MRTI amplifies these seeded modes and drives further mode merger events.

Relative to the axially magnetized liner-only targets, the gas-on-liner (GoL) targets exhibit a more complex spectrum, which appears to be a mix of liner and gas modes. It often shows two dominant modes simultaneously: a smaller wavelength mode (≈ 2 mm) from the liner and a larger wavelength mode (> 3 mm) from the gas. The persistence of both spectra throughout the implosion suggests that they may either evolve independently from each other (decoupled evolution of the two interfaces) or that there may be mode competition occurring between them. This finding suggests that density imprinting from the low-density plasma may not play a significant role in seeding instabilities onto the liner, at least for our experiment.

A significant finding of this experiment is that a gas layer provides a powerful stabilizing effect on an imploding liner. The GoL targets were consistently more stable against the MRTI than their liner-only counterparts. This conclusion is supported by two key metrics: the GoL targets exhibited smaller peak instability amplitudes, and their calculated MRTI growth rates were significantly lower. While several stabilization mechanisms are likely at play (such as a smoothed density profile or a decreased aspect ratio), the analysis showed that reduced acceleration is not the dominant cause of the observed stability.

The final experiment investigated the role of magnetic imprinting of helical instabilities in a magnetized gas-on-liner (MGoL) target. The primary motivation was to determine whether, in a fully integrated MGoL target, the helical structure and the compressed magnetic field originating from the gas imprint a more pronounced helical instability onto the liner. The short answer is yes. The key results show a liner-only target with a strong axial magnetic field ($B_{z0} = 0.75$ T) producing angles of only $\approx 8 \pm 1^\circ$. By contrast, an MGoL target with a much weaker axial magnetic field ($B_{z0} = 0.25$ T) produced significantly steeper angles of $\approx 16 \pm 2^\circ$ at a similar radius. The investigation reveals that the steep pitch angles observed in the MGoL targets are similar to the pitch angles that are characteristic of the gas plasma upon its interaction with the liner. Despite the apparent absence of perturbation wavelength transfer from the gas to the liner, it is reasonable to assume that the pitch angle is nonetheless transferred from the gas shell to the thin-foil liner. We are reluctant to conclude that the pitch angle observed in the liner is attributable to magnetic imprinting from

the enhanced axial magnetic field without directly measuring the axial field strength on the liner surface. Nevertheless, the helical angle on the liner is much steeper with an axially magnetized gas layer.

Additionally, while adding an axial magnetic field enhances helical instabilities, it also has a significant impact on the overall implosion performance. Most notably, the MGoL targets provide a significant stabilizing effect against MRTI. The measured instability amplitude systematically decreases with increasing axial magnetic field (B_{z0}) from ≈ 1 mm to ≈ 0.2 mm with $B_{z0} = 0$ and $B_{z0} = 0.75$ T, respectively. By contrast, the axially magnetized liner-only target produced an instability amplitude of ≈ 0.8–1 mm with $B_{z0} = 0.75$ T. This stability comes at the cost of convergence and peak implosion velocity. The interplay between the stability of MRTI and implosion velocity suggests the potential existence of an optimal configuration. Although the $B_{z0} = 0.75$ T MGoL target was the most stable, its convergence was poor. By contrast, the $B_{z0} = 0.25$ T MGoL target achieved a convergence on par with the $B_{z0} = 0.75$ T liner-only target, but with approximately half the instability growth.

This work demonstrates that low-density plasma can be a dominant factor in seeding liner instabilities (likely due to magnetic imprinting and less to do with density imprinting). The results show that even a small compressed axial magnetic field can have a large impact on the final instability morphology of the liner. Additionally, a modest axial magnetic field in tandem with a low-density outer gas layer significantly mitigates the MRTI growth for a thin-foil liner implosion.

In the future, our understanding of these systems could be further improved by: (1) directly measuring the flux compression occurring within the low-density plasma layer (perhaps via axial Faraday rotation imaging [123]); and (2) the development of penetrating radiography (perhaps via X-pinch-based radiography [135]) to be able to image both the gas and liner boundaries simultaneously. Nevertheless, the quantitative datasets presented in this dissertation on instability growth, mode evolution, flux compression, and implosion trajectory dynamics serve as a robust foundation for future simulation code benchmarking, particularly for codes such as PERSEUS [139], FLASH [140], or GORGON [8].

APPENDIX A

Angular Filter Refractometer

This section investigated the potential of utilizing an angular filter refractometer (AFR) as a laser based diagnostic tool to probe and understand underdense plasma produced in pulsed power facilities. There are several laser based diagnostics that can probe lower electron density plasma of 10^{-15}–10^{-20} cm^{-3}, such as interferometry (phase-difference), schlieren imaging (refraction angle), and shadowgraphy (intensity modulation). Laser schlieren is a simple yet powerful tool for measuring spatial structure formation and density gradients in gasses and plasmas. The basis of this technique relies on the deflection of light due to a change in the index of refraction of the medium. The total deflection of the rays is caused by the perpendicular gradient of the index of refraction relative to the incoming ray.

An angular filter refractometer (AFR) is a modified schlieren imaging technique that relies on a Fourier mask to filter bands of refraction angles and produce a contour image of the refracted probe beam. This would allow for a quantitative measurement of the electron density, as each pass through the band would correspond to a specific density gradient that is related to the electron density. Since this is a refractive based diagnostic, the angular resolution is only limited by the collection angle of the optics rather than the wavelength of the probe beam, as in an interferometer.

A.1 Design and Operation

The AFR is designed to have five circular opaque bands and transparent band pairs of width 2.5 mm, as shown in Figure A.1. The refracted image passes through this Fourier filter, the opaque bands will reflect or absorb light, while the transparent bands will allow a refracted image to pass through. A center beam block with a diameter of 500 microns is placed at the center of the AFR to block the probe beam. This center beam block constrains the lower limit of the density gradient, while the largest radius opaque band defines the upper limit. The opaque band structure is created using material sputtering onto an ultra transparent

glass silica substrate. The masking material is made of a mixture of Gold and Titanium on a side of this glass substrate, which is 50 microns thick. One of the limiting factors of the AFR is the edge diffraction from the sharp transition of the metal to the glass. This effect is due to the interaction between a collimated beam of light and a sharp edge. This diffracts the wave like beam into bands of the diffraction pattern parallel to the edge. This effect can blur the information contained in the transparent regions of the AFR. So, this limits the number of band pairs that can be designed.



Figure A.1: (Left) A bulls-eye pattern of the angular Fourier filter. (Right) The fabricated AFR.

A.2 Calibration

The performance of the AFR is limited by the diameter of the optical lens within the imaging system. This includes the initial collection lens and the subsequent lens responsible for relaying the perturbed rays to the imaging CCD. It is important because you want to collect the maximum number of perturbed rays possible, as their exit angle of the perturbed rays will relate to the density gradient; otherwise, there will be a loss of refractive information. In a system comprising three lenses and applying the paraxial approximation, the refraction angle from the AFR is related to equation A.1, where r_{AFR} denotes the maximum radius of the AFR image, θ_1 represents the maximum angle of acceptance from the collection lens, and f_3 corresponds to the focal length of the final imaging lens.

$$r_{\mathrm{AFR}} = \sin(\theta_1) * f_3 \tag{A.1}$$

The AFR is designed for large density gradients on the order of 10^{19}–10^{20} cm^{-3}. For such gradients, the deflection angle can be calculated, as shown in Figure A.2. The input length parameters consist of a plasma length gradient of 2 mm and a probe length of 3 mm.

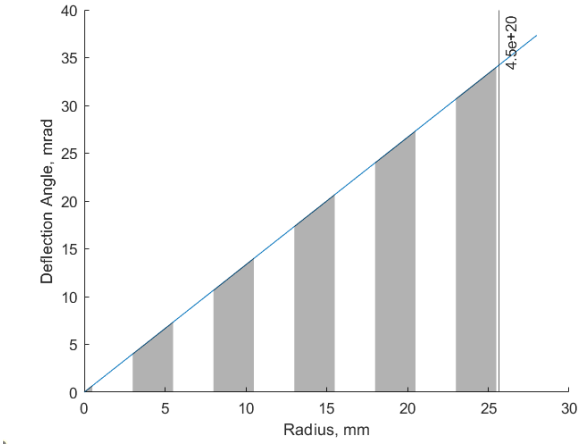


Figure A.2: Deflection angle as a function of radius on the Fourier plane. The grey bars indicated the opaque bands while the black vertical line indicate the upper deflection limit.

The AFR is calibrated with an f-number of -2.5 for a concave lens and a -0.4 cylindrical lens at the load to validate the operation of this diagnostic. The results show that the diagnostic is working properly; however, only three of the bands are showing up. This is due to the limitation of the collection angle of the first lens. For the current system, the maximum collection angle is approximately 34 mRad, and the maximum imaged radius is 13.5 mm, which underfills the current AFR. So, the image would correspond to a maximum of three transparent bands.

The results show the expected refracted image, where there are circular bands that cut off at a radius of 13.5 mm. The cylindrical lens is placed half-way out to show that the spatial image information is preserved while the refraction information is overlaid as bright bands. The image position is moved back to enhance the refraction effect of the cylindrical lens. The images form horizontal lines, which is expected since the cylindrical lens refracts only in a single direction. So, the recreated image shows bands in only one direction while keeping the spatial information in the other direction.

Figure A.3 shows the AFR image using the calibration lens and a resolution target. The resolution of the AFR is shown to be approximately 14.25 lp/mm or 35 microns, which should be sufficient to resolve the gas plasma.

A.3 Ray Tracing

Ray tracing was used to simulate the refracted image resulting photon rays deflected from an arbitrary electron density profiles. These rays are then propagated through a lens, which is

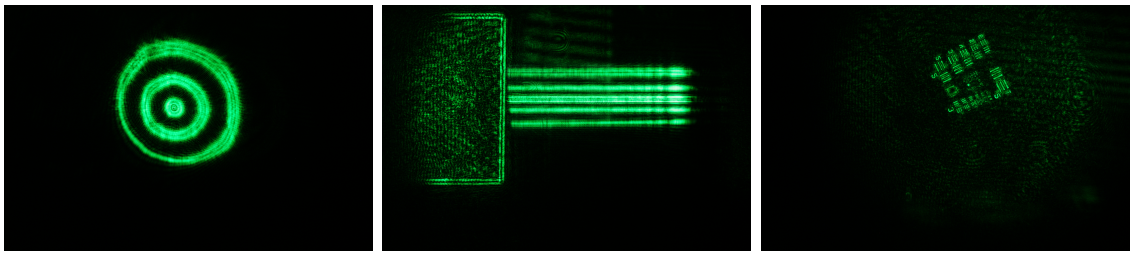


Figure A.3: (Left) Calibration with a concave lens showing angular bands. (Middle) Calibration with a cylindrical lens showing horizontal bands. (Right) 1951 USAF resolution target at load center.

modeled using the ray transfer matrix. The final image is then captured by a detector where the detector is treated as a histogram and bin the photons into each pixel on the detector.

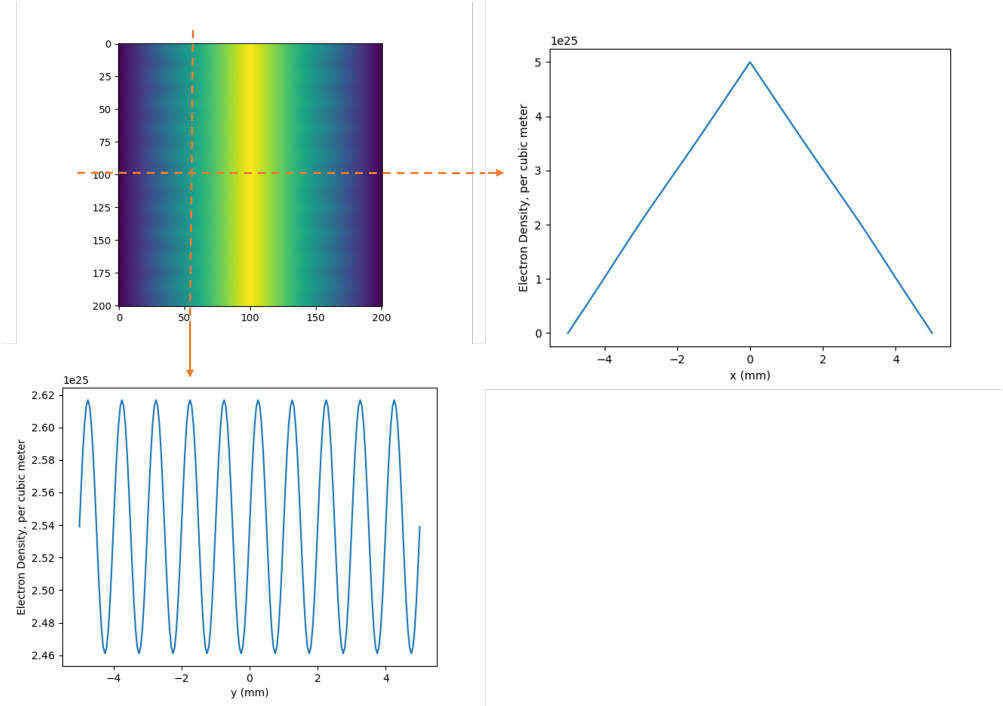


Figure A.4: Electron density profile with radial and axial lineouts. (Top left) The electron density map. (Bottom left) The axial lineout. (Top right) The radial lineout.

We test the AFR using this ray tracing tool by passing rays through the electron density profile shown in Fig. A.4. This is a cylindrically symmetric electron density plasma that has a linear decay radially outward and an axially sinusoidal perturbation.

Fig. A.5(a,c,d) shows the resultant image at the exit plane of the plasma, the Fourier plane where the AFR resides, and the image plane of the final recorded image, respectively. The recorded image shows the band pattern where it is possible to reconstruct the density of

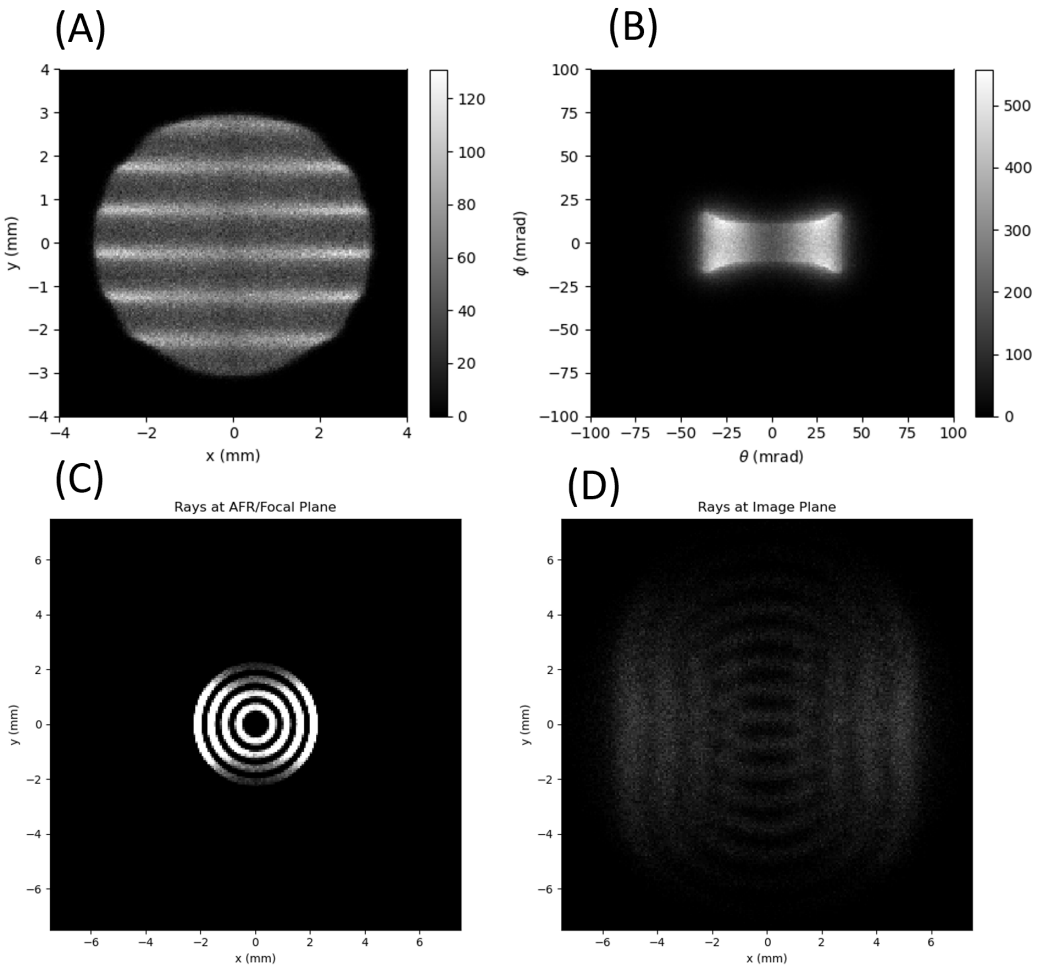


Figure A.5: (a) The rays exiting the plasma. (b) The angle distribution of the refracted rays. (c) The image at the Fourier plane where the AFR resides. (d) The resultant schlieren image at the detector plane.

the plasma object. As noted, the final density map is characterized by a number of discrete points that corresponds precisely to the band pairs on the AFR, amounting to five in this instance.

APPENDIX B

MATLAB Code for Helical Angle Tracing

B.1 HeliTrace Function

Listing B.1: MATLAB function for interactively tracing helical striations in images.

```
function [allPaths] = HeliTrace(img, n, box)
    % Display the image initially
    figure;
    imshow(img);
    title('Click a point to start tracking, press Enter to exit');

    % Initialize a cell array to store all paths
    allPaths = {};

    % Loop continuously to allow multiple selections
    while true
        % Get a starting point interactively
        [x, y, button] = ginput(1);
        if isempty(button)
            break; % Exit loop if 'Enter' is pressed
        end

        startCol = round(x);
        startRow = round(y);

        choice = questdlg('Track maximum or minimum values?', ...
            'Selection', 'Maximum', 'Minimum', 'Cancel', 'Maximum'
                );
```

```
if strcmp(choice, 'Cancel') || isempty(choice)
    break; % Exit loop if cancel is chosen
end

% Initialize the tracked path
trackedPath = NaN(1, size(img, 2));
trackedPath(startCol) = startRow;

n_steps = min([n, size(img, 2) - startCol]);

% Track to the right
for col = startCol + 1 : startCol + n_steps
    prevRow = trackedPath(col - 1);
    rowRange = max(1, prevRow - box) : min(size(img, 1),
        prevRow + box);

    if strcmp(choice, 'Maximum')
        % Maximum value tracking
        [~, localIdx] = max(img(rowRange, col));
    else
        % Minimum value tracking
        [~, localIdx] = min(img(rowRange, col));
    end

    trackedPath(col) = rowRange(localIdx);
end

% Store the tracked path
allPaths{end + 1} = trackedPath;

% Plot the tracked path on top of the image
hold on;
if strcmp(choice, 'Maximum')
    plot(1:size(img, 2), trackedPath, '-', 'LineWidth', 1,
        Color="#A2142F"); % Red line
```

```
        else
            plot(1:size(img, 2), trackedPath, '-', 'LineWidth', 1,
                Color="#0072BD"); % Blue line
        end
        hold off; % Release hold for next potential plot overlay
    end
    title('Tracking Completed'); % Update title when done
end
```

BIBLIOGRAPHY

[1] D. D. Ryutov, M. S. Derzon, and M. K. Matzen, "The physics of fast Z pinches," Rev. Mod. Phys. 72, 167 (2000).

[2] R. B. Spielman, C. Deeney, G. A. Chandler, M. R. Douglas, D. L. Fehl, M. K. Matzen, D. H. McDaniel, T. J. Nash, J. L. Porter, T. W. L. Sanford, J. F. Seamen, W. A. Stygar, K. W. Struve, S. P. Breeze, J. S. McGurn, J. A. Torres, D. M. Zagar, T. L. Gilliland, D. O. Jobe, J. L. McKenney, R. C. Mock, M. Vargas, T. Wagoner, and D. L. Peterson, "Tungsten wire-array Z-pinch experiments at 200 TW and 2 MJ," Phys. Plasmas 5, 2105 (1998).

[3] M. C. Jones, D. J. Ampleford, M. E. Cuneo, R. Hohlfelder, C. A. Jennings, D. W. Johnson, B. Jones, M. R. Lopez, J. MacArthur, J. A. Mills, T. Preston, G. A. Rochau, M. Savage, D. Spencer, D. B. Sinars, and J. L. Porter, "X-ray power and yield measurements at the refurbished Z machine," Rev. Sci. Instrum. 85, 083501 (2014).

[4] D. J. Ampleford, B. Jones, C. A. Jennings, S. B. Hansen, M. E. Cuneo, A. J. Harvey-Thompson, G. A. Rochau, C. A. Coverdale, A. R. Laspe, T. M. Flanagan, N. W. Moore, D. B. Sinars, D. C. Lamppa, E. C. Harding, J. W. Thornhill, J. L. Giuliani, Y.-K. Chong, J. P. Apruzese, A. L. Velikovich, A. Dasgupta, N. Ouart, W. A. Sygar, M. E. Savage, J. K. Moore, R. Focia, T. C. Wagoner, K. L. Killebrew, A. D. Edens, G. S. Dunham, M. C. Jones, P. W. Lake, D. S. Nielsen, M. Wu, A. L. Carlson, M. D. Kernahan, C. R. Ball, R. D. Scharberg, T. D. Mulville, E. W. Breden, C. S. Speas, G. Olivas, M. A. Sullivan, A. J. York, D. W. Justus, J. C. Cisneros, T. Strizic, J. Reneker, M. Cleveland, M. P. Vigil, G. Robertson, D. Sandoval, C. Cox, A. J. Maurer, D. A. Graham, N. B. Huynh, S. Toledo, L. P. Molina, M. R. Lopez, F. W. Long, G. R. McKee, J. L. Porter, and M. C. Herrmann, "Contrasting physics in wire array z pinch sources of 1-20 keV emission on the Z facility," Phys. Plasmas 21, 056708 (2014).

[5] D. B. Sinars, M. A. Sweeney, C. S. Alexander, D. J. Ampleford, T. Ao, J. P. Apruzese, C. Aragon, D. J. Armstrong, K. N. Austin, T. J. Awe, A. D. Baczewski, J. E. Bailey, K. L. Baker, C. R. Ball, H. T. Barclay, S. Beatty, K. Beckwith, K. S. Bell, J. F. Benage, Jr., N. L. Bennett, K. Blaha, D. E. Bliss, J. J. Boerner, C. J. Bourdon, B. A. Branch, J. L. Brown, E. M. Campbell, R. B. Campbell, D. G. Chacon, G. A. Chandler, K. Chandler, P. J. Christenson, M. D. Christison, E. B. Christner, R. C. Clay, III, K. R. Cochrane, A. P. Colombo, B. M. Cook, C. A. Coverdale, M. E. Cuneo, J. S. Custer, A. Dasgupta, J.-P. Davis, M. P. Desjarlais, D. H. Dolan, III, J. D. Douglass, G. S. Dunham, S. Duwal, A. D. Edens, M. J. Edwards, E. G. Evstatiev, B. G. Farfan, J. R.

Fein, E. S. Field, J. A. Fisher, T. M. Flanagan, D. G. Flicker, M. D. Furnish, B. R. Galloway, P. D. Gard, T. A. Gardiner, M. Geissel, J. L. Giuliani, M. E. Glinsky, M. R. Gomez, T. Gomez, G. P. Grim, K. D. Hahn, T. A. Haill, N. D. Hamlin, J. H. Hammer, S. B. Hansen, H. L. Hanshaw, E. C. Harding, A. J. Harvey-Thompson, D. Headley, M. C. Herrmann, M. H. Hess, C. Highstrete, O. A. Hurricane, B. T. Hutsel, C. A. Jennings, O. M. Johns, D. Johnson, M. D. Johnston, B. M. Jones, M. C. Jones, P. A. Jones, P. E. Kalita, R. J. Kamm, J. W. Kellogg, M. L. Kiefer, M. W. Kimmel, P. F. Knapp, M. D. Knudson, A. Kreft, G. R. Laity, P. W. Lake, D. C. Lamppa, W. L. Langston, J. S. Lash, K. R. LeChien, J. J. Leckbee, R. J. Leeper, G. T. Leifeste, R. W. Lemke, W. Lewis, S. A. Lewis, G. P. Loisel, Q. M. Looker, A. J. Lopez, D. J. Lucero, S. A. MacLaren, R. J. Magyar, M. A. Mangan, M. R. Martin, T. R. Mattsson, M. K. Matzen, A. J. Maurer, M. G. Mazarakis, R. D. McBride, H. S. McLean, C. A. McCoy, G. R. McKee, J. L. McKenney, A. R. Miles, J. A. Mills, M. D. Mitchell, N. W. Moore, C. E. Myers, T. Nagayama, G. Natoni, A. C. Owen, S. Patel, K. J. Peterson, T. D. Pointon, J. L. Porter, A. J. Porwitzky, S. Radovich, K. S. Raman, P. K. Rambo, W. D. Reinhart, G. K. Robertson, G. A. Rochau, S. Root, D. V. Rose, D. C. Rovang, C. L. Ruiz, D. E. Ruiz, D. Sandoval, M. E. Savage, M. E. Sceiford, M. A. Schaeuble, P. F. Schmit, M. S. Schollmeier, J. Schwarz, C. T. Seagle, A. B. Sefkow, D. B. Seidel, G. A. Shipley, J. Shores, L. Shulenburger, S. C. Simpson, S. A. Slutz, I. C. Smith, C. S. Speas, P. E. Specht, M. J. Speir, D. C. Spencer, P. T. Springer, A. M. Steiner, B. S. Stoltzfus, W. A. Stygar, J. Ward Thornhill, J. A. Torres, J. P. Townsend, C. Tyler, R. A. Vesey, P. E. Wakeland, T. J. Webb, E. A. Weinbrecht, M. R. Weis, D. R. Welch, J. L. Wise, M. Wu, D. A. Yager-Elorriaga, A. Yu, and E. P. Yu, "Review of pulsed power-driven high energy density physics research on Z at Sandia," Phys. Plasmas 27, 070501 (2020).

[6] M. G. Haines, S. V. Lebedev, J. P. Chittenden, F. N. Beg, S. N. Bland, and A. E. Dangor, "The past, present, and future of Z pinches," Phys. Plasmas 7, 1672 (2000).

[7] C. Deeney, M. R. Douglas, R. B. Spielman, T. J. Nash, D. L. Peterson, P. L'Eplattenier, G. A. Chandler, J. F. Seamen, and K. W. Struve, "Enhancement of X-Ray Power from a Z Pinch Using Nested-Wire Arrays," Phys. Rev. Lett. 81, 4883 (1998).

[8] J. P. Chittenden, S. V. Lebedev, S. N. Bland, F. N. Beg, and M. G. Haines, "One-, two-, and three-dimensional modeling of the different phases of wire array Z-pinch evolution," Phys. Plasmas 8, 2305 (2001).

[9] M. E. Cuneo, E. M. Waisman, S. V. Lebedev, J. P. Chittenden, W. A. Stygar, G. A. Chandler, R. A. Vesey, E. P. Yu, T. J. Nash, D. E. Bliss, G. S. Sarkisov, T. C. Wagoner, G. R. Bennett, D. B. Sinars, J. L. Porter, W. W. Simpson, L. E. Ruggles, D. F. Wenger, C. J. Garasi, B. V. Oliver, R. A. Aragon, W. E. Fowler, M. C. Hettrick, G. C. Idzorek, D. Johnson, K. Keller, S. E. Lazier, J. S. McGurn, T. A. Mehlhorn, T. Moore, D. S. Nielsen, J. Pyle, S. Speas, K. W. Struve, and J. A. Torres, "Characteristics and scaling of tungsten-wire-array z -pinch implosion dynamics at 20 MA," Phys. Rev. E 71, 046406 (2005).

[10] R. D. McBride, T. A. Shelkovenko, S. A. Pikuz, D. A. Hammer, J. B. Greenly, B. R. Kusse, J. D. Douglass, P. F. Knapp, K. S. Bell, I. C. Blesener, and D. A. Chalenski, "Implosion dynamics and radiation characteristics of wire-array Z pinches on the Cornell Beam Research Accelerator," Phys. Plasmas 16, 012706 (2009).

[11] T. A. Shelkovenko, S. A. Pikuz, I. N. Tilikin, M. D. Mitchell, S. N. Bland, and D. A. Hammer, "Evolution of X-pinch loads for pulsed power generators with current from 50 to 5000 kA," Matter and Radiation at Extremes 3, 267 (2018).

[12] G. V. Dowhan, J. M. Chen, K. Rezac, J. Novotny, V. Munzar, D. E. J. White, A. P. Shah, L. R. Tafoya, M. A. Mangan, N. M. Jordan, D. Klir, and R. D. McBride, "Neutron Generation in a Deuterated- Polyethylene-Fiber Hybrid X-Pinch on the MAIZE LTD," IEEE Trans. Plasma Sci. 53, 1186 (2025).

[13] R. D. McBride, M. R. Martin, R. W. Lemke, J. B. Greenly, C. A. Jennings, D. C. Rovang, D. B. Sinars, M. E. Cuneo, M. C. Herrmann, S. A. Slutz, C. W. Nakhleh, D. D. Ryutov, J.-P. Davis, D. G. Flicker, B. E. Blue, K. Tomlinson, D. Schroen, R. M. Stamm, G. E. Smith, J. K. Moore, T. J. Rogers, G. K. Robertson, R. J. Kamm, I. C. Smith, M. Savage, W. A. Stygar, G. A. Rochau, M. Jones, M. R. Lopez, J. L. Porter, and M. K. Matzen, "Beryllium liner implosion experiments on the Z accelerator in preparation for magnetized liner inertial fusion," Phys. Plasmas 20, 056309 (2013).

[14] T. J. Awe, R. D. McBride, C. A. Jennings, D. C. Lamppa, M. R. Martin, D. C. Rovang, S. A. Slutz, M. E. Cuneo, A. C. Owen, D. B. Sinars, K. Tomlinson, M. R. Gomez, S. B. Hansen, M. C. Herrmann, J. L. McKenney, C. Nakhleh, G. K. Robertson, G. A. Rochau, M. E. Savage, D. G. Schroen, and W. A. Stygar, "Observations of Modified Three-Dimensional Instability Structure for Imploding Z-Pinch Liners that are Premagnetized with an Axial Field," Physical Review Letters 111, 235005 (2013).

[15] T. J. Awe, C. A. Jennings, R. D. McBride, M. E. Cuneo, D. C. Lamppa, M. R. Martin, D. C. Rovang, D. B. Sinars, S. A. Slutz, A. C. Owen, K. Tomlinson, M. R. Gomez, S. B. Hansen, M. C. Herrmann, M. C. Jones, J. L. McKenney, G. K. Robertson, G. A. Rochau, M. E. Savage, D. G. Schroen, and W. A. Stygar, "Modified helix-like instability structure on imploding z-pinch liners that are pre-imposed with a uniform axial magnetic field," Phys. Plasmas 21, 056303 (2014).

[16] D. A. Yager-Elorriaga, P. Zhang, A. M. Steiner, N. M. Jordan, P. C. Campbell, Y. Y. Lau, and R. M. Gilgenbach, "Discrete helical modes in imploding and exploding cylindrical, magnetized liners," Phys. Plasmas 23, 124502 (2016).

[17] D. A. Yager-Elorriaga, Y. Y. Lau, P. Zhang, P. C. Campbell, A. M. Steiner, N. M. Jordan, R. D. McBride, and R. M. Gilgenbach, "Evolution of sausage and helical modes in magnetized thin-foil cylindrical liners driven by a Z-pinch," Phys. Plasmas 25, 056307 (2018).

[18] S. A. Sorokin, "Magnetic implosion of thin aluminum foil liners," Plasma Phys. Control. Fusion 64, 065005 (2022).

[19] J. W. Mather and P. J. Bottoms, "Characteristics of the Dense Plasma Focus Discharge," Phys. Fluids 11, 611 (1968).

[20] M. Krishnan, "The Dense Plasma Focus: A Versatile Dense Pinch for Diverse Applications," IEEE Trans. Plasma Sci. 40, 3189 (2012).

[21] C. Goyon, A. J. Link, O. B. Drury, A. E. Youmans, J. Angus, S. Jiang, S. Rocco, S. F. Chapman, C. M. Cooper, M. McMahon, A. Jibodu, D. Max, R. Anaya, P. C. Campbell, J. Park, B. Shaw, J. Sin, and A. E. Schmidt, "Neutron generation dynamics inside a MA-class dense plasma focus Z-pinch," Phys. Plasmas 32, 033105 (2025).

[22] J. L. Giuliani and R. J. Commisso, "A Review of the Gas-Puff Z -Pinch as an X-Ray and Neutron Source," IEEE Trans. Plasma Sci. 43, 2385 (2015).

[23] E. S. Lavine, S. V. Rocco, J. T. Banasek, W. M. Potter, J. B. Greenly, H. Wilhelm, N. Qi, D. A. Hammer, and B. R. Kusse, "Implosion dynamics of triple-nozzle gas-puff z pinches on COBRA," Phys. Plasmas 28, 022703 (2021).

[24] J. M. Chen, G. V. Dowhan, B. J. Sporer, D. A. Yager-Elorriaga, N. M. Jordan, and R. D. McBride, "Helical Striations and Magnetic Flux Compression in an Axially Premagnetized Gas-Puff z -Pinch Imploding Onto a Dense Central Target," IEEE Trans. Plasma Sci. , 1 (2024).

[25] D. Klir, S. Jackson, J. Cikhardt, B. Cikhardtova, P. Kubes, J. Malir, V. Munzar, J. Novotny, and K. Rezac, "Optimal conditions for efficient ion acceleration and neutron production in deuterium gas-puff z-pinches," Nucl. Fusion 65, 026014 (2024).

[26] A. P. Shah, B. J. Sporer, G. V. Dowhan, K. W. Elliott, M. Krishnan, N. M. Jordan, and R. D. McBride, "Development of a Gas-Puff Z-Pinch for the MAIZE Linear Transformer Driver," IEEE Trans. Plasma Sci. 52, 4794 (2024).

[27] T. R. Boehly, D. L. Brown, R. S. Craxton, R. L. Keck, J. P. Knauer, J. H. Kelly, T. J. Kessler, S. A. Kumpan, S. J. Loucks, S. A. Letzring, F. J. Marshall, R. L. McCrory, S. F. B. Morse, W. Seka, J. M. Soures, and C. P. Verdon, "Initial performance results of the OMEGA laser system," Optics Communications 133, 495 (1997).

[28] D. D. Meyerhofer, J. Bromage, C. Dorrer, J. H. Kelly, B. E. Kruschwitz, S. J. Loucks, R. L. McCrory, S. F. B. Morse, J. F. Myatt, P. M. Nilson, J. Qiao, T. C. Sangster, C. Stoeckl, L. J. Waxer, and J. D. Zuegel, "Performance of and initial results from the OMEGA EP Laser System," J. Phys.: Conf. Ser. 244, 032010 (2010).

[29] G. H. Miller, E. I. Moses, and C. R. Wuest, "The National Ignition Facility: Enabling fusion ignition for the 21st century," Nucl. Fusion 44, S228 (2004).

[30] A. B. Zylstra, O. A. Hurricane, D. A. Callahan, A. L. Kritcher, J. E. Ralph, H. F. Robey, J. S. Ross, C. V. Young, K. L. Baker, D. T. Casey, T. Döppner, L. Divol, M. Hohenberger, S. Le Pape, A. Pak, P. K. Patel, R. Tommasini, S. J. Ali, P. A. Amendt, L. J. Atherton, B. Bachmann, D. Bailey, L. R. Benedetti, L. Berzak Hopkins, R. Betti,

S. D. Bhandarkar, J. Biener, R. M. Bionta, N. W. Birge, E. J. Bond, D. K. Bradley, T. Braun, T. M. Briggs, M. W. Bruhn, P. M. Celliers, B. Chang, T. Chapman, H. Chen, C. Choate, A. R. Christopherson, D. S. Clark, J. W. Crippen, E. L. Dewald, T. R. Dittrich, M. J. Edwards, W. A. Farmer, J. E. Field, D. Fittinghoff, J. Frenje, J. Gaffney, M. Gatu Johnson, S. H. Glenzer, G. P. Grim, S. Haan, K. D. Hahn, G. N. Hall, B. A. Hammel, J. Harte, E. Hartouni, J. E. Heebner, V. J. Hernandez, H. Herrmann, M. C. Herrmann, D. E. Hinkel, D. D. Ho, J. P. Holder, W. W. Hsing, H. Huang, K. D. Humbird, N. Izumi, L. C. Jarrott, J. Jeet, O. Jones, G. D. Kerbel, S. M. Kerr, S. F. Khan, J. Kilkenny, Y. Kim, H. Geppert Kleinrath, V. Geppert Kleinrath, C. Kong, J. M. Koning, J. J. Kroll, M. K. G. Kruse, B. Kustowski, O. L. Landen, S. Langer, D. Larson, N. C. Lemos, J. D. Lindl, T. Ma, M. J. MacDonald, B. J. MacGowan, A. J. Mackinnon, S. A. MacLaren, A. G. MacPhee, M. M. Marinak, D. A. Mariscal, E. V. Marley, L. Masse, K. Meaney, N. B. Meezan, P. A. Michel, M. Millot, J. L. Milovich, J. D. Moody, A. S. Moore, J. W. Morton, T. Murphy, K. Newman, J.-M. G. Di Nicola, A. Nikroo, R. Nora, M. V. Patel, L. J. Pelz, J. L. Peterson, Y. Ping, B. B. Pollock, M. Ratledge, N. G. Rice, H. Rinderknecht, M. Rosen, M. S. Rubery, J. D. Salmonson, J. Sater, S. Schiaffino, D. J. Schlossberg, M. B. Schneider, C. R. Schroeder, H. A. Scott, S. M. Sepke, K. Sequoia, M. W. Sherlock, S. Shin, V. A. Smalyuk, B. K. Spears, P. T. Springer, M. Stadermann, S. Stoupin, D. J. Strozzi, L. J. Suter, C. A. Thomas, R. P. J. Town, E. R. Tubman, C. Trosseille, P. L. Volegov, C. R. Weber, K. Widmann, C. Wild, C. H. Wilde, B. M. Van Wonterghem, D. T. Woods, B. N. Woodworth, M. Yamaguchi, S. T. Yang, and G. B. Zimmerman, "Burning plasma achieved in inertial fusion," Nature 601, 542 (2022).

[31] D. A. Yager-Elorriaga, M. R. Gomez, D. E. Ruiz, S. A. Slutz, A. J. Harvey-Thompson, C. A. Jennings, P. F. Knapp, P. F. Schmit, M. R. Weis, T. J. Awe, G. A. Chandler, M. Mangan, C. E. Myers, J. R. Fein, B. R. Galloway, M. Geissel, M. E. Glinsky, S. B. Hansen, E. C. Harding, D. C. Lamppa, W. E. Lewis, P. K. Rambo, G. K. Robertson, M. E. Savage, G. A. Shipley, I. C. Smith, J. Schwarz, D. J. Ampleford, K. Beckwith, K. J. Peterson, J. L. Porter, G. A. Rochau, and D. B. Sinars, "An overview of magneto-inertial fusion on the Z machine at Sandia National Laboratories," Nucl. Fusion 62, 042015 (2022).

[32] B. Levitt, E. T. Meier, R. Umstattd, J. R. Barhydt, I. A. M. Datta, C. Liekhus-Schmaltz, D. A. Sutherland, and B. A. Nelson, "The Zap Energy approach to commercial fusion," Phys. Plasmas 30, 090603 (2023).

[33] A. Alexander, L. R. Benedetti, I. Bhattacharyya, J. Bowen, J. Cabatu, V. Cacdac, C. Chhavi, C. Chen, K. Chen, D. Clark, J. Clark, T. Cope, W. Dannemann, S. Davidson, D. DeHaan, J. Dugan, M. Eihusen, C. L. Ellison, C. Esquivel, D. Ethridge, B. Ferguson, B. Ferguson, J. Fry, F. Garcia-Rubio, T. Goyal, G. Grim, J. Grodman, B. Haid, F. Howland, V. Huynh, V. John, P. Knapp, I. Kravitz, E. S. Lander, S. Langendorf, K. LeChien, A. Link, N. Meezan, D. S. Miller, N. Nardelli, Q. Ogirri, J. H. Peng, A. Pinto, R. Powser, F. R. Puno, K. Quang, B. Rahn, W. Regan, K. Reichenbach, A. Reyes, C. Richardson, D. Rose, J. Samaniego, P. F. Schmit, V. Silva, N. Simon, S. Sitaraman, H. Sullan, J. Trebesch, M. Truong, C. V. Muench, C. Waltz, D. Williams,

E. Wood, S. Wu, and A. B. Zylstra, "Affordable, manageable, practical, and scalable (AMPS) high-yield and high-gain inertial fusion," Phys. Plasmas 32, 092703 (2025).

[34] J. E. Bailey, T. Nagayama, G. P. Loisel, G. A. Rochau, C. Blancard, J. Colgan, P. Cosse, G. Faussurier, C. J. Fontes, F. Gilleron, I. Golovkin, S. B. Hansen, C. A. Iglesias, D. P. Kilcrease, J. J. MacFarlane, R. C. Mancini, S. N. Nahar, C. Orban, J.-C. Pain, A. K. Pradhan, M. Sherrill, and B. G. Wilson, "A higher-than-predicted measurement of iron opacity at solar interior temperatures," Nature 517, 56 (2015).

[35] M. D. Knudson, "Megaamps, megagauss, and megabars: Using the Sandia Z Machine to perform extreme material dynamics experiments," in *SHOCK COMPRESSION OF CONDENSED MATTER - 2011: Proceedings* (Chicago, Illinois, 2012) pp. 35–42.

[36] J. D. Hare, L. Suttle, S. V. Lebedev, N. F. Loureiro, A. Ciardi, G. C. Burdiak, J. P. Chittenden, T. Clayson, C. Garcia, N. Niasse, T. Robinson, R. A. Smith, N. Stuart, F. Suzuki-Vidal, G. F. Swadling, J. Ma, J. Wu, and Q. Yang, "Anomalous Heating and Plasmoid Formation in a Driven Magnetic Reconnection Experiment," Physical Review Letters 118, 085001 (2017).

[37] J. D. Hare, L. G. Suttle, S. V. Lebedev, N. F. Loureiro, A. Ciardi, J. P. Chittenden, T. Clayson, S. J. Eardley, C. Garcia, J. W. D. Halliday, T. Robinson, R. A. Smith, N. Stuart, F. Suzuki-Vidal, and E. R. Tubman, "An experimental platform for pulsed-power driven magnetic reconnection," Phys. Plasmas 25, 055703 (2018).

[38] T. W. O. Varnish, J. Chen, S. Chowdhry, R. Datta, G. V. Dowhan, L. S. Horan, IV, N. M. Jordan, E. R. Neill, A. P. Shah, R. Shapovalov, B. J. Sporer, R. D. McBride, and J. D. Hare, "Quadrupolar density structures in driven magnetic reconnection experiments with a guide field," Phys. Plasmas 32, 022118 (2025).

[39] S. V. Lebedev, "Exploring astrophysics-relevant magnetohydrodynamics with pulsed-power laboratory facilities," Rev. Mod. Phys. 91 (2019), 10.1103/RevModPhys.91.025002.

[40] M. P. Valdivia, G. W. Collins IV, F. Conti, and F. N. Beg, "Wire, hybrid, and laser-cut X-pinches as Talbot–Lau backlighters for electron density diagnostics," Plasma Phys. Control. Fusion 64, 035011 (2022).

[41] R. G. Kraus, S. Root, R. W. Lemke, S. T. Stewart, S. B. Jacobsen, and T. R. Mattsson, "Impact vaporization of planetesimal cores in the late stages of planet formation," Nature Geosci 8, 269 (2015).

[42] E. G. Harris, "Rayleigh-Taylor Instabilities of a Collapsing Cylindrical Shell in a Magnetic Field," Phys. Fluids 5, 1057 (1962).

[43] E. Ott, "Nonlinear Evolution of the Rayleigh-Taylor Instability of a Thin Layer," Phys. Rev. Lett. 29, 1429 (1972).

[44] R. Reinovsky, W. Anderson, W. Atchison, C. Ekdahl, R. Faehl, I. Lindemuth, D. Morgan, M. Murillo, J. Stokes, and J. Shlachter, "Instability growth in magnetically imploded high-conductivity cylindrical liners with material strength," IEEE Trans. Plasma Sci. 30, 1764 (2002).

[45] A. R. Miles, "Nonlinear Rayleigh–Taylor instabilities in fast Z pinches," Phys. Plasmas 16, 032702 (2009).

[46] Y. Y. Lau, "Anisotropy and feedthrough in magneto-Rayleigh-Taylor instability," Phys. Rev. E 83 (2011), 10.1103/PhysRevE.83.066405.

[47] P. Zhang, Y. Y. Lau, I. M. Rittersdorf, M. R. Weis, R. M. Gilgenbach, D. Chalenski, and S. A. Slutz, "Effects of magnetic shear on magneto-Rayleigh-Taylor instability," Phys. Plasmas 19, 022703 (2012).

[48] A. L. Velikovich and P. F. Schmit, "Bell-Plesset effects in Rayleigh-Taylor instability of finite-thickness spherical and cylindrical shells," Phys. Plasmas 22, 122711 (2015).

[49] D. E. Ruiz, D. A. Yager-Elorriaga, K. J. Peterson, D. B. Sinars, M. R. Weis, D. G. Schroen, K. Tomlinson, J. R. Fein, and K. Beckwith, "Harmonic Generation and Inverse Cascade in the z-Pinch Driven, Preseeded Multimode, Magneto-Rayleigh-Taylor Instability," Phys. Rev. Lett. 128, 255001 (2022).

[50] D. E. Ruiz and M. Simmons, "Nonlinear analysis of the degradation effects on Z-pinch implosions due to azimuthal magneto-Rayleigh–Taylor instabilities," Phys. Plasmas 32, 082701 (2025).

[51] J. Lehr and P. Ron, "Foundations of Pulsed Power Technology," (Wiley, Piscataway, NJ, 2017) Chap. 3, pp. 1–54, 1st ed.

[52] I. Smith, V. Carboni, A. Miller, R. Crumley, P. Corcoran, P. Spence, W. Rix, W. Powell, P. Sincerny, J. Ennis, and D. Bell, "Fast Marx Generator development for PRS drivers," in *PPPS-2001 Pulsed Power Plasma Science 2001*, Vol. 1 (2001) pp. 582–586 vol.1.

[53] J. Lehr and P. Ron, "Foundations of Pulsed Power Technology," (Wiley, Piscataway, NJ, 2017) Chap. 4, pp. 147–231, 1st ed.

[54] A. P. Shah, P. C. Campbell, S. M. Miller, J. M. Woolstrum, B. J. Sporer, S. G. Patel, N. M. Jordan, R. M. Gilgenbach, and R. D. McBride, "Optimization of switch diagnostics on the MAIZE linear transformer driver," Rev. Sci. Instrum. 90, 124707 (2019).

[55] M. E. Savage, K. LeChien, M. Lopez, B. Stoltzfus, W. Stygar, D. Artery, J. Lott, and P. Corcoran, "Status of the Z pulsed power driver," in *2011 IEEE Pulsed Power Conference* (2011) pp. 983–990.

[56] "Relative permittivity," Wikipedia (2025).

[57] L. Brillouin, "A Theorem of Larmor and Its Importance for Electrons in Magnetic Fields," Phys. Rev. 67, 260 (1945).

[58] W. A. Stygar, "Analytic model of a magnetically insulated transmission line with collisional flow electrons," Phys. Rev. ST Accel. Beams 9 (2006), 10.1103/PhysRevSTAB.9.090401.

[59] D. V. Rose, T. C. Genoni, R. E. Clark, D. R. Welch, and W. A. Stygar, "Electron flow stability in magnetically insulated vacuum transmission lines," Phys. Plasmas 18, 033108 (2011).

[60] R. D. McBride, W. A. Stygar, M. E. Cuneo, D. B. Sinars, M. G. Mazarakis, J. J. Leckbee, M. E. Savage, B. T. Hutsel, J. D. Douglass, M. L. Kiefer, B. V. Oliver, G. R. Laity, M. R. Gomez, D. A. Yager-Elorriaga, S. G. Patel, B. M. Kovalchuk, A. A. Kim, P.-A. Gourdain, S. N. Bland, S. Portillo, S. C. Bott-Suzuki, F. N. Beg, Y. Maron, R. B. Spielman, D. V. Rose, D. R. Welch, J. C. Zier, J. W. Schumer, J. B. Greenly, A. M. Covington, A. M. Steiner, P. C. Campbell, S. M. Miller, J. M. Woolstrum, N. B. Ramey, A. P. Shah, B. J. Sporer, N. M. Jordan, Y. Y. Lau, and R. M. Gilgenbach, "A Primer on Pulsed Power and Linear Transformer Drivers for High Energy Density Physics Applications," IEEE Trans. Plasma Sci. 46, 3928 (2018).

[61] A. Kim, B. Kovalchuk, E. Kumpjak, and N. Zoi, "0.75 MA, 400 ns rise time LTD stage," in *Digest of Technical Papers*, Vol. 2 (IEEE, Monterey, CA, USA, 1999) pp. 955–958.

[62] W. A. Stygar, "Conceptual designs of two petawatt-class pulsed-power accelerators for high-energy-density-physics experiments," Phys. Rev. ST Accel. Beams 18 (2015), 10.1103/PhysRevSTAB.18.110401.

[63] P. C. Campbell, J. M. Woolstrum, F. Antoulinakis, T. M. Jones, D. A. Yager-Elorriaga, S. M. Miller, N. M. Jordan, Y. Y. Lau, R. M. Gilgenbach, and R. D. Mcbride, "Diagnostic and Power Feed Upgrades to the MAIZE Facility," IEEE Trans. Plasma Sci. 46, 3973 (2018).

[64] J. D. Douglass, B. T. Hutsel, J. J. Leckbee, T. D. Mulville, B. S. Stoltzfus, M. L. Wisher, M. E. Savage, W. A. Stygar, E. W. Breden, J. D. Calhoun, M. E. Cuneo, D. J. De Smet, R. J. Focia, R. J. Hohlfelder, D. M. Jaramillo, O. M. Johns, M. C. Jones, A. C. Lombrozo, D. J. Lucero, J. K. Moore, J. L. Porter, S. D. Radovich, S. A. Romero, M. E. Sceiford, M. A. Sullivan, C. A. Walker, J. R. Woodworth, N. T. Yazzie, M. D. Abdalla, M. C. Skipper, and C. Wagner, "100 GW linear transformer driver cavity: Design, simulations, and performance," Phys. Rev. Accel. Beams 21, 120401 (2018).

[65] J. B. Greenly, J. D. Douglas, D. A. Hammer, B. R. Kusse, S. C. Glidden, and H. D. Sanders, "A 1MA, variable risetime pulse generator for high energy density plasma research," Rev. Sci. Instrum. 79, 073501 (2008).

[66] S. V. Lebedev, D. J. Ampleford, S. N. Bland, S. C. Bott, J. P. Chittenden, J. Goyer, C. Jennings, M. G. Haines, G. N. Hall, D. A. Hammer, J. B. A. Palmer, S. A. Pikuz, T. A. Shelkovenko, and T. Christoudias, "Physics of wire array Z-pinch implosions: Experiments at Imperial College," Plasma Phys. Control. Fusion 47, A91 (2005).

[67] B. Bauer, V. Kantsyrev, N. Le Galloudec, R. Presura, G. Sarkisov, A. Shlyaptseva, S. Batie, W. Brinsmead, H. Faretto, B. Le Galloudec, A. Oxner, M. Al-Shorman, D. Fedin, S. Hansen, I. Paraschiv, H. Zheng, D. McCrorey, J. Farley, J. Glassman, and J. De Groot, "Two-terawatt Zebra Z-pinch at the Nevada terawatt facility," in *Digest of Technical Papers. 12th IEEE International Pulsed Power Conference*, Vol. 2 (1999) pp. 1045–1047 vol.2.

[68] R. M. Gilgenbach, L. D. Horton, and R. F. Lucey, "Microsecond Electron Beam Diode Closure Experiments," (1985).

[69] R. M. Gilgenbach, M. R. Gomez, J. C. Zier, W. W. Tang, D. M. French, Y. Y. Lau, M. G. Mazarakis, M. E. Cuneo, M. D. Johnston, B. V. Oliver, T. A. Mehlhorn, A. A. Kim, V. A. Sinebryukhov, B. R. Kusse, and D. A. Hammer, "MAIZE: A 1 MA LTD-Driven Z-Pinch at The University of Michigan," in *AIP Conference Proceedings* (AIP, Alexandria, Virginia (USA), 2009) pp. 259–262.

[70] F. Conti, A. Williams, H. U. Rahman, V. Fadeev, D. P. Higginson, A. Youmans, N. Aybar, E. Ruskov, and F. N. Beg, "Neutron-producing gas puff Z-pinch experiments on a fast, low-impedance, 0.5 MA linear transformer driver," J. Appl. Phys. 136, 095901 (2024).

[71] C. Evans, T. Rocha, W. Warner, J. S. Werdin-Kennicott, S. Palko, M. Brito, J. Chen, R. Beattie-Rossberg, J. Schumer, R. Allen, and S. Portillo, "Development of a fast rise time air-insulated linear transformer driver for use in high energy density physics," Phys. Rev. Accel. Beams 28, 060402 (2025).

[72] P.-A. Gourdain, M. Evans, B. Foy, D. Mager, R. McBride, and R. Spielman, "HADES: A High Amperage Driver for Extreme States," (2017), arXiv:1705.04411 [physics] .

[73] H. Abu-Shawareb, "Achievement of Target Gain Larger than Unity in an Inertial Fusion Experiment," Phys. Rev. Lett. 132, 065102 (2024).

[74] "Fuse - Accelerating the World's Transition to Fusion Energy," https://www.f.energy/.

[75] J. D. Lawson, "Some Criteria for a Power Producing Thermonuclear Reactor," Proc. Phys. Soc. B 70, 6 (1957).

[76] P. Rodriguez-Fernandez, A. Creely, M. Greenwald, D. Brunner, S. Ballinger, C. Chrobak, D. Garnier, R. Granetz, Z. Hartwig, N. Howard, J. Hughes, J. Irby, V. Izzo, A. Kuang, Y. Lin, E. Marmar, R. Mumgaard, C. Rea, M. Reinke, V. Riccardo, J. Rice, S. Scott, B. Sorbom, J. Stillerman, R. Sweeney, R. Tinguely, D. Whyte,

J. Wright, and D. Yuryev, "Overview of the SPARC physics basis towards the exploration of burning-plasma regimes in high-field, compact tokamaks," Nucl. Fusion 62, 042003 (2022).

[77] T. Klinger, T. Andreeva, S. Bozhenkov, C. Brandt, R. Burhenn, B. Buttenschön, G. Fuchert, B. Geiger, O. Grulke, H. Laqua, N. Pablant, K. Rahbarnia, T. Stange, A. von Stechow, N. Tamura, H. Thomsen, Y. Turkin, T. Wegner, I. Abramovic, S. Äkäslompolo, J. Alcuson, P. Aleynikov, K. Aleynikova, A. Ali, A. Alonso, G. Anda, E. Ascasibar, J. Bähner, S. Baek, M. Balden, J. Baldzuhn, M. Banduch, T. Barbui, W. Behr, C. Beidler, A. Benndorf, C. Biedermann, W. Biel, B. Blackwell, E. Blanco, M. Blatzheim, S. Ballinger, T. Bluhm, D. Böckenhoff, B. Böswirth, L.-G. Böttger, M. Borchardt, V. Borsuk, J. Boscary, H.-S. Bosch, M. Beurskens, R. Brakel, H. Brand, T. Bräuer, H. Braune, S. Brezinsek, K.-J. Brunner, R. Bussiahn, V. Bykov, J. Cai, I. Calvo, B. Cannas, A. Cappa, A. Carls, D. Carralero, L. Carraro, B. Carvalho, F. Castejon, A. Charl, N. Chaudhary, D. Chauvin, F. Chernyshev, M. Cianciosa, R. Citarella, G. Claps, J. Coenen, M. Cole, M. Cole, F. Cordella, G. Cseh, A. Czarnecka, K. Czerski, M. Czerwinski, G. Czymek, A. da Molin, A. da Silva, H. Damm, A. de la Pena, S. Degenkolbe, C. Dhard, M. Dibon, A. Dinklage, T. Dittmar, M. Drevlak, P. Drewelow, P. Drews, F. Durodie, E. Edlund, P. van Eeten, F. Effenberg, G. Ehrke, S. Elgeti, M. Endler, D. Ennis, H. Esteban, T. Estrada, J. Fellinger, Y. Feng, E. Flom, H. Fernandes, W. Fietz, W. Figacz, J. Fontdecaba, O. Ford, T. Fornal, H. Frerichs, A. Freund, T. Funaba, A. Galkowski, G. Gantenbein, Y. Gao, J. García Regaña, D. Gates, J. Geiger, V. Giannella, A. Gogoleva, B. Goncalves, A. Goriaev, D. Gradic, M. Grahl, J. Green, H. Greuner, A. Grosman, H. Grote, M. Gruca, C. Guerard, P. Hacker, X. Han, J. Harris, D. Hartmann, D. Hathiramani, B. Hein, B. Heinemann, P. Helander, S. Henneberg, M. Henkel, J. Hernandez Sanchez, C. Hidalgo, M. Hirsch, K. Hollfeld, U. Höfel, A. Hölting, D. Höschen, M. Houry, J. Howard, X. Huang, Z. Huang, M. Hubeny, M. Huber, H. Hunger, K. Ida, T. Ilkei, S. Illy, B. Israeli, S. Jablonski, M. Jakubowski, J. Jelonnek, H. Jenzsch, T. Jesche, M. Jia, P. Junghanns, J. Kacmarczyk, J.-P. Kallmeyer, U. Kamionka, H. Kasahara, W. Kasparek, Y. Kazakov, N. Kenmochi, C. Killer, A. Kirschner, R. Kleiber, J. Knauer, M. Knaup, A. Knieps, T. Kobarg, G. Kocsis, F. Köchl, Y. Kolesnichenko, A. Könies, R. König, P. Kornejew, J.-P. Koschinsky, F. Köster, M. Krämer, R. Krampitz, A. Krämer-Flecken, N. Krawczyk, T. Kremeyer, J. Krom, M. Krychowiak, I. Ksiazek, M. Kubkowska, G. Kühner, T. Kurki-Suonio, P. Kurz, S. Kwak, M. Landreman, P. Lang, R. Lang, A. Langenberg, S. Langish, H. Laqua, R. Laube, S. Lazerson, C. Lechte, M. Lennartz, W. Leonhardt, C. Li, C. Li, Y. Li, Y. Liang, C. Linsmeier, S. Liu, J.-F. Lobsien, D. Loesser, J. Loizu Cisquella, J. Lore, A. Lorenz, M. Losert, A. Lücke, A. Lumsdaine, V. Lutsenko, H. Maaßberg, O. Marchuk, J. Matthew, S. Marsen, M. Marushchenko, S. Masuzaki, D. Maurer, M. Mayer, K. McCarthy, P. McNeely, A. Meier, D. Mellein, B. Mendelevitch, P. Mertens, D. Mikkelsen, A. Mishchenko, B. Missal, J. Mittelstaedt, T. Mizuuchi, A. Mollen, V. Moncada, T. Mönnich, T. Morisaki, D. Moseev, S. Murakami, G. Náfrádi, M. Nagel, D. Naujoks, H. Neilson, R. Neu, O. Neubauer, U. Neuner, T. Ngo, D. Nicolai, S. Nielsen, H. Niemann, T. Nishizawa, R. Nocentini, C. Nührenberg, J. Nührenberg,

S. Obermayer, G. Offermanns, K. Ogawa, J. Ölmanns, J. Ongena, J. Oosterbeek, G. Orozco, M. Otte, L. Pacios Rodriguez, N. Panadero, N. Panadero Alvarez, D. Papenfuß, S. Paqay, E. Pasch, A. Pavone, E. Pawelec, T. Pedersen, G. Pelka, V. Perseo, B. Peterson, D. Pilopp, S. Pingel, F. Pisano, B. Plaum, G. Plunk, P. Pölöskei, M. Porkolab, J. Proll, M.-E. Puiatti, A. Puig Sitjes, F. Purps, M. Rack, S. Récsei, A. Reiman, F. Reimold, D. Reiter, F. Remppel, S. Renard, R. Riedl, J. Riemann, K. Risse, V. Rohde, H. Röhlinger, M. Romé, D. Rondeshagen, P. Rong, B. Roth, L. Rudischhauser, K. Rummel, T. Rummel, A. Runov, N. Rust, L. Ryc, S. Ryosuke, R. Sakamoto, M. Salewski, A. Samartsev, E. Sanchez, F. Sano, S. Satake, J. Schacht, G. Satheeswaran, F. Schauer, T. Scherer, J. Schilling, A. Schlaich, G. Schlisio, F. Schluck, K.-H. Schlüter, J. Schmitt, H. Schmitz, O. Schmitz, S. Schmuck, M. Schneider, W. Schneider, P. Scholz, R. Schrittwieser, M. Schröder, T. Schröder, R. Schroeder, H. Schumacher, B. Schweer, E. Scott, S. Sereda, B. Shanahan, M. Sibilia, P. Sinha, S. Sipliä, C. Slaby, M. Sleczka, H. Smith, W. Spiess, D. Spong, A. Spring, R. Stadler, M. Stejner, L. Stephey, U. Stridde, C. Suzuki, J. Svensson, V. Szabó, T. Szabolics, T. Szepesi, Z. Szökefalvi-Nagy, A. Tancetti, J. Terry, J. Thomas, M. Thumm, J. Travere, P. Traverso, J. Tretter, H. Trimino Mora, H. Tsuchiya, T. Tsujimura, S. Tulipán, B. Unterberg, I. Vakulchyk, S. Valet, L. Vano, B. van Milligen, A. van Vuuren, L. Vela, J.-L. Velasco, M. Vergote, M. Vervier, N. Vianello, H. Viebke, R. Vilbrandt, A. Vorköper, S. Wadle, F. Wagner, E. Wang, N. Wang, Z. Wang, F. Warmer, T. Wauters, L. Wegener, J. Weggen, Y. Wei, G. Weir, J. Wendorf, U. Wenzel, A. Werner, A. White, B. Wiegel, F. Wilde, T. Windisch, M. Winkler, A. Winter, V. Winters, S. Wolf, R. Wolf, A. Wright, G. Wurden, P. Xanthopoulos, H. Yamada, I. Yamada, R. Yasuhara, M. Yokoyama, M. Zanini, M. Zarnstorff, A. Zeitler, D. Zhang, H. Zhang, J. Zhu, M. Zilker, A. Zocco, S. Zoletnik, and M. Zuin, "Overview of first Wendelstein 7-X high-performance operation," Nucl. Fusion 59, 112004 (2019).

[78] R. Post, "The magnetic mirror approach to fusion," Nucl. Fusion 27, 1579 (1987).

[79] T. Roche, S. Dettrick, A. Fontanilla, S. Gupta, M. Onofri, J. A. Romero, L. C. Steinhauer, M. T. Tobin, E. M. Granstedt, L. Galeotti, S. Karbashewski, R. M. Magee, P. Yushmanov, E. Trask, H. Gota, S. Abramov, I. Allfrey, R. Andow, V. Arceo, J. Aviles, D. C. Barnes, M. Beall, N. G. Bolte, D. Bui, F. Ceccherini, R. Clary, T. DeHaas, B. Denlinger, A. Van Drie, P. Feng, D. K. Gupta, K. Hubbard, J. S. Kinley, K. Knapp, B. Koop, S. A. Korepanov, A. Korepanov, C. K. Lau, D. Lieurance, D. MacDonald, D. Madura, J. A. Margarit, J. Margo, P. Marsden Sr, T. Matsumoto, M. P. Meekins, R. Mendoza, R. Michel, H. Monkhorst, M. E. Morehouse, M. Nations, A. Necas, B. S. Nicks, R. Page, E. Parke, J. Paulson, K. Phung, T. W. Rogers, L. Schmitz, J. H. Schroeder, G. N. Settles, A. G. H. Sibley, M. Signorelli, R. J. Smith, G. L. Snitchler, V. Sokolov, Y. Song, G. Strashnoy, L. Tagney, J. B. Titus, J. Ufnal, T. Valentine, C. E. Weixel, S. Weixel, C. White, M. Wollenberg, K. Zhai, S. Ziaei, M. Tuszewski, A. Smirnov, S. Putvinski, T. Tajima, and M. W. Binderbauer, "Generation of field-reversed configurations via neutral beam injection," Nat Commun 16, 3487 (2025).

[80] M. R. Gomez, S. A. Slutz, A. B. Sefkow, D. B. Sinars, K. D. Hahn, S. B. Hansen,

E. C. Harding, P. F. Knapp, P. F. Schmit, C. A. Jennings, T. J. Awe, M. Geissel, D. C. Rovang, G. A. Chandler, G. W. Cooper, M. E. Cuneo, A. J. Harvey-Thompson, M. C. Herrmann, M. H. Hess, O. Johns, D. C. Lamppa, M. R. Martin, R. D. McBride, K. J. Peterson, J. L. Porter, G. K. Robertson, G. A. Rochau, C. L. Ruiz, M. E. Savage, I. C. Smith, W. A. Stygar, and R. A. Vesey, "Experimental Demonstration of Fusion-Relevant Conditions in Magnetized Liner Inertial Fusion," Phys. Rev. Lett. 113, 155003 (2014).

[81] A. J. Harvey-Thompson, M. E. Geissel, W. E. Lewis, D. A. Yager-Elorriaga, M. R. Weis, C. A. Jennings, J. R. Fein, D. J. Ampleford, M. R. Gomez, E. C. Harding, S. B. Hansen, D. E. Bliss, G. A. Chandler, G. S. Dunham, E. S. Field, B. R. Galloway, M. Glinsky, K. D. Hahn, P. F. Knapp, D. C. Lamppa, L. M. Lucero, M. A. Mangan, R. R. Paguio, L. Perea, K. J. Peterson, J. L. Porter, P. K. Rambo, G. K. Robertson, G. A. Rochau, D. E. Ruiz, C. L. Ruiz, M. A. Schaeuble, J. Schwarz, J. E. Shores, D. B. Sinars, S. A. Slutz, G. E. Smith, I. C. Smith, C. S. Speas, K. Whittemore, and E. P. Yu, "Development of a high performance MagLIF target platform using high aspect ratio coated liners and low-mix laser preheat," Phys. Plasmas 31, 072711 (2024).

[82] S. A. Slutz, M. C. Herrmann, R. A. Vesey, A. B. Sefkow, D. B. Sinars, D. C. Rovang, K. J. Peterson, and M. E. Cuneo, "Pulsed-power-driven cylindrical liner implosions of laser preheated fuel magnetized with an axial field," Phys. Plasmas 17, 056303 (2010).

[83] M. R. Gomez, S. A. Slutz, C. A. Jennings, D. J. Ampleford, M. R. Weis, C. E. Myers, D. A. Yager-Elorriaga, K. D. Hahn, S. B. Hansen, E. C. Harding, A. J. Harvey-Thompson, D. C. Lamppa, M. Mangan, P. F. Knapp, T. J. Awe, G. A. Chandler, G. W. Cooper, J. R. Fein, M. Geissel, M. E. Glinsky, W. E. Lewis, C. L. Ruiz, D. E. Ruiz, M. E. Savage, P. F. Schmit, I. C. Smith, J. D. Styron, J. L. Porter, B. Jones, T. R. Mattsson, K. J. Peterson, G. A. Rochau, and D. B. Sinars, "Performance Scaling in Magnetized Liner Inertial Fusion Experiments," Phys. Rev. Lett. 125, 155002 (2020).

[84] D. C. Rovang, D. C. Lamppa, M. E. Cuneo, A. C. Owen, J. McKenney, D. W. Johnson, S. Radovich, R. J. Kaye, R. D. McBride, C. S. Alexander, T. J. Awe, S. A. Slutz, A. B. Sefkow, T. A. Haill, P. A. Jones, J. W. Argo, D. G. Dalton, G. K. Robertson, E. M. Waisman, D. B. Sinars, J. Meissner, M. Milhous, D. N. Nguyen, and C. H. Mielke, "Pulsed-coil magnet systems for applying uniform 10–30 T fields to centimeter-scale targets on Sandia's Z facility," Rev. Sci. Instrum. 85, 124701 (2014).

[85] R. D. McBride, S. A. Slutz, C. A. Jennings, D. B. Sinars, M. E. Cuneo, M. C. Herrmann, R. W. Lemke, M. R. Martin, R. A. Vesey, K. J. Peterson, A. B. Sefkow, C. Nakhleh, B. E. Blue, K. Killebrew, D. Schroen, T. J. Rogers, A. Laspe, M. R. Lopez, I. C. Smith, B. W. Atherton, M. Savage, W. A. Stygar, and J. L. Porter, "Penetrating Radiography of Imploding and Stagnating Beryllium Liners on the Z Accelerator," Phys. Rev. Lett. 109, 135004 (2012).

[86] D. Mikitchuk, C. Stollberg, R. Doron, E. Kroupp, Y. Maron, H. R. Strauss, A. L. Velikovich, and J. L. Giuliani, "Mitigation of Instabilities in a Z-Pinch Plasma by a Preembedded Axial Magnetic Field," IEEE Trans. Plasma Sci. 42, 2524 (2014).

[87] L. Atoyan, D. A. Hammer, B. R. Kusse, T. Byvank, A. D. Cahill, J. B. Greenly, S. A. Pikuz, and T. A. Shelkovenko, "Helical plasma striations in liners in the presence of an external axial magnetic field," Phys. Plasmas 23, 022708 (2016).

[88] D. A. Yager-Elorriaga, P. Zhang, A. M. Steiner, N. M. Jordan, Y. Y. Lau, and R. M. Gilgenbach, "Seeded and unseeded helical modes in magnetized, non-imploding cylindrical liner-plasmas," Phys. Plasmas 23, 101205 (2016).

[89] E. P. Yu, T. J. Awe, K. R. Cochrane, K. J. Peterson, K. C. Yates, T. M. Hutchinson, M. W. Hatch, B. S. Bauer, K. Tomlinson, and D. B. Sinars, "Seeding the Electrothermal Instability through a Three-Dimensional, Nonlinear Perturbation," Phys. Rev. Lett. 130, 255101 (2023).

[90] T. M. Hutchinson, "Experimental observation of the stratified electrothermal instability on aluminum with thickness greater than a skin depth," Phys. Rev. E 97 (2018), 10.1103/PhysRevE.97.053208.

[91] J. M. Woolstrum, D. E. Ruiz, N. D. Hamlin, K. Beckwith, and M. R. Martin, "Hall interchange instability as a seed for helical magneto-Rayleigh–Taylor instabilities in magnetized liner inertial fusion Z-Pinches scaled from Z-Machine parameters to a next generation pulsed power facility," Phys. Plasmas 30, 072712 (2023).

[92] J. M. Woolstrum, C. E. Seyler, and R. D. McBride, "Hall instability driven seeding of helical magneto-Rayleigh–Taylor instabilities in axially premagnetized thin-foil liner Z-pinch implosions," Phys. Plasmas 29, 122701 (2022).

[93] D. D. Ryutov, T. J. Awe, S. B. Hansen, R. D. McBride, K. J. Peterson, D. B. Sinars, and S. A. Slutz, "Effect of axial magnetic flux compression on the magnetic Rayleigh-Taylor instability (theory)," AIP Conference Proceedings 1639, 63 (2014).

[94] C. E. Seyler, M. R. Martin, and N. D. Hamlin, "Helical instability in MagLIF due to axial flux compression by low-density plasma," Phys. Plasmas 25, 062711 (2018).

[95] N. Bennett, D. R. Welch, K. Cochrane, K. Leung, C. Thoma, M. E. Cuneo, and G. Frye-Mason, "Electrode Plasma Formation and Melt in {{Z}}-Pinch Accelerators," Phys. Rev. Accel. Beams 26, 040401 (2023).

[96] D. Zimmer, M. R. Gomez, N. Bennett, C. A. Jennings, C. E. Myers, D. C. Lamppa, F. Conti, and F. N. Beg, "Understanding the impact of an applied axial magnetic field on efficient current coupling on the Z machine," Phys. Rev. Accel. Beams 27, 100401 (2024).

[97] M. R. Gomez, R. M. Gilgenbach, M. E. Cuneo, C. A. Jennings, R. D. McBride, E. M. Waisman, B. T. Hutsel, W. A. Stygar, D. V. Rose, and Y. Maron, "Experimental study of current loss and plasma formation in the Z machine post-hole convolute," Phys. Rev. Accel. Beams 20, 010401 (2017).

[98] N. Bennett, D. Lamppa, A. Porwitzky, C. Jennings, D. Welch, E. Evstatiev, C. Myers, K. Chandler, J. Banasek, S. Patel, E. Watson, D. Yager-Elorriaga, M. Savage, M. Johnston, M. Hess, D. Rose, and M. Cuneo, *MRT 7365: Power Flow Physics and Key Physics Phenomena*, Tech. Rep. SAND–2023-10724, 2430180 (2023).

[99] M. Gomez, D. Yager-Elorriaga, M. Weis, C. Jennings, N. Hamlin, M. Martin, G. Shipley, E. Yu, D. Ampleford, and K. Beckwith, "Investigating the role of magnetic flux compression in the formation of helical structures in axially magnetized implosions." in *Presentation at the APS DPP 2022 in Spokane, WA.* (US DOE, Spokane, WA, 2022).

[100] R. D. McBride, S. A. Slutz, R. A. Vesey, M. R. Gomez, A. B. Sefkow, S. B. Hansen, P. F. Knapp, P. F. Schmit, M. Geissel, A. J. Harvey-Thompson, C. A. Jennings, E. C. Harding, T. J. Awe, D. C. Rovang, K. D. Hahn, M. R. Martin, K. R. Cochrane, K. J. Peterson, G. A. Rochau, J. L. Porter, W. A. Stygar, E. M. Campbell, C. W. Nakhleh, M. C. Herrmann, M. E. Cuneo, and D. B. Sinars, "Exploring magnetized liner inertial fusion with a semi-analytic model," Phys. Plasmas 23, 012705 (2016).

[101] R. D. McBride and S. A. Slutz, "A semi-analytic model of magnetized liner inertial fusion," Physics of Plasmas 22, 052708 (2015).

[102] J. Narkis, H. U. Rahman, J. C. Valenzuela, F. Conti, R. D. McBride, D. Venosa, and F. N. Beg, "A semi-analytic model of gas-puff liner-on-target magneto-inertial fusion," Phys. Plasmas 26, 032708 (2019).

[103] Y. Lawrence, J. R. Davies, R. D. McBride, and A. B. Sefkow, "Transport coefficient sensitivities in a semi-analytic model for magnetized liner inertial fusion," Phys. Plasmas 31, 112703 (2024).

[104] S. A. Sorokin, "High-Magnetic-Field Generation by Magnetic Flux Compression in Imploding Plasma Liners," IEEE Trans. Plasma Sci. 38, 1723 (2010).

[105] D. E. Bliss, R. D. McBride, M. Martin, and T. Intrator, "Direct Measurement of Magnetic Flux Compression in Imploding Liners by Faraday Rotation." (Sandia National Laboratories (SNL-NM), Albuquerque, NM (United States), 2017).

[106] M. Cvejić, D. Mikitchuk, E. Kroupp, R. Doron, P. Sharma, Y. Maron, A. L. Velikovich, A. Fruchtman, I. E. Ochs, E. J. Kolmes, and N. J. Fisch, "Self-Generated Plasma Rotation in a Z-Pinch Implosion with Preembedded Axial Magnetic Field," Phys. Rev. Lett. 128, 015001 (2022).

[107] E. S. Lavine, A. Rososhek, J. Angel, E. Freeman, C. Chen, W. M. Potter, H. Wilhelm, D. A. Hammer, and B. R. Kusse, "Energetics of Triple-Nozzle Gas-Puff Z-Pinch Implosions on COBRA," IEEE Trans. Plasma Sci. 52, 4817 (2024).

[108] A. T. Elshafiey, J. H. Musk, S. A. Pikuz, T. A. Shelkovenko, and D. A. Hammer, "Studies and optimization of hybrid X-pinches," Plasma Res. Express 3, 015004 (2021).

[109] L. Rayleigh, Cambridge University Press, London, **2**, 200 (1900).

[110] G. Taylor, "The instability of liquid surfaces when accelerated in a direction perpendicular to their planes. I," Proc. R. Soc. Lond. A 201, 192 (1950).

[111] D. Sharp, "An overview of Rayleigh-Taylor instability," Physica D: Nonlinear Phenomena 12, 3 (1984).

[112] M. R. Weis, P. Zhang, Y. Y. Lau, P. F. Schmit, K. J. Peterson, M. Hess, and R. M. Gilgenbach, "Coupling of sausage, kink, and magneto-Rayleigh-Taylor instabilities in a cylindrical liner," Phys. Plasmas 22, 032706 (2015).

[113] P. F. Schmit, A. L. Velikovich, R. D. McBride, and G. K. Robertson, "Controlling Rayleigh-Taylor Instabilities in Magnetically Driven Solid Metal Shells by Means of a Dynamic Screw Pinch," Physical Review Letters 117, 205001 (2016).

[114] G. A. Shipley, C. A. Jennings, and P. F. Schmit, "Design of dynamic screw pinch experiments for magnetized liner inertial fusion," Phys. Plasmas 26, 102702 (2019).

[115] P. C. Campbell, "Stabilization of Liner Implosions via a Dynamic Screw Pinch," Physical Review Letters 125 (2020), 10.1103/PhysRevLett.125.035001.

[116] P. C. Campbell, *Stability and Power Coupling in Dynamic Screw Pinch Plasmas*, Ph.D. thesis, University of Michigan (2020).

[117] P. C. Campbell, T. M. Jones, J. M. Woolstrum, N. M. Jordan, P. F. Schmit, A. L. Velikovich, J. B. Greenly, W. M. Potter, E. S. Lavine, B. R. Kusse, D. A. Hammer, and R. D. McBride, "Liner implosion experiments driven by a dynamic screw pinch," Phys. Plasmas 28, 082707 (2021).

[118] G. A. Shipley, D. E. Ruiz, C. A. Jennings, D. A. Yager-Elorriaga, and P. F. Schmit, "Numerical study of implosion instability mitigation in magnetically driven solid liner dynamic screw pinches," Phys. Plasmas 31, 022704 (2024).

[119] D. B. Sinars, S. A. Slutz, M. C. Herrmann, R. D. McBride, M. E. Cuneo, K. J. Peterson, R. A. Vesey, C. Nakhleh, B. E. Blue, K. Killebrew, D. Schroen, K. Tomlinson, A. D. Edens, M. R. Lopez, I. C. Smith, J. Shores, V. Bigman, G. R. Bennett, B. W. Atherton, M. Savage, W. A. Stygar, G. T. Leifeste, and J. L. Porter, "Measurements of Magneto-Rayleigh-Taylor Instability Growth during the Implosion of Initially Solid Al Tubes Driven by the 20-MA, 100-ns Z Facility," Phys. Rev. Lett. 105, 185001 (2010).

[120] S. Atzeni and J. Meyer-ter-Vehn, "The Physics of Inertial Fusion: BeamPlasma Interaction, Hydrodynamics, Hot Dense Matter," (Clarendon Press, New York, 2004) Chap. 8, pp. 284–285.

[121] A. Shah, *Effects of Pre-Ionization on the Gas-Puff Z-Pinch*, Ph.D. thesis, University of Michigan (2022).

[122] G. Dowhan, *Characterization of X-Pinches on the MAIZE Linear Transformer Driver*, Thesis, University of Michigan (2023).

[123] G. V. Dowhan, A. P. Shah, B. J. Sporer, N. M. Jordan, S. N. Bland, S. V. Lebedev, R. A. Smith, L. Suttle, S. A. Pikuz, and R. D. McBride, "High-magnification Faraday rotation imaging and analysis of X-pinch implosion dynamics," Review of Scientific Instruments 95, 043504 (2024).

[124] J. Greenly, M. Martin, I. Blesener, D. Chalenski, P. Knapp, R. McBride, B. R. Kusse, and D. A. Hammer, "The Role of Flux Advection in the Development of the Ablation Streams and Precursors of Wire Array Z-pinches," in *AIP Conference Proceedings* (AIP, Alexandria, Virginia (USA), 2009) pp. 53–56.

[125] "Ultra High Speed Framing," https://www.invisiblevision.com/products/ultra-high-speed-framing/.

[126] "Introduction to Modulation Transfer Function," https://www.edmundoptics.com/knowledge-center/application-notes/optics/introduction-to-modulation-transfer-function/.

[127] "NL122 - EKSPLA | Laser," https://www.gophotonics.com/products/lasers/ekspla/29-268-nl122.

[128] S. S. Harilal, M. C. Phillips, D. H. Froula, K. K. Anoop, R. C. Issac, and F. N. Beg, "Optical diagnostics of laser-produced plasmas," Rev. Mod. Phys. 94, 035002 (2022).

[129] I. H. Hutchinson, "Principles of Plasma Diagnostics," (Cambridge University Press, New York, 2002) Chap. 4, pp. 104–133, 2nd ed.

[130] T. J. Smith, P. C. Campbell, G. V. Dowhan, N. M. Jordan, M. D. Johnston, M. E. Cuneo, G. R. Laity, and R. D. McBride, "Additively manufactured electrodes for plasma and power-flow studies in high-power transmission lines on the 1-MA MAIZE facility," Rev. Sci. Instrum. 92, 053550 (2021).

[131] A. G. Rousskikh, A. S. Zhigalin, V. I. Oreshkin, V. Frolova, A. L. Velikovich, G. Yu. Yushkov, and R. B. Baksht, "Effect of the axial magnetic field on a metallic gas-puff pinch implosion," Phys. Plasmas 23, 063502 (2016).

[132] D. A. Yager-Elorriaga, A. M. Steiner, S. G. Patel, N. M. Jordan, Y. Y. Lau, and R. M. Gilgenbach, "Technique for fabrication of ultrathin foils in cylindrical geometry for liner-plasma implosion experiments with sub-megaampere currents," Rev. Sci. Instrum. 86, 113506 (2015).

[133] J. M. Woolstrum, D. A. Yager-Elorriaga, P. C. Campbell, N. M. Jordan, C. E. Seyler, and R. D. McBride, "Extended magnetohydrodynamics simulations of thin-foil Z-pinch implosions with comparison to experiments," Physics of Plasmas 27, 092705 (2020).

[134] J. Woolstrum, *Hall Magnetohydrodynamics Simulations of Hall-Physics-Driven Effects in Low-Density Plasmas Surrounding Dense Z-Pinch Liners*, Thesis, University of Michigan (2022).

[135] J. D. Douglass, S. A. Pikuz, T. A. Shelkovenko, D. A. Hammer, S. N. Bland, S. C. Bott, and R. D. McBride, "Structure of the dense cores and ablation plasmas in the initiation phase of tungsten wire-array Z pinches," Physics of Plasmas 14, 012704 (2007).

[136] J. P. Chittenden, R. Aliaga Rossel, S. V. Lebedev, I. H. Mitchell, M. Tatarakis, A. R. Bell, and M. G. Haines, "Two-dimensional magneto-hydrodynamic modeling of carbon fiber Z-pinch experiments," Physics of Plasmas 4, 4309 (1997).

[137] B. A. Remington, S. W. Haan, S. G. Glendinning, J. D. Kilkenny, D. H. Munro, and R. J. Wallace, "Large growth, planar Rayleigh–Taylor experiments on Nova," Phys. Fluids 4, 967 (1992).

[138] B. A. Remington, S. V. Weber, M. M. Marinak, S. W. Haan, J. D. Kilkenny, R. J. Wallace, and G. Dimonte, "Single-mode and multimode Rayleigh–Taylor experiments on Nova," Phys. Plasmas 2, 241 (1995).

[139] C. E. Seyler and M. R. Martin, "Relaxation model for extended magnetohydrodynamics: Comparison to magnetohydrodynamics for dense Z-pinches," Physics of Plasmas 18, 012703 (2011).

[140] B. Fryxell, K. Olson, P. Ricker, F. X. Timmes, M. Zingale, D. Q. Lamb, P. MacNeice, R. Rosner, J. W. Truran, and H. Tufo, "FLASH: An Adaptive Mesh Hydrodynamics Code for ModelingAstrophysical Thermonuclear Flashes," The Astrophysical Journal Supplement Series 131, 273 (2000).